Design and Evaluation of Support Structures in Selective Laser Melting: A Practical Engineering Approach to Improved Performance

A Thesis Submitted for the Degree of Doctor of Philosophy

By

Antonios Dimopoulos

Department of Mechanical and Aerospace Engineering,
Brunel University London

Principal Supervisor: Prof Tat-Hean Gan
Supervisor: Dr Panagiotis Chatzakos

Submission Date: 15-11-2024

Abstract

Additive Manufacturing (AM), particularly Powder Bed Fusion-Laser Beam for Metals (PBF-LB/M) or Selective Laser Melting (SLM), has revolutionised various industries, including aerospace, automotive, and medical, by enabling the production of complex, thin, lightweight, and customized metal parts. Despite its advantages, key challenges remain in optimizing and designing support structures, which are critical for ensuring part quality, reducing defects caused by thermal stresses, and minimizing post-processing efforts and overall costs. This thesis systematically investigates block-type support structures, evaluating their performance through a Multi-Response Optimization (MRO) approach, experimental studies, and numerical simulations, while comparing them with alternative support geometries, including line, contour, and cone-type supports. It aims to address key challenges in SLM, such as support generation, support removal effort, material consumption, and relevant defects.

The research is organized around three key objectives. First, it introduces a framework using multi-response optimization approach to evaluate block-type support structures, aiming to propose optimized geometries that minimize support volume, prevent warping deformation, and enhance support removal efficiency. For layers aligned parallel to the build plate (e.g., 0° overhangs), the findings revealed that block-type supports with a tooth height of 2.7 mm, a tooth top length of 0.2 mm, and a hatch distance of 0.7 mm provide an optimal balance between mechanical stability, minimal warping deformation, material consumption, and ease of removal. Conversely, for layers inclined relative to the build plate (e.g., 25°- 45° overhangs), the optimal balance was observed with a tooth height of 4 mm, a tooth top length of 0.05 mm, and a hatch distance of 2.5 mm.

Second, thermo-mechanical simulations examine the thermal behaviour of alternative support geometries, including block, line, contour, and cone-type supports, with the goal of mitigating defects caused by thermal stresses and identifying configurations that offer optimal thermal performance. The outcome, consisting of plots and tables, provide valuable guidelines for achieving effective printing and ensuring the production of defect-free parts. Additionally, the numerically optimized results of this study were validated through experimental testing. It was found that block-type support structures, despite their larger volume and the challenges associated with their removal, demonstrate slightly improved thermal behaviour compared to the other support types analysed.

Finally, the study presents an innovative design framework for optimising the SLM workflow, introducing a web-based platform for automated support generation, optimization, and thermal performance assessment. This platform serves as a valuable research tool for managing and visualizing experimental data, allowing researchers and professionals to improve AM production and produce defect-free, high-quality prints while reducing printing time and costs. By integrating and visualizing experimental data and simulation results, the platform allows users to import 3D models, adjust orientation, generate and visualize optimized support structures, and export ready-to-print designs. Moreover, this tool is designed to be accessible to non-expert users, simplifying complex support design decisions while effectively reducing trial-and-error approaches and streamlining the SLM process. Validation on a small L-shaped mounting bracket demonstrates that the platform effectively generates and visualises block-type support structures for imported parts while facilitating successful SLM printing. The printed outcome exhibited excellent dimensional accuracy, minimal warping deformation, and easy support removal (achieved within 2-4 minutes of manual effort) along with satisfactory surface roughness.

By leveraging experimental, optimization, and computational tools, such as SLM 3D printing machines, Design-Expert, and COMSOL Multiphysics, this thesis presents a structured methodology for optimizing metal support structures, reducing defects, and enhancing the efficiency of the SLM process. These contributions not only address current challenges but also create opportunities for future advancements in the field, such as improved quality control during pre-printing preparations, ultimately establishing SLM as a viable production method.

Table of Contents

List of Figures

List of Tables

List of Abbreviations

Abbreviation:	Definition
2D:	Two Dimensional
3D:	Three Dimensional
ANOVA:	Analysis of Variance
AM:	Additive Manufacturing
API:	Application Programming Interface
ASTM:	American Society for Testing and Materials
CAD:	Computer-Aided Design
CCD:	Central Composite Design
DC motor:	Direct Current motor
DFAM:	Design for Additive Manufacturing
DMLS:	Direct Metal Laser Sintering
DOE:	Design of Experiments
DOM:	Document Object Model
EBM:	Electron Beam Melting
EDM:	Electrical Discharge Machining
ET-Sup:	Escaping Tree-Support
FDM:	Fused Deposition Modelling
FEA:	Finite Element Analysis
FEM:	Finite Element Method
GUI:	Graphical User Interface
HTTP:	HyperText Transfer Protocol
IN625:	Inconel alloy 625
ISO:	International Organization for Standardization
JMMP:	Journal of Manufacturing and Materials Processing
LOF:	Lack-of-fusion
LPBF:	Laser Powder Bed Fusion
MDPI:	Multidisciplinary Digital Publishing Institute
MOGA-II:	Multi-Objective Genetic Algorithm II

MRO:	Multi-response Optimization
PBF:	Powder Bed Fusion
PBF-LB/M:	Powder Bed Fusion-Laser Beam for Metals
PI:	Producibility Index
PLY:	Polygon File Format
REST API:	Representational State Transfer Application Programming Interface
RSM:	Response Surface Methodology
RVE:	Representative Volume Element
SDKs:	Software Development Kits
SiC:	Silicon Carbide
SLA	Stereolithography
SLM:	Selective Laser Melting
SLS:	Selective Laser Sintering
STEP:	Standard for the Exchange of Product model data
STL:	Stereolithography
TEM:	Transverse Electromagnetic Mode
TMA:	Thermal Mechanical Analysis
TO:	Topology Optimization
VM:	Virtual Machine
WebGL:	Web Graphics Library

List of Symbols

Notation:	Definition
%:	Percent
ºC:	Degrees Celsius
α:	Coefficient of thermal expansion
ε_{inel}:	Thermal expansion
λ:	Conductivity coefficient
µm:	Micrometres
ρ:	Density
Al:	Aluminium
C:	Carbon
c:	Heat capacity
cm^2:	Square centimeters
Cr:	Chromium
D:	Desirability score
d:	Diametrical distance
d_1:	Beam diameter
E:	Young's Modulus
E_v:	Energy density
Fe:	Iron
GPa:	Gigapascals
g:	Grams
g/cm^3:	Grams per cubic centimeter
I_0:	Irradiance
h:	Hatch distance (laser parameters)
h:	Convection heat transfer coefficient (Fourier Law)
J:	Joules
J/g°C:	Joules per gram per degree Celsius
J/mm^3:	Joules per cubic millimetre
K:	Degrees Kelvin

Mg:	Magnesium
MPa:	Megapascals
mA:	Milliamperes
mm:	Millimetres
mm/s:	Millimetres per second
Ni:	Nickel
P:	Laser power
q:	Internal heat source
r:	Radial distance
r_0:	Spot radius
Si:	Silicon
T:	Temperature
T_0:	Powder bed initial temperature
T_e:	Environment temperature
T_{ref}:	Reference temperature
Ti:	Titanium
t:	Powder layer thickness
V:	Vanadium
v:	Scanning speed/velocity
W:	Watt
W/mK:	Watts per meter per Kelvin
wt%:	Weight percent (or weight percentage)

Author's Declarations

I declare that the work presented in this thesis is my own, except where due acknowledgment is made.

I declare that this thesis has not been submitted, in whole or in part, for any degree or diploma at any other institution.

I declare that all sources of information have been appropriately referenced, and the experimental work was conducted by me unless otherwise stated.

I declare that any assistance, collaboration, or support received during the research and writing process has been clearly acknowledged in the relevant sections of this thesis.

I take full responsibility for the content, interpretation, and analysis presented in this document.

Antonios Dimopoulos
Brunel University London
15/11/2024

Acknowledgements

First of all, I would like to express my deepest gratitude to my supervisors, **Prof. Tat-Hean Gan** and **Dr. Panagiotis Chatzakos**, for their invaluable guidance, insightful feedback, and continuous support throughout the course of this research.

I would also like to express my appreciation and gratefulness to my sponsor '**Lloyd's Register Foundation**'. The work was enabled through and undertaken at the **National Structural Integrity Research Centre** (NSIRC), a postgraduate engineering facility for industry-led research into structural integrity, established and managed by **TWI Ltd**. through a network of both national and international universities.

I am profoundly grateful to **Brunel University London** and the **Department of Mechanical and Aerospace Engineering** for providing financial support and resources that were essential in making this research possible.

Special thanks to my colleagues and friends, **Giorgos Chryssinas**, **Dimitra Mavroforaki**, and **Mohamad Salimi**, for their invaluable assistance and collaboration throughout the research process. Their support, whether through insightful discussions, technical advice, or general encouragement, contributed greatly to the completion of this work.

I would also like to thank **TWI Hellas**, **Kanfit3D**, and **FAMA3D** for providing the equipment, materials, and technical support necessary for conducting the experiments in this research. Their contributions were essential to the successful completion of the experimental work.

Finally, I would like to express my heartfelt appreciation to my **family**, for their unwavering encouragement, patience, and understanding during the long hours of research and writing.

Thank you to all who contributed, both directly and indirectly, to the completion of this thesis.

Antonios Dimopoulos
Brunel University London, 2024

Chapter 1: Introduction

1.1 Introduction and Research Motivation

Additive Manufacturing (AM), also known as professional or industrial 3D printing, is a relatively new technology within the broader manufacturing industry. In recent years, it has gained significant prominence due to its flexibility and wide range of applications across various sectors [1]. Precedence Research reports that additive manufacturing has grown into an $18 billion industry and is now utilized by major aerospace and automotive companies, military and healthcare organizations, architectural and industrial design firms, small-scale manufacturers, and research institutions and universities [2].

Aligned with its name, AM builds material layer by layer to create the final shape of a part, effectively forming it "from scratch". Additionally, it can produce complex geometries that traditional manufacturing methods cannot achieve, create virtually any shape without the need for changing tools, is eco-friendly with nearly zero waste, enables single-build assemblies to reduce time and labour, supports in-house production to mitigate supply chain vulnerabilities, and is cost-effective for producing unique and customized products [1]. AM utilizes a variety of technologies, including methods that extrude plastics through a nozzle, those that use light to solidify liquid plastics in a vat, and techniques that employ lasers to fuse powdered materials into solid forms, among other approaches.

Selective Laser Melting (SLM), also known as Laser Powder Bed Fusion (LPBF) or, according to ISO/ASTM standards [3], Powder Bed Fusion-Laser Beam for Metals (PBF-LB/M), is one of the most promising and rapidly evolving AM technologies. In SLM, 3D printers employ high-powered lasers to selectively melt metal powder. The melted particles fuse together layer by layer at a molecular level, building up the model until it is fully formed and homogeneous. It is effective in producing optimized geometries, high-performance parts, complex features, and lightweight components using a wide range of metals such as titanium, aluminium, copper, nickel, and stainless steel. This technology is widely used across various industries, including aerospace, automotive, medical, energy, and machining.

Subsequently, pre-processing activities such as preparing a digital Computer-Aided Design (CAD) file, determining 3D print orientation, generating support structures, and setting process parameters, along with post-processing tasks including support removal, surface cleaning, and heat treatment, are crucial for ensuring efficient prints and non-defective parts. For instance, optimizing print orientation can reduce printing time and costs, while support structures are essential for stabilizing the part and managing thermal stresses. Laser power and laser speed, among other parameters, are essential for achieving optimal printing results. Additionally, effective support removal and surface cleaning significantly influence the quality of the final part, as well as labour hours and overall production costs.

However, successfully implementing these tasks, particularly in terms of support structure generation and optimization, demands a deep understanding of AM principles. Therefore, there is a crucial demand for integrated research tools, methodologies, and comprehensive experimental approaches that can optimise the printing process and post-processing [4]. This demand motivates research into the effect of support structures on both geometric and thermal performance, aiming to develop innovative strategies and tools that enhance the efficiency and reliability of SLM processes.

To address this challenge, this research introduces a web-based platform designed to automate and optimize support structure generation in SLM. By integrating data from experimental studies and numerical simulations, this solution aims to reduce costs, enhance print reliability, and provide an accessible tool for manufacturers, researchers, and engineers looking to optimize and refine their SLM workflows. The development of this platform represents a key practical outcome of this research, bridging the gap between theoretical advancements and industrial implementation.

1.2 Problem Statement

As previously mentioned, SLM has revolutionised industries such as aerospace, automotive, machining, and healthcare by enabling the production of complex, lightweight, thin, and customised metal parts. However, despite its rapid growth and widespread adoption, significant challenges remain in optimizing key aspects, particularly the construction of overhang structures and mitigating warping deformation caused by thermal stresses. Support structures play a critical role in SLM, as they anchor the part to the build plate, stabilize it during printing, provide a suitable platform for overhanging surfaces, and act as heat sinks to control cooling and ensure the part's dimensional accuracy. Insufficient or absent supports result in defective or collapsed parts, while the addition of unnecessary supports increases post-processing, the time and effort required to remove them, the risk of damaging the part, and material consumption. In SLM, various types of support structures exist, including block, point, web, contour, line, and cone supports, each suited to different overhang geometries and process requirements. For instance, block supports are commonly used for large, volumetric parts, such as tooling components, due to their high stability, while line supports are preferred for intricate metal components, such as those found in automotive applications, due to their ease of removal.

Existing approaches employed by companies, researchers, and users involved in AM to optimize SLM performance, including print orientation, process parameters, support structures, and post-processing, often require expert knowledge and extensive in-house experimentation, following a repeatable trial-and-error approach. These experiments typically involve printing multiple test geometries with varying support and process parameters to evaluate their impact on part stability, material consumption, and ease of removal. Each iteration requires significant machine time, material usage, and post-processing labour, making the process costly and time-consuming. For example, in aerospace applications, manufacturers frequently conduct iterative builds on turbine blades or lightweight lattice structures to fine-tune support configurations, often resulting in scrap parts if warping or detachment occurs [5], [6]. Similarly, in the medical field, implant manufacturers optimize support structures for patient-specific geometries, requiring repeated testing to balance mechanical integrity with biocompatibility [7].

Current methods and conventional support designs [4] relies on predefined geometric guidelines (usually derived from previous prints) without integrating thermal or mechanical performance considerations. This can result in non-optimal configurations that either overuse material, increasing costs and post-processing time, or fail to provide sufficient support, leading to collapsed or defective parts. Additionally, computational simulation-based approaches, demand significant expertise in finite element modelling (FEM) and validation, making them inaccessible for non-expert users. Consequently, there is a need for an approach that minimizes reliance on trial-and-error, integrates performance-based optimisation, and automates the design process to enhance efficiency in SLM functionality and support generation.

This research initially investigates the performance of block-type support structures for SLM through multi-response optimization. It aims to optimise support parameters by reducing post-processing efforts, material usage, and printing defects. Specifically, the reduction of post-processing steps, with a primary focus on support removal, is targeted. This reduction is quantified using experimental metrics such as support removal time, volume of material used, and geometric accuracy measurements obtained after printing. The study also examines various support types based on their thermal behaviour to identify optimal geometries and parameters, minimising defective parts in SLM. Additionally, it introduces an innovative framework for efficient additive manufacturing, based on a web-based platform for automated support generation and optimization, leveraging collected experimental data. This approach proposes key principles for preserving SLM’s mass-production potential without requiring expert knowledge, effectively balancing minimal printing time and cost with zero-defect components.

1.3 Research Objectives

The problem statement highlights key challenges in SLM, including the inefficient knowledge on optimal support configurations, the extensive reliance on experimental trial-and-error approaches, and the lack of thermal and mechanical performance considerations in support design. Based on the literature reviewed in Chapter 2, support structures have not been thoroughly investigated regarding their impact on producing defect-free parts, nor their role in minimizing material usage, printing time, and post-processing requirements, such as ease of support removal.

The high costs associated with industrial SLM machines, specialized software, and post-processing has significantly hindered extensive experimental research in this field. According to a report by CADS Additive, low-end metal 3D printers start at approximately $200.000, mid-range machines are around $500.000, and high-end models can reach $1.5 million or more [8]. Additionally, post-processing units, essential for completing metal parts, can add significantly to the overall expense. For example, the combined cost of a printer and its necessary post-processing units can be around $165.000 [9]. These substantial financial requirements contribute to the limited number of studies focusing on optimizing support structures, despite their critical role in reducing material waste, improving print reliability, and minimizing post-processing efforts. Moreover, while many commercial software solutions exist for support generation and optimization, they are often expensive and require a strong understanding of SLM principles. Most rely on predefined support structures rather than incorporating experimental-based approaches, thermal performance considerations, and heuristic models that could further optimize 3D printing outcomes. To directly address these issues, this research defines the following 3 objectives:

Conventional block supports often result in excessive material usage and difficult post-processing. There is a lack of systematic investigation into optimizing support geometries to balance ease of removal, minimal material consumption, and defect mitigation. The first objective of this study is to establish a comprehensive optimization framework for evaluating the performance of block-type supports by integrating multi-response optimization techniques. Various support and process parameters will be examined, including support hatching, tooth height, tooth top length, laser power, and laser speed. Through experimentation with small ledge specimens, utilizing Design of Experiments (DOE) methodology, precise measurements, data analysis, and result generalization, the research will identify optimized support configurations that minimize material waste, simplify support removal, and reduce printing defects such as warping deformation.

Existing support designs primarily rely on established geometric guidelines without incorporating thermal and mechanical performance considerations, often resulting in part defects such as warping, residual stress accumulation, and insufficient structural integrity. The second objective of this study is to investigate the thermal behaviour of various support types, including block, line, contour, and cone supports. Thermo-mechanical simulations will be performed using COMSOL Multiphysics software [10] to assess heat dissipation, stress distribution, and deformation across different support geometries and critical areas. These areas, primarily the contact interfaces between the part, supports, and build plate, will be identified through 3D printing experiments using SLM and insights from the literature. The simulation outcome will be generalized and validated through experimental tests to identify optimal support structures that enhance part stability and print reliability, including defect-free prints with easily removable support structures.

Current support generation approaches require expert knowledge in finite element modelling and significant in-house experimentation, making them expensive and inaccessible to non-expert users involved in metal AM. The third objective of this study is to propose a design framework for metal AM as a production method, including the development of a web-based platform for automated support generation and optimization. Challenges encountered during the support structure generation phase included accurately building and visualizing defect-free support geometries using Python, as well as ensuring reliable solid STL export with specific thickness requirements, both of which were addressed through iterative debugging and geometry validation. The tool will allow users to import 3D models, determine print orientation, select optimal parameters through a support optimization engine, customize block-type support parameters, visualize optimized supports, and export ready-to-print STL files. By leveraging experimental data and numerical studies, this platform will provide an efficient, user-friendly solution to help both companies and researchers optimize support structures in SLM, while reducing defective parts and in-house experimental costs.

1.4 Dissertation Format

This dissertation follows the typical format of a thesis presented as a collection of papers. It is composed of an abstract, introduction, literature review, research papers, conclusions, and discussion. Three papers are included, each addressing specific research objectives and presenting original findings. These papers also outline the research methodology, results, and corresponding discussions, integrating new contributions to the field.

The first chapter provides an introduction to the research, outlining the motivation behind the study, the problem statement, the key research objectives, and the contribution to knowledge. It also presents an overview of the dissertation's structure and format.

The second chapter provides a comprehensive review of the key background literature. It begins with an overview of AM, detailing its fundamental principles and classifying various AM processes. The chapter then explores the SLM process, examining the process mechanism, key parameters, common defects, materials used, and practical applications. Three main topics are subsequently analysed. The first is support structures in SLM, focusing on the role of supports, types of supports, cost models, and post-processing strategies. The second topic addresses thermomechanical modelling in SLM and metal printing, discussing thermal phenomena, equations, and strategies for optimizing support structures. Finally, the third topic covers algorithms and software for support generation and optimization, with an emphasis on genetic algorithms and commercial software.

The third chapter is based on a paper published in the Journal of Manufacturing and Materials Processing (JMMP), part of the Multidisciplinary Digital Publishing Institute (MDPI) journal series. It investigates various support and process parameters in SLM through a multi-response optimisation framework and proposes optimized supports that minimise support volume, reduce the effort required for their removal, and mitigate warping deformation.

The fourth chapter, based on a paper published in Materials (MDPI), provides a numerical examination of block, line, contour, and cone support structures in SLM. It aims to identify optimal configurations that minimize support volume and residual stress while ensuring high-quality prints.

The fifth chapter, also based on a paper published in Materials (MDPI), introduces an innovative framework aimed at improving the efficiency of metal AM. It presents a web-based platform for automated support generation and optimization, leveraging experimental data to enable users to achieve high-quality printing results without the need for expert knowledge.

The sixth and final chapter summarizes and critically discusses the main findings of the research. It explores the theoretical and practical significance of the work, highlighting its contribution to the field. Additionally, the chapter recommends directions for future research.

1.5 Contribution to Knowledge

This research makes significant contributions to the field of metal additive manufacturing, particularly SLM, by introducing a comprehensive framework for optimizing support structures. It provides a rigorous set of validated principles for quality control in pre-printing preparations, enhancing both process efficiency and reliability. The study integrates experimental data and numerical simulations, offering deeper insights into process dynamics and minimizing the occurrence of defects. The generalized findings are translated into a custom, user-friendly web-based platform that enables automated support generation and optimization, effectively streamlining the SLM workflow. This research tool allows both researchers and industry professionals to design and optimize support structures without requiring expert knowledge, minimizing material waste, printing times, post-processing efforts, defective parts, and overall printing costs.

Feedback received during conferences and subsequently implemented in the study highlighted the value of the proposed framework for optimizing SLM, particularly the effective integration and visualization of experimental results through a user-friendly platform that supports further research. The research thus advances SLM as a scalable, cost-effective method for producing high-performance metal components, bridging the gap between theoretical advancements and practical industrial application.

Chapter 2: Literature Review

2.1 Additive Manufacturing

Additive manufacturing, formerly known as rapid prototyping and commonly referred to as 3D printing, is the formal designation for a process used across various industries to quickly generate a representation of a system or part before its final release or commercialisation. In the realm of product development, the term rapid prototyping was commonly used to describe technologies that directly generated physical prototypes from digital model data. However, enhancements in the output quality of the printing machines have resulted in a significantly tighter connection to the final product. Numerous components are presently fabricated directly within these machines, thus making it inappropriate to categorize them solely as "prototypes". Moreover, the term rapid prototyping fails to acknowledge the fundamental principle of these technologies, as they all construct parts through an additive process [11]. Recognizing this, a Technical Committee within ASTM International reached a consensus that new terminology should be embraced. Consequently, ASTM consensus standards now employ the term Additive Manufacturing, aligning with the majority of standards bodies globally [12].

The ISO/ASTM terminology standard [3] defines additive manufacturing as the process of joining materials to make parts from 3D model data, usually layer upon layer, as opposed to subtractive manufacturing and formative manufacturing methodologies. A part can be generated using a 3D CAD system and fabricated directly without the need for significant process planning. Unlike other manufacturing processes, such as machining and moulding, which require meticulous examination of the part's geometry, necessary tools, and any additional fixtures needed to finalize the part, additive manufacturing only requires basic dimensional details and a fundamental understanding of how the respective AM machine operates and the materials used for part construction [11].

As mentioned above, the fundamental principle of additive manufacturing lies in the layer-by-layer addition of material to fabricate 3D parts, with each layer corresponding to a thin slice of the original CAD design. As each layer must have a finite thickness in the physical world, the resulting part approximates the original data, as illustrated in Figure 1. Thinner layers lead to greater accuracy in replicating the original design. All commercially available AM machines to date utilize a layer-based approach, differing mainly in materials, layer creation methods, and bonding techniques. These variances impact factors such as part accuracy, material and mechanical properties, production speed, post-processing requirements, machine size, and overall costs [11].

Figure 1: CAD images of a teacup showing effects of different layer thicknesses [11].

In additive manufacturing, simpler components may exclusively utilize this technology for creating visualization models and prototypes. Conversely, larger and more complex products with heightened engineering sophistication could integrate additive manufacturing across multiple phases of the manufacturing process. Figure 2 illustrates the standard procedure involving eight steps for producing a part from a CAD model utilizing additive manufacturing [11]. Step 1 involves starting the part from a software model that fully describes the external geometry. This can be accomplished using various professional CAD solid modelling software, ensuring the output is a 3D solid or surface representation. Additionally, reverse engineering equipment such as laser and optical scanning can be utilized to generate this representation. In step 2, the CAD software exports the model in STL file format (stereolithography), a format that is most commonly used in AM to describe the external closed surfaces of the original CAD model using triangular meshes. Next (steps 3 and 4), the STL model is processed in the slicing software of the respective AM machine or third-party software such as Magics from Materialise [13] and Cura from Ultimaker [14]. Basic pre-processing tasks include slicing the STL file into multiple layers at a specified thickness, orienting the part for optimal printability, adding support structures where required, and adjusting various machine and process parameters such as printing speed and printing temperatures. Ensuring the proper setup of the AM machine is crucial before initiating the build process, either through direct configuration from the slicing software as mentioned before or through manual adjustments such as bed levelling, calibration of the feeding system, adherence to material constraints, management of energy sources, timing considerations, and other relevant factors. In step 5, the model is constructed via an automated process, allowing the machine to operate without constant supervision. Minimal supervision is required during this step, primarily to conduct periodic checks on the machine to prevent errors such as material depletion, power interruptions, software glitches, and other potential issues.

In step 6, once the build job is completed, the printed model is removed carefully, adhering to the relevant safety interlocks to mitigate any potential issues stemming from high temperatures and moving parts. After being taken out of the machine, post-processing (step 7) is required depending on the AM process used and the final application (step 8). The printed model might be fragile or have support structures that need removal. It may also need priming, sanding, and painting to achieve the desired surface texture and appearance. Additionally, heat treatment might be necessary, particularly for metal parts. Post-processing can be expensive, time-consuming, and labour-intensive, especially if the finishing standards are high. Therefore, a good level of knowledge in AM is essential to achieve optimal prints and prevent potential time and cost-consuming issues during post-processing.

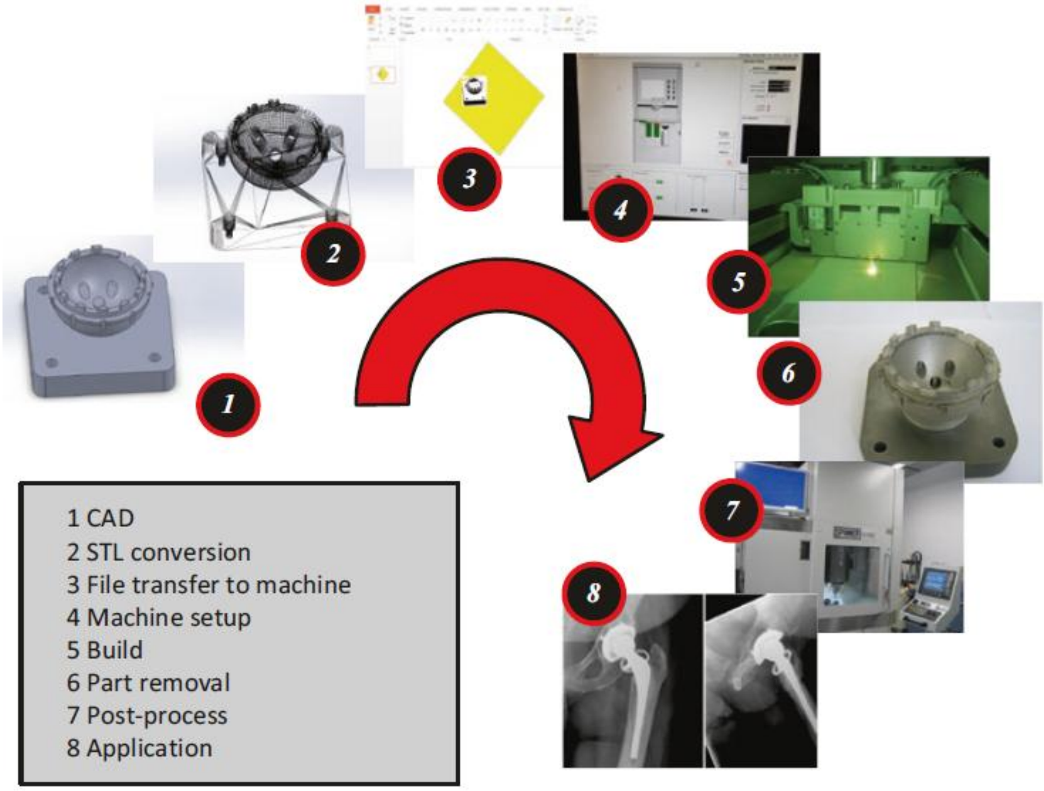

Figure 2: Generic process of CAD to part, showing all eight stages [11].

There are several approaches to categorizing AM technologies, with one common method being to classify them based on baseline technology. This involves considering factors such as whether the process uses lasers, printer technology, extrusion technology, etc. According to the ISO/ASTM classification [3], seven major categories of AM technologies are outlined, as illustrated in Figure 3. These classifications primarily stem from their processing mechanisms, with each category subsequently subdivided into different processes based on the materials and/or energy source [15], [16].

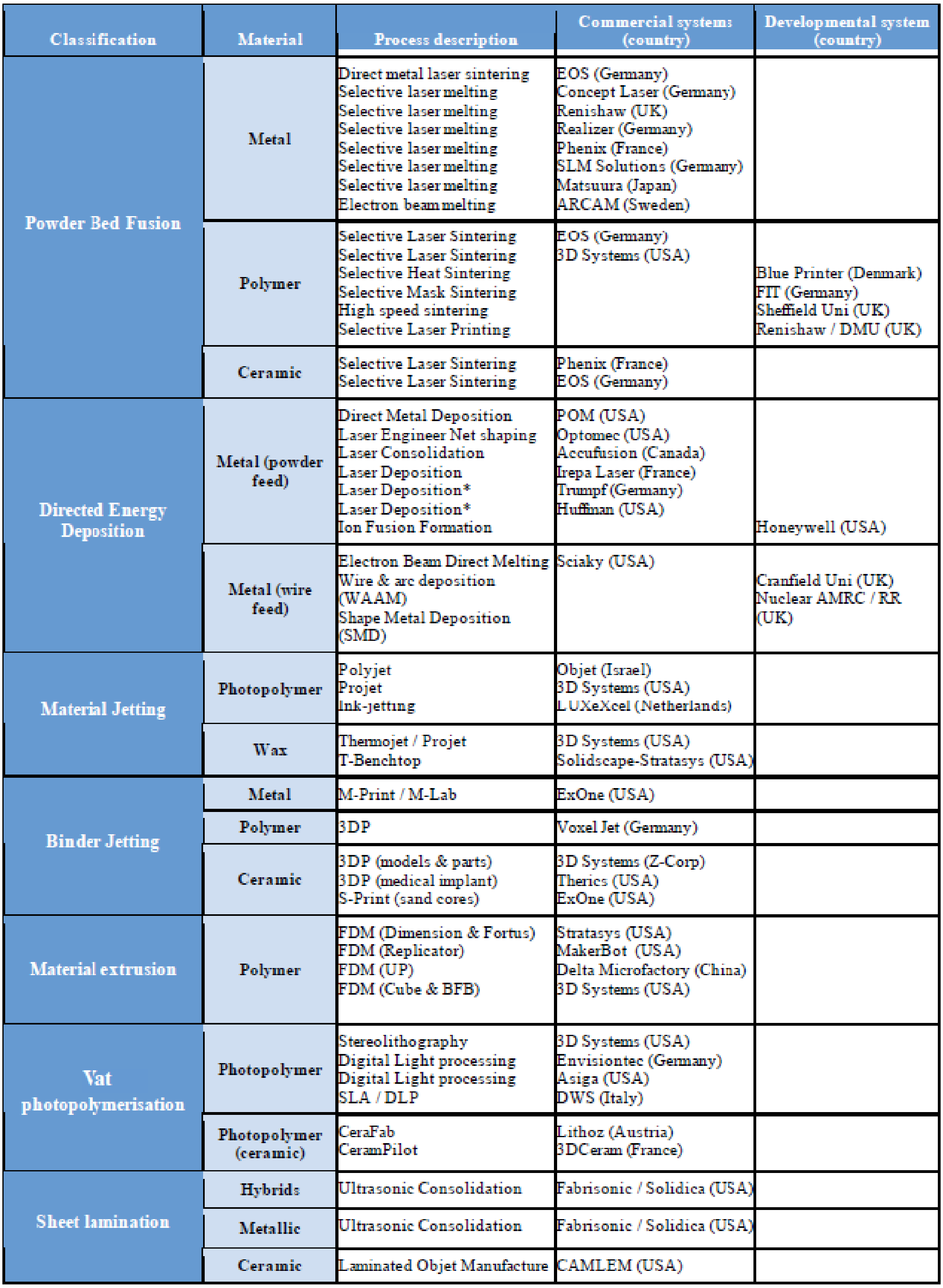

Classification	Material	Process description	Commercial systems (country)	Developmental system (country)
Powder Bed Fusion	Metal	Direct metal laser sintering	EOS (Germany)	
		Selective laser melting	Concept Laser (Germany)	
		Selective laser melting	Renishaw (UK)	
		Selective laser melting	Realizer (Germany)	
		Selective laser melting	Phenix (France)	
		Selective laser melting	SLM Solutions (Germany)	
		Selective laser melting	Matsuura (Japan)	
		Electron beam melting	ARCAM (Sweden)	
	Polymer	Selective Laser Sintering	EOS (Germany)	
		Selective Laser Sintering	3D Systems (USA)	
		Selective Heat Sintering		Blue Printer (Denmark)
		Selective Mask Sintering		FIT (Germany)
		High speed sintering		Sheffield Uni (UK)
		Selective Laser Printing		Renishaw / DMU (UK)
	Ceramic	Selective Laser Sintering	Phenix (France)	
		Selective Laser Sintering	EOS (Germany)	
Directed Energy Deposition	Metal (powder feed)	Direct Metal Deposition	POM (USA)	
		Laser Engineer Net shaping	Optomec (USA)	
		Laser Consolidation	Accufusion (Canada)	
		Laser Deposition	Irepa Laser (France)	
		Laser Deposition*	Trumpf (Germany)	
		Laser Deposition*	Huffman (USA)	
		Ion Fusion Formation		Honeywell (USA)
	Metal (wire feed)	Electron Beam Direct Melting	Sciaky (USA)	
		Wire & arc deposition (WAAM)		Cranfield Uni (UK) Nuclear AMRC / RR (UK)
		Shape Metal Deposition (SMD)		
Material Jetting	Photopolymer	Polyjet	Objet (Israel)	
		Projet	3D Systems (USA)	
		Ink-jetting	LUXeXcel (Netherlands)	
	Wax	Thermojet / Projet	3D Systems (USA)	
		T-Benchtop	Solidscape-Stratasys (USA)	
Binder Jetting	Metal	M-Print / M-Lab	ExOne (USA)	
	Polymer	3DP	Voxel Jet (Germany)	
	Ceramic	3DP (models & parts)	3D Systems (Z-Corp)	
		3DP (medical implant)	Therics (USA)	
		S-Print (sand cores)	ExOne (USA)	
Material extrusion	Polymer	FDM (Dimension & Fortus)	Stratasys (USA)	
		FDM (Replicator)	MakerBot (USA)	
		FDM (UP)	Delta Microfactory (China)	
		FDM (Cube & BFB)	3D Systems (USA)	
Vat photopolymerisation	Photopolymer	Stereolithography	3D Systems (USA)	
		Digital Light processing	Envisiontec (Germany)	
		Digital Light processing	Asiga (USA)	
		SLA / DLP	DWS (Italy)	
	Photopolymer (ceramic)	CeraFab	Lithoz (Austria)	
		CeramPilot	3DCeram (France)	
Sheet lamination	Hybrids	Ultrasonic Consolidation	Fabrisonic / Solidica (USA)	
	Metallic	Ultrasonic Consolidation	Fabrisonic / Solidica (USA)	
	Ceramic	Laminated Objet Manufacture	CAMLEM (USA)	

Figure 3: Classification of additive manufacturing processes [16].

2.2 Metal Powder Bed Fusion-Laser Beam

As previously noted, and in accordance with ISO/ASTM standards [3], Powder Bed Fusion-Laser Beam for Metals (PBF-LB/M), commonly known as Selective Laser Melting (SLM) or Direct Metal Laser Sintering (DMLS), falls under the category of Powder Bed Fusion (PBF) additive technology (see Figure 3). PBF-LB/M stands as one of the most commonly employed and rapidly developing additive manufacturing technologies nowadays, capable of directly fabricating complex, thin, and lightweight metal components with precision and high performance for various industries including aerospace, biomedical, defence, and automotive [17]. It is also worth noting that the mechanical properties of the resulting parts can be comparable to or even superior to those produced through conventional methods such as machining and moulding [18]. Figure 4 illustrates several components manufactured via SLM.

Figure 4: SLM-produced parts and components [19].

Compared to other AM technologies, PBF-LB/M presents a unique combination of high process complexity, stringent thermal control requirements, and critical support structure dependency. Unlike extrusion-based or photopolymerization AM methods that involve polymers or resin and benefit from inherent self-supporting features or support material that is easily removed, PBF-LB/M deals with high-temperature metal processing, leading to significant thermal gradients and residual stress accumulation. These phenomena can cause warping, delamination, and part failure, especially in unsupported regions or complex geometries. Moreover, the necessity for precise thermal management and robust mechanical anchoring makes support structures in PBF-LB/M not only essential but also a major factor in part quality, build success, and post-processing. The bonding of supports to the part, combined with the use of the same material, unlike dual-material systems in Fused Deposition Modelling (FDM) or Stereolithography (SLA), leads to difficult, labor-intensive support removal and increased risk of damaging the part during post-processing [11]. These challenges, not typically encountered in other AM categories, justify the need for a focused investigation into support structure optimization in PBF-LB/M, as conducted in this thesis.

In terms of materials, a wide range of metals can be utilised, typically, any metal that can be welded is considered to be a good candidate. This includes several types of steels, such as stainless and tool steels, titanium and its alloys, nickel-based alloys, some aluminium alloys, and cobalt-chrome. All have been processed and are commercially available in powder form. Moreover, certain companies within the industry provide PBF-LB/M services for precious metals including silver and gold [11].

2.2.1 SLM Process Mechanism

A schematic diagram of a typical SLM process mechanism is illustrated in Figure 5. SLM machines employ a powder deposition technique that involves a recoating mechanism (roller or blade) to distribute a layer of powder onto a substrate plate, along with a powder reservoir. Pre-heating of the powder bed is carried out (usually 200 and 500 ºC for alloys such as titanium) to eliminate the humidity of the powder and enable a strong connection between the first layers and the build plate. Pre-heating has a significant effect on minimizing residual stresses as it mitigates the thermal gradients and improves the surface quality of the produced parts [20]. Once the powder is uniformly distributed, laser scanning begins. SLM employs a high-power laser to trace the geometry of a single layer from the sliced 3D model on the surface of the powder bed. Throughout the process, the powder particles are fused together, leading to solidification. After the scanning of a layer is completed, the build platform is lowered by the depth of a layer, and new powder is distributed over the previous layer. Typically, the thickness of each powder layer is set to at least the diameter of the powder particles (usually between 20 and 80 μm [21]) and can be adjusted according to user preferences. This sequence is iterated continuously, with each new layer being added upon the previous ones until the fabrication of the part [11], [22].

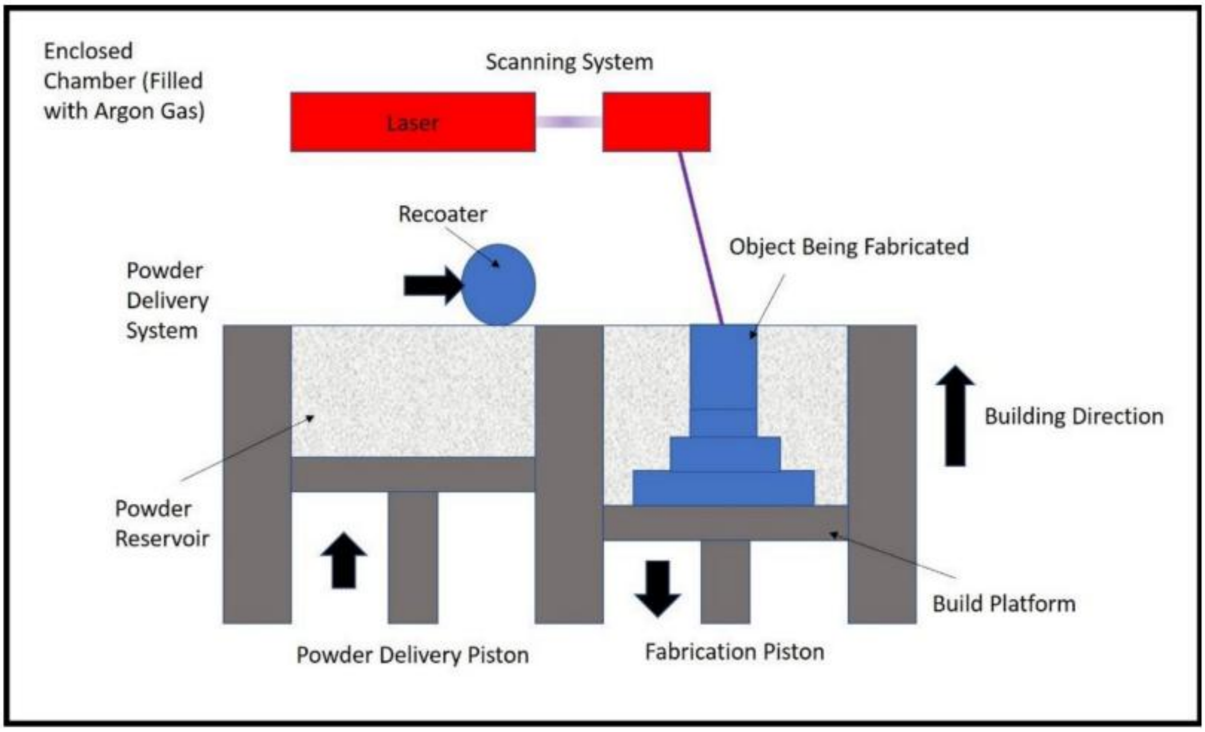

Figure 5: Schematic diagram of the SLM process [22].

2.2.2 SLM Process Parameters

In SLM, process parameters can be categorized into four main groups: (i) scan-related parameters such as scanning speed, hatch spacing, scanning pattern, and scanning strategy (ii) energy source-related parameters such as laser power, spot size, pulse duration, and pulse frequency, (iii) powder-related parameters including particle shape, size and distribution, powder bed density, layer thickness, and material properties, and (iv) temperature-related parameters including inert atmosphere, powder bed temperature, powder feeder temperature, and temperature uniformity [11]. Most of these parameters, especially laser power, scanning speed, hatch spacing, and layer thickness, are strongly interconnected, requiring a good level of AM knowledge for their tuning to achieve the optimal printing outcome [23].

Thus, among the four groups of SLM process parameters described above, the scan-related and energy source-related parameters, particularly laser power, scanning speed, hatch spacing, and layer thickness, represent the greatest challenge for optimization. These parameters are not only strongly interdependent, but also directly impact the volumetric energy density, a critical factor that controls melt pool stability, material consolidation, and defect formation. Improper tuning can result in defects such as balling, keyholing, porosity, or lack of fusion, all of which significantly compromise part quality. The terminology of the volumetric energy density will be explained in detail later in this literature. Figure 6, presents a visual overview of the key process parameters used in the SLM process. To manage this complexity, the experimental design presented in this thesis adopted a two-step strategy. First, preliminary screening experiments were conducted to explore the interaction effects between laser power, scanning speed, and various geometric parameters of the support structures. Subsequently, small ledge specimens were fabricated using support structures with different configurations to evaluate their performance under controlled conditions. This approach facilitated a robust assessment of the key variables while minimizing the risk of print failures, ultimately enabling the development of a multi-response optimization framework that considers support removability, warping deformation, and material efficiency is SLM.

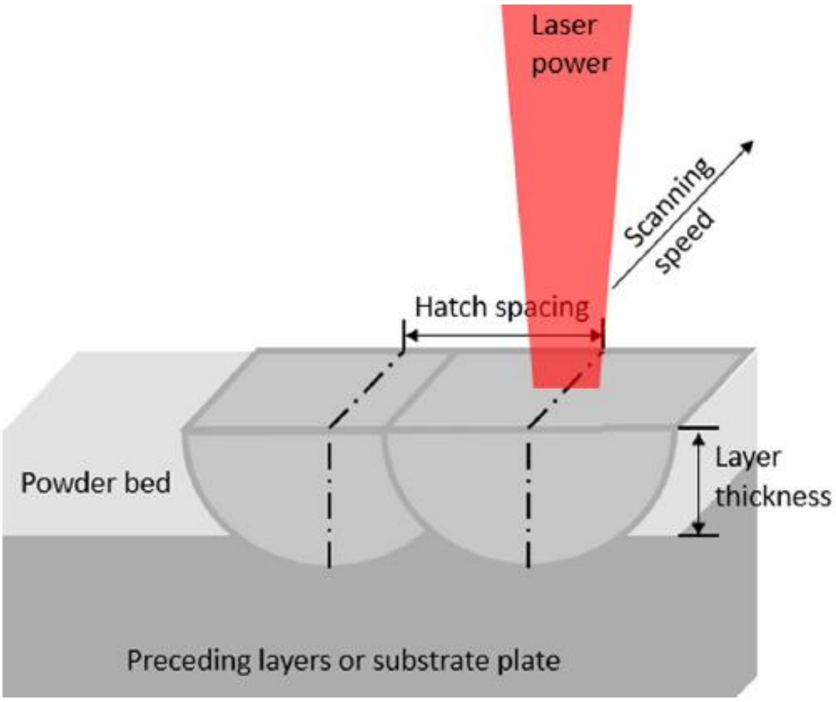

Figure 6: Main SLM process parameters [23].

Regarding scanning, it operates in two modes: contour mode and fill mode, as illustrated in Figure 7. In contour mode, the part cross-section's outline for a specific layer is scanned. This is usually performed to ensure precision and enhance surface finish along the perimeter. Subsequently, the remaining cross-section is scanned using a fill pattern. The fill section is generally divided into stripes, where each stripe is scanned sequentially, and the angle of the stripes is rotated with each layer, or into squares, with each square processed individually [11]. The selected scan strategy plays a pivotal role in metal additive manufacturing, as it can significantly influence the accumulation of residual stress within a part, thereby affecting its structural integrity and performance.

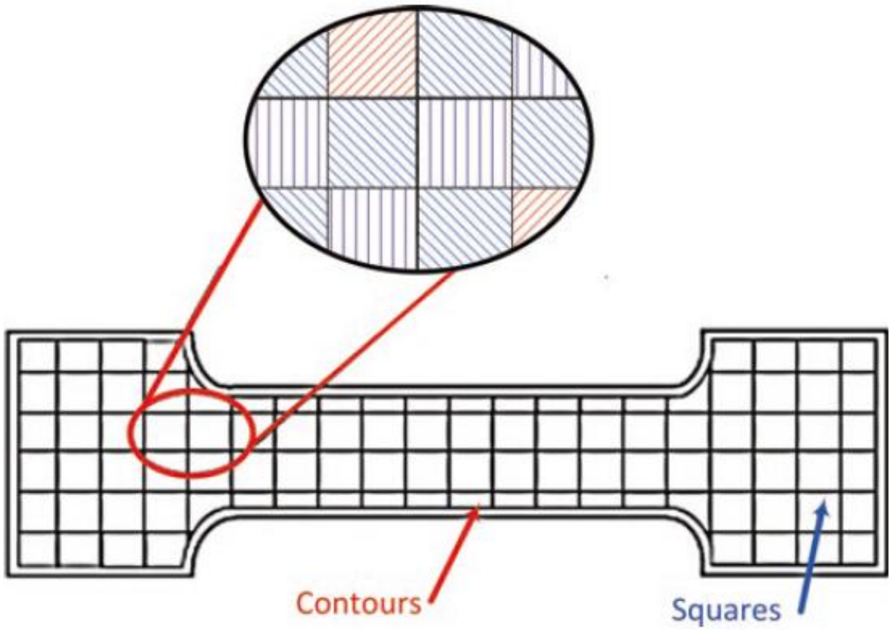

Figure 7: Scan strategies employed in PBF [11].

Regarding the energy source-related parameters, the required laser power is adjusted in correlation with the material's properties, such as the material's melting point, and its absorbance to laser irradiation. Together with the powder's absorptance, laser power, scanning speed, hatch spacing, and layer thickness influence the volumetric energy density available for heating and melting the powder into a part. For instance, insufficient energy, typically a combination of low laser power, high scanning speed, and large layer thickness, often leads to balling [23] due to inadequate wetting of the molten pool with the preceding layer. Conversely, high laser power and low scanning speed may result in extensive material evaporation and the keyhole effect [24], [25]. Additionally, poor hatch spacing often results in consistent porosity in fabricated parts, as adjacent melt lines fail to fuse together completely [23]. Figure 8 illustrates five cases of temperature distribution during the SLM process with different laser power (P) and scanning speed (v). It is clear that the longer the laser remains in a particular area, the deeper the fusion depth and the size of the melt pool, which depend heavily on the settings of laser power, scanning speed, hatch spacing, and layer thickness as mentioned earlier. Thus, when operating at lower laser powers, lower scan speeds are necessary to guarantee proper particle fusion. Typical layer thicknesses range from 20 to 150 µm, while scan spacing should be carefully selected to guarantee sufficient overlap of melt pools between adjacent lines of fused material, ensuring robust mechanical properties of the part [11], [26].

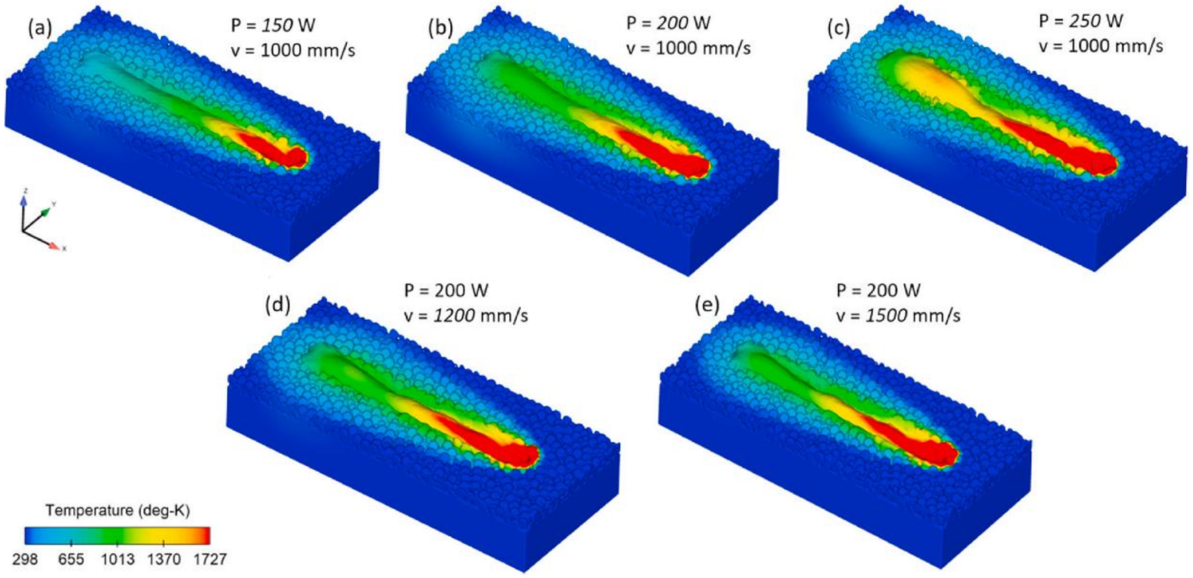

Figure 8: Temperature distribution with different laser power and scanning speed [26].

In terms of powder-related parameters, the characteristics of metal powders, including their particle size, shape, and distribution, significantly influence several aspects of the laser absorption process, as well as the density and thermal conductivity of the powder bed, and its spreading behaviour [11]. Finer particles, such as gas and plasma-atomized spherical metal powders, facilitate high powder bed density and flowability providing a larger surface area and absorbing laser energy more effectively compared to coarser ones, such as water-atomized powders. Figure 9 illustrates the powder morphology utilized in metal additive manufacturing, sourced from various conventional powder production methods including water, gas, and plasma atomization [27]. Choosing the ideal powder size distribution demands careful consideration. Larger particles exhibit lower packing densities and demand higher energy inputs for effective melting. Conversely, smaller particles, while offering benefits like enhanced pack densities and reduced surface roughness, may generate fumes that complicate the layering process [18]. Typically, it is suggested to have a balanced combination of small and large particles to optimize the properties of the powder bed. Moreover, ensuring good powder flowability during the build is essential for achieving a constant and homogeneous layer thickness, which is a necessary requirement for uniform laser energy absorption [20]. Several studies have investigated bimodal or multimodal distributions, where combining fine and coarse particles improves both packing density and flowability simultaneously [28]. Nevertheless, a universal agreement on the ideal powder size distribution remains elusive, largely due to variations in materials, machine types, and specific application requirements.

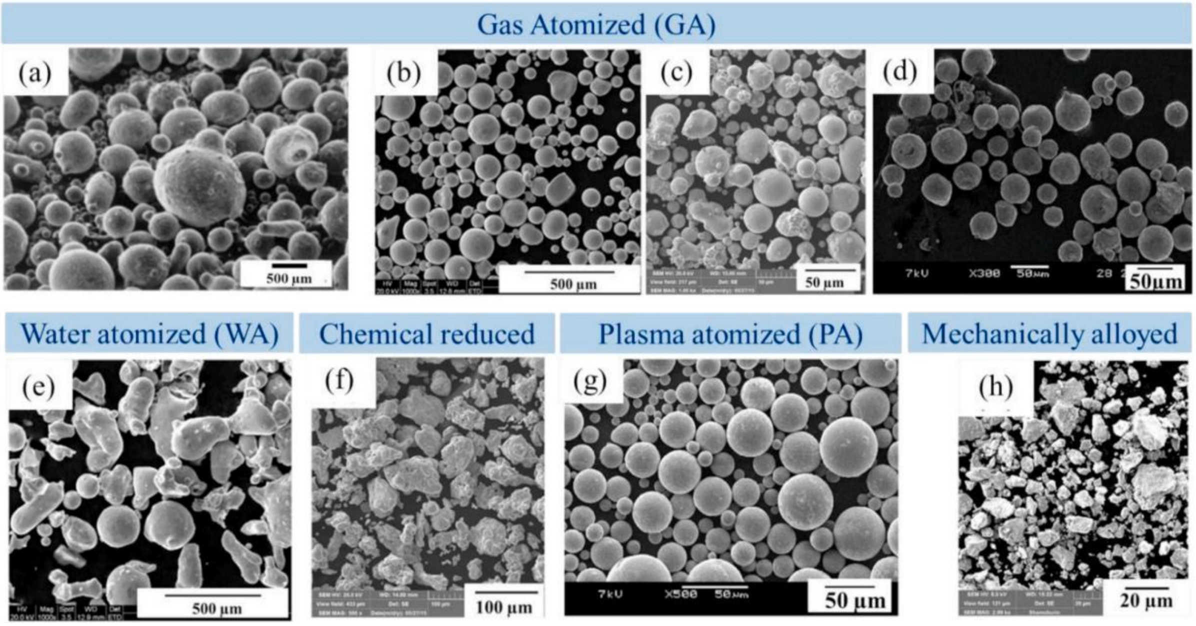

Figure 9: Morphology of powder used in metal AM obtained from different conventional powder production techniques. (a) Ti47Al3Cr, (b) 316L stainless steel, (c) 316L stainless steel, (d) inconel-718, (e) Fe, (f) Ti6Al4V, (g) Ti6Al4V, (h) Fe18Cr8Ni12MnN [27].

Achieving optimal results in metal AM involves balancing factors such as powder morphology and size, powder bed temperature, layer thickness, laser power, scanning speed, and hatch spacing to find the best compromise between melt pool size, dimensional accuracy, surface quality, production speed, and mechanical properties. Maintaining a uniform and consistent powder bed temperature is essential for obtaining consistent outcomes. Typically, configurations with high laser power and bed temperature yield dense parts but may lead to issues like part enlargement, reduced recyclability, and cleaning difficulties. Conversely, low laser power and bed temperature combinations enhance dimensional precision but result in lower density parts and an increased risk of layer separation. High laser power coupled with low bed temperatures can exacerbate issues such as uneven shrinkage and residual stress buildup, causing parts to curl [11].

2.2.3 SLM Printing Defects

The concentrated laser energy during SLM creates significant thermal gradients, resulting in thermal stress within the component. This, combined with improper fine-tuning of the process parameters, often results in common defects such as deformation, cracking, internal porosity, and dimensional inaccuracies, ultimately leading to part failure or reduced performance. However, even with optimal process parameters, such defects could still occur, leading to unpredictable part behaviour [20], [29]. Bi Zhang et al. [30], investigated the effect of the process parameters on defect formation in SLM and the impact of defect formation on the mechanical properties of a fabricated part. Figure 10 presents optical images highlighting defects identified in parts fabricated via SLM using the titanium alloy Ti6Al4V, the primary material investigated in this thesis.

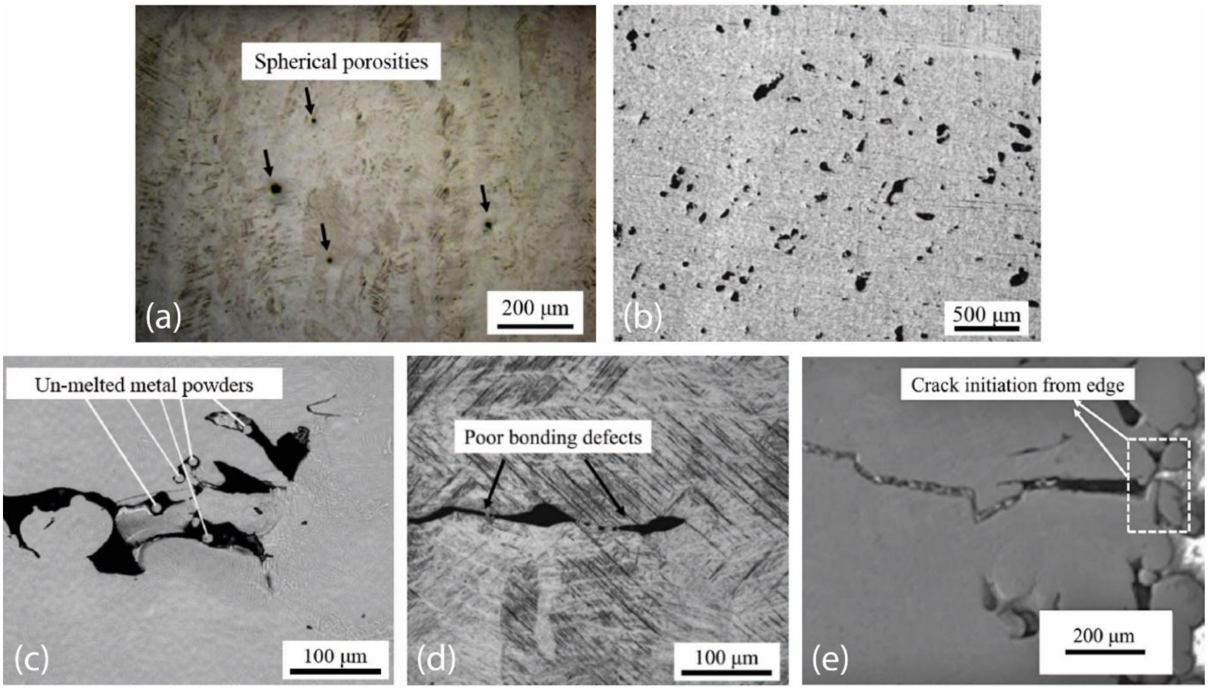

Figure 10: Optical images of defects found in SLM-fabricated Ti6Al4V parts. (a) Spherical porosities, (b) Incomplete fusion holes, (c) Lack-of-Fusion defects with un-melted metal powders, (d) Poor bonding defects, (e) Crack morphology [30].

Overall, sources of defects in SLM typically arise from various factors such as partially melted or unmelted metal powder particles, gas entrapment during atomization or solidification, insufficient fusion, and layer delamination. Additionally, defects can be influenced by powder properties like composition, morphology, and particle size distribution. Other notable defects in SLM using Ti6Al4V include dimensional inaccuracies, stress-induced cracking, dimensional warping, as well as microstructural issues like balling and porosity, which significantly impact the dynamic mechanical performance of the printed part [20].

Porosity, a primary defect in SLM, correlates with specific scanning strategies and the use of insufficient or excessive laser energy intensities, resulting in adverse effects on the part's mechanical performance. Many studies have been conducted over the past years to optimize porosity focusing on the design of the scan strategies, the melt pool behaviour, the stability, the laser energy, and stress concentrations [28], [31]. A common issue is that the protective gas going into the melt pool fails to escape before solidification as a result of the high cooling rates.

These lack-of-fusion (LOF) defects, also known as incomplete fusion holes (see Figure 10c), occur due to inadequate laser energy penetration into the melt pool. The deposition of a new layer before the complete melting of the metal powders complicates the re-melting process, leading to the formation of incomplete fusion holes situated between the scanned tracks and the newly deposited layer [30].

Residual stresses developed during the SLM process often result in additional common defects, including cracks (see Figure 10e), warping, layer delamination, and relevant recoater issues that can cause detachment of the part from the build plate. These problems are primarily attributed to the high thermal gradients and high cooling rates inherent to the process, which occur due to the rapid transition from the melting temperature to a lower preheating temperature during solidification. Figure 11a illustrates a typical example of warping deformation at the bottom of the part, while Figure 11b depicts the cracks observed in the same sample during the research conducted by Z. Zhao et al. [32]. Respectively, as shown in Figure 11c delamination leads to interlayer cracking [31]. Much research has been conducted over the past years on reducing thermal stresses in metal additive manufacturing including in-process powder bed preheating [33], in-situ process control such as in-situ feedback control, thermal gradient control, scanning strategy control, and mechanical control, as well as post-process control such as post heat treatment, post-annealing, and machining [34]. However, the preheating capabilities of the current machines available in the market are limited by the risk of cake formation [35] at high temperatures and the challenges involved in recycling unused metal powder [20].

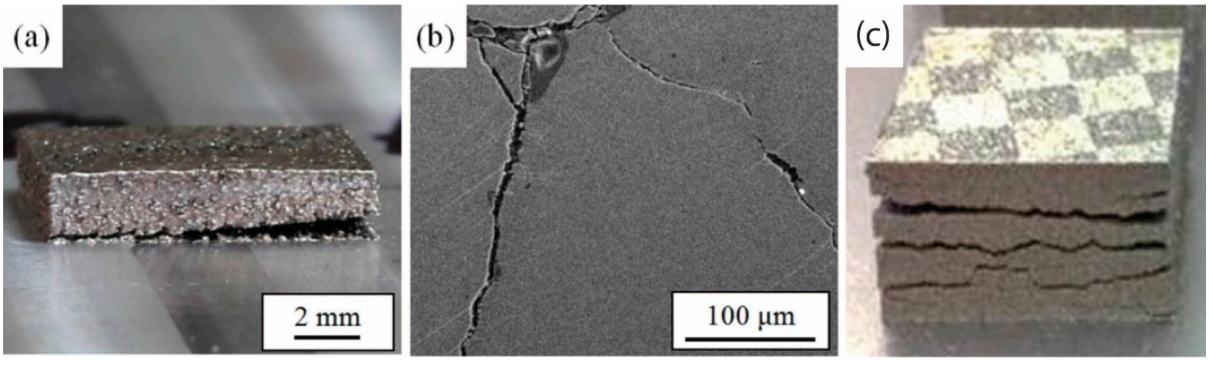

Figure 11: Experimental samples of SLM defects. (a) Warping deformations, (b) Cracking, (c) Layer delamination.

Among the various defects discussed in this section, warping deformation is the most directly influenced by the design of support structures. This defect results from uneven thermal gradients and inadequate heat dissipation during the layer-by-layer fabrication process, especially in overhang regions. As the literature emphasizes, support structures serve not only as mechanical anchors but also as thermal sinks that help manage heat flow, thus reducing thermal stress accumulation and associated distortion. In response, the support optimization strategies in this research were tailored to minimize warping deformation by investigating the thermal behaviour of different support types (block, line, contour, and cone) using small ledge specimens. Both experimental and thermo-mechanical simulation studies guided the selection of support geometries that enhance heat conduction away from critical regions while maintaining printability and minimizing material consumption. Parameters related to the contact area, such as tooth height and tooth top length, as well as those influencing support density, such as hatching distance, were carefully optimized to achieve a balance between mechanical stability, thermal management, and ease of removal.

2.2.4 SLM Support Structures and Post-Processing

In AM, support structures are often required for several reasons. They provide a suitable platform for building the next layer in cases of overhanging geometries and complex features; serve as fixtures anchoring the part to the build plate, particularly with unbalanced parts; and act as heat sinks, aiding controlled cooling rates, especially when fabricating metal parts [36]. Thus, support structures are of significant importance, exist in all AM processes in various forms, and their generation requires careful consideration. Many parts produced in AM can be self-supported or rely on surrounding support materials, such as the powder in Selective Laser Sintering (SLS) processes and sheet material in sheet lamination processes; however, several other AM processes such as extrusion-based systems, vat photopolymerization, direct printing, and SLM processes cannot be supported by surrounding materials. For these technologies, extra supports are required to connect the part to the build plate and to construct overhanging surfaces, which can be made using the same or a secondary material. Additionally, in metal-based technologies including SLM, support structures are necessary to resist distortion and similar defects caused by high thermal stresses applied on the part during the process [29]. Figure 12 illustrates two typical examples of commonly used support geometries in SLM. It can be observed that they are thin, scaffold-like formations equipped with tiny pointed teeth to minimize contact area, ensuring easy detachment from the part [37], [38].

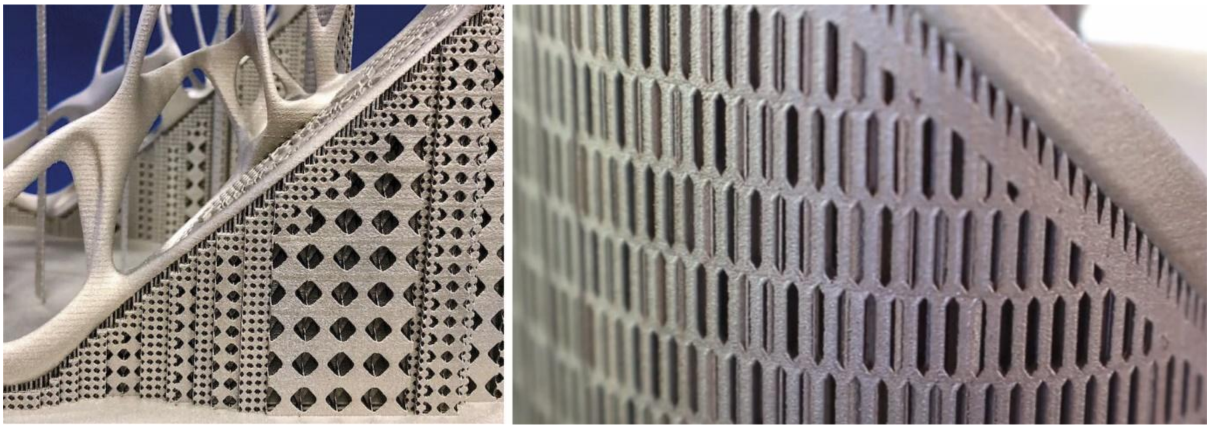

Figure 12: Commonly employed support geometries in SLM [37], [38].

Further exploration of support structure design, generation, and optimization in SLM will be explored in subsequent sections of this literature. In terms of post-processing, as previously noted, techniques such as post-heat treatment, annealing, and machining are utilised to enhance both the mechanical properties and aesthetic appeal of metal-produced parts. Additionally, post-processing related to support removal holds significant importance in SLM and additive manufacturing in general. While removing plastic-based support structures after printing might be relatively simple and straightforward, eliminating metal-based supports often demands significant manual labour, resulting in both time and financial costs [36]. Therefore, methods such as milling, band saws, cutoff blades, wire EDM (electrical discharge machining), or pneumatically driven chisels are utilized for support structure removal in SLM, with some techniques resulting in rough surfaces that may require polishing or further machining [11].

2.3 Support Structures in Metal Powder Bed Fusion-Laser Beam

2.3.1 The Role of Supports

The preceding sections have outlined the fundamental principles of the SLM process, including its mechanism, key parameters, typical defects, and the critical factors influencing part quality. While the understanding of scanning strategies, energy input, and material properties is vital for controlling part integrity, these factors alone are often insufficient to fully prevent defects such as warping, distortion, or cracking, particularly in overhanging features and unsupported regions. To address these challenges, the design and implementation of effective support structures play a crucial role in stabilizing parts during fabrication, enhancing thermal management, and improving surface quality and post-processing. Therefore, a focused investigation of support structures, their functions, types, and optimization strategies is essential for advancing the reliability and efficiency of SLM manufacturing.

As mentioned in section 2.2.4, support structures are essential in PBF-LB/M processes. They serve to anchor the part to the build plate, provide a suitable platform for the next layer to be built upon, and act as a heat sink resisting the thermal stresses and enabling the part to cool at more controlled rates. High thermal stress presents a risk of causing substantial deformations to the part, potentially leading to build failure due to delamination from the base plate, as well as inducing cracks during printing before the part is completed. It could also be assumed that the unmelted powder surrounding the part can provide sufficient support for overhang structures, thus eliminating the necessity for external supports, as SLS does. However, relevant research by Poyraz et al. [39] and Cheng and Chou [40] revealed that this assumption is not valid. They discovered that the unmelted powder lacks thermal conductivity, leading to several quality issues such as curling, warping, and distortion, particularly in overhang regions where the highest temperatures are experienced. Therefore, printing an object without or insufficient support structures results in defective parts, while the addition of unnecessary supports may increase the post-processing, the time and effort required for support removal, the risk of part damage, the material usage, the printing time, and the overall costs.

2.3.2 Cost Estimation for Supports

Optimized process parameters, appropriate part orientation, and accurate support strategies can significantly reduce the amount of support material required, minimize post-processing efforts, and therefore lower overall printing costs. Griffiths et al. [41], for instance, investigated the combined build orientation and irregular bin packing problem in SLM, and it was found that reducing support structure volume led to significant cost improvements.

Various AM cost estimation models have been developed over the past years [42], however, there has been limited research focused on developing cost models and analysing support strategies for cost reduction in metal AM and PBF-LB/M processes. An improved cost model that is suitable for the calculation of today’s AM has been developed by Lindemann et al. [43] encompassing the entire production process and investigating factors such as development and lifecycle costs. This model, along with the average of those examined in the literature, categorizes the total cost in four main phases. These phases include: i) build preparation, involving CAD preparation and machine preparation; ii) manufacturing, covering the build process; iii) post-processing, involving support removal and surface treatment; and iv) quality control, involving verification and documentation. The cost breakdown of a typical example showed that the largest contributor to the total building costs was the machine costs (74%), followed by material costs (12%). Post-processing, including support removal, represented the third-largest cost, accounting for 7%, however, the model does not provide a mechanism to distinguish the impacts of different support geometries or removal complexities, which are crucial in SLM.

A more focused approach is presented by Rickenbacher et al. [44], who incorporated both preprocessing and post-processing aspects in their model and quantified the benefits of part consolidation during the build. Various components were fabricated under different printing conditions, with the total cost subsequently computed. The results revealed a significant reduction in manufacturing and setup time for parts printed simultaneously compared to those printed separately. Consequently, the total cost per part could be significantly reduced by an average of 41%. The main parameter values used in the cost model, along with their units, are illustrated in Figure 13. However, while the model incorporates the material usage and the time required for support removal during post-processing as variables, it does not critically evaluate how variations in support type, density, or geometry influence these costs. Thus, its application in comparative analysis of support strategies remains limited. In summary, while these models provide valuable cost insights at different stages of the AM workflow, their utility in evaluating support structure-specific costs in SLM is constrained. Future methods and models should incorporate more detailed representations of support design parameters and post-processing complexity to better guide support strategy optimization from a cost perspective.

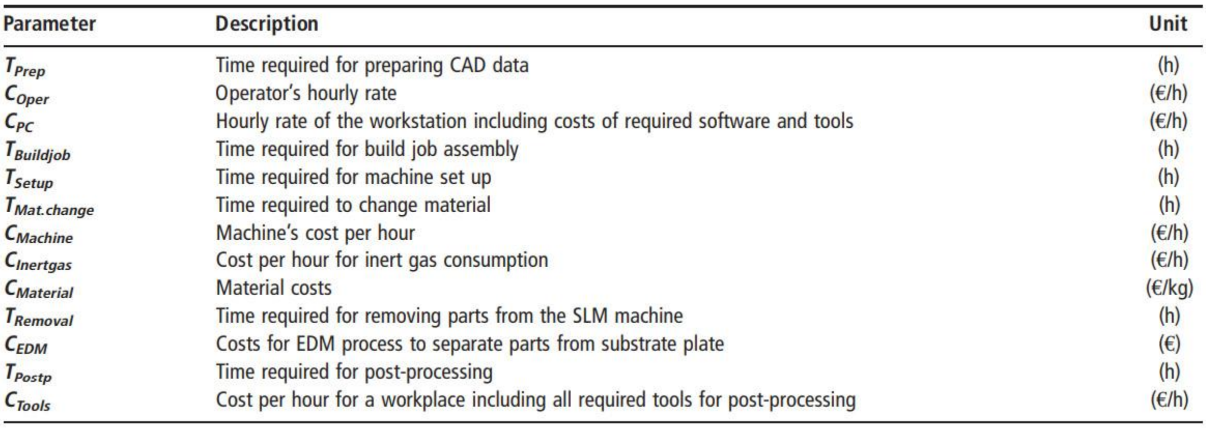

Parameter	Description	Unit
T_{Prep}	Time required for preparing CAD data	(h)
C_{Oper}	Operator's hourly rate	(€/h)
C_{PC}	Hourly rate of the workstation including costs of required software and tools	(€/h)
$T_{Buildjob}$	Time required for build job assembly	(h)
T_{Setup}	Time required for machine set up	(h)
$T_{Mat.change}$	Time required to change material	(h)
$C_{Machine}$	Machine's cost per hour	(€/h)
$C_{Inertgas}$	Cost per hour for inert gas consumption	(€/h)
$C_{Material}$	Material costs	(€/kg)
$T_{Removal}$	Time required for removing parts from the SLM machine	(h)
C_{EDM}	Costs for EDM process to separate parts from substrate plate	(€)
T_{Postp}	Time required for post-processing	(h)
C_{Tools}	Cost per hour for a workplace including all required tools for post-processing	(€/h)

Figure 13: Main parameter values used in the cost model [44].

In this research, the cost-related aspects of support structures were evaluated by prioritizing two main factors: support material consumption and post-processing effort, particularly on support removal. These elements were selected based on their direct and repeated contribution to production costs in SLM, as highlighted in the cost models presented above and the experimental literature. Material usage was quantified by calculating the volume of the support structures for each configuration tested, while post-processing costs were assessed experimentally by measuring the time required to remove each support configuration, using manual tools commonly employed in industrial practice. By integrating these factors into a multi-response optimization framework, this research enabled the comparative evaluation of various support configurations not only from a mechanical and thermal standpoint, but also in terms of cost-efficiency.

2.3.3 Types of Supports and Key Parameters

Various software and tools for support generation and optimisation tailored to specific parts are commercially available. Although highly sophisticated, these tools primarily rely on rule-based or geometry-based heuristics, often leading to over-supporting or sub-optimal support placement, which increases material usage and post-processing. Moreover, their optimisation routines typically lack multi-objective criteria, such as balancing thermal stress, part distortion, and material usage, and do not fully incorporate mechanical performance or heat dissipation aspects in a holistic manner. Custom-made support geometries are also limited in many tools, restricting users from implementing case-specific strategies or integrating novel support structures. As a result, these shortcomings highlight the necessity for more intelligent, adaptable, and performance-driven support optimisation methodologies, motivating the need for the approaches explored in this thesis. A detailed analysis of these tools, including their capabilities and unique features, will be presented later in this literature.

Such tools provide users with the flexibility to select from a range of fundamental support configurations used in SLM, including block, point, web, contour, and line [45] as shown in Figure 14. It can be observed that all these support structures typically consist of thin, scaffold-like frameworks (or walls) with small pointed teeth on top. These features are designed to offer a suitable platform for building overhanging surfaces with minimal material, while also minimising contact with the part, thus facilitating easy removal using manual tools [46].

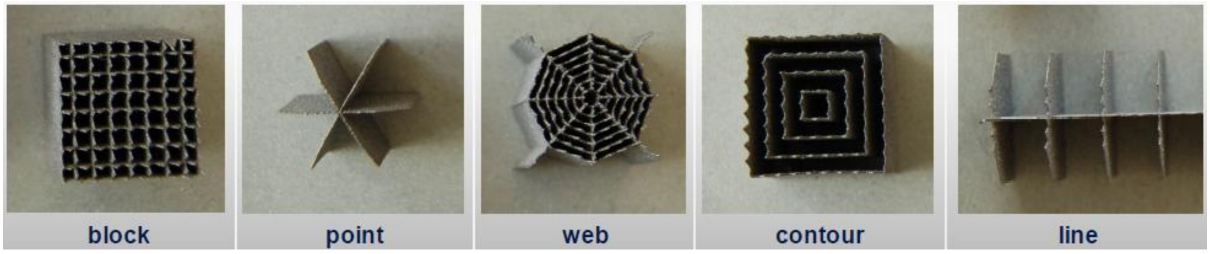

block point web contour line

Figure 14: Different support types for metal- and powder-based AM [45].

Each support type, however, exhibits specific advantages and limitations, which make them more or less suitable depending on the application: Block supports provide high structural stability and effective heat dissipation, making them ideal for large, heavy components like tooling forms. However, they consume more material, lead to longer build times, and can be more difficult to remove, thus increasing post-processing effort. Line supports are commonly used for parts with thin walls or sheet-like geometry, such as automotive components. They strike a balance between stability and ease of removal, but they may not offer sufficient support for large overhangs or heavy features. Point supports are advantageous when minimal contact with the part is needed, such as in fine or detailed geometries. They reduce the risk of surface damage and facilitate removal. However, their low structural strength makes them unsuitable for supporting large overhangs or heavy features. Web and contour supports offer improved conformity to part geometry, especially curved or organic surfaces, enhancing thermal control and surface finish. However, their generation and removal may be more complex and require careful tuning to avoid process-induced defects. Therefore, a critical selection process is essential, as using an unsuitable support type may lead to issues such as part distortion, insufficient anchoring, or excessive post-processing demands [11], [47].

Apart from the support type, the respective geometrical parameters also significantly influence the performance and removability of support structures. As observed in Figure 14, a typical support structure in SLM consists of the main support body and the teeth area, which connects the build plate, the support structure, and the actual part. The geometry of the teeth should be designed to act as a heat sink, withstand tensile loads and warping, and be easily removed. This heat sink function is critical because it facilitates the dissipation of excess thermal energy during the layer-by-layer fabrication process, which is especially important in metal additive manufacturing. Poor thermal management can result in localised heat accumulation, leading to residual stresses, part distortion, and even cracking. By designing the teeth geometry to act as an effective thermal sink, heat can be more efficiently conducted away from the part, thus maintaining a more uniform temperature distribution throughout the build.

This not only improves dimensional accuracy but also enhances the mechanical integrity of the final component by reducing the likelihood of thermally induced defects [48], [49].

According to the literature and relevant experimental work [45], [50] key parameters for teeth geometry include top length, base interval, and tooth height, as illustrated in Figure 15. Moreover, there are additional significant geometrical parameters that influence support performance. For instance, support walls can be fragmented for easier removal. The main support can be perforated (usually with diamond or rectangular-based perforations) to reduce material usage and improve loose powder removal. Bottom teeth may also be serrated to facilitate detachment. The grid distance (or hatch distance), which is the distance between individual block support walls can be customised, enabling better control over support volume. Users have the flexibility to modify and fine-tune this range of parameters based on the application and the respective support type provided by the software. Therefore, selecting the appropriate support type and optimising the respective support parameters can result in successful prints with zero defects, while also reducing printing times, overall costs, and the required post-processing, including the time and effort needed for support removal.

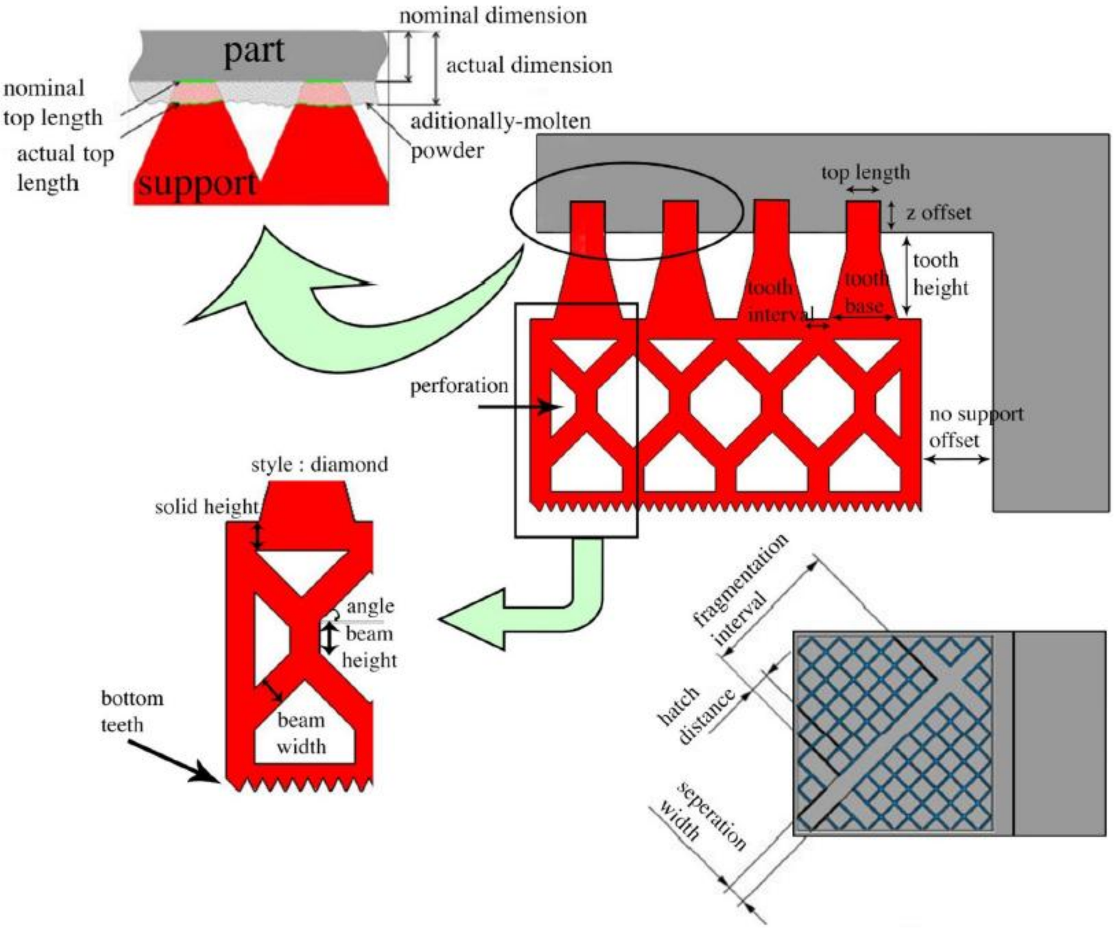

Figure 15: Block support structures with diamond perforations and other geometrical parameters [50].

As the primary focus of this research, block-type support structures were selected due to their broad industrial applicability, particularly for both small and large solid components, where high mechanical stability and effective heat dissipation are essential. As discussed earlier in this thesis, these supports function not only as mechanical anchors but also as thermal sinks, making them highly relevant for mitigating warping deformation, a defect identified as strongly influenced by support design. Furthermore, block supports are well-suited for customizable parameterization (e.g., tooth height, tooth top length, hatch spacing), enabling in-depth investigation of their influence on multiple performance criteria such as support removability, warping, and material consumption. This flexibility, combined with their recognized challenge in post-processing, provided a strong justification for selecting block-type supports as a representative structure for the development of a multi-response optimization framework. Their performance also served as a baseline reference for subsequent comparative analyses involving line, contour, and cone support types.

2.3.4 Strategies for Support Removal and Optimization

Delving deeper into the characteristics that define a good support structure in metal AM and SLM processes, it should prioritise minimizing support material, preventing build failures and potential part damage, and ensuring effortless post-processing. Specifically, the optimal support structure should elevate the part from the platform for easy removal, anchor the overhanging and floating sections of the part to the build plate, reinforce thin and tall features during the build to prevent toppling and part destruction caused by recoating mechanism forces, and mitigate part curling or distortion resulting from thermal stresses by dissipating heat away from the newly melted surface and ensuring consistent thermal conditions in the consolidation zone [51]. Thus, producing an object without or with insufficient support structures results in defective and collapsed parts, while the addition of unnecessary supports increases the overall material usage, post-processing time and effort required for support removal, as well as the risk of damaging the part. In addition to the geometric characteristics described in section 2.3.3., part orientation also significantly influences support generation and removal. It should aim to achieve a balance between minimising the use of support material, facilitating easy removal, and minimising build time [11]. Considering the preceding, extensive research has been conducted on the design and optimisation of support structures in metal AM, aiming to reduce the amount of support material required and introduce inventive methods for easy removal, all while maintaining high-quality prints at a low cost.

2.3.4.1 Build Orientation-based Strategies

Designing and fabricating support structures may be a procedure that requires extra post-processing, increased printing time, and printing costs. Furthermore, the removal of these support materials can be challenging, negatively affecting the surface finish. Hence, there is a growing demand for strategies to minimize their use. One such approach involves rotating components to achieve self-support or minimal required support, thereby mitigating the need for extensive support structures.

Frank et al. [52] first developed an expert system tool for rapid prototyping processes that considers the various parameters that affect the production of a prototype and interacts with the user to recommend the optimal build direction. They employed a multi-objective function to optimise build time and surface finish by minimising support structure volume and contact area. Majhi et al. [53] developed efficient geometric algorithms to simultaneously address multiple criteria, including the number of layers, volume, and contact area of support structures, as well as surface finish. Their objective was to solve this multi-criteria problem and propose the optimal build orientation for layered manufacturing. Jain et al. [54] developed and implemented an algorithm to determine the optimal part build orientation for enhancing part strength. Dog-bone specimens made of polyamide powder were fabricated using SLS to evaluate the experimental results, while a multi-objective decision-making method was proposed for future work to enhance part quality, including surface finish and build time.

Significant research was also conducted by Wang et al. [55], where the challenges and strategies for improving the quality of overhanging surfaces in SLM processes were discussed. Their research presents findings from experiments investigating the effects of various factors such as inclined angle, scanning speed, laser power, residual stress, and scanning vector length on overhanging surface fabrication. The analysis reveals relationships between these factors, such as the mutual restraint between laser power, scanning speed, and inclined angle. The study identifies two effective methods for optimizing overhanging surface fabrication: adjusting part orientation and controlling regional parameters. These methods have been proven effective in improving the quality of overhanging surfaces in complex metal parts manufactured using SLM and in reducing the need for manually added support structures, thereby providing preliminary solutions for mitigating risk in the fabrication process.

Brika et al. [56] introduced an integrated method for determining the optimal build orientation in LPBF. This approach optimizes mechanical properties, surface roughness, support structure volume, and build time/cost simultaneously. The method establishes objective functions for various mechanical properties and surface roughness through experimental data analysis. It estimates support structure volume based on part geometry to evaluate build time and cost. Significant achievements include the consideration of multiple objectives and the establishment of an objective function that accounts for various load directions and heat treatments. Additionally, they developed a user-friendly graphical interface for controlling optimization factors and providing visualization and evaluation tools.

Samant et al. [57] developed a method to determine the optimal build orientation for a part, aiming to reduce the total build time while improving support removal and minimizing the contact area between the part surface and the supports. They utilized a hierarchical octree data structure to analyse support accessibility and the area of contact between the supports and the part. However, while build orientation optimization has focused on support accessibility, the contact areas between supports and the part surface, and build time, incorporating additional manufacturability factors—such as the volume of support structures, design for additive manufacturing (DFAM) parameters, and part tolerances—into the model may provide a more comprehensive approach for determining the optimal part build orientation.

Qin et al. [58] developed an automatic method to determine the optimal build orientation for PBF-LB. This method uses a weighted relation that includes support volume, volumetric error, surface roughness, build time, and build cost. The weights for these factors were determined through pairwise comparison. A weighted sum model was then used to calculate a summary value for each alternative orientation. Based on these summary values, the optimal build orientation was selected. Demonstration results indicated that the proposed method was effective for both regular and freeform surface models, producing stable, reasonable results with the desired efficiency.

2.3.4.2 Geometric and Topology-based Strategies

In recent years, there has been extensive exploration into the utilization of innovative cellular support structures in SLM to reduce the volume of support material, shorten build time, and facilitate support removal, while simultaneously maintaining high-quality prints. Hussein et al. [51], [59] utilized direct metal laser sintering technology along with titanium alloy Ti6Al4V powder to investigate support structure geometry. They suggested optimized lattice support structures (Schoen gyroid and Schwartz diamond lattice types as shown in Figure 16) aimed at minimizing both support material usage and build time, while still meeting the necessary structural requirements for metallic support structures. The experimental findings revealed that support structures with minimal volume could result in substantial savings in support material and considerable reductions in build time, primarily influenced by the structure type, volume fraction, and cell size.

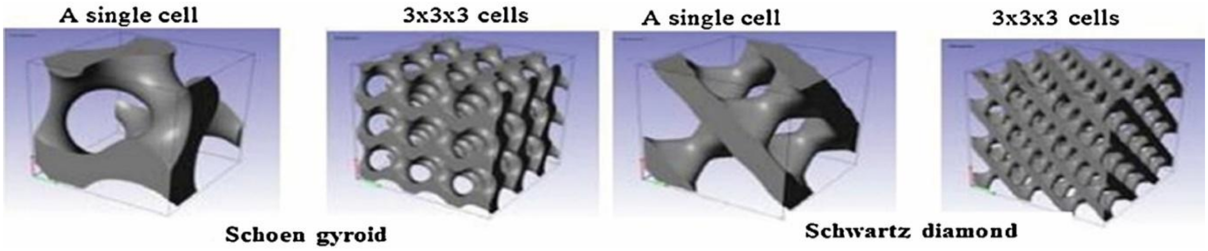

Figure 16. CAD model of Schoen gyroid and Schwartz diamond lattice structures [51].

Cloots et al. [60], to successfully produce metal parts using SLM, developed a component segmentation strategy enabling the division of critical areas of the component through a specific scanning strategy with appropriate energy input. They also proposed optimised support strategies to minimise the need for extensive support structures and decrease post-processing labour, all while maintaining part quality intact. As illustrated in Figure 17, there is an absence of wall structure, and the connection between supports and the part occurs through fixation points within the grid support structure. The optimization of the support structure was accomplished through the utilization of the design of experiment methodology, aimed at determining the optimal values for three normalized process parameters: hatching distance, distance to fixation point, and scan speed.

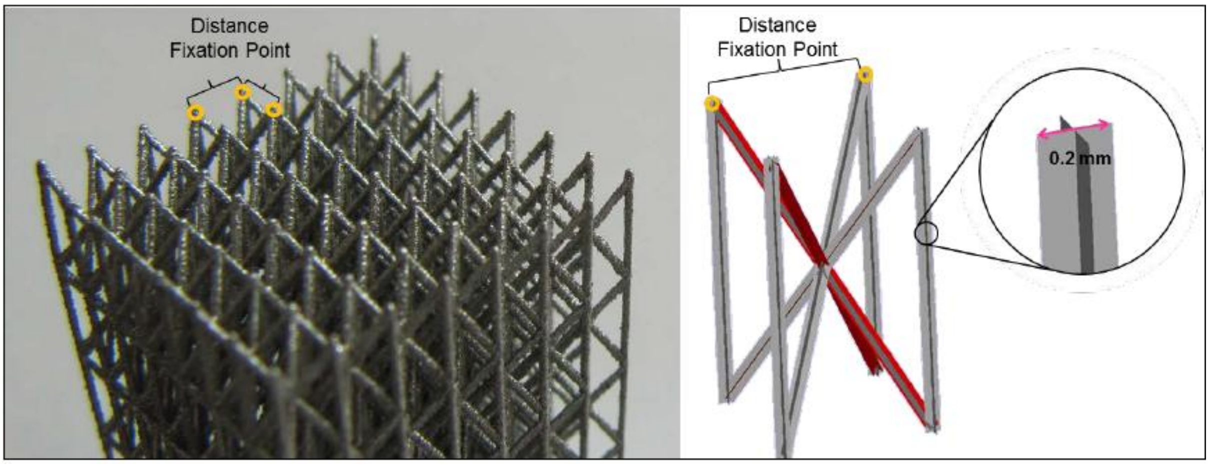

Figure 17. Grid support structures with fixation points and no walls [60].

Strano et al. [61] introduced a novel method for designing support structures that optimise both the orientation of the part and the cellular structure of the support. The approach utilises a new optimisation algorithm that employs pure mathematical 3D implicit functions to design and generate cellular support structures for SLM, including graded supports. A visual representation of the surfaces produced by these functions is depicted in Figure 18. The periodic surfaces examined in this study include the Schwartz equations, as well as two others created through combinations of trigonometric functions, the Gyroid and Diamond equations. This method is highly versatile, allowing for the simple design of geometries through mathematical expressions. It enables the easy definition and optimisation of different cellular structures, particularly graded ones that provide robust support where the part's weight is concentrated and less support elsewhere. Evaluation of this approach for a complex geometry demonstrated significant material savings, thereby enhancing the sustainability and efficiency of metal additive manufacturing.

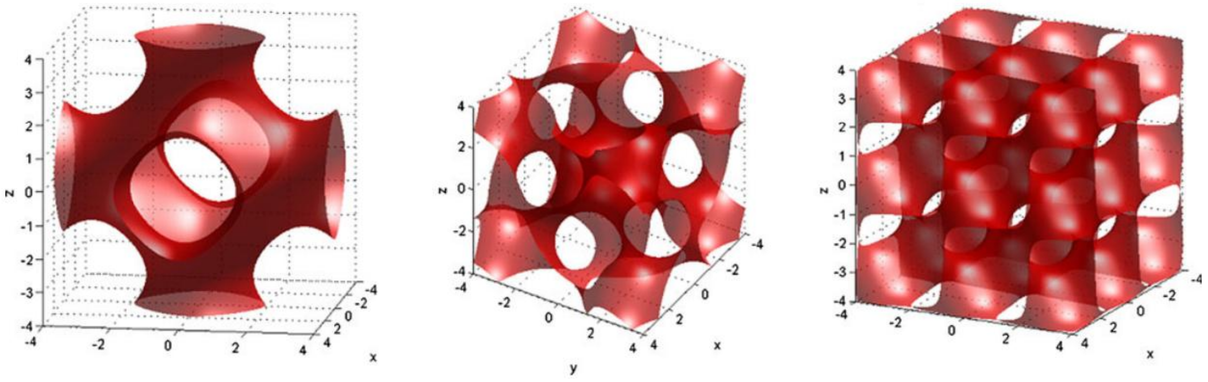

Figure 18. Graded support structures including Schwartz, Gyroid, and Diamond equations respectively [61].

Li et al. [62] introduced a design method named the lightweight and support-free design method, outlining the detailed design process and highlighting its advantages. The process involved utilizing topology optimization (TO) to achieve lightweight designs and developing a support-free design approach to fulfil the requirement for support-free AM. As a practical example, they applied this method to design a cross-beam component, which was successfully produced using the SLM process. The results confirmed the effectiveness of the proposed design method for creating lightweight and support-free metal parts.

Langelaar [63] proposed a method based on two-dimensional (2D) test problems to optimise part geometry, support layout, and build orientation in terms of topology optimisation. This approach allows designers to balance manufacturing costs and part performance for PBF-LB processes. Notably, the computational cost of this method remains relatively low, yet it consistently yields high-quality outcomes in numerical experiments. Langelaar's method integrates both the support structure and the actual part into the optimization algorithm, thus enabling the determination of the optimal build orientation while effectively managing manufacturing costs.

Omid et al. [64] examined the viability of lattice-based support structures for PBF-LB systems. The objective of this research was to assess the effectiveness of various lattice designs as support structures for a gas turbine component. Different lattice types were developed, tested, compared, and validated. The findings indicated that the lattice-based supports generated were potentially suitable for PBF-LB applications. It was essential for these supports to be appropriately designed to maintain the part's geometry while ensuring a rapid fabrication process and easy removal, ideally without the need for machining or sawing.

Overall, much research has been conducted towards the implementation of structural and topological optimisation in additive manufacturing. This involves distributing material in a geometric domain to match targets for mass, displacement, structural stiffness, cost, and other characteristics as closely as possible [65], [66], [67], [68], [69]. However, most of this research primarily focuses on optimising the part itself, often neglecting the support and process parameters that define the geometry of support structures and their ease of removal.

2.3.4.3 Support and Process Parameter Strategies

The optimisation of support and process parameters in metal AM presents a major challenge for researchers, given the potential to enhance the printing procedure by minimising printing time, post-processing efforts, printing defects, overall costs, and other related factors. Jukka-Pekka et al. [70] utilized SLM technology to investigate and compare the effectiveness of two different support structures, namely web and tube, aiming to examine support removability and part surface quality. For the experiments, two trapezoidal specimens were utilized, each composed of multiple bars featuring inclinations ranging from 25 to 65 degrees, where supports were generated. It was observed that the removability of web supports was much better than tube supports. Additionally, while all bottom surfaces exhibited poor quality, web supports demonstrated slightly better performance than tube supports.

Poyraz et al. [39] examined the effects of various design parameters on block-type supports applied to ledge overhanging specimens manufactured using DMLS technology and Inconel alloy 625 (IN625) as the material. The aim of this study was to provide guidance for designing optimised support structures capable of reducing the amount of material required, production time, and post-processing efforts. The results revealed that hatching parameters significantly impact the support structures more than tooth parameters. Increasing the hatch distance leads to greater part distortion and can even cause separation after a certain level. The best outcomes among the tested values were achieved with a 0.5 mm hatch distance. Moreover, the microstructural analysis showed that support structures built with higher hatch distance and fragmentation interval detached from the part easily, while lower values of tooth top length led to weaker support attachments as well. On the other hand, some micrographs revealed that the self-detaching of the support structures from the part can lead to irregularities in surface quality as well as some porosity formation, as shown in Figure 19.

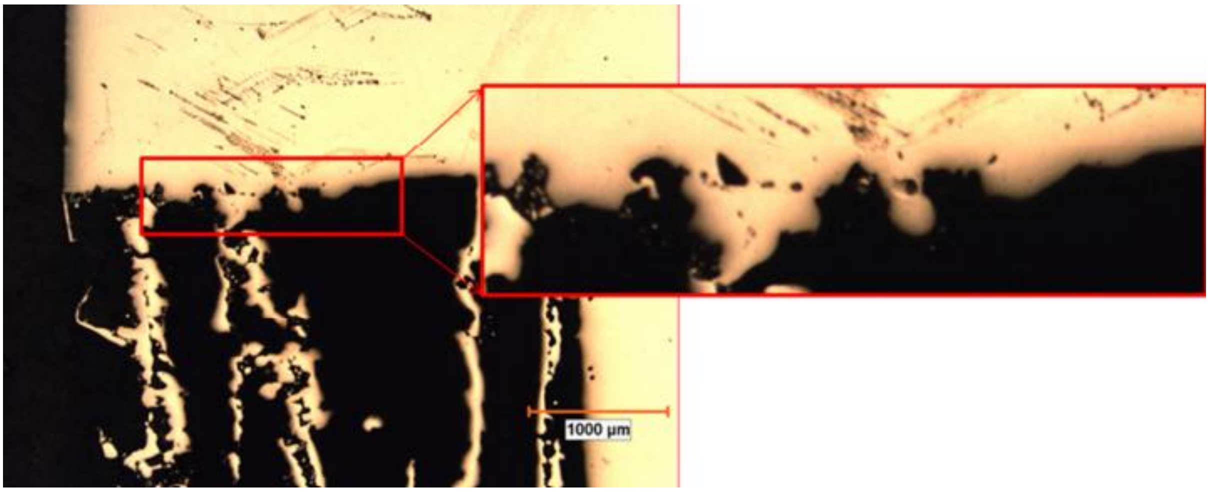

Figure 19. Micrograph showing irregularities in surface quality and porosity formation [39].

Lindecke et al. [71] investigated through experiments on SLM and tensile tests, the strength of the connection between optimised support structures and the part, focusing on support removability, material usage, surface quality after removal, and the specific strength of the support structure itself. Various types of support structures were fabricated using Ti6Al4V alloy powder and subjected to tension with a constant velocity until fracture occurred. The displacement of the machine was recorded along with the corresponding tensile force. Figure 20 illustrates the experimental setup and the areas of investigation. The findings led to the proposal of a set of guidelines designed to assist process engineers in choosing the appropriate support structure design for print job preparation. Additionally, alternative solutions of equal significance were suggested to minimize support material usage and optimise post-processing.

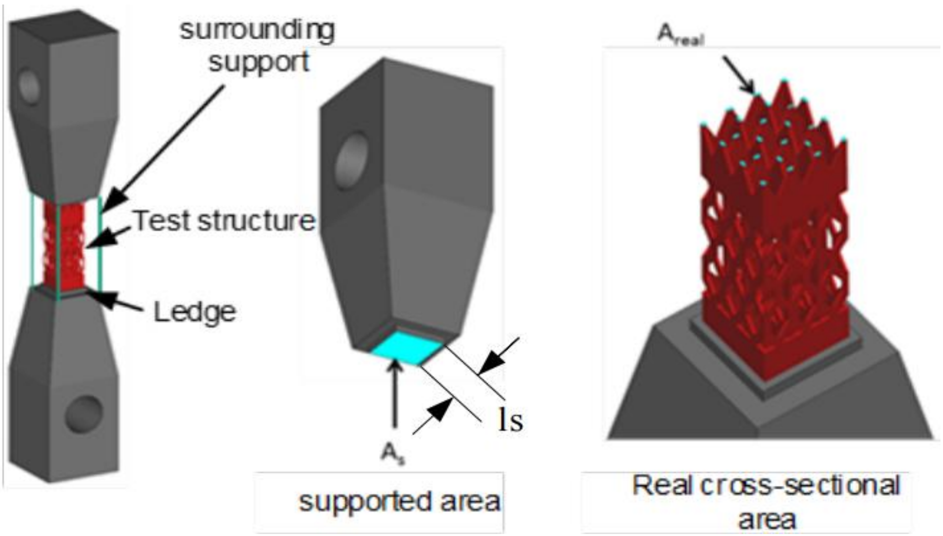

Figure 20. Tensile strength test specimen and areas for strength calculations [71].

Zhang. Z. et al. [72] conducted a study comparing the weight and effectiveness of branch (or tree-like) support structures and straight columns (referred to as lattice support structures in their research) on the same plane. They created a set of standard specimens with branch support using SLM technology and analysed their weight and scanning time. Subsequently, they subjected these samples to compression testing using a compression testing machine to assess how different support parameters affect the strength of the support structures. The findings indicated that branch supports offer advantages in terms of material, energy, and time efficiency during construction. Moreover, the yield strength of branch supports generally increases with the diameter of the support and the angle of inclination of the branches. Additionally, branch supports exhibited greater strength compared to traditional lattice support structures. However, they also identified trade-offs that are often overlooked in broader discussions. In particular, tree-like supports tend to exhibit lower structural stiffness near the base and connection points, which can lead to premature failure during the recoating process or poor thermal conduction in highly stressed overhanging regions.

Zhang. K. et al. [73] examined the distance between the walls (or hatch distance) and the incorporation of cuboids into conventional block-type support structures to enhance heat dissipation. They utilized the Taguchi method to assess how the geometric design of these supports affects part deformation and surface roughness. Figure 21 illustrates the block supports used, as well as the integrated solid pieces or cuboids. The findings indicated that cuboids as support structures can reduce deformation, though not as effectively as tooth structures, which provide stronger connections. Noteworthy, narrowing the gap between cuboids and overhangs can weaken the strength of tooth structures, resulting in increased part deformation. In general, the spacing between adjacent support walls and the gap between cuboids and overhangs were identified as having the most significant impact on part deformation and surface quality, respectively.

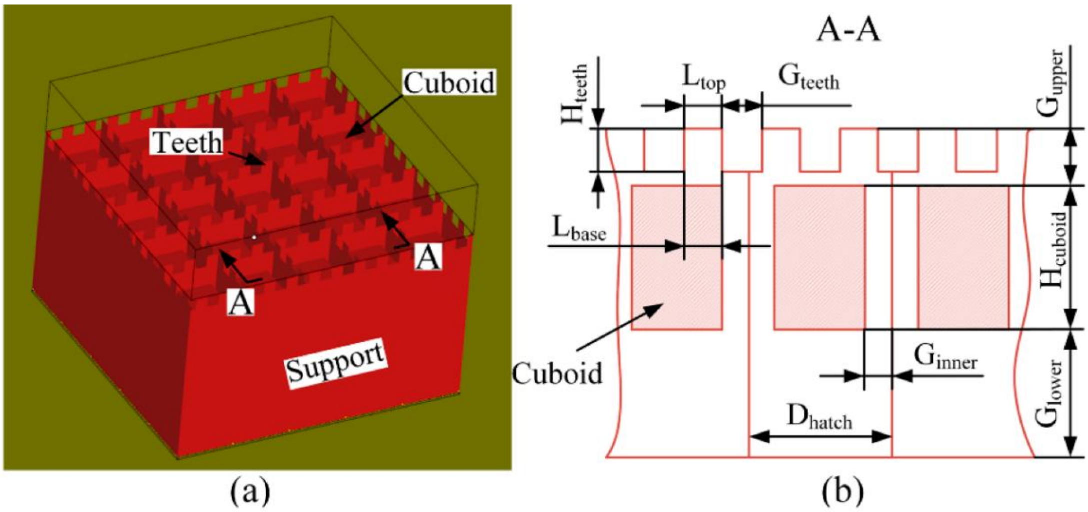

Figure 21. Block support structure with cuboids: (a) 3D shape (b) A-A cross section [73].

Ameen et al., [74] conducted an initial investigation into how various support structure designs affect the removal of unmelted powder from overhanging surfaces fabricated through Electron Beam Melting (EBM) technology. Their objective was to reduce printing costs, minimize material waste, and mitigate environmental impact, while also ensuring that support structures avoided any enclosed hollow spaces prone to accumulating unmelted powder. Their experimental results revealed that optimizing the design parameters of support structures could improve powder removal efficiency. Consequently, Ameen et al. [75], explored and evaluated various support and process parameters for EBM through the application of multi-objective genetic algorithms such as response surface methodology (RSM), analysis of variance (ANOVA), and Multi-Objective Genetic Algorithm II (MOGA-II). Their objective was to propose support structures that facilitate easy removal and minimize the consumption of support material, all while maintaining high-quality prints. To collect the data required for optimization, ninety small L-shaped specimens were fabricated, each consisting of different support and process parameters. The study determined that the optimal solution was characterised by a large tooth height (4 mm), large tooth base interval (4 mm), large fragmented separation width (2.5 mm), high beam current (6 mA), and low beam scan speed (1200 mm/s). Furthermore, to validate the optimization results, a bearing bracket model was designed and fabricated, employing both default and optimized support structures. Figure 22 illustrates a sample of four printed specimens implementing various support parameters. Similar research was also conducted by Ameen et al. [76] who aimed to design optimal support structures for fabricating Ti6Al4V alloy overhangs using EBM. Their goal was to create supports that are easy to remove and use less material without affecting part quality. To achieve this, they evaluated and optimized the design and process parameters of perforated block support structures using RSM and multi-objective genetic algorithms.

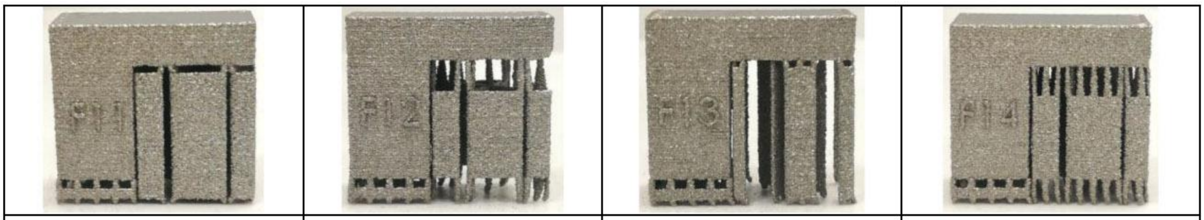

Th=1,Tbi=4,Fsw=0.5, $B_c = 6$, $B_{ss} = 1200$

Th=4,Tbi=4,Fsw=0.5, $B_c = 6$, $B_{ss} = 1200$

Th=1,Tbi=1,Fsw=2.5, $B_c = 6$, $B_{ss} = 1200$

Th=4,Tbi=1,Fsw=2.5, $B_c = 6$, $B_{ss} = 1200$

Figure 22. Sample of specimens fabricated with different support parameters (Th: tooth height, Tbi: tooth base interval, Fsw: fragmented separation width, Bc: beam current, Bss: beam scan speed) [75].

Schmitt et al. [77] proposed optimized support parameters for PBF-LB processes, focusing on support strength and removability. These parameters include laser power, scan speed, layer thickness, lattice density, tooth connection, and geometric perforations. Their experimental findings, derived from 3D printing and torsion/tensile testing, highlighted the significant impact of these parameters on both the shear and tensile strength of support structures. Additionally, adjustments in lattice density were found to alleviate residual stresses and accommodate part geometry, with varying effects observed across different layer heights. Notably, lower perforation rates were associated with enhanced powder removal and a slight increase in tensile strength, whereas higher perforation rates led to decreased tensile strength, particularly dependent on layer height.

Weber et al. [78] investigated the parameters influencing both the manufacturing process and support structure design in PBF-LB. They presented matrices that illustrate the cause-effect relationships between support and process parameters and their impact on build properties including support removal, printing time, support strength, etc. Additionally, they identified correlations among these parameters. From this analysis, they derived action recommendations for experimental procedures using the DOE method. They concluded that a thin and insufficient number of branches result in breakage during the wrapping of overhang features due to high thermal stresses. Consequently, well-optimized support parameters are crucial, particularly for tree-like supports, due to their inherently low stiffness. Thus, despite their lightweight nature, tree-like supports may introduce reliability concerns in industrial contexts where repeatability and thermal consistency are critical. These limitations justify the need for further research into support structure parameterization and simulation-based optimization techniques.

Mele et al. [79] examined how the geometrical parameters of overhangs and supports affected distortion and roughness in stainless steel parts fabricated via PBF-LB. They designed supported overhang surfaces using line-type support structures with different interval distances, while through a series of experimental tests, they identified the most effective process parameters. Measurements of displacement and roughness using optical and contact systems revealed significant discrepancies, emphasizing the importance of designing support structures based on overhang thickness and inclination to minimize distortions. The study also identified local defects on the edges, and after annealing, all geometries exhibited upward warping. Surface inclination was found to be the primary factor affecting roughness, with support design effectively managing thermal energy from overhangs.

Markovits et al. [80] investigated various support parameters, including tooth top length, hatch distance, and Z offset, to create a model-support connection strength map. This map enables the selection of the most suitable connection type between the support and the model based on the specific requirements of different scenarios. They evaluated the strength of these connections through torsion testing, focusing on shearing properties. Results were compared across different support parameters and materials, specifically 316L stainless steel and Ti6Al4V alloy. The study identified distinct failure modes depending on the chosen parameters, revealing that top length and hatch distance significantly impacted the mechanical properties of the support, while Z offset had the least effect.

2.3.4.4 Other Strategies

In addition to the strategies mentioned above for improving support performance and removability, many other studies have proposed alternative methods for removing the various support structures from metal parts fabricated through laser-based additive manufacturing. This includes research by Jamasp et al. [81] where a novel laser manufacturing method was proposed by combining pulsed and continuous modes of radiation aiming to build support structures in SLM that are easy to remove while having sufficient mechanical properties to withstand deformation and evacuate heat. Continuous radiation was employed for building the main object to ensure the desired mechanical properties, while pulsed radiation was used for fabricating the support structures. The study revealed that this approach significantly reduces printing time by utilizing the same laser in both modes. Additionally, the use of pulsed radiation allows for very high scanning speeds with high power during the fabrication of supports.

K. Zeng [29] developed an innovative framework for support structure design and optimization, addressing the challenge of effectively handling and removing supports in SLM processes. For that purpose, both analytical solutions and Finite Element Method (FEM) were applied to optimize the support structure parameters. Furthermore, seven sets of experiments were conducted using both uniform and non-uniform support structures, with hatch spacing as the main geometric parameter. The aim was to evaluate printability, including surface finishing, warping defects caused by thermal stresses, and the overall support material required. Figure 23 illustrates two samples of the specimen used during the experiments, each with a large support hatch spacing, indicating the defects observed on the bottom surfaces.

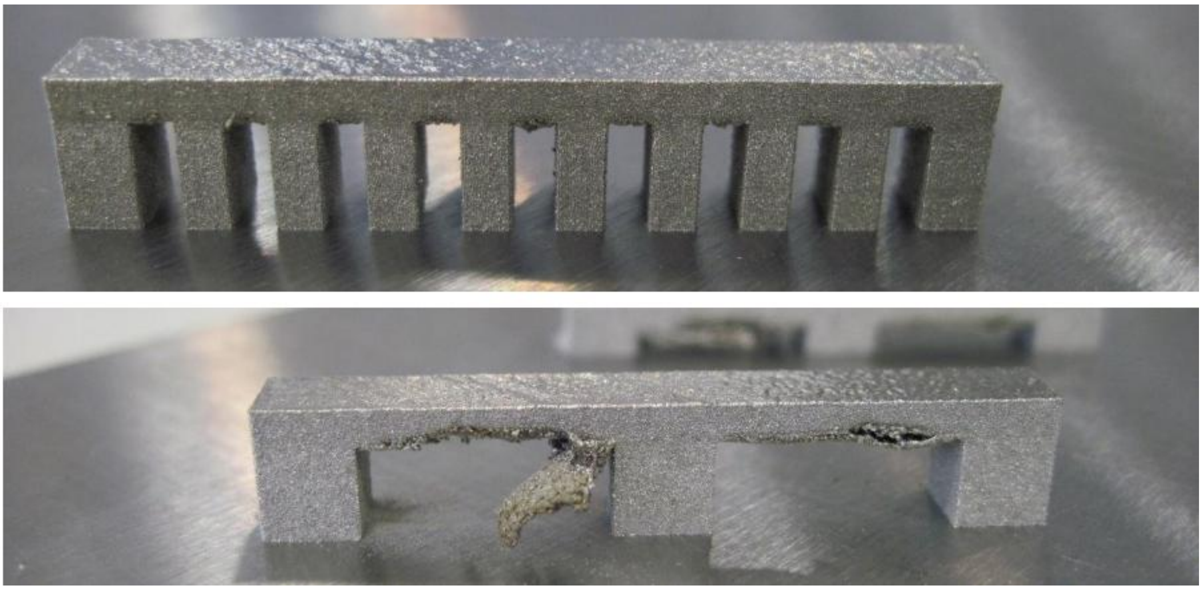

Figure 23. Defects observed for different support structures with a large hatch spacing of 2 mm and 12.5 mm [29].

Another alternative method for selectively removing metal support structures in powder bed fusion was proposed by Lefky et al. [82], [83]. In their study, for the first time, dissolvable supports were investigated, and two different approaches were proposed: direct dissolution and self-terminating electrochemical etching. It was found that the electrochemical process drastically reduces the complexity, costs, and time associated with support removal by replacing laborious machining and grinding operations with simple sensitization and etching processes. The sensitization process has been designed to be easily integrated into the normal thermal annealing step used to reduce internal stresses, while the etching process has been designed to be self-terminating and easy to apply.

A different direction was also followed by Tripathi et al. [84] who examined the milling performance of Inconel 718 block support structures of differing heights, measuring tool wear, milling force, and cutting energy. Similarly, Qiqiang et al. [85] studied the removability of metal support structures in SLM through milling, comparing various cutting lengths, and developing a FEM model to explain the support removal mechanisms. Specifically, they examined the milling performance of cone and block supports in terms of surface finish, surface roughness, and milling force. The results revealed that cone supports were subjected to severe collapse, while block supports were primarily removed through localized shearing. Additionally, the milling force and specific cutting energy required for cutting block supports were lower than those for cone supports.

Wei et al. [86] proposed an easily removable support material, namely SiC-316L composite, and its associated processing procedure for fabricating support structures for PBF-LB 316L steel alloy components, based on the new multiple material PBF-LB method. The experimental findings demonstrated the feasibility of using SiC-316L composite with 40 vol% 320 grit silicon carbide (SiC) as a support material, as it could generate the necessary mechanical defects for easy removal. The results also revealed that a transition zone between the building material and support material was prone to breakage under low external force due to the presence of cracks and pores in the support structure.

2.3.4.5 Critical Analysis and Research Gap Identification

The current research on support structure optimization in metal AM through process and design parameter control has shown promising but fragmented results. Studies such as those by Jukka-Pekka et al. [70] and Poyraz et al. [39] highlight the critical influence of support morphology and hatching parameters on removability and surface quality. Others, like Lindecke et al. [71] and Zhang Z. et al. [72], emphasize the mechanical strength and efficiency trade-offs between different support geometries. Despite these valuable contributions, in reviewing the strategies for support removal and optimization, including build orientation adjustments, geometric/topological approaches, support and process parameter tuning, and alternative strategies, it becomes evident that while individual methods can reduce support material or ease post-processing, most studies approach these factors separately.

Current literature often optimizes a single objective (e.g., minimizing support volume, improving surface quality, or reducing removal effort) without simultaneously addressing the complex interdependencies among thermal management, mechanical stability, build time, and part quality. Furthermore, most optimization strategies are highly material- and machine-specific, limiting the transferability of findings across different AM systems. Critically, there is a lack of integrated, multi-objective optimization frameworks that holistically consider mechanical, thermal, geometric, and economic performance. Future research should move beyond isolated parameter studies toward comprehensive, experimentally validated strategies and computational frameworks that unify support design, process parameters, and thermomechanical considerations into practical, broadly applicable guidelines. Addressing this gap is vital for achieving consistently high-quality, cost-effective metal additive manufacturing production.

2.4 Thermomechanical Modelling in SLM

2.4.1 Thermal Phenomenon and Heat Transfer

As mentioned earlier in the literature, in SLM, a high-density laser beam is applied from the top of the machine to selectively melt the powder material, creating a molten pool that solidifies quickly to form the bulk part. Parameters such as laser power, laser speed, spot size, scan strategy, and material properties play a major role in solidification, as they define the size of the melt pool and the time it needs to solidify [87], [88]. Figure 24 illustrates a schematic representation of heat transfer in SLM. As the laser beam irradiates the surface of the powder bed, a portion of the laser energy is reflected, while the remaining energy is absorbed by the powder. This absorbed energy melts the metal powder, creating a small molten pool. During the heating and cooling process, the material undergoes multiple phase changes from solid to liquid and back to solid. As solidification occurs, metallurgical bonds form between adjacent tracks and neighbouring layers. To accurately describe the thermal behaviour, it is also important to consider not only thermal conduction but also heat loss due to convection and radiation [89]. In a typical SLM process, such as the commercial EOS machines [90], the build occurs within a closed chamber, where convection across the surface dissipates a certain amount of energy. When the temperature surpasses the material's vaporization point, vaporization may occur. In this scenario, heat radiation becomes significant due to the elevated temperature [29].

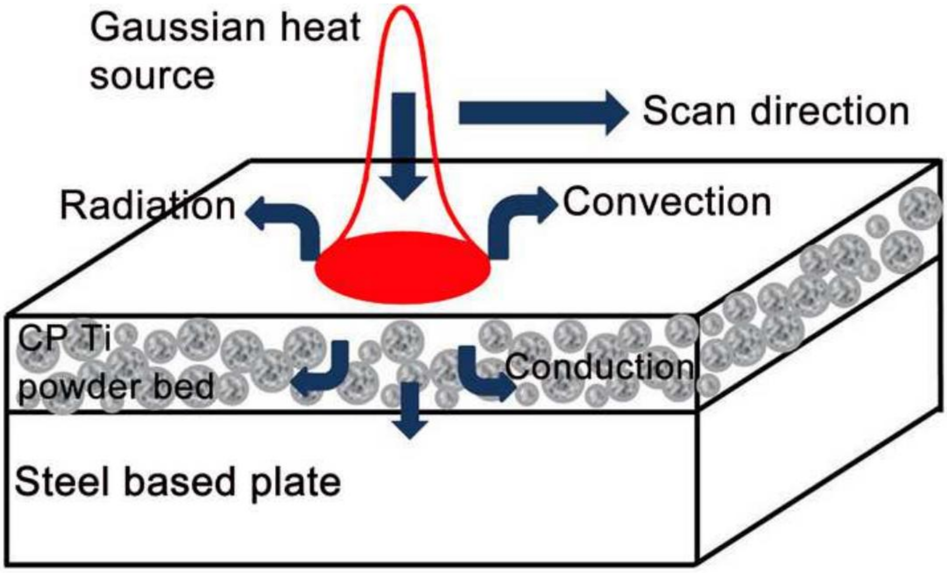

Figure 24. Schematic representation of heat transfer in SLM [89].

2.4.2 Equations and Boundary Conditions

Many models have been developed to describe the energy sources and various heat conduction issues in SLM, aiming to accurately represent the process through numerical modelling and simulations [20], [87], [88], [89]. As an additive manufacturing process with multiple influencing factors, SLM is significantly affected by various parameters related to the laser, powder, and melting process. Key SLM parameters (refer also to section 2.2.2) that demand careful selection to improve part performance in terms of mechanical properties, microstructures, and dimensional accuracies, include laser power, spot size, scan speed, scanning strategy, layer thickness, hatch spacing, and powder characteristics like morphology, flow properties, and composition [20].

When considering in-process parameters, an equation known as the volumetric energy density (Equation 2.1), which describes the average applied energy per volume of material, is used to examine the effects of process parameters during the SLM processing [91]. Where E_v is the energy density (J/mm^3), P is the laser power (W), v is the scanning velocity (mm/s), h is the hatch distance (mm), and t is the powder layer thickness (mm). However, Prashanth et al. [92] noted that critical factors affecting the energy density, such as gas flow direction, laser diameter, and hatch style, have not been taken into consideration.

$$E_v = \frac{P}{v \cdot h \cdot t} \qquad (2.1)$$

Understanding the volumetric energy density is essential in the context of SLM, as it offers a consolidated metric that captures the cumulative influence of key process parameters (laser power, scan speed, hatch spacing, and layer thickness) on the energy delivered to the powder bed [93]. The significance of the volumetric energy density lies in its direct correlation with melt pool dynamics, which determine the microstructural evolution, mechanical performance, and defect formation in printed parts. A higher volumetric energy density generally increases the likelihood of full melting and strong interlayer bonding, while an excessively high volumetric energy density may cause keyholing, vaporization, and balling phenomena. Conversely, a low volumetric energy density may lead to lack-of-fusion defects due to insufficient energy input. Therefore, achieving an optimal volumetric energy density is critical to balance the competing needs of geometric accuracy, material consolidation, and thermal stress mitigation. Numerous studies have attempted to map the optimal volumetric energy density range for different alloys and geometries, yet generalization remains challenging due to machine- and material-specific variability. Thus, the volumetric energy density provides not only a predictive tool for defect control but also a framework for parameter optimization in both experimental design and simulation-driven process planning.

Regarding heat transfer in SLM, Fourier's heat conduction theory [94] is the most commonly employed framework for addressing various heat conduction challenges and can be adopted for simulating the moving heat source problem and studying thermal evolution in SLM processes. Zeng [29], noted that most researchers use Equation 2.2 as the primary equation for heat conduction. Additionally, Equation 2.3 represents an initial boundary condition with a constant temperature throughout the domain, while Equations 2.4 and 2.5 serve as examples of surface convection and constraint boundary conditions, respectively.

$$\lambda(T)(\frac{\partial^2 T}{\partial x^2} + \frac{\partial^2 T}{\partial y^2} + \frac{\partial^2 T}{\partial z^2}) + q = \rho(T)c(T)\frac{\partial T}{\partial t} \qquad (2.2)$$

$$T(x, y, z, 0) = T_0 \qquad (2.3)$$

$$-\lambda(T)\frac{\partial T}{\partial z} = h(T - T_e) \qquad (2.4)$$

$$-\lambda \frac{\partial T}{\partial z}|_{z=0} = 0 \qquad (2.5)$$

Where T is the temperature, λ is the conductivity coefficient, ρ is the density, c is the heat capacity, q is the internal heat source, T_0 is the powder bed initial temperature, T_e is the environment temperature, and h is the convection heat transfer coefficient.

Besides the above-mentioned equations and boundary conditions related to heat conduction in SLM, surface heat source models are also of significant importance for representing the laser's thermal behaviour on the built surface. While it can be assumed that a laser beam is a point or line source, this assumption does not align with reality. The Gaussian model, which is the most widely adopted laser energy model, utilises the symmetrical distribution of laser irradiance across the beam [87]. It proposes that the laser irradiance exhibits symmetry around its propagation direction, and in most cases, the maximum irradiance Io (power per unit area) is at the centre of the beam pattern. Equation 2.6 describes the Gaussian laser beam distribution for the fundamental mode TEM_{00} (Transverse Electromagnetic Mode).

$$I(r) = I_0 e^{-\frac{d^2}{d_1^2}} \qquad (2.6)$$

Where d_1 is the beam diameter corresponding to the point where the irradiance I_0 diminishes to $1/e^2$, and d is the diametrical distance of a point from the centre. Likewise, the thermal heat flux is characterized by the thermal energy per unit area and is represented by Equation 2.7. Where P is the laser power, r_0 is the spot radius, and r is the radial distance.

$$q(r) = \frac{2P}{\pi r_0^2} e^{-\frac{2r^2}{r_0^2}} \qquad (2.7)$$

Surface heat source models are frequently utilized in SLM to simulate the laser beam. Nonetheless, alternative models have also been developed, considering laser beam penetration into the powder bed due to its porosity. Wang et al. [95] for instance, examined energy absorption and penetration in SLS. They measured the amount of energy absorbed by the powder bed and its penetration depth and proposed a ray tracing model that considers the geometry and structure of the powder.

In summary, the equations and models discussed above are essential foundations for analysing thermal conduction in SLM processes. Furthermore, commercial software such as COMSOL Multiphysics [10] and Abaqus [96] enables thermomechanical simulations to predict the thermal performance of components, including those manufactured via SLM. These tools provide extensive customization of parameters such as temperature, boundary conditions, and heat flux to suit specific applications and user requirements. In this study, such software was utilized to explore the thermal behaviour of small samples and various support structures within SLM printing conditions.

2.4.3 Thermomechanical Analysis Strategies

In the fields of mechanics and thermodynamics, thermal stress refers to the mechanical stress induced by changes in a material's temperature. Thermal Mechanical Analysis (TMA) proves to be a powerful tool for exploring the behaviour of materials during powder bed fusion. TMA is a technique used to measure a material's dimensional changes under precisely controlled heating and cooling conditions, providing valuable insights into its thermal and mechanical properties [97]. When the cumulative thermal stress surpasses a material's yield stress, it can cause fracturing or plastic deformation. In PBF-LB/M, when a hot layer is deposited, the lower part usually contacts a metal surface, while the upper part is exposed to air. The upper layer cools faster than the lower layer, leading to shrinkage at the top due to the different thermal diffusivities of the metal and air [98], [99].

Several past and recent studies have employed thermomechanical analysis and experimentation to examine the thermal expansion and deformation behaviour of parts printed in PBF-LB/M, utilising a wide range of materials including titanium, aluminium, and nickel alloys. Nickel et al. [100] investigated the impact of deposition patterns on stresses and deflections in laser-deposited metal parts. Their finite element modelling demonstrated that deposition patterns significantly influence part stresses and deflections. Experimental results were consistent with modelling predictions, confirming the crucial role of deposition patterns in determining part behaviour.

Dai et al. [101] developed a 3D thermo-mechanical finite element model incorporating the powder-to-solid transition effect to investigate the transient temperature, transient stresses, residual stresses, and warpage of a layer-by-layer build part in PBF-LB processes. Their findings indicated that transitioning from initial solid elements to powder elements leads to higher temperature gradients, greater transient and residual stresses, and increased warpage.

Zaeh and Branner [102] investigated specific approaches using finite element analysis (FEA) to simulate transient physical effects in SLM. Their investigations focused on coupled thermo-mechanical models that incorporate specific boundary conditions and temperature-dependent material properties to identify the heat impact on residual stresses and deformations. Additionally, in order to evaluate structural effects and simultaneously validate the simulations, analysis of residual stresses based on neutron diffractometry, along with considerations towards part deformations, were presented.

Song et al. [103] examined residual stresses in SLM-built parts using X-ray diffraction strain measurement and finite element simulation. They analysed the microstructure and texture of the parts and proposed a conceptual model of residual stress generation based on fictitious thermal expansion. Their model suggests that residual stresses result from strain incompatibility "frozen in" within the workpiece during fabrication. Through simulation results and experimental data, particularly from a simplified conceptual thermal expansion model, they concluded that the creation of residual stresses can be understood by considering thermal strain incompatibility with the base plate and thermal gradients within the built part itself.

Li et al. [104] devised a comprehensive multi-scale modelling approach to swiftly forecast part distortion. Their methodology incorporates a micro-scale laser scan model, a meso-scale layer hatch model, and a macro-scale part model. They introduced the concept of an equivalent heat source in the micro-scale laser scan model and utilized it to predict the local residual stress field in the meso-scale layer hatch model. This residual stress field was subsequently integrated into the macro-scale model to forecast both part distortion and residual stress. Validation of the predicted part distortions was conducted using experimental data obtained from four distinct scanning strategies.

Javid and Ghoreishi [105] developed a thermomechanical finite element model to analyse the thermal deformation behaviour of Inconel 718 alloy during PBF-LB. Their study results indicated that the temperature profile and clad dimensions are highly dependent on the heat source and material conductivity. Laser power and cladding velocity significantly affect residual stresses, with longitudinal stresses being about three times greater than transverse stresses. Mechanical analysis shows that increasing input energy leads to higher residual stresses but reduces the number of cracks in the cladded layer.

Chen et al. [17] developed a layer-by-layer model to evaluate the residual stress distribution and quantitative variation in typical parts fabricated by PBF-LB. Their study, based on both simulated results and experimental data, revealed that hollow and semi-hollow parts exhibited lower residual stress compared to solid parts. They also recommended design modifications, such as using rounded corners instead of sharp ones and arc structures instead of straight ones, to further minimise stress during the printing process.

Yang et al. [106] examined the thermal deformation behaviour of 17-4PH stainless steel during PBF-LB using TMA. They observed significant deformation in the material during the process, influenced by scanning speed and laser power. Moreover, the study suggested that by optimizing the printing process parameters and post-processing techniques, the quality of the printed parts could be improved to rival or exceed that of commercial products, taking into account factors such as defect levels, surface roughness, gloss, and tactile sensation.

Burkhardt et al. [107] examined the accuracy and efficiency of various modelling assumptions and numerical settings in thermo-mechanical simulations of PBF-LB processes. Using the deal.II C++ library, they validated a highly parallelized and adaptive finite element method to investigate the impact of assumptions such as omitting surrounding powder and using linearized material models. They also identified necessary temporal and spatial discretizations for simulating PBF-LB of Ti6Al4V alloy. Insights from a simple geometry were applied to a more complex profile, showing minimal deviations in displacements and residual stresses with significantly reduced computational time. The efficient approach yielded a maximum deviation of 8% in displacements and 3.5% in residual stresses while significantly reducing computational time.

Raun et al. [108] developed a thermo-mechanical phase-field fracture model, which is based on a thermodynamically consistent derivation. Employing the finite element method, the model was numerically implemented to simulate hot cracking in additive manufacturing and PBF-LB systems. Notably, the model accounts for both thermal strain and solidification shrinkage. Their study, in conjunction with experimental findings, revealed that solidification shrinkage strain plays a major role in circumferential crack formation, while temperature gradients predominantly contribute to central crack formation. Further analysis through process parameter investigation indicated that higher laser power and slower scanning speed result in keyhole mode hot cracking, whereas lower laser power and quicker scanning speed tend to induce conduction mode cracking.

2.4.4 Thermomechanical Analysis and Support Structures

Expanding on the aforementioned methods to investigate the thermal behaviour of a component during PBF-LB processes, significant work has also been conducted regarding support structures. Zeng et al. [109] developed a finite element model to calculate the effective thermal conductivity of lattice support structures in SLM, consisting of solidified material and entrapped powder. They applied homogenization and periodic boundary conditions to study the steady-state thermal behaviour of the representative volume element (RVE), examining both linear and nonlinear thermal properties. The study analysed the impact of volume fraction, number of cells in the RVE, and boundary conditions. This method efficiently predicts temperature by using effective thermal conductivity, simplifying finite element analysis.

Gan and Wong [110] conducted experiments and finite element analysis to evaluate the flatness of overhang thin plates and cuboids, assessing distortion resulting from the use of three different types of support structures (Y, IY, and pin) fabricated in SLM. These three types of support structures are illustrated in Figure 25. It was found that thermal warpage caused the Y-type support structure to fail due to nonuniform and lengthy distances between connection points, resulting in uneven heat dissipation. In contrast, the IY support type displayed better performance than the Y-type, characterized by fewer overhang-support contact points and greater spacing between them. Additionally, the pin support structure exhibited greater uniformity and reduced distortion compared to the other two cases.

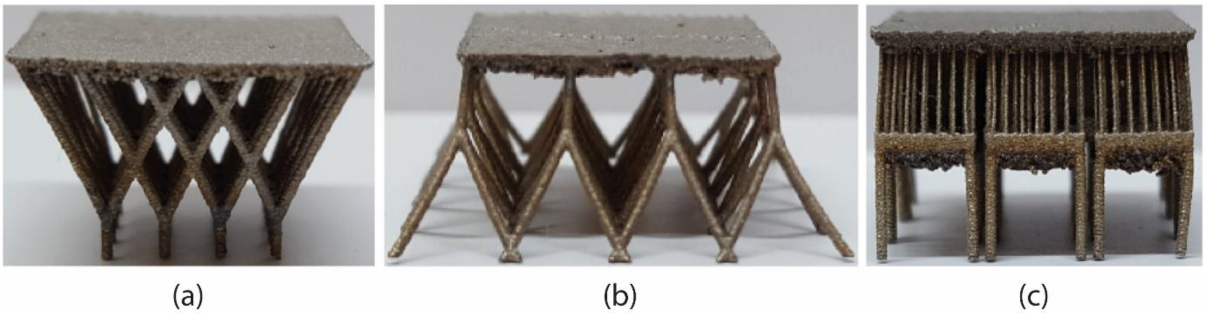

Figure 25. Side view of printed supports and thin plate: (a) “Y” type, (b) “IY” type, (c) “pin” type [110].

Malekipour et al. [111] contributed to the field of remanufacturing by introducing a method based on a MATLAB [112] code to reduce heat stress in the SLM process, minimizing the temperature gradient between the heat-accumulated zone in overhangs and the underlying layers. This is done by creating complex support structures that ensure mechanical stability and enhance heat conduction. The study evaluates different geometries to find an efficient design that uses less material while maintaining similar heat conduction properties. Figure 26 illustrates the methodology and the model used to represent temperature distribution between the overhang surface, the support structures, and the layer beneath. However, their framework remains largely conceptual, with limited empirical validation or sector-specific guidance for implementation in real-world design workflows.

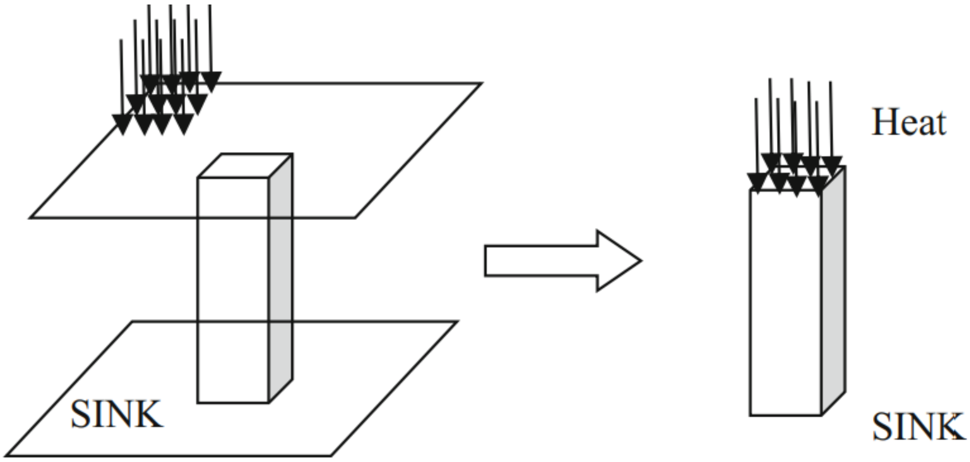

Figure 26. Model used with overhang, support structures, and the layer beneath [111].

Cheng et al. [113] explored the potential of using topology optimisation to design support structures aimed at reducing residual stress and preventing build failures. They utilised the inherent strain method to quickly predict residual stress in PBF-LB processes. The support structures were designed with graded lattice structures, leveraging their open-celled and self-supporting properties. The optimisation objective was to minimise the mass of the sacrificial supports while adhering to stress constraints. It was found that by keeping the maximum stress below the yield strength, cracking due to residual stress could be avoided. To experimentally validate their approach, optimised support structures were designed for a double cantilever beam and a hip implant. Figure 27 presents the simulation results, including total displacement and residual stress distribution for the three fabricated beams. The support structure after optimization achieved a weight reduction of approximately 60%. The optimized support structures showed no stress-induced cracking when produced using AM, confirming the method's effectiveness. However, despite the robustness of the simulation methodology, the approach is limited in generalisability and does not address other important factors, such as the ease of post-build removal of lattice-structured supports.

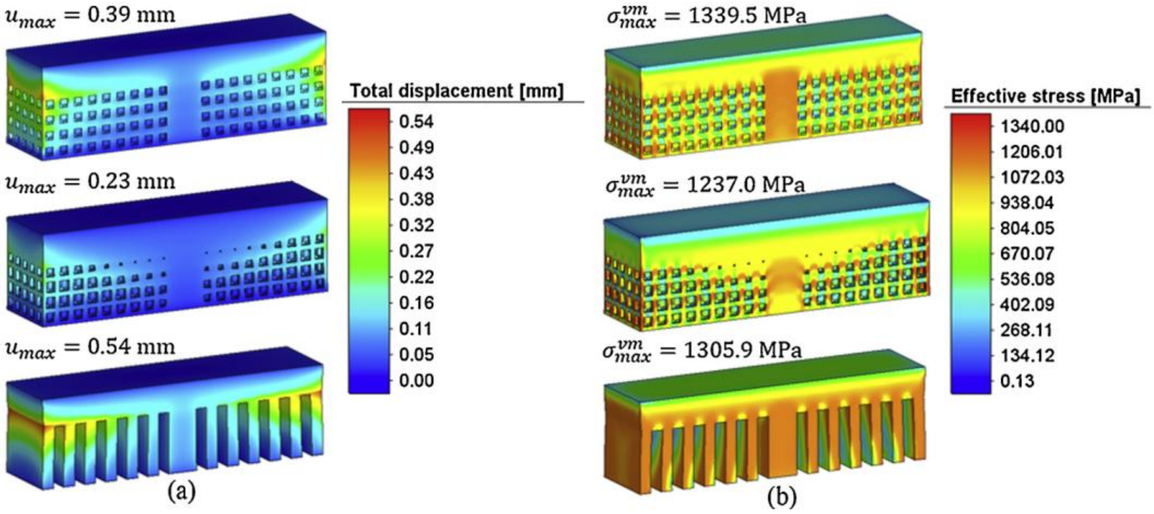

Figure 27. Beams' simulation results: (a) displacement distribution, (b) residual stress distribution [113].

In a subsequent study, Cheng and To [114] introduced a new optimization framework using fast process modelling to determine the optimal build orientation by minimising residual stress and support volume. They proposed a voxel-based method for support generation, which systematically captures support surfaces from an STL file, forms the support structure, and generates a Cartesian mesh for rapid process modelling. Instead of conformal meshing, they employed the voxel-based fictitious domain method to calculate stress distribution across the design domain, including the support structure represented by a homogenized model. Experimental validation was also conducted on a complex geometric part. Comparisons with parts and support structures lacking build orientation optimization showed that the proposed framework effectively reduces residual stress impact on printed parts, ensures manufacturability, and lowers material consumption for sacrificial support structures.

Umer et al. [115] developed 2D thermo-mechanical finite element models to predict stresses and deformation in the fabrication of overhang structures in EBM using Ti6Al4V alloy. They modelled and evaluated different support structure geometries, as shown in Figure 28, and validated the numerical results through experimental work. The experimental analysis showed that deformation and warping in EBM parts were influenced by the choice of support structure. A notable finding was that increasing the number of pins effectively reduced distortion. The FEA concluded that the 2D plane strain models could accurately predict these variations, aligning with the experimental results.

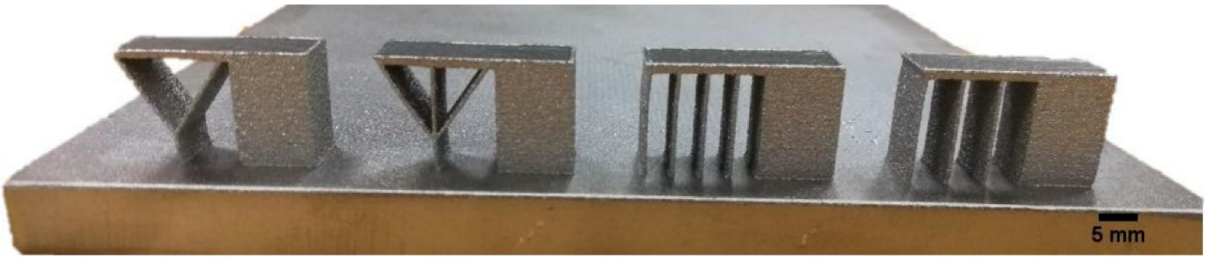

Figure 28. Printed models with various support structures [115].

Bartsch et al. [116] conducted a comparative evaluation of pin and block type support structures, taking into consideration part geometry. This evaluation enabled them to assess both the technical and economic aspects of support structures or support strategies. According to their findings, pin-type supports demonstrated greater tensile strength, lower shear resistance, and a higher heat dissipation ratio compared to block-type supports, despite requiring less amount of material.

Ravichander et al. [117] studied how different types of support structures and various geometric parameters, including wall thickness and gap distance, influence both the quality and cost of Inconel 718 parts produced in SLM. Their analysis, which accounted for several cost factors, revealed that support properties have a significant impact on part quality, primarily due to their effectiveness in thermal management and heat dissipation. Furthermore, they emphasized the importance of closely monitoring wall thickness and gap distance as these are critical design parameters. Notably, they observed an improvement in the hardness value of the fabricated samples with thinner support wall thickness.

Xiaohui et al. [118] introduced a method in their study to select and design support structures for fabricating SLM components with diverse structural features, aiming to minimize residual stress in the overhanging sections of these components. After utilizing thermomechanical models and residual stress testing, they concluded that block support structures are better suited for small, low-height overhangs, while contour supports are more appropriate for larger overhang surfaces.

Miki and Nishiwaki [119] introduced a topology optimization approach for improving heat dissipation in PBF-LB processes. Initially, they developed a numerical method to calculate the temperature field during building, considering transient heat conduction with volume heat flux. Subsequently, they formulated an optimization problem aimed at maximizing heat dissipation and devised an optimization algorithm that integrates level-set-based topology optimization. The sensitivity analysis of the objective function was conducted using the adjoint variable method. Figure 29 illustrates a sample of their numerical results comparing optimized and conventional support structures. It was observed that the maximum temperature at the contact points between the supports and the part was higher when using conventional supports. However, their study did not consider other critical factors including support removability, especially concerning the large contact areas of the optimized support structures.

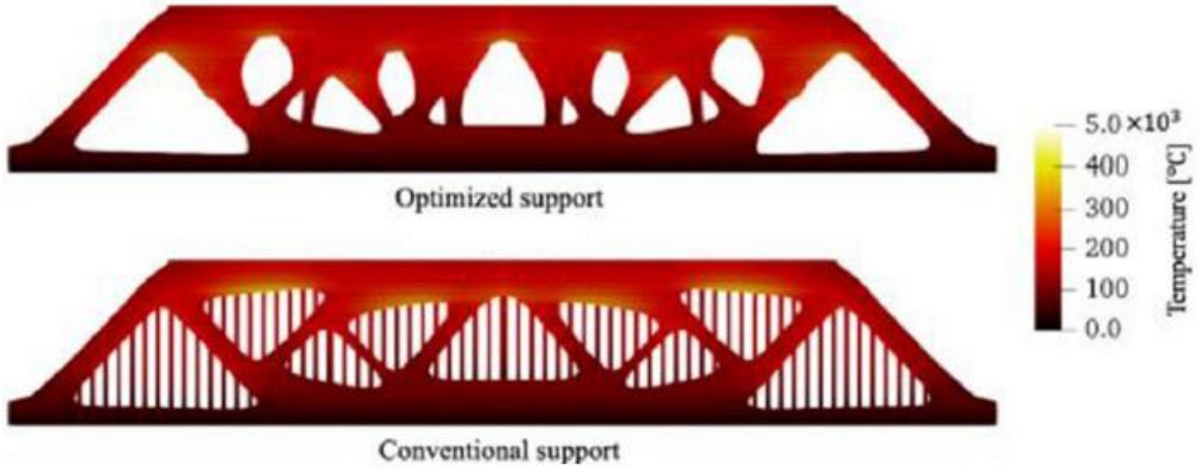

Figure 29. Temperature field of laser irradiation for optimised and conventional supports [119].

Building on the approach mainly used in Malekipour's work, this research prioritized key thermal phenomena in thermomechanical simulations, including conduction and convection, with particular emphasis on heat transfer between the part, the support structures, and the build plate. This focus was critical for accurately assessing and minimizing warping deformation and thermal stress accumulation during the SLM process. The models incorporated realistic boundary conditions, a representative heat source distribution, and the material properties of Ti6Al4V to simulate the thermal response accurately. Model validation was conducted by comparing simulation outputs, such as overhang displacement, build plate temperature, and stress concentration zones, against experimental results obtained from printed test specimens. The strong agreement between simulated and experimental data confirmed the accuracy and reliability of the numerical models and demonstrated their effectiveness in supporting the optimization of support structure design.

2.4.5 Contact-free Support Structures

Contact-free or contactless support structures have also been developed in metal additive manufacturing. These supports utilize a loose powder interface between the solid support structure and the part. This thin layer of unfused powder provides sufficient support for the solidified material and some degree of thermal conduction. As a result, the time required for support removal can be reduced. The gap distance should be minimal but must be thick enough to prevent partial fusion of the component and the support surface [50]. As illustrated in Figure 30, contactless support structures can improve heat dissipation through uniform heat flow (Figure 30a and Figure 30b) and achieve better surface roughness and less deformation compared to no supports (Figure 30c and Figure 30d) [120].

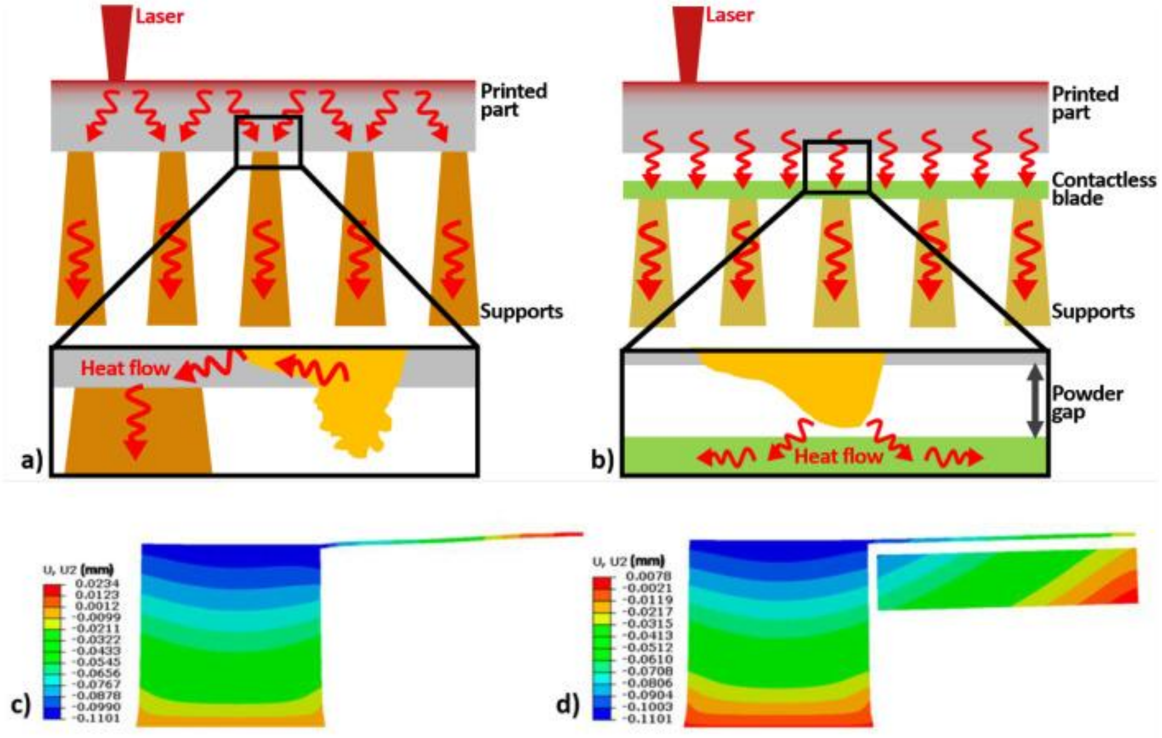

Figure 30. Heat dissipation: (a) Conventional pin supports, (b) Contactless supports; Deformation contour: (c) Without supports, (d) With contactless support [120].

Cheng and Chou [121] introduced a numerical approach to simulate thermomechanical responses in the EBM process for overhang structures and contactless support structures. The study developed a 2D thermomechanical model using FEM to evaluate temperature-induced deformation on different overhang support patterns. It was found that the model effectively simulates overhang deformation, significantly influenced by overhang length. Traditional solid column supports reduce warping, and their size can be minimized to meet deformation constraints while reducing material usage. Additionally, a solid piece beneath the overhang, acting as a heat sink, can also reduce deformation, provided an appropriate gap is maintained to prevent fusion with the overhang area. In their subsequent study [122], they explored a method for designing supports to minimize both material usage and post-processing efforts in EBM. This research introduced a novel approach that combines heat supports with support anchors. A thermomechanical model was utilized to assess the stress and deformation of overhang configurations. Simulations showed that overhang warping can be significantly mitigated by the application of heat supports beneath the overhang region and support anchors which connect the overhang and heat support.

Cooper et al. [123] conducted a study investigating the feasibility of contact-free support structures for part overhangs in EBM processes. Their objective was to develop support designs that minimize post-processing while effectively reducing overhang distortions. Their innovative approach involved integrating a heat sink, termed "heat support," beneath overhangs during part fabrication to mitigate adverse thermal effects. Thermomechanical modelling using FEA and experimental validation with a powder-bed electron beam additive manufacturing system were utilized to assess the effectiveness of contact-free heat supports. Results confirmed the concept's feasibility and demonstrated its efficacy across various overhang geometries and parameters.

Paggi et al. [124] initially examined the feasibility of novel contactless support structures in PBF-LB, focusing on surface quality and geometric accuracy. They employed numerical modelling of heat transfer phenomena to analyse the thermal history of the printing process and identify which parameters define the optimal distance for the thermal supports. Additionally, they used topology optimization methods to design contactless support structures with an optimal shape, aiming to minimise material usage while ensuring adequate thermal conductivity. The results showed that the optimised contactless supports effectively reduce warping deformation, particularly on large overhang surfaces exceeding 2×2 cm^2.

In a follow-up work, Paggi et al. [120] developed and validated a new type of support structure in PBF-LB systems that does not touch the printed part, creating a thin powder gap for thermal conduction and stabilisation of the liquid melt pool. To demonstrate the benefits of this technique, an impeller case with complex features was printed using both conventional and contactless supports. Comparing processing time and surface roughness, the results showed a significant increase in productivity and improved quality with the new strategy. Specifically, the use of this contactless support type reduced post-processing time by 66% and decreased surface roughness from 19.55 to 17.67 µm.

Çelik et al. [125] investigated the feasibility of contact-free supports for overhang surfaces in SLM, focusing on the effects of two key parameters: the gap distance between supports and overhang surfaces, and the inclination angle of overhang surfaces. Their study aimed to understand how these parameters influence surface topography and microstructural properties. Characterization methods, including visual inspection, roughness measurements, and optical microscopy, were employed. Results revealed that contact-free supports can effectively reduce surface roughness across all build angles when the gap distance is carefully adjusted to avoid powder sintering or excessively large gaps that compromise the intended enhancement of thermal conductivity. In their subsequent experimental study [126], they examined the impact of design variables such as the contactless support gap, the thickness of each contactless support piece, and the spacing between two support pieces as shown in Figure 31. They analysed performance outputs including dimensional variations, microhardness distribution, microstructural changes in bottom surfaces, and surface roughness of overhang features. The findings revealed that reducing support thickness, spacing, and gap resulted in decreased dimensional deviation and surface roughness. Moreover, as the ratio of supported area to unsupported area decreased, there was a tendency for microstructure coarsening and hardness reduction due to reduced heat dissipation.

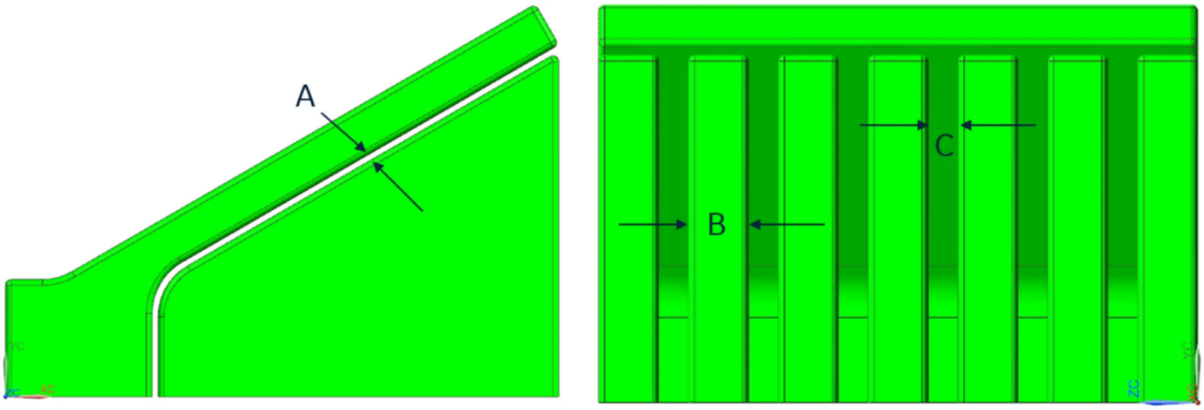

Figure 31. Design variables: support gap (A), thickness of each support piece (B), spacing between two support pieces (C) [126].

In conclusion, contact-free support structures offer several potential advantages over traditional supports. These include reduced post-processing effort, minimal surface damage, and improved surface quality on overhang regions due to the lack of direct contact with the part surface. By eliminating mechanical bonding, these structures aim to address one of the key challenges in SLM, support removal and surface finishing. However, contact-free supports also present notable limitations. They typically offer lower mechanical stability during the build process, making them unsuitable for both small and large (or heavy) geometries. Additionally, their thermal conduction capacity is significantly reduced, limiting their effectiveness in mitigating warping and residual stress, especially in materials like Ti6Al4V that are prone to thermal distortion. Given the objectives of this research, particularly the need to study thermomechanical behaviour, warping deformation, and support removability, traditional support structures were selected as the primary focus. Their direct mechanical and thermal interaction with the part makes them more relevant for analysing the interdependence of support design parameters and thermal stress outcomes. Moreover, traditional supports are more widely used in industrial applications, providing a realistic basis for developing practical and transferable optimization strategies.

2.5 Algorithms & Software for Support Generation and Optimization

2.5.1 Generic Algorithms in Metal AM

Extensive research has also delved into support structure generation and optimization within AM, utilizing approaches ranging from genetic algorithms to the utilization of commercial software solutions. Vanek et al. [127] introduced an efficient method for generating support structures, initially designed for fused deposition modelling (FDM) but later extended to other AM processes, to reduce the number of supports required. The algorithm first identifies the optimal build orientation and the respective overhang surfaces, and subsequently, it progressively generates support structures based on contact points while minimizing the length of the struts. This approach has been adopted by software developers such as Autodesk Meshmixer [128] to produce cost-effective tree-like and pin supports. However, the stability and suitability of such support structures have not been fully addressed for SLM processes.

Zhang et al. [129] developed a series of computational pre-processing algorithms tailored for PBF-LB processes. These algorithms begin with the generation of customized CAD-based support structures for a given part build orientation, based on an initial part design. On-the-fly calculations of various AM parameters and DFAM metrics enable the assignment of producibility scores across different part build orientations. Stand-alone computational geometry-based algorithms, equipped with graphical user interfaces (GUI), facilitate the computation of support structure parameters and the detection of challenging DFAM features. These tools offer quantified outputs for each parameter or feature, which are subsequently utilized in the producibility index (PI) calculation. An algorithm that evaluates support removal effort during post-processing and recommends the optimal number of setups for support structure removal was also developed. Lastly, the PI, a weighted optimization metric, integrates outputs from DFAM analysis, support structure parameters, and accessibility analysis to suggest optimal build orientations for the given part. A sample component imported into the platform is shown in Figure 32a, while Figure 32b illustrates the supports generated for the part's 90° orientation.

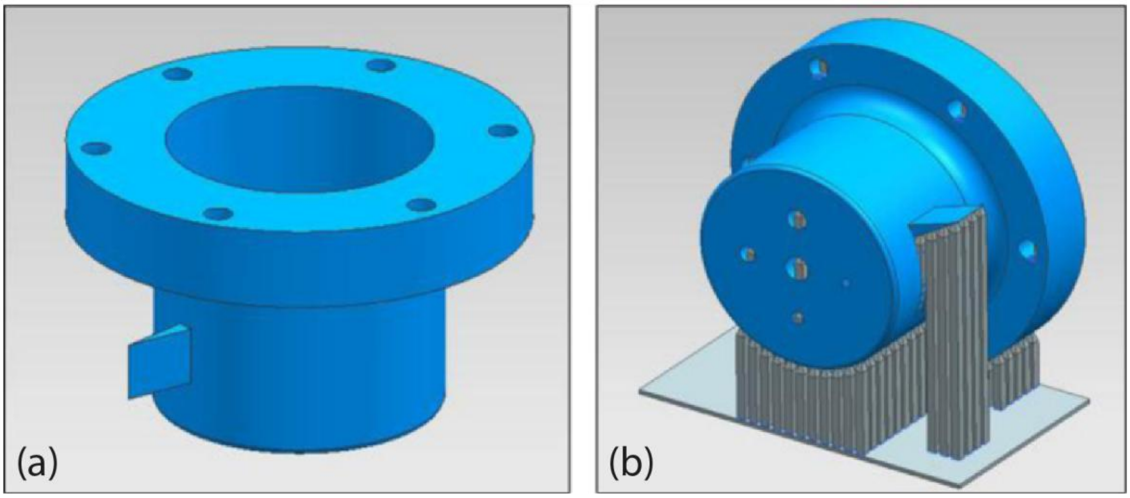

Figure 32. Platform's user interface: (a) Imported part, (b) Generated supports [129].

Vaissier et al. [130] introduced a novel genetic algorithm-based framework for optimizing the geometry and topology of both inner and outer support structures. Beginning with a uniform lattice structure that fills both areas requiring support, their approach aims to remove the maximum number of beams in order to minimize support volume. The optimal initial lattice structure geometry was selected based on considerations of manufacturing capabilities. Subsequently, a genetic algorithm fine-tunes the structure, with parameters adjusted using design of experiments methodology. The effectiveness of the approach was validated across multiple test cases featuring various geometries encompassing both inner and outer support requirements. Figure 33 illustrates various supports generated by (a) the proposed framework, (b) Meshmixer, (c) SLA, and (d) SLM support strategies for the same component. It was observed that the proposed support structures had lower material consumption compared to those generated by several state-of-the-art methods.

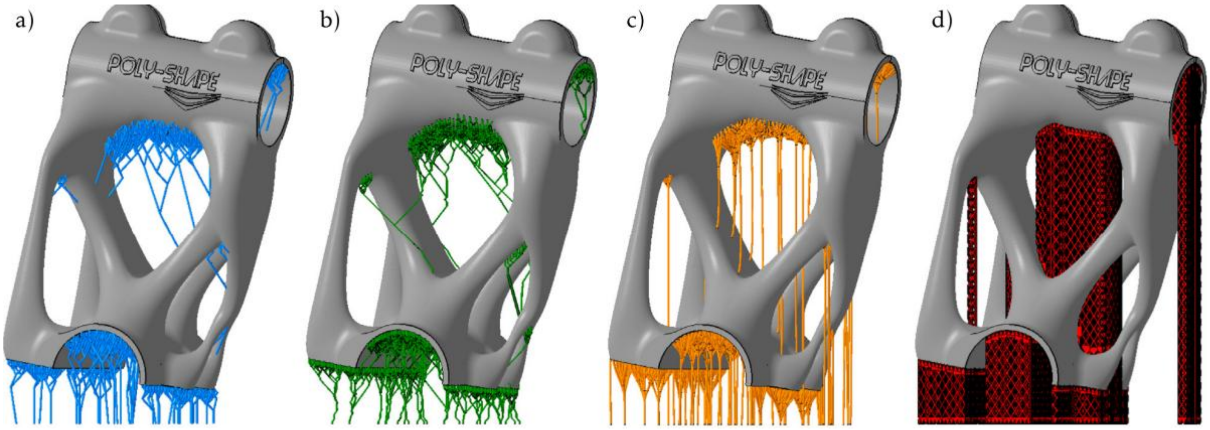

Figure 33. Generated support structures by (a) the proposed framework, (b) Meshmixer, (c) SLA support strategies, (d) SLM support strategies [130].

Zhang et al. [131] proposed a bio-inspired generative design method to improve the automation of preparation while reducing support structure volume, post-processing time, and cost. This approach integrates parametric L-systems, evolutionary optimization, and an AM processing simulation model to create lightweight, easy-to-remove, and heat-diffusion-friendly biomimetic support structures for PBF-LB systems. Dental components were modelled and manufactured to validate the proposed method. The results were compared with those obtained using existing commercial software, demonstrating improvements in efficiency and performance.

Kwok [132] developed a new type of tree-like support structure named Escaping Tree-Support (ET-Sup), designed to build all supports onto the build plate rather than on the model itself, aiming to minimize the number of contact points and simplify support removal during post-processing. By testing the method with various overhang features, including a lattice ball and a mushroom shape with a concave cap, it was observed that all the supports generated found their way to the build plate, effectively escaping from the model.

Weber et al. [133] investigated the design of tree-like support structures, contributing to a better understanding of support structure design in PBF-LB. They developed a workflow for creating tree-like supports and optimizing their parameters using a meta-model. Two exemplary geometries in a cantilever design with different support faces were chosen, standard block support and optimized tree-like support, to determine which parameters exhibit similar behaviour. Through experimental study, the validation showed that better performance and less warpage compared to standard block support could be achieved by carefully designing the tree parameters.

2.5.2 Commercial Software

In addition to the techniques and genetic algorithms mentioned in section 2.5.1., numerous commercial software options are available for support structure design, generation, and optimisation. These tools allow users to modify and tune support parameters and generate support geometries based on the imported model.

Materialise Magics [13] is one of the most sophisticated and widely used software packages for support design and generation in PBF-LB/M. It enables users to set part orientation, choose from a variety of support geometries such as block, line, point, web, contour, gusset, combi, volume, and cones, and generate support structures either automatically or manually based on the imported model. Users can also modify and fine-tune various support parameters. Advanced versions of Materialise Magics feature a robust tool called Materialise e-Stage [134], which offers a fully automatic support generation solution designed to bridge the experience gap and reduce data preparation time, powder consumption, and relevant post-processing efforts.

Moreover, the Magics Ansys Simulation module [135], a powerful plug-in developed recently, offers key capabilities for metal AM and SLM printing, such as mitigating part deformation, preventing recoater contact, predicting shrink lines, simulating support structures, and preventing overheating. Specifically, this tool allows users to assess part distortion to effectively position and adapt support structures, minimizing costly test builds, accelerating time-to-market, and reducing development costs. It also helps avoid overheating, improves surface quality, and generates compensated part geometry to enhance geometrical accuracy. Additionally, the tool predicts build risks for large parts prone to residual stresses and distortion, identifying potential failures through advanced AM simulations. By simulating and evaluating part orientation, it also ensures proper support placement and enables users to make informed decisions throughout the part preparation process. Figure 34 illustrates a numerical simulation of the generated support structures for a random component using the Magics Ansys Simulation module.

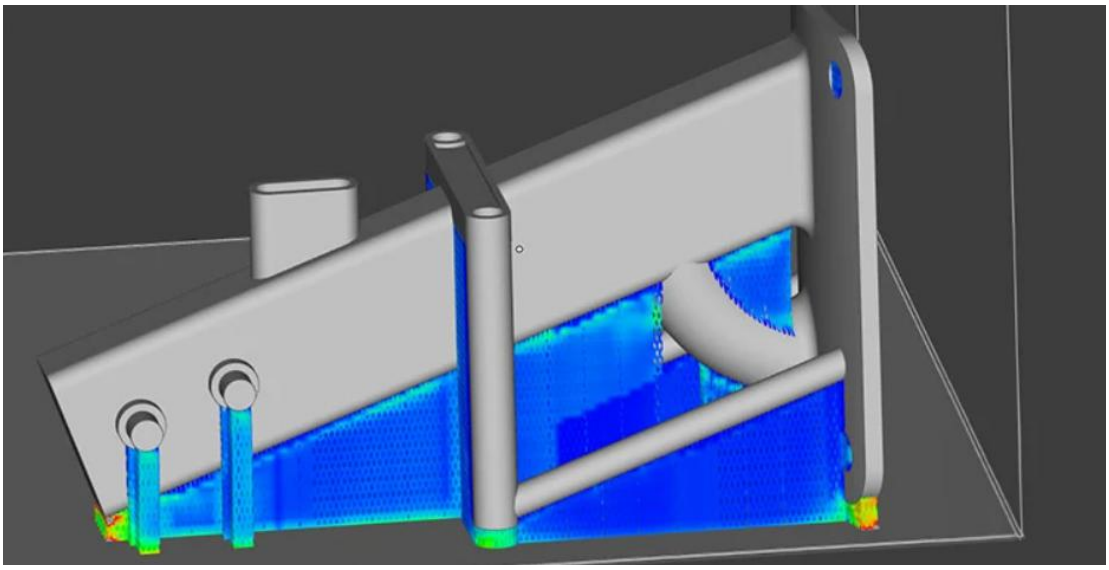

Figure 34. Support simulation in Magics Ansys Simulation [135].

Amphyon [136] and 3DXpert [137], developed by Oqton, are simulation-based process preparation tools for AM that offer advanced analysis and simulation features to support every stage of the AM workflow, from design to printing. These tools enable users to maximize part performance through topology optimisation, minimize manufacturing costs by reducing printing time and material consumption, and ensure thermal stability and defect-free parts by conducting thermal and structural simulations to calculate residual stress and distortions.

AM-Studio software [138], a collaboration between Hexagon and CADS Additive, is a sophisticated additive manufacturing solution that provides comprehensive guidance throughout the entire printing process, including post-processing. It facilitates tasks such as defining part orientation, automatically repairing damaged 3D files, and generating advanced support geometries such as tree support and AdaptiveCell support, alongside traditional options like block, rod, and line supports.

The 4D_Additive Manufacturing Software Suite [139] from Core Technologies is capable of importing 3D models from common CAD formats and converting them into precise, intelligent, lightweight B-Rep geometries suitable for AM processes. Its support generation module allows users to define the ideal part orientation, and a diverse range of specialized support structures can be automatically or manually generated as needed.

Another robust 3D printing build preparation software, compatible with both metal and plastic additive manufacturing technologies, is VoxelDance Additive [140]. Apart from repairing 3D files, determining the best part orientation, and optimising nesting efficiency, its support generation module provides a wide array of support geometries such as bar, point, line, block, and intelligent supports.

Finally, Autodesk Fusion 360 with Netfabb [141] provides a comprehensive toolset for design and implementation in AM. Within this platform, users can import 3D files, assess printability, repair models, generate support structures, and minimize build failures through process simulations that analyse residual stresses and part distortion.

2.5.3 Critical Analysis and Research Gap Identification

Despite the extensive capabilities offered by commercial software and genetic algorithms developed by researchers, several critical gaps remain when considering their application in research-driven, multi-objective support optimization for metal PBF-LB processes. Most commercial solutions prioritize automation, user-friendliness, and production efficiency, which are highly valuable for industrial applications but limit their adaptability for highly customized or experimental research needs. In particular, these tools often focus on basic support generation, build orientation, and deformation prediction based on default templates or parameter sets, without offering the detailed control needed to tune supports for multiple competing objectives such as minimizing material use, thermal stresses, support removal effort, and overhang quality simultaneously.

Additionally, while the various simulation modules can predict distortions and overheating risks, they typically require high computational resources and expert calibration, making their deployment in repetitive experimental workflows cumbersome and time-consuming. Importantly, none of the commercial tools currently offers integrated frameworks to optimize multiple performance metrics across different support types (block, line, contour, cone) under varying thermomechanical constraints, which is the focus of this research. Therefore, while commercial software provides a valuable foundation for part preparation and risk mitigation, achieving a high degree of customization, optimization flexibility, and experimental validation still demands the development of custom-made methodologies, as undertaken in the subsequent chapters of this thesis.

Thus, while existing software solutions provide a strong foundation for automated support generation and industrial production workflows, they lack the flexibility and multi-objective customization required in research contexts. This research identified the need for a more adaptable approach that accommodates detailed parametric tuning and considers thermal, mechanical, and economic factors simultaneously. In response, a novel framework was developed that integrates experimental and simulation data, enabling the optimization of various support types (block, line, contour, cone) under realistic constraints. This methodology, along with a custom-built web-based platform, allows users to visualize, configure, and export optimized supports tailored to specific research or production needs, addressing the limitations identified in current commercial and algorithmic solutions.

2.6 Chapter Summary

In this chapter, existing research on metal AM was reviewed with a particular focus on PBF-LB processes, thermal phenomena, and tools for support generation and optimization. Specifically, the SLM process was examined in depth, addressing its mechanisms, common defects, key process parameters, and support geometries, along with their influence on final part quality. Additionally, support structures were evaluated in terms of their essential role in the manufacturing process, including different support types, their impact on overall costs, and strategies for effective support removal. Furthermore, thermomechanical models in SLM were investigated to understand critical thermal phenomena, boundary conditions, and strategies for managing heat transfer during the process, with particular emphasis on the contribution of support structures to thermal modelling. Finally, a range of tools and software solutions used for support generation and optimization were documented, providing a comprehensive overview of the resources available to improve both process efficiency and final part quality.

However, successfully implementing these solutions, particularly in support structure generation and optimisation, requires a deep understanding of AM principles. Many companies and users engaged in AM rely on extensive in-house experimentation to identify efficient production methods, a process that is often costly and time-consuming. For example, aerospace manufacturers may perform iterative builds to ensure part integrity, while medical device firms focus on patient-specific geometries that require fine-tuning of support structures. Rather than viewing this experimentation solely as a limitation, it presents an opportunity: by systematically capturing and analysing the data generated, organisations can develop integrated tools and data-driven frameworks that streamline the printing process. This approach not only reduces time and cost but also improves the repeatability and quality of the printed parts.

This research aims to investigate the performance of various support structures in SLM through multi-response optimization, numerical studies, and experimentation. The objective is to develop optimized support strategies that improve process performance, producing defect-free parts with minimal material use, enhanced post-processing efficiency, and reduced labour hours. These strategies are presented within theoretical frameworks designed to be broadly applicable. Additionally, a web-based platform has been introduced as a valuable tool for managing and visualizing the key principles derived from this study.

Chapter 3: Multi-Response Optimisation of Block-type Support Structures for SLM

3.1 Introduction

Based on the literature cited, it is evident that fabricating overhang surfaces in metal AM and PBF-LB systems is closely related to the design of support structures. Effective and optimized supports are crucial for reducing material usage, shortening removal time, decreasing post-processing effort, minimizing printing time and cost, and lowering the risk of part damage. This chapter introduces a design approach aimed at achieving effortless, reliable, and sustainable AM. It investigates optimized support structures that are easy to remove and use minimal support material without compromising part quality. SLM technology is used to conduct experiments, with titanium alloy (Ti6Al4V) as the material. The optimization process, grounded in a multi-response optimization framework, evaluates various support and process parameters for block-type supports, including tooth height, tooth top length, hatch distance, and laser speed, aiming to optimize support volume, support removal effort, and part warping deformation. To achieve this, design of experiments (DOE) methodology and relevant optimization algorithms were employed.

3.2 Methodology

3.2.1 Design of Experiments Setup

Multi-response optimization is a systematic technique used to optimize multiple outcomes or performance metrics simultaneously within a given process or system. It is particularly valuable in scenarios where various objectives may conflict or require trade-offs, such as maximizing quality while minimizing cost and production time. By employing statistical methods and optimization algorithms, MRO allows for the identification of optimal solutions that balance these competing criteria, leading to improved overall performance and efficiency. This approach is widely applicable in fields such as manufacturing, engineering, and finance, where complex decision-making is essential for achieving desired results across multiple dimensions [142], [143].

In metal AM and PBF-LB processes, a variety of support types are available, including block, line, web, contour, and cone supports. Their selection depends on the geometry and features of the part, the material used, and the compatible slicing software. According to the literature, block-type supports are commonly employed in PBF-LB/M; thus, this chapter focuses exclusively on investigating this particular support type. Fragmented block-type supports are also preferred for many applications because their configurable morphology helps reduce material consumption and removal effort. An example of their morphology is shown in Figure 35. As seen, they consist of two parts: the support body, which forms the main geometry of the support structures, and the tooth area, based on the contact area between the supports and the part's overhang surface, as illustrated in Figure 35a. After selecting the support type, the next step was to identify the input parameters (free variables that can be changed and controlled) and their respective levels. Drawing from the literature and a series of screening experiments conducted to determine these parameters, four main areas were chosen for investigation: (i) the tooth area, including tooth height and tooth top length as depicted in Figure 35b, (ii) the main body of the support, involving x, y hatching as shown in Figure 35c, (iii) the process parameters including laser speed, and (iv) the specimen geometry obtained by generating different overhang angles. Table *1* outlines the selected parameters and their respective levels, with each parameter having three levels: minimum, average, and maximum values, as determined during the DOE setup. All the selected input parameters, tooth height, tooth top length, x, y hatching, laser speed, and overhang angle, were found to be critical in influencing the response variables. Their significance was confirmed through the analysis, where main effects and interaction effects were systematically evaluated. The influence of each parameter on support volume, removal effort, and warping deformation is clearly demonstrated in the plots presented in Section 3.3, highlighting their integral role in the optimization process.

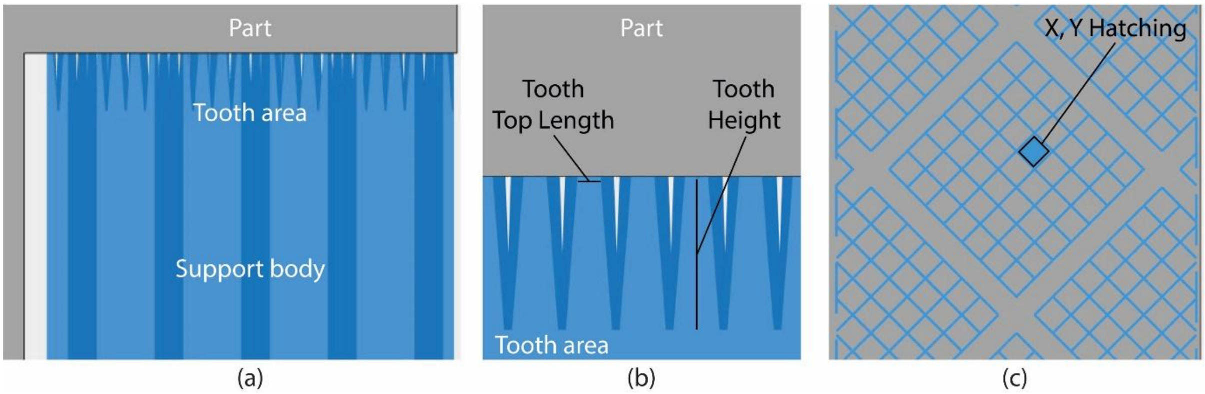

Figure 35. Block-type support structures: (a) Main body, (b) Tooth area, (c) X, Y Hatching.

Table 1. Selected support parameters and their levels.

Parameter	Level 1	Level 2	Level 3
Tooth Height	1 mm	2.5 mm	4 mm
Tooth Top Length	0.05 mm	0.175 mm	0.3 mm
X, Y Hatching	0.5 mm	1.5 mm	2.5 mm
Laser Speed	1000 mm/s	1400 mm/s	1800 mm/s
Overhang Angle	0°	22.5°	45°

To assess the impact of these parameters on support structures and the manufacturing process, small "ledge" overhang specimens were designed in SOLIDWORKS [144], a CAD software used in engineering, manufacturing, and product design for creating 3D models, assemblies, and 2D drawings. Three specimen cases including 0°, 22.5°, and 45° were selected to represent the different overhang angle levels. Figure 36 details the geometry and dimensions (in millimetres) of these specimens, including their supported areas (highlighted in green) and the build direction.

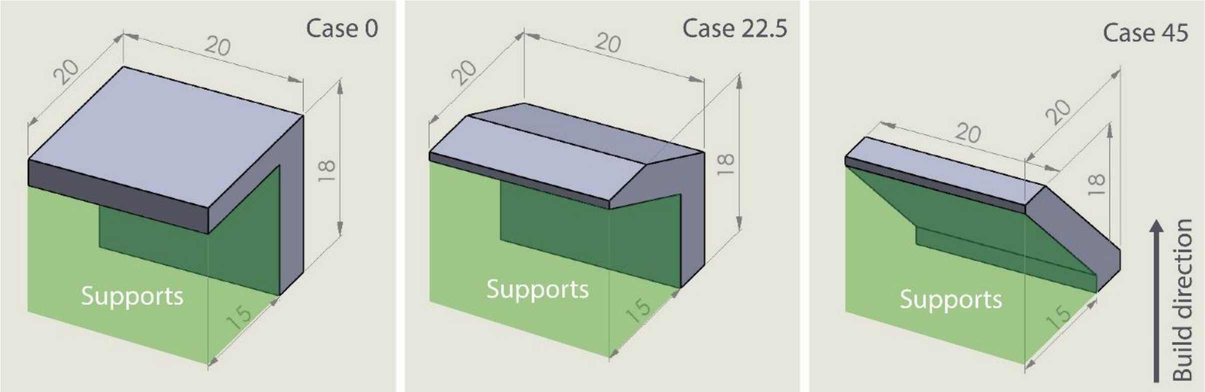

Figure 36. Specimen geometry, supported area, and build direction for the 3 cases.

During the design of experiments based on the input values from Table *1*, Response Surface Methodology (RSM) using Central Composite Design (CCD) was employed to perform the experiments and define the various configurations. This method was selected for its effectiveness in analysing and optimizing responses, as supported by the literature. A total of 90 runs were conducted according to the specified parameters and levels. For the CCD setup, 2 replicates of factorial points, 2 replicates of axial points, and 6 replicates of center points were utilized. A face-centered design approach with an alpha value of 1 was applied. Design-Expert 13 software [145] was utilized for DOE preparation and visualization of optimization results. The initial setup is illustrated in Figure 37.

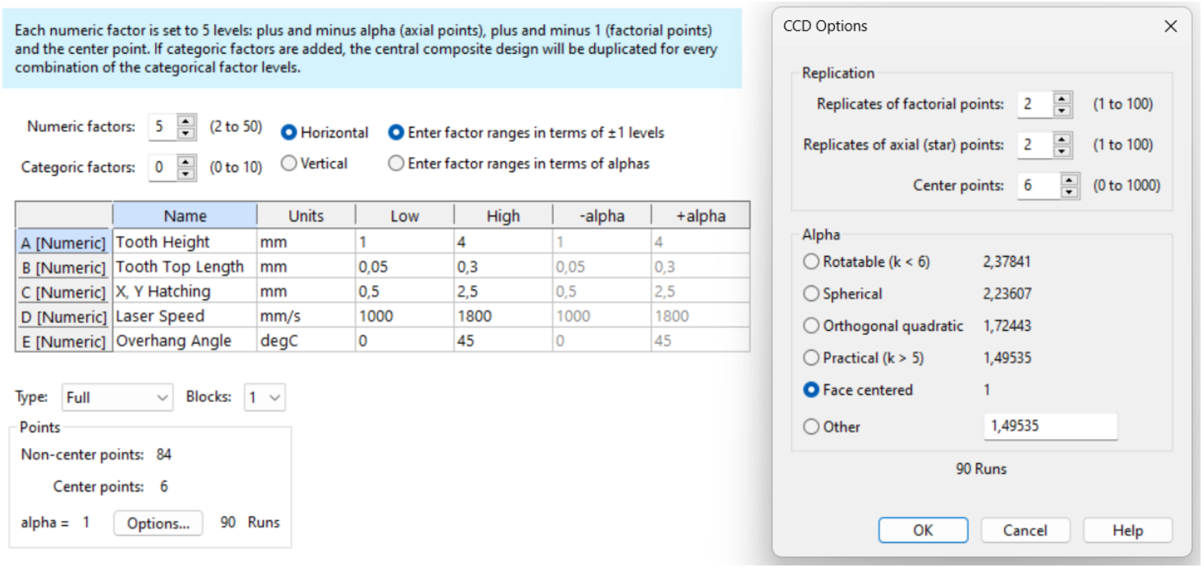
Each numeric factor is set to 5 levels: plus and minus alpha (axial points), plus and minus 1 (factorial points) and the center point. If categoric factors are added, the central composite design will be duplicated for every combination of the categorical factor levels.

Numeric factors: 5 (2 to 50)
Categoric factors: 0 (0 to 10)
● Horizontal
○ Vertical
● Enter factor ranges in terms of ±1 levels
○ Enter factor ranges in terms of alphas

	Name	Units	Low	High	-alpha	+alpha
A [Numeric]	Tooth Height	mm	1	4	1	4
B [Numeric]	Tooth Top Length	mm	0,05	0,3	0,05	0,3
C [Numeric]	X, Y Hatching	mm	0,5	2,5	0,5	2,5
D [Numeric]	Laser Speed	mm/s	1000	1800	1000	1800
E [Numeric]	Overhang Angle	degC	0	45	0	45

Type: Full
Blocks: 1

Points
Non-center points: 84
Center points: 6
alpha = 1
90 Runs

CCD Options

Replication
Replicates of factorial points: 2 (1 to 100)
Replicates of axial (star) points: 2 (1 to 100)
Center points: 6 (0 to 1000)

Alpha

○ Rotatable (k < 6)	2,37841
○ Spherical	2,23607
○ Orthogonal quadratic	1,72443
○ Practical (k > 5)	1,49535
● Face centered	1
○ Other	1,49535

90 Runs

Figure 37. Design of experiments setup in Design-Expert 13.

As mentioned above, block-type supports were selected as the initial focus of this study due to their widespread use in industrial metal AM applications in SLM, particularly for parts where mechanical stability is critical. Unlike line, contour, or cone supports, block supports offer a greater heat conduction path, which helps mitigate warping and delamination during printing, an essential consideration for early-stage experimental validation. Line and cone supports, while advantageous for ease of removal and reduced material consumption, typically provide insufficient thermal mass, making them more prone to instability under high thermal loads. Additionally, cone supports, offer limited contact area and structural rigidity, especially for flat or thin overhangs. Contour supports, on the other hand, pose challenges during removal. Web supports were excluded from initial testing due to their complexity in parameterization and limited availability in standard support generation algorithms and tools. It is acknowledged that findings related to support removal effort and warping deformation might differ with alternative support types. For instance, line and cone supports would likely result in lower removal efforts but increased deformation, while contour supports might achieve a balance in certain geometries. These differences were later explored numerically in Chapter 4 to generalize the principles established in this chapter.

3.2.2 3D Printings in SLM

Regarding the experiments, an EOS M290 machine equipped with a 400 W Yb-fiber laser and a 100 μm focus diameter, based on the SLM process, was used to fabricate the specimens. In this study, all the specimens were fabricated using the optimal parameters recommended by the manufacturer for the EOS M290 machine, with a layer thickness of 60 μm. The various support structures were built based on the parameters detailed in Table *1*, alongside constant geometric parameters including 0.1 mm tooth base interval, 1 mm tooth base length, 0.06 mm Z offset, 0.2 mm thickness, 8 mm fragmentation interval, 1 mm separation width, a 45° support rotation angle, and 135-watt laser power. The material used for the experiments was the 'EOS Titanium Ti64 Grade 5' (or Ti6Al4V) in powder form, a titanium alloy known for its strength, lightweight properties, and excellent corrosion resistance, commonly utilised in SLM applications. The powder had a generic particle size distribution of 20–80 μm and a chemical composition predominantly comprising Ti (balance), Al (5.50–6.75 wt%), V (3.50–4.50 wt%), and 1.05 wt% of other elements. Table *2* presents the thermal and mechanical properties of Ti6Al4V Grade 5 alloy typically used in additive manufacturing, referenced from MatWeb [146] and manufacturer datasheets from companies including EOS or Materialise [147].

Table 2. Material properties of Ti6Al4V Grade 5.

Property	**Value**
Density	4.43 g/cm³
Melting Point	1550-1668 °C
Young's Modulus (E)	114 GPa
Yield Strength	880 MPa
Ultimate Tensile Strength	950 MPa
Elongation at Break	10-14%
Poisson's Ratio	0.34
Thermal Conductivity	6.7 W/(m·K) at 20°C
Specific Heat Capacity	0.52 J/g·K at 20°C

Materialise Magics [13] software and EOS Build tool [148] were used for generating the various support structures and preparing the final slicing jobs. Figure 38 illustrates a part of the printed outcome after removing the unmelted powder from the build plate. Out of ninety specimens, sixty-eight were successfully printed, while twenty-two failed during fabrication due to lack of support material and recoater crashing issues. Notably, all failed specimens belonged to "case 0" (level 1 - overhang angle 0°). Among the support parameters, the hatch distance had the most significant impact on the failures, with sixteen out of twenty-two failures occurring at the maximum hatching of 2.5 mm. These unsuccessful specimens were included in the study and considered in the analysis and optimization process as "printing failures". To address this, specific corrective actions were implemented during the screening phase (detailed in the next section), including fine-tuning of both support geometries and machine parameters. However, the combination of extreme parameter settings used in accordance with the DOE, and the decision to fabricate all specimens in a single build job ultimately contributed to the observed failures. To some extent, these failures were anticipated.

Figure 38. Printed outcome attached to the build plate.

3.2.3 Preliminary Screening Experiments

Prior to the final printings described in Section 3.2.2, screening experiments were conducted to define the support and process parameters that will be used for the design of experiment setup, including their numeric ranges, which encompassed both minimum and maximum values for each parameter. In addition to tooth height, tooth top length, hatching, laser speed, and overhang angle, laser power was used as an input parameter, with a range of 150-380 watts. According to the literature and insights from industry professionals, these are among the most significant and influential parameters in SLM printing, while all other support and process parameters were held constant at their optimal values. This implies that selecting alternative support and process parameters would likely have minimal impact on the printed outcome and would not significantly mitigate the observed defects. As a result of various combinations of laser speed and laser power, some specimens failed early in the process, exhibiting warping that affected the recoater of the machine and caused the entire print to stop. The process and a sample of warping, outlined in red, are illustrated in Figure 39. It is also important to note that all parameter ranges that were adjustable and controllable were carefully selected based on similar findings from the literature review, direct input from experienced SLM professionals, and continuous, repeatable experimentation.

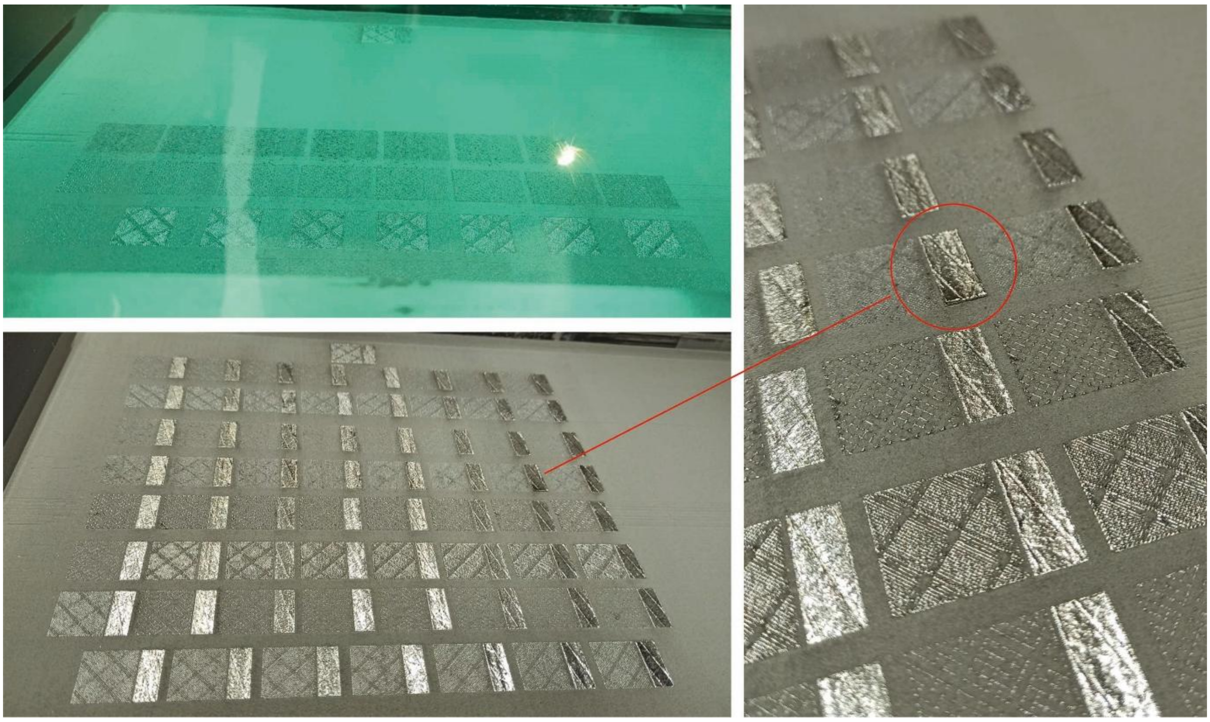

Figure 39. Warming defect due to various combinations of laser power and laser speed.

To address this issue, the laser power and laser speed parameters were adjusted to identify an optimal range for successful prints. While the laser speed was slightly modified, the laser power was set between 120 and 180 watts, and the most extreme cases, including combinations of the minimum and maximum values, were investigated. As a result, three specimens were fabricated under different conditions. In Case 1, the specimen was printed using maximum laser speed and minimum laser power, representing the softest condition in terms of support removability due to the smaller melt pool size. This configuration failed early in the process, as the high scanning speed combined with low laser power resulted in weak solidification and poor layer adhesion, making it impossible for the part to build successfully. Case 2 represented the hardest condition, with minimum laser speed and maximum laser power. While the print completed successfully, support removal failed. The specimen could not be detached from the build plate, the supports were extremely difficult to remove, and the part cracked during the removal process. This outcome was attributed to excessive energy input, which caused over-melting and improper solidification at the interface between the part, the build plate, and the supports, effectively fusing the entire structure into a single, solid mass. Case 3 was fabricated using average parameter values. Although the specimen was successfully printed and detached from the build plate, support removal proved nearly impossible, likely due to similar issues with excessive fusion between the support structures and the part. Figure

40 illustrates the three specimens, highlighting the specific defects observed during post-processing and manual support removal.

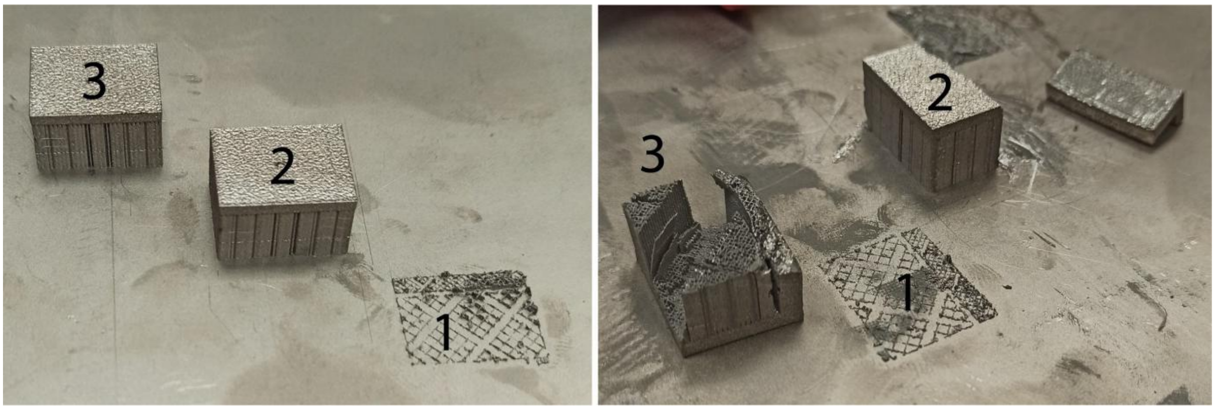

Figure 40. The 3 cases utilizing combinations of max, min, and avg values for laser power and speed.

Considering all the observations, it was decided to exclude laser power from the input parameters in the DOE setup, maintaining it at the optimal value of 135 watts. Therefore, the final DOE was characterized by a total of five input parameters, as described in Section 3.2.1. To ensure the correct printability before the final print of the ninety alternatives, two "case 0" overhang specimens were printed using combinations of the minimum and maximum values of tooth height, tooth top length, hatching, and laser speed. As these specimens were printed successfully and support removal was acceptable, the final print was conducted. Figure 41 illustrates the printed outcome including all the alternatives.

Figure 41. Printed outcome from the SLM machine after removing the unmelted powder.

3.2.4 Performance Measures

To assess the performance of various support structures, three key responses were examined: support volume, support removability, and warping deformation of the specimens. Support volume was measured using the online platform ViewSTL [149], a lightweight, browser-based tool designed for the quick visualization and analysis of STL files. Its integration into the workflow enabled immediate verification of geometric integrity and file correctness without the need to open more resource-intensive CAD or slicing software. Although not included in the literature review due to its general-purpose nature, ViewSTL was particularly valuable during the early stages of design evaluation, especially when iterating through multiple support geometry variants. Specifically, each support structure was exported from Materialise Magics software in STL format, imported into the ViewSTL platform individually, and their volumes were calculated.

To facilitate clearer interpretation of support volume, the data were normalized on a Likert scale [150] from 1 (representing the minimum volume) to 5 (representing the maximum volume). This approach, commonly used in engineering and behavioural studies for ordinal classification, facilitated qualitative interpretation and cross-response comparison. It is important to note that this normalization was applied post hoc for visualization and grouping purposes only. The raw support volume data (in mm^3) was retained and used in all statistical modelling, including ANOVA and multi-response optimization. Therefore, the normalization did not introduce bias or distort the quantitative relationships between the input parameters and the response variable. The Likert scale was used solely to support the categorization of support densities and make it easier to understand trends across different configurations.

The removability of the supports was evaluated based on the time and effort required to remove them and clean the overhang surface of any partially fused powder or solidified material remnants. While the manual evaluation of support removability provided a practical and representative insight into real-world post-processing conditions, it is acknowledged that this method introduces a level of subjectivity. Factors such as operator strength, technique, and perception of effort may vary, which can affect the consistency of the assessment. To improve the reliability and repeatability of future studies, objective metrics such as applied force or torque measurements, could be incorporated. These quantitative methods would enable more consistent comparisons across different support configurations, enhancing the scientific rigour of removability evaluations. Although such technical approaches are discussed in the literature, this study deliberately focused on replicating and optimizing the manual procedures typically employed by operators in industrial practice.

Notably, most support structures were removed when detaching the specimens from the build plate. The remaining supports were manually removed using basic tools such as wire cutters, pliers, and files. Three different conditions were considered for this evaluation. In "Condition 1", supports were very easy to remove, requiring minimal effort to clean the surface (approximately 1–2 minutes). In "Condition 2", supports were easy to remove but required more effort to clean the overhang surface and remove fused remnants (approximately 4-5 minutes). In "Condition 3", supports were very difficult to remove manually, risking the quality of the printed part, requiring basic tools, and sometimes were nearly impossible to remove (over 5 minutes). These three conditions are illustrated in Figure 42. The non-printed specimens were excluded from the removability evaluation.

Figure 42. The three conditions of support removability.

The warping deformation was assessed by measuring the upward displacement of the overhang surfaces relative to the actual geometry of each specimen. Using a digital calliper and supporting fixtures and equipment, the distance from the lower edge of the overhang was measured at three distinct points. The base of the small, non-overhang area was used as the primary reference point, while a 2 mm-thick subsidiary metal plane, aligned with the dotted lines shown in Figure 43, served as a guide to ensure consistent and accurate calliper positioning. The final warping deformation for each specimen was calculated as the average of the three displacement values along the Z-axis $(dis_1 + dis_2 + dis_3) / 3$. The measured warping deformation ranged from a minimum of 0.13 mm (observed in the 22.5° overhang specimens with a tooth height of 2.5 mm, tooth top length of 0.05 mm, x, y hatching of 1.5 mm, and a laser speed of 1400 mm/s) to a maximum of 1.83 mm (observed in the 0° overhang specimens with a tooth height of 1 mm, tooth top length of 0.05 mm, x, y hatching of 0.5 mm, and a laser speed of 1000 mm/s).

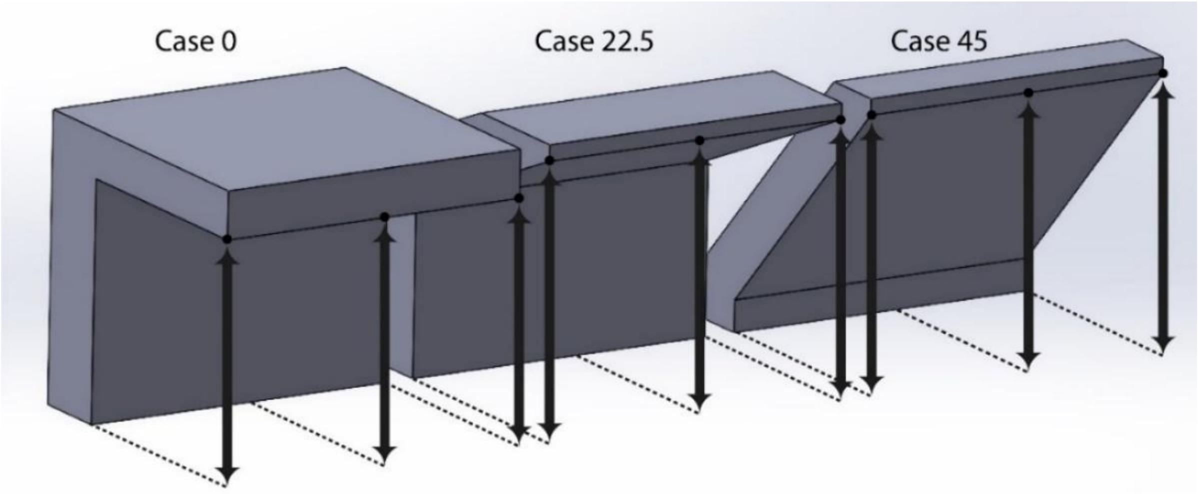

Figure 43. Reference points for evaluating warping deformation along the Z-axis.

Specimens that failed to print successfully, categorized as “failed prints”, were also considered in the warping evaluation. These were assigned a nominal warping value of 2 mm to represent conditions that led to entirely defective, collapsed, or incomplete builds. This fixed value enabled their inclusion in the design of experiments and subsequent numerical optimization without compromising the integrity of the analysis. During the numerical optimization process presented later in this study, specimens exhibiting severe warping (e.g., greater than 1.5 mm) or those assigned the failure value (2 mm) were excluded to ensure robust and meaningful optimization outcomes.

Following the evaluation of performance measures for all specimens, the final measurements were imported into Design-Expert 13 software to conduct analysis of variance (ANOVA) for analysing and validating the selected model. Numerical optimization was performed next to determine optimal input parameters for each overhang specimen, with the goal of minimizing support volume and support removal effort while eliminating warping deformation. It is also important to note that, although the identified optimal parameter settings effectively minimized the targeted response variables, they may be sensitive to small variations in input parameters, particularly in practical manufacturing environments where process fluctuations are common. While the experimental design included replicates and employed a quadratic model to account for curvature and interactions, a formal robustness analysis (e.g., using sensitivity or tolerance studies) was not conducted in this study. To improve the robustness of future recommendations, alternative simulations and modelling approaches could be investigated, such as Taguchi methods [151], which systematically evaluate the influence of noise factors on performance, and probabilistic design techniques, which use statistical distributions to predict system behaviour under variability. These approaches can help assess the stability of the optimal settings and ensure consistent support structure performance across a wider range of operating conditions.

3.3 Results and Discussion

3.3.1 Support Volume Analysis

For the detailed analysis of support volume, a quadratic model was employed, which allows capturing both linear and interaction effects as well as curvature in the relationship between design parameters and the output [152]. The model showed an Adjusted R^2 of 0.9972 and a Predicted R^2 of 0.9962, indicating a reasonable agreement. Adjusted R^2 reflects the proportion of variance explained by the model while adjusting for the number of predictors, preventing overfitting. Predicted R^2 estimates how well the model can predict new data, thus assessing its generalizability [143]. Adeq Precision evaluates the signal-to-noise ratio, quantifying how well the model's signal (i.e., effect of factors) stands out against random noise. A ratio above 4 is considered desirable. In this case, the observed value of 112.346 suggests an adequate signal and robust model. This strengthen the reliability of using the model for optimization (relevant data and DOE setup can be found in Appendix A). The ANOVA results presented in Table *3* showed an F-value of 1605.40 with a p-value < 0.05, confirming that the model is significant. The F-value is a ratio of model variance to residual (error) variance. Higher values indicate that model terms explain much more variability than random error. The p-value indicates the probability that the observed effect is due to chance (values below 0.05 support rejecting the null hypothesis, confirming the model's predictive relevance) [152]. Significant model terms include A, B, C, E, AB, AC, BC, CE, C^2, and E^2, whereas terms with p-values exceeding 0.1000 are typically considered statistically non-significant. The Mean Square, calculated by dividing the sum of squares by degrees of freedom, helps determine the contribution of each factor to the total variance. It is the basis for computing the F-value [153]. Based on the criteria outlined, the quadratic model for support volume was deemed suitable for further analysis and optimization.

Table 3. ANOVA results for the quadratic model of support volume.

Source	Sum of Squares	Mean Square	F-value	p-value
Model	176.50	8.82	1605.40	< 0.0001
A-Tooth Height	0.4288	0.4288	78.01	< 0.0001
B-Top Length	0.1700	0.1700	30.93	< 0.0001
C-X, Y Hatching	147.65	147.65	26,859.87	< 0.0001
D-Laser Speed	0.0006	0.0006	0.1070	0.7446
E-Angle	11.20	11.20	2037.92	< 0.0001
AB	0.0400	0.0400	7.28	0.0088
AC	0.0900	0.0900	16.37	0.0001
AD	0.0025	0.0025	0.4548	0.5023
AE	0.0025	0.0025	0.4548	0.5023
BC	0.1225	0.1225	22.29	< 0.0001
BD	0.0000	0.0000	0.0000	1.0000
BE	0.0000	0.0000	0.0000	1.0000
CD	0.0000	0.0000	0.0000	1.0000
CE	4.41	4.41	802.26	< 0.0001
DE	0.0025	0.0025	0.4548	0.5023
A^2	0.0057	0.0057	1.03	0.3127
B^2	0.0057	0.0057	1.03	0.3127
C^2	5.60	5.60	1018.50	< 0.0001
D^2	0.0057	0.0057	1.03	0.3127
E^2	0.1667	0.1667	30.33	< 0.0001
Residual	0.3793	0.0055		
Lack of Fit	0.3793	0.0172		
Pure Error	0.0000	0.0000		
Cor Total	176.88			

The ANOVA results revealed that tooth height (A), tooth top length (B), and x, y hatching (C), along with their interactions, significantly impact support volume. According to the Sum of Squares values, x, y hatching exerts the most significant influence, while laser speed (D) remains independent. Overhang angle (E) also affects support volume significantly, although this is due to the variations in specimens' geometries and the uneven volume of their supported areas. The influence of tooth height, tooth top length, and x, y hatching on support volume is clearly depicted in Figure 44. It was observed that increasing tooth height and decreasing tooth top length have only a minimal effect on reducing support volume, whereas higher values of x, y hatching result in a substantial reduction in support volume. This is attributed to the substantial removal of material from the support structure's main body as the number of internal walls decreases. Further analysis indicated that the minimum support volume across all specimens could be achieved with higher levels of tooth height (4 mm), lower levels of tooth top length (0.05 mm), and higher levels of x, y hatching (2.5 mm). This relationship is also illustrated in Figure 45, where relative contour plots demonstrate the interaction between support parameters and different overhang angles on support volume.

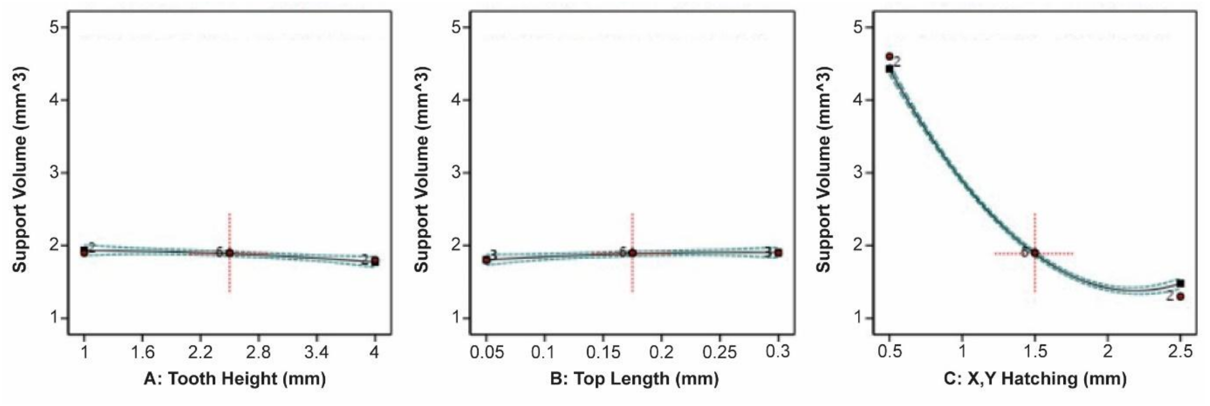

Figure 44. Main plots of support volume in Design-Expert 13

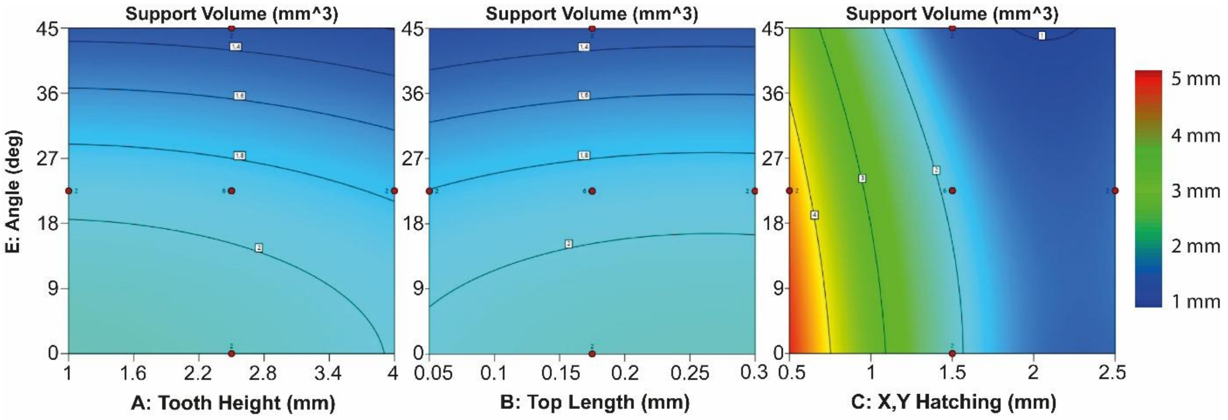

Figure 45. Contour plots of support parameters and overhang angle on support volume.

3.3.2 Support Removal Effort Analysis

For the detailed analysis of support removal effort, a quadratic model was also utilized with Adjusted $R^2 = 0.9529$ and Predicted $R^2 = 0.9323$, indicating a reasonable agreement. An Adeq Precision value of 22.3995 (greater than 4) also indicates a sufficient signal-to-noise ratio (data available in Appendix A). Non-printed parts were not included in this analysis. Table *4* displays the ANOVA results, showing an F-value of 68.75 with a $p\text{-value} < 0.05$, indicating that the model is significant. Significant model terms include A, B, E, AC, BC, CE, A^2, and B^2, while terms with $p\text{-values} > 0.1000$ are considered non-significant. Based on these findings, the quadratic model for support removal effort was also deemed suitable for further analysis.

Table 4. ANOVA results for the quadratic model of support removal effort.

Source	Sum of Squares	Mean Square	F-Value	p-Value
Model	46.47	2.32	68.75	<0.0001
A-Tooth Height	0.2439	0.2439	7.22	0.0100
B-Top Length	9.94	9.94	294.14	<0.0001
C-X, Y Hatching	0.0000	0.0000	0.0000	1.0000
D-Laser Speed	0.0894	0.0894	2.64	0.1106
E-Angle	0.3404	0.3404	10.07	0.0027
AB	0.0762	0.0762	2.25	0.1399
AC	0.2503	0.2503	7.41	0.0091
AD	0.0698	0.0698	2.06	0.1574
AE	0.0052	0.0052	0.1543	0.6962
BC	3.41	3.41	101.04	<0.0001
BD	0.0766	0.0766	2.27	0.1390
BE	0.0074	0.0074	0.2177	0.6430
CD	0.1149	0.1149	3.40	0.0715
CE	0.3472	0.3472	10.27	0.0024
DE	0.0006	0.0006	0.0192	0.8904
A^2	0.8610	0.8610	25.48	<0.0001
B^2	0.8610	0.8610	25.48	<0.0001
C^2	0.0215	0.0215	0.6364	0.4290
D^2	0.0215	0.0215	0.6364	0.4290
E^2	0.0858	0.0858	2.54	0.1178
Residual	1.59	0.0338		
Lack of Fit	1.59	0.1444		
Pure Error	0.0000	0.0000		
Cor Total	48.06			

Based on the ANOVA results, it was noted that tooth height (A), tooth top length (B), and overhang angle (E), along with some interactions, significantly influence support removal effort. The Sum of Squares analysis highlights that tooth top length exerts the most substantial effect compared to other parameters, whereas x, y hatching (C) and laser speed (D) do not significantly impact the removal effort. The impact of tooth height, tooth top length, x, y hatching, laser speed, and overhang angle on support removal effort is depicted in Figure 46. Notably, support removal effort decreases with average values of tooth height. Additionally, decreasing tooth top length results in a significant reduction in removal effort. This is attributed to stronger bonding between the part and supports at higher tooth top length levels, making supports more difficult to remove and requiring more effort to clear metal remnants from the surface. X, y hatching and laser speed have minimal effects on removal effort, whereas an increase in overhang angle correlates with decreased removal effort. Figure 47 illustrates the interaction between support parameters and various overhang angles on support removal effort. It was observed that minimal removal effort was achieved at average tooth height values (2.5 mm), lower tooth top length values (0.05 mm), and higher overhang angle values (45°). For 0°

overhangs, removal effort decreases with lower x, y hatching values (0.5 mm), while for larger overhangs, lower removal effort is observed at higher x, y hatching values (2.5 mm). Various laser speed values can be employed without significantly impacting the removal effort.

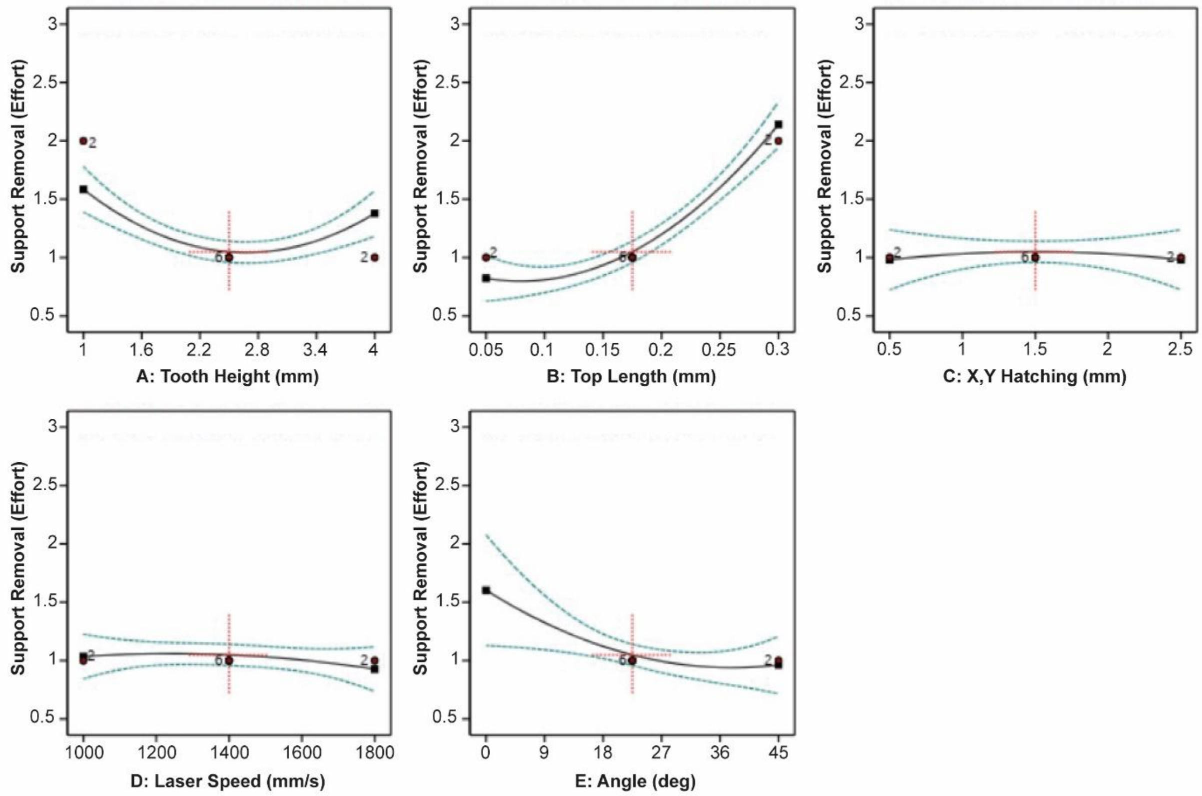

Figure 46. Main plots of support removal effort in Design-Expert 13.

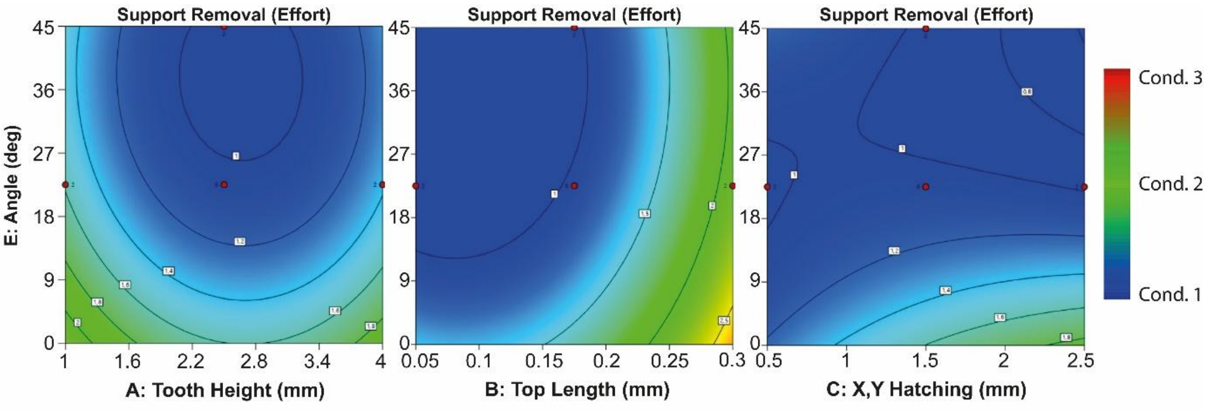

Figure 47. Contour plots of support parameters and overhang angle on support removal effort.

3.3.3 Warping Deformation Analysis

Towards the warping deformation analysis, a quadratic model was also utilised, with an Adjusted R^2 of 0.8069 and a Predicted R^2 of 0.7403. The close alignment between these values, with a difference of less than 0.2 indicates a reasonable agreement (fit statistics can be found in Appendix A). Non-printed parts were included in the analysis and are represented by a value of "2 mm," representing fully warped and defective parts. Table *5* presents the ANOVA results, where the model's significance is supported by an F-value of 19.59 and a p-value of less than 0.05. Significant model terms include E, AE, BC, BE, CE, and E^2, while terms with a p-value greater than 0.1000 are not significant. An Adeq Precision of 14.2794 (Appendix A) indicated a sufficient signal, validating the quadratic model for further analysis.

Table 5. ANOVA results for the quadratic model of support warping deformation.

Source	Sum of Squares	Mean Square	F-Value	*p*-Value
Model	32.40	1.62	19.59	<0.0001
A-Tooth Height	0.0861	0.0861	1.04	0.3111
B-Top Length	0.0005	0.0005	0.0058	0.9397
C-X, Y Hatching	0.0124	0.0124	0.1505	0.6992
D-Laser Speed	0.0076	0.0076	0.0922	0.7623
E-Angle	17.22	17.22	208.23	<0.0001
AB	0.0049	0.0049	0.0592	0.8084
AC	0.0182	0.0182	0.2204	0.6402
AD	0.1444	0.1444	1.75	0.1907
AE	0.4225	0.4225	5.11	0.0270
BC	1.20	1.20	14.50	0.0003
BD	0.0025	0.0025	0.0302	0.8625
BE	0.6084	0.6084	7.36	0.0084
CD	0.0132	0.0132	0.1599	0.6905
CE	2.81	2.81	33.92	<0.0001
DE	0.0169	0.0169	0.2044	0.6526
A^2	0.0232	0.0232	0.2809	0.5978
B^2	0.0130	0.0130	0.1570	0.6932
C^2	0.0142	0.0142	0.1716	0.6800
D^2	0.0106	0.0106	0.1279	0.7217
E^2	2.76	2.76	33.39	<0.0001
Residual	5.71	0.0827		
Lack of Fit	5.71	0.2594		
Pure Error	0.0000	0.0000		
Cor Total	38.11			

The ANOVA results indicated that overhang angle (E) and its interactions significantly influence warping deformation. The Sum of Squares analysis reveals that overhang angle has the most substantial effect compared to other parameters, which have minimal impact on warping deformation. Figure 48 illustrates the effects of tooth height, tooth top length, x, y hatching, laser speed, and overhang angle on warping deformation. It shows a significant decrease in warping deformation as overhang angle increases, which is partly because all non-printed specimens had 0° overhangs. The printed outcomes revealed that the highest x, y hatching value (2.5 mm) resulted in low-density support structures inadequate to support the 0° overhang area, explaining why none of the 0° specimens with a 2.5 mm hatching distance were printed successfully. Figure 49 provides a detailed view of how tooth height, tooth top length, x, y hatching, laser speed, and different overhang angles affect warping deformation. For 0° overhangs, warping deformation decreases with higher tooth top length (0.3 mm) and lower x, y hatching (0.5 mm), while tooth height and laser speed have negligible effects. For 45° overhangs, warping deformation reduces with higher tooth height (4 mm), lower tooth top length (0.05 mm), and higher x, y hatching (2.5 mm), with laser speed again having minimal impact. Across all parameters, the lowest warping deformation was observed at overhang angles between 20° and 40°.

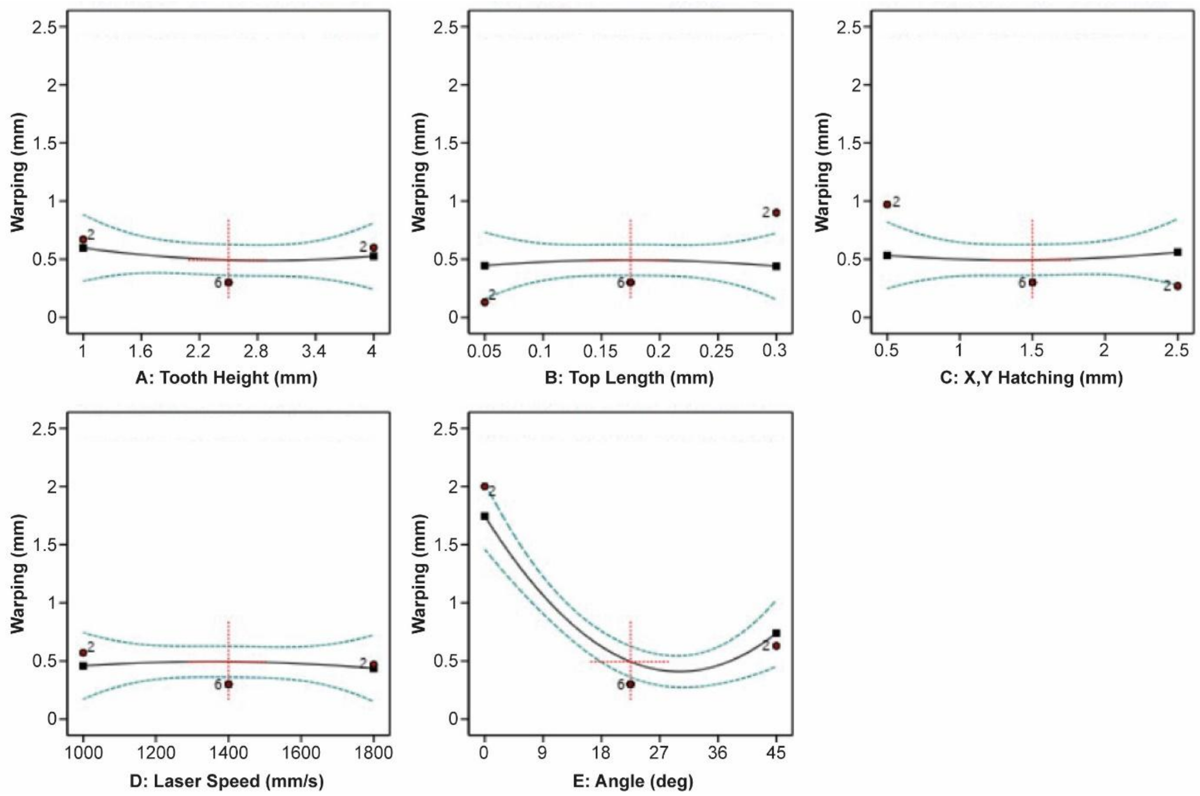

Figure 48. Main plots of warping deformation in Design-Expert 13.

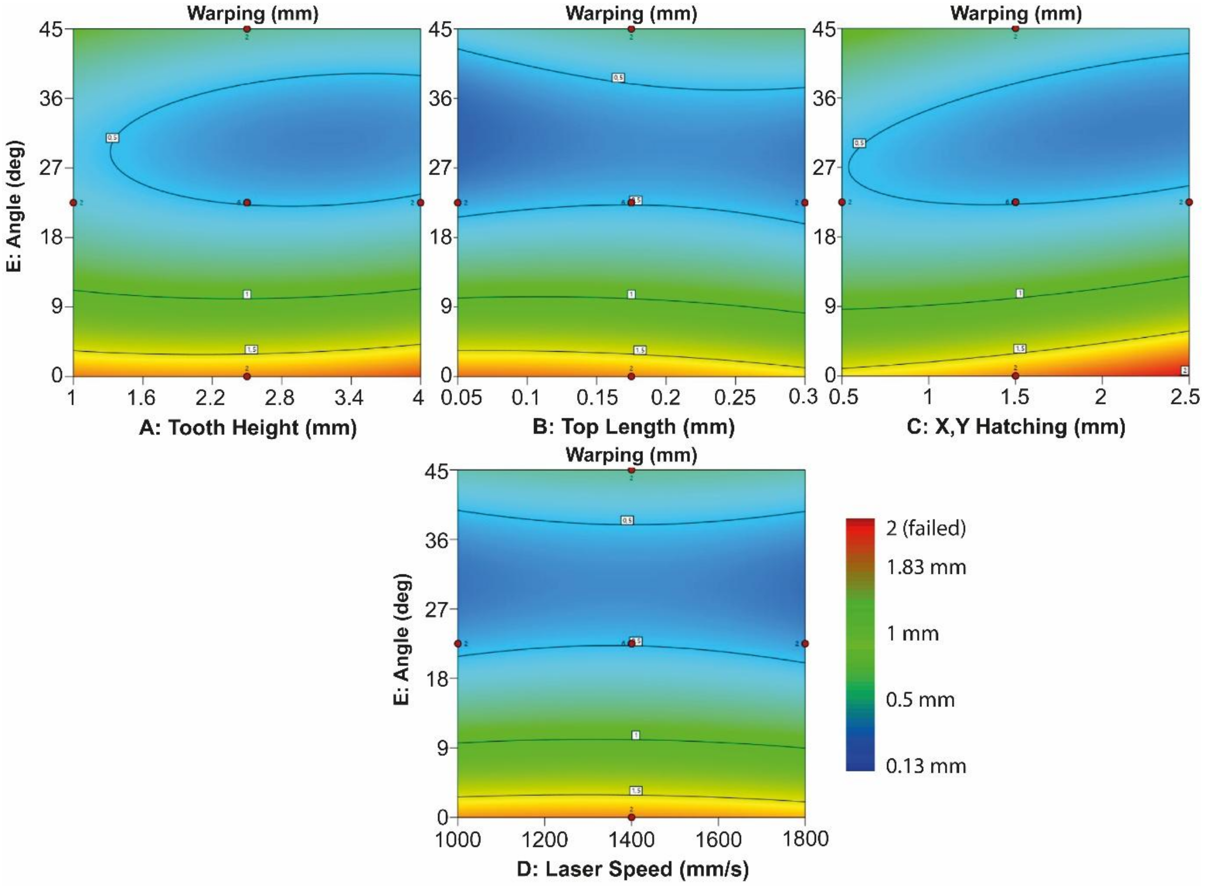

Figure 49. Contour plots of support parameters and overhang angle on warping deformation.

The experimental results presented in Sections 3.3.1 to 3.3.3 serve as the foundational input for the numerical optimization process detailed in Section 3.3.4 below. Each performance metric, including support volume, support removal effort, and warping deformation, was quantitatively assessed and normalized where applicable to ensure consistent integration into the optimization framework. These metrics represent the core responses targeted for improvement using a multi-response optimization strategy. Specifically, support volume was minimized to reduce material consumption and cost, support removal effort was minimized to improve post-processing efficiency, and warping deformation was minimized to enhance print quality and part integrity. These objectives were incorporated into the desirability function within the Design-Expert 13 software, where each response contributed to a combined score guiding the identification of optimal parameter settings. Thus, the outcomes of the experimental analyses were not merely observational but directly informed the design constraints and goals of the desirability-based optimization process.

3.3.4 Numerical Optimization

To determine the optimal combinations parameters that minimize support volume, support removal effort, and warping deformation, a multi-response optimization technique known as the desirability approach was employed in Design-Expert 13. This method transforms each individual response into a dimensionless desirability function, *di*, that ranges between 0 (completely undesirable) and 1 (fully desirable). The individual desirability scores are then combined using the geometric mean to calculate the overall desirability score (D), which reflects how well all responses meet their target criteria simultaneously. A score of D = 1 indicates that all goals have been perfectly achieved, whereas D = 0 suggests that at least one response falls outside acceptable limits and invalidates the solution.

The desirability approach is particularly suitable for this study, as it allows simultaneous consideration of multiple conflicting objectives, such as minimizing support volume and warping deformation while also ensuring easy support removal, by balancing trade-offs across these metrics. The three overhang angles of 0°, 22.5°, and 45° were analysed separately using consistent criteria constraints. Each goal (e.g., minimize, or maximize) is defined along with lower and upper acceptable limits, as summarized in Table *6*. For example, support volume was normalized on a scale from 1 to 5 and set to be minimized, while non-printed specimens (value of 2 mm), warping deformation above 1.5 mm, and very difficult support removal (condition 3) were excluded from the optimization domain.

Table 6. Criteria constraints as set up in Design-Expert 13.

Name	Goal	Lower Limit	Upper Limit
A: Tooth Height	in range	1 mm	4 mm
B: Tooth Top Length	in range	0.05 mm	0.3 mm
C: X, Y Hatching	in range	0.5 mm	2.5 mm
D: Laser Speed	in range	1000 mm/s	1800 mm/s
Support Volume	minimize	1 (normalised)	5 (normalised)
Support Removal	minimize	Condition 1	Condition 2
Warping Deformation	minimize	0.13 mm	1.5 mm

However, a well-known limitation of the desirability approach is its sensitivity to extreme values. If one response receives a score of 0, the overall desirability also drops to 0, regardless of how well the other responses perform. Additionally, setting overly restrictive constraints may lead to fewer feasible solutions or overly conservative recommendations.

Despite these limitations, this method remains a widely accepted and practical tool for engineering design optimization due to its simplicity, transparency, and ability to handle multi-objective problems effectively.

The three optimal solutions, one for each overhang angle level, are presented in Table 7. For the 0° overhang, the combined desirability was relatively low, primarily due to a limited number of successfully printed specimens and the constraints defined during the numerical optimization setup. The lowest desirability was observed in warping deformation, leading to higher levels of warping. To address this, the upper limit of warping deformation could be further reduced (e.g., from 1.5 mm to 1 mm), but this would impact the combined desirability and the total number of results. The selected optimal solution features an average tooth height, large tooth top length, low x, y hatching, and high laser speed. For 22.5° and 45° overhangs, the high desirability levels indicate that all goals are perfectly met. Both solutions are characterized by large tooth height, the lowest tooth top length, and high values of x, y hatching and laser speed. The selected optimal solutions for 0°, 22.5°, and 45° overhangs are illustrated in Figure 50. These optimal solutions were selected based on their high desirability; however, the optimization software also proposed additional results with very similar characteristics.

Table 7. Optimum results of 0°, 22.5°, and 45° overhangs. Parameters include tooth height, tooth top length, and hatching (all in mm), laser speed (mm/s), support volume (mm^3, normalized using a Likert scale), support removal effort (qualitative scale), and warping deformation (mm).

Angle.	Tooth Height	Tooth Top Length	X, Y Hatching	Laser Speed	Support Volume	Support Removal	Warping Deform.	Desirability
0°	2.738	0.230	0.722	1800	4.074	1.700	1.437	0.147
22.5°	3.557	0.050	2.227	1799.9	1.216	1.000	0.313	0.936
45°	4.000	0.050	2.500	1800	1.000	1.000	0.195	0.984

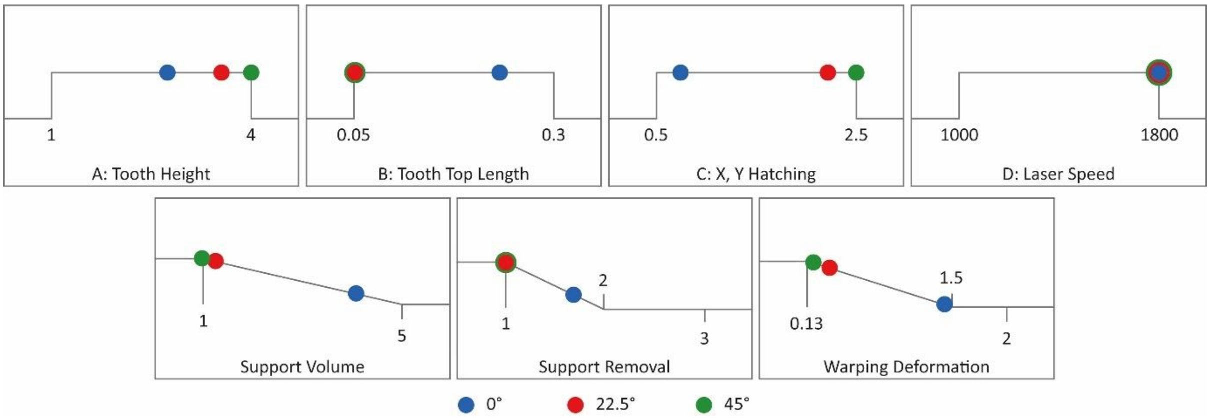

Figure 50. Graphical representation of the selected optimal solutions for 0°, 22.5°, and 45° overhangs.

One of the main challenges in developing the multi-response optimization framework was managing the inherent conflict between the three target responses: support volume, removal effort, and warping deformation. Reducing support volume and enhancing removability often compromised mechanical or thermal stability, leading to increased warping and unsuccessful prints, especially for 0° overhangs. To resolve these trade-offs, a desirability function approach was applied in the Design-Expert software, where each response was normalized and assigned a goal (minimized or excluded if outside acceptable limits). An overall desirability score was computed as the geometric mean of the individual desirabilities, which allowed the optimization algorithm to seek a balanced compromise. Support configurations classified as "very difficult" to remove or with excessive warping (>1.5 mm) were automatically excluded. While this method provided a structured way to integrate competing objectives, it also highlighted sensitivity to extreme values, since any single poor-performing metric could drive the overall desirability score to zero. This limitation was mitigated by carefully setting the desirability limits through experimental data, ensuring feasible and balanced optimization outcomes.

3.4 Chapter Summary

The objective of this chapter was to propose a framework of optimal configurations that minimize support volume, support removal effort, and warping deformation for a wide range of design and process parameters of block-type support structures for small ledge specimens fabricated using SLM. Ti6Al4V alloy was utilized for this investigation, focusing on three different overhang angle levels: 0°, 22.5°, and 45°. A multi-response optimization approach was employed, combining screening experiments, 3D printing trials, and data analysis to reveal the significant impact of design and process parameters on support performance.

The main and contour plots presented serve as valuable resources for researchers and professionals, enabling them to adapt the results to their specific needs and enhance their additive manufacturing production. Additionally, they can experiment with their own data by following a similar approach based on the proposed optimization framework. From the analysis and optimization of this research, the following principles were established:

- The absence of successful 0° specimens due to printing failures significantly affected the optimization process, resulting in a limited number of optimal configurations that inadequately minimized support volume and warping deformation. This emphasizes the need for improved support design strategies and the reconsideration of input parameter ranges, both geometric and process-related, to better reflect the practical constraints and challenges associated with 0° overhangs.

- X, Y Hatching exerted the most substantial influence on support volume, with minimal volume observed at higher hatching levels (4 mm), while tooth height and tooth top length had negligible effects. Thus, when the objective is to minimize support volume, optimization efforts should prioritize hatching over tooth geometry parameters.
- Tooth top length had the greatest impact on support removal effort, with minimal effort observed at lower tooth top length levels (0.05 mm), while other parameters showed minimal influence on removal effort.
- Overhang angle had the most significant effect on warping deformation, with minimal deformation observed at higher overhang angle levels (45°), while other parameters had marginal impact on deformation.
- For 0° overhangs, the optimal solution featured average tooth height (2.74 mm), large tooth top length (0.23 mm), low x, y hatching (0.72 mm), and high laser speed (1800 mm/s).
- For 22.5° overhangs, the optimal solution included large tooth height (3.56 mm), low tooth top length (0.05 mm), high x, y hatching (2.23 mm), and high laser speed (1799.9 mm/s).
- For 45° overhangs, the optimal solution comprised large tooth height (4 mm), low tooth top length (0.05 mm), high x, y hatching (2.5 mm), and high laser speed (1800 mm/s).

From a practical standpoint, the findings of this study offer immediate value to professionals working with SLM. Engineers and designers can adopt the optimized support parameter sets, such as appropriate hatch distance and refined tooth geometries, to minimise post-processing time and improve print reliability, particularly for flat or moderately inclined overhang surfaces. These improvements contribute to a more efficient AM workflow by enabling shorter build preparation cycles, reduced material consumption, and more consistent part quality. Embedding these optimised support strategies into pre-processing software tools or design guidelines can help manufacturers reduce reliance on trial-and-error, mitigate the risk of print failures, and accelerate the transition from digital design to functional components. Ultimately, this work supports a shift towards more automated, data-driven approaches to support structure design in metal additive manufacturing.

However, while the proposed multi-response optimisation framework yielded promising results for block-type support structures under controlled conditions, the scalability of this analysis remains a key limitation, particularly for 0° overhangs. The current approach was developed and validated using small, simplified geometries with moderate overhang features. Consequently, its generalisability to larger or more complex industrial components, where thermal and mechanical interactions are more intricate, is not yet established. In such cases, the thermal behaviour, residual stress distribution, and mechanical stability of the support structures may exhibit nonlinear responses, potentially disrupting the identified balance between material usage, support removability, and part quality.

To address these limitations, future work should expand the analysis through high-accuracy thermomechanical simulations and targeted experimental studies on similar or more complex geometries, incorporating a wider range of support types. Additionally, exploring adaptive or feature-sensitive support strategies that dynamically respond to local part characteristics could enhance the robustness of the framework. Incorporating these elements will be essential to ensure the broader applicability and industrial relevance of scalable support design methodologies for SLM and metal additive manufacturing.

Chapter 4: Finite Element Analysis of Alternative Support Types to Broaden the Applicability of Established Principles

4.1 Introduction

According to the referenced literature, significant efforts have been made to predict and evaluate the thermo-mechanical behaviour of metal parts using finite element methods and other advanced modelling techniques. A comprehensive understanding of the transient physical effects during manufacturing is essential to establish PBF/LB as a viable production technology. However, there is limited research on the performance of support structures, particularly when considering the supports and the overhanging part as a unified assembly.

In this chapter, four types of support structures are examined through finite element analysis, supported by experimental studies to validate the results. A multi-response optimization methodology was employed to propose optimized support structures that effectively transmit heat from a fixed heat source while ensuring high print quality. This optimization approach involved evaluating various geometric parameters of block, line, contour, and cone support structures through design of experiments methodology and relevant optimization techniques. Based on the previous research and key findings described in Chapter 3, optimized parameters are proposed to achieve low-volume, easily removable support structures without significantly compromising part quality. Relevant experiments to validate the optimal solutions were also conducted, focusing on the supports' removability, surface finish, and part warping deformation in terms of the upward displacement of overhang surfaces relative to the intended geometry.

4.2 Screening Experiments for Block-Type Supports

Prior to numerically investigating the thermal behaviour of various support structures, screening experiments were conducted to evaluate support parameters and identify key areas of main defects including overhang warping and supports distortion. This analysis aimed not only to evaluate the performance of different support geometries in terms of heat transmission and distortion due to thermal stresses but also to investigate the behaviour of the part and supports during printing and under high laser temperatures. Therefore, small ledge specimens were 3D printed using SLM technology, and fragmented block-type support structures with configurable geometric parameters were performed. For the experiments, the same EOS M290 machine mentioned in Chapter 3 was used to fabricate the specimens, and the material employed was again EOS Titanium Ti64 Grade 5 (see Table *2* for material properties).

These screening experiments aimed to determine the optimal range of support parameters that produce specimens without significant printing defects or build failures. It was observed that low-density support structures were more prone to distortion and cracking due to high thermal stresses, as shown in Figure 51a. Additionally, most low-density supports resulted in collapsed parts and build failures because they lacked sufficient material to support the overhanging surfaces; however, they were very easy to remove, as illustrated in Figure 51b. Conversely, high-density support structures, as shown in Figure 51c, were generally less prone to overall distortion, and most specimens were printed successfully. However, measurable geometric deviations were observed, where upward warping of the overhang surfaces resulted in misalignments of approximately 1-2 mm from the intended geometry. This inclination created a visible gap between the specimen's main body and the support structures. Notably, this distortion occurred despite the increased support density, highlighting the limitations of structural rigidity in mitigating warping caused by residual thermal stresses. These deviations emphasize the need for more robust thermo-mechanical analyses to better predict and minimise such defects. Moreover, support removal was considerably more challenging than with low-density configurations, requiring greater manual effort and posing a higher risk of part damage.

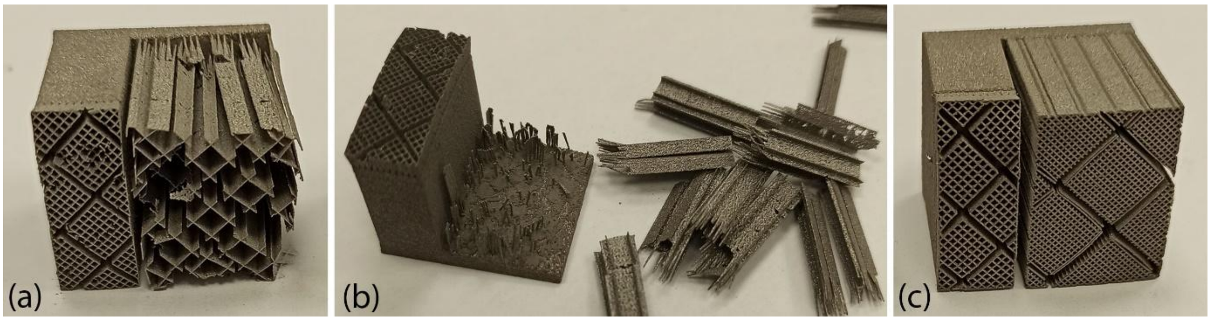

Figure 51. Screening experiments to evaluate support parameters: (a) distorted low-density supports, (b) easy-to-remove low-density supports, (c) warped high-density supports.

Moreover, the high temperatures and thermal stresses during SLM printing significantly impacted the quality of the printed specimens, regardless of support density. Specifically, as highlighted in Figure 52, the region near the build plate was the most critical, experiencing the most pronounced warping deformations. Geometric assessments also revealed substantial distortions in the overhanging surfaces of most printed specimens, especially when low-density support structures were used. Based on the findings, it became essential to conduct numerical investigations into the thermo-mechanical behaviour of typical support structures used in metal

AM and PBF/LB systems. The objective was to design optimal support configuration and provide principles that are applicable to a wide range of cases. To achieve this, a series of numerical simulations were conducted to validate the experimental data and explore additional support types. The study initially focused on analysing block support structures and later expanded to investigate line, contour, and cone supports.

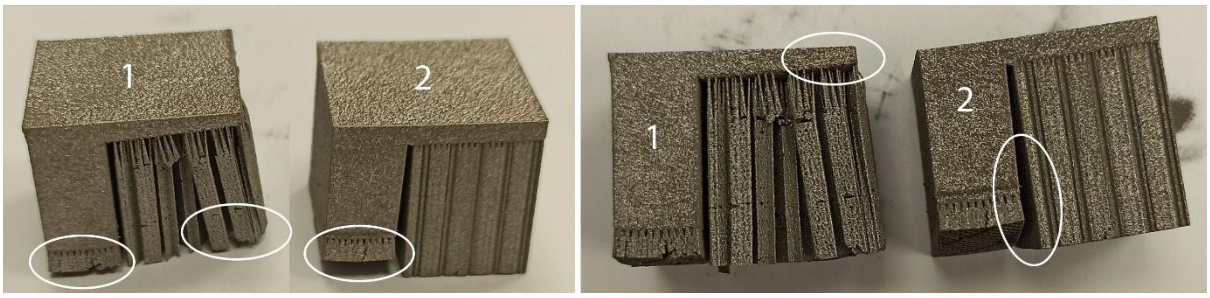

Figure 52. Warped low-density (#1) and high-density (#2) ledge specimens fabricated using SLM.

4.3 Initial Simulations and Setup

4.3.1 Specimen and Areas of Investigation

To validate the experimental results described in Section 4.2, FEA was applied using COMSOL Multiphysics software [10], and a similar small L-shaped specimen was designed. COMSOL was selected as the simulation environment for this study due to its robust capabilities in multiphysics modelling, particularly its strength in coupling thermal and structural physics through the heat transfer and solid mechanics interfaces. This feature is critical for accurately simulating the thermo-mechanical behaviour experienced during the PBF-LB process, where temperature-induced stresses can cause significant part deformation and warping. Additionally, COMSOL provides a highly customizable finite element environment, allowing for the incorporation of user-defined material properties, heat source definitions (such as the Gaussian heat flux model described in the literature), and realistic boundary conditions. Its compatibility with CAD tools like SOLIDWORKS facilitated a seamless workflow where complex geometries, including block-type support structures, were designed and transferred efficiently. These features collectively enabled high-fidelity simulations that mirror experimental conditions, thereby supporting the validation and interpretation of the results obtained in the previous section.

As observed in the literature, such small ledge overhang specimens are commonly used in PBF-LB studies to test and evaluate the performance of support structures. The specimen's geometry, along with its dimensions and the support design domains, is illustrated in Figure

53. The two domains where support structures were generated are highlighted in light grey (transparent mode), while the L-shaped specimen is shown in dark grey. Domain 1 (20×20×20 mm) supports the larger ledge overhang, while domain 2 (20×5×5 mm) supports the smaller overhang, which initially anchors the specimen to the build plate. A part of the build plate is also illustrated beneath the two domains (26×20×1 mm). This build plate was included as part of the FEA simulations to realistically reflect the heat transfer from the support structures into the plate, as well as to account for the thermal stresses occurring at the contact interface between the supports and the build surface. Including the build plate in the model allowed for a more accurate simulation of thermal gradients and mechanical constraints present during the printing process, especially in regions prone to warping and stress accumulation. In this study, only the performance of the supports in domain 1 was investigated. Domain 2 remained a fully dense support volume for every support alternative.

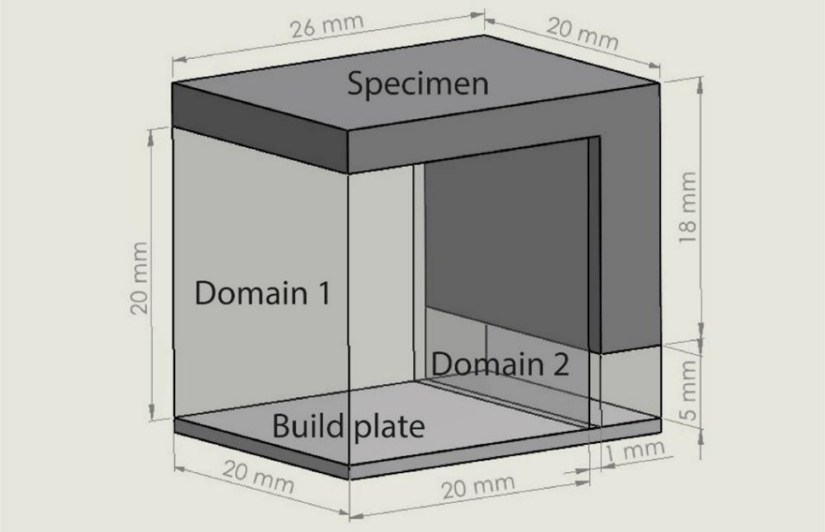

Figure 53. L-shaped specimen and support structure design domains.

4.3.2 Scene Setup and Numerical Modelling

Before initiating the thermo-mechanical simulations on the component with block-type support structures, preliminary simulation tests were conducted using the assembly shown in Figure 53 to establish the foundational framework and identify the key areas for thermal and mechanical analysis. The aim was to simulate key features of the PBF/LB process and record the thermo-mechanical behaviour of the assembled model. Titanium alloy was chosen as the material, and a heat source of 1550 °C, approximately the melting point of titanium, was applied between the supports and the overhang surface of the part. It is also important to clarify here, that the simulations presented in this chapter do not model the full layer-by-layer growth typical of actual SLM processes. Instead, a static thermal load was applied to evaluate the heat dissipation capability and thermal conductivity performance of different support structures under simplified but representative conditions. The goal was to assess how well each support geometry transmits heat from the overhanging region to the build plate, which is directly related to thermal stress and potential warping in practice.

All the simulations were performed in COMSOL Multiphysics software, while the 3D models were designed in SOLIDWORKS [144]. Importing 3D models from SOLIDWORKS to COMSOL is a straightforward process. This transfer allows for a smooth transition between the two software platforms, enabling users to effectively utilize the features and capabilities of both programs. By importing parts, including specimens and support structures, from SOLIDWORKS to COMSOL, users can take advantage of COMSOL's advanced modelling and simulation capabilities while benefiting from SOLIDWORKS' design and engineering functionalities. This integration enhances the overall efficiency and effectiveness of the design and analysis process, enabling users to work with complex models and simulations.

Various materials can be used in metal AM and PBF/LB systems, including steels (Fe + C +...), aluminium-based alloys (Al + Si + Mg), titanium-based alloys (Ti + Al +...), and nickel-based alloys (Ni + Cr +...). The choice of material depends on the application, material properties, and compatibility with the 3D printing machine. In the experiments, Ti6Al4V Grade 5 was used as the material, and its properties are listed in Table *2*. However, in the simulations conducted in COMSOL, titanium Grade 4 was selected from the default material library due to software limitations and to maintain simulation consistency across different geometries. While Grade 4 titanium is not identical to Ti6Al4V Grade 5, particularly in terms of alloy composition and mechanical strength, the two grades exhibit comparable thermal properties relevant for heat transfer and deformation analysis in PBF/LB simulations. The primary purpose of the simulation was to observe relative thermal trends and stress distributions among different support structures rather than to replicate exact mechanical values. Nevertheless, this limitation is acknowledged, and future studies could involve custom material input based on experimentally measured Ti6Al4V Grade 5 data to enhance accuracy. Grade 4 titanium is a strong, lightweight alloy with excellent corrosion resistance, a maximum melting temperature of 1660 °C, and a specific heat capacity of 0.53 J/g°C. For modelling purposes, the modulus of elasticity was assumed to be 105 GPa with a Poisson’s ratio of 0.37, and the thermal conductivity was assumed to be 17.2 W/mK.

Regarding the heat source, a value of 1550 °C was set beneath the overhang surface of the part, representing the melting point of titanium during SLM printing (usually between 1550

°C and 1660 °C). The energy transferred from the heat source to the powder is directly linked to the laser power used. For example, when the laser power is set to 400 W for a volume of 1 mm^3, the total power applied to the powder matches this value, causing the powder to melt and temperatures to exceed 1550 °C. However, the primary focus of this research is to investigate the heat transfer process from the component to the support structure after the powder transitions from a molten liquid to a solid state. This correlation is crucial as it ensures the heating source effectively delivers the intended energy to the powder, enabling precise management of thermal effects throughout the SLM process. By aligning the heating source energy with the actual laser power, the system can achieve reliable and precise temperature control and material transformation. This synchronization between the heating source and laser power is essential for attaining consistent and accurate results in the overall process.

Specifically, in the simulation setup, the laser power was implemented in COMSOL as a heat source, applied directly beneath the overhang surface. This approach was not intended to replicate the full dynamics of the SLM process, but rather to assess the thermal performance of different support structures under consistent heating conditions. This modelling strategy is based on the methodology proposed by Malekipour et al. [111], where a fixed heat source was employed to isolate and evaluate heat conduction characteristics across various support geometries. Accordingly, a volumetric heat flux was applied to the entire assembly in COMSOL, excluding domain 1, which represented the main support structure under investigation. By omitting domain 1 from the direct heat flux application, the simulation focused on quantifying how effectively the support conducted heat away from the part, under conditions representing post-solidification heat transfer. This deliberate simplification allowed for meaningful comparisons between support alternatives and their influence on temperature distribution and thermal stress, rather than on process-specific melting dynamics.

To demonstrate thermal stress, heat distribution, temperature spectrum, and heat transmission between domains, various branches of physics, including heat transfer in solids and solid mechanics, were employed. These disciplines were utilized to analyse thermal behaviour and demonstrate how heat was transferred within the system, including the various support structures. To maintain simplicity and focus on the main assembly, the surrounding metal powder as well as the chamber's controlled atmosphere of inert gas were excluded from the numerical simulations.

In thermo-mechanical modelling, a crucial aspect involves studying thermal expansion, which describes how a material changes its volume in response to temperature fluctuations. In this modelling framework, heat transfer is computed alongside structural mechanics, treating them as integrated aspects of the same problem. Throughout the modelling process, it was assumed that the component's surface in contact with the support maintained a temperature of 1550 °C. This enabled the calculation of the thermal expansion (ε_{inel}) specific to that layer using the formula: $\varepsilon_{inel} = \alpha \cdot (T - T_{ref})$, where α represents the coefficient of thermal expansion, T denotes the applied temperature, and T_{ref} represents the reference temperature at which no thermal stress exists. The coefficient of thermal expansion was assumed to be 8.5×10^{-6} (°C), and the applied temperature T was set to 1550 °C. Heat dissipation was also considered, assuming that the entire model was surrounded by a reference temperature of 21 °C (T_{ref}). Consequently, heat loss occurs from both heat transfer through the supports and radiation into the surrounding environment.

Regarding boundary conditions, the modelling process included two boundary conditions: one related to the build plate and the other concerning the connection point where the specimen contacted domain 2 (Figure 53). The bottom surface of the build plate was fixed using a mechanical constraint to simulate rigid contact with the machine's base, thereby preventing displacement during the simulation. Thermally, a convective heat flux boundary condition was applied to all external surfaces, representing heat loss to the surrounding atmosphere. These constraints, consistent with prior studies such as Zaeh and Branner [102], Zeng et al. [109], Malekipour et al. [111], and Miki and Nishiwaki [119], ensured thermal and structural stability of the simulation domain while focusing the analysis on the effect of support geometry on heat dissipation and resulting thermal stresses.

As this study is focused on evaluating the relative thermal and mechanical performance of different support structures, rather than predicting absolute failure thresholds, no strict target values were enforced for stress or displacement. The thermal simulations in this study report peak stress values that exceed the typical yield strength of Ti6Al4V (~880–950 MPa), especially for thin cone-type supports. This is a known artefact of static thermomechanical simulations, which apply simplified thermal loads without modelling transient effects, plastic deformation, or temperature-dependent softening. As such, these stress values should not be interpreted as physically realistic but rather as relative indicators of thermal concentration and structural behaviour under consistent boundary conditions.

However, practical guidelines suggest that thermal stresses should remain below the material yield strength, vertical displacements should be kept within ±0.2–0.3 mm, and temperature gradients should ideally stay below ~100 °C/mm to reduce the risk of warping, cracking, or delamination. Overall, this comparative approach offers valid insight into the influence of support geometries on heat dissipation and stability. Future work could enhance physical realism through transient analysis and advanced material models, though this would require significantly greater computational effort.

4.3.3 Results and Discussion for Fully Dense Supports

Based on the setup detailed in Section 4.3.2, numerical simulations were conducted on fully dense support structures (Figure 53) to analyse heat transfer from the ledge part to the supports. As depicted in Figure 54a, significant thermal stresses were observed in the build plate, particularly around the edges near the supports. These stresses can lead to warping, distortion, or even detachment of the part from the build plate during SLM printing. As noted in Section 4.2, due to these high thermal stresses, the shorter supports anchoring the part to the build plate could experience considerable warping, while supports under the overhang surface might develop cracks. Regarding temperature distribution (Figure 54b), in this specific simulation setup, peak temperatures were concentrated near the heat source positioned between the supporting structures and the overhang surface of the component. It was also noted that high temperatures extended throughout the entire support structure up to the build plate; however, the exact temperature distribution varied depending on the morphology of the supports in each case. Examining the displacement magnitude plot (Figure 54c), the most significant deformations were observed on the overhang surface of the component, particularly at the front edge. Similar observations were made during screening experiments shown in Figure 52, where geometric verification indicated significant distortion of the front edge of the overhang surface from its actual position. The stress distribution is attributed to thermal expansion, exacerbated by the boundary condition imposed at the base plate to restrict displacement, which contributed to the higher stress values observed.

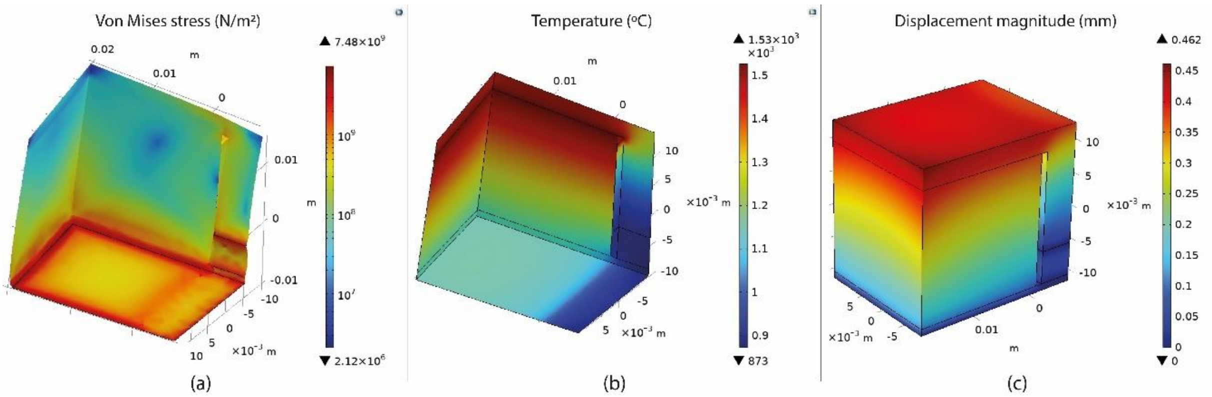

Figure 54. Fully dense supports: (a) thermal stress; (b) temperature distribution; (c) displacement.

As mentioned above, these initial simulations focused on evaluating the thermal stress, temperature distribution, and displacement during the printing process, utilising a constant heat source on top of the supports. It should be noted that material phase changes, such as melting and solidification, were not explicitly modelled in this study. Instead, a temperature-dependent material property approach was adopted to approximate thermal behaviour, which is a common practice in SLM simulations to reduce computational complexity while maintaining acceptable accuracy. This simplification allows for capturing the key thermal and mechanical responses without incorporating the highly nonlinear effects of latent heat.

4.4 Numerical Simulations for Block Support Structures

4.4.1 Methodology and Simulations

In PBF-LB processes, scanning speed and laser power are critical parameters that significantly influence the ease of support removal during post-processing and the deformation behaviour of the printed part. As detailed in Section 4.3.2, this study utilized laser power as the primary heat source for the thermo-mechanical simulations, while examining various support structures and their parameters. Metal AM and PBF-LB offer various support types, with the choice depending on part geometry, material selection, and compatible slicing software. According to the literature, some of the most commonly used support structures in SLM are block, line, contour, and cone supports; therefore, this study specifically focused on these types. Initially, block-type supports were examined to illustrate the phenomena observed in the experimental study of Section 4.2. Figure 55 displays the morphology associated with these supports. They can be divided into two areas: (i) the support body, which determines the geometry and density of the supports, and (ii) the tooth area, which pertains to the contact points between the supports and the overhang surface of the part (Figure 55a).

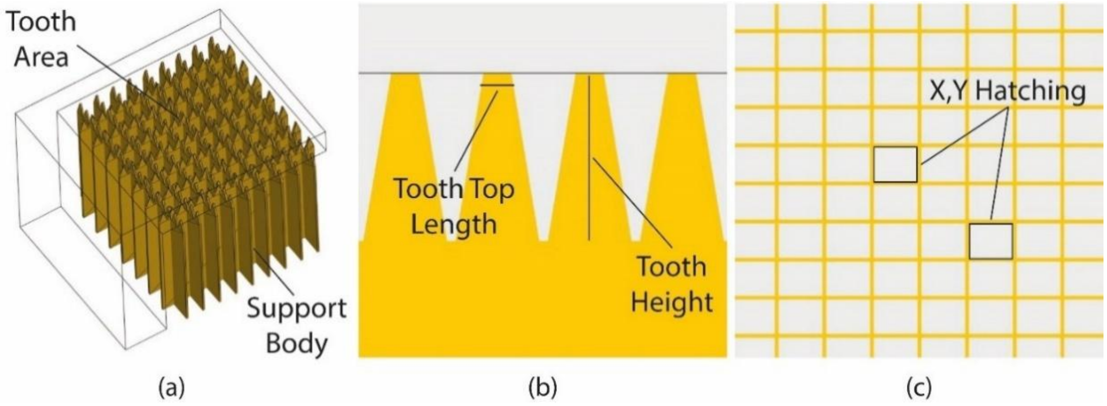

Figure 55. (a) Morphology of block-type support structures, (b) tooth area, (c) grid density.

The next step involved defining the input parameters (modifiable and controllable variables) to be investigated, along with their respective levels. Three primary geometric parameters were chosen for examination: tooth height, tooth top length, and x, y hatching (Figure 55b, 55c). These parameters were specifically chosen due to their significant influence on key performance metrics, including support removal effort, warping deformation, and support volume. This selection was guided by an extensive literature review and previous experimental findings, which consistently identify these three factors as the most critical for controlling thermal conduction and detachment behaviour. Other parameters, such as support thickness or laser process variables, were considered but ultimately excluded from the optimization framework due to challenges in simulation and DOE setups or due to high correlation with the selected variables. Table *8* outlines these selected parameters and their corresponding levels. Each parameter has three levels: the minimum, the average, and the maximum value. The Design-Expert 13 software [145] was used for preparing the DOE and visualizing the optimization results, with the initial setup illustrated in Figure 56.

Table 8. Selected block-type support parameters and levels.

Support Type	Parameter	Level 1	Level 2	Level 3
Block	Tooth Height	1 mm	2.5 mm	4 mm
	Tooth Top Length	0.1 mm	0.3 mm	0.5 mm
	X, Y Hatching	0.5 mm	1.25 mm	2 mm

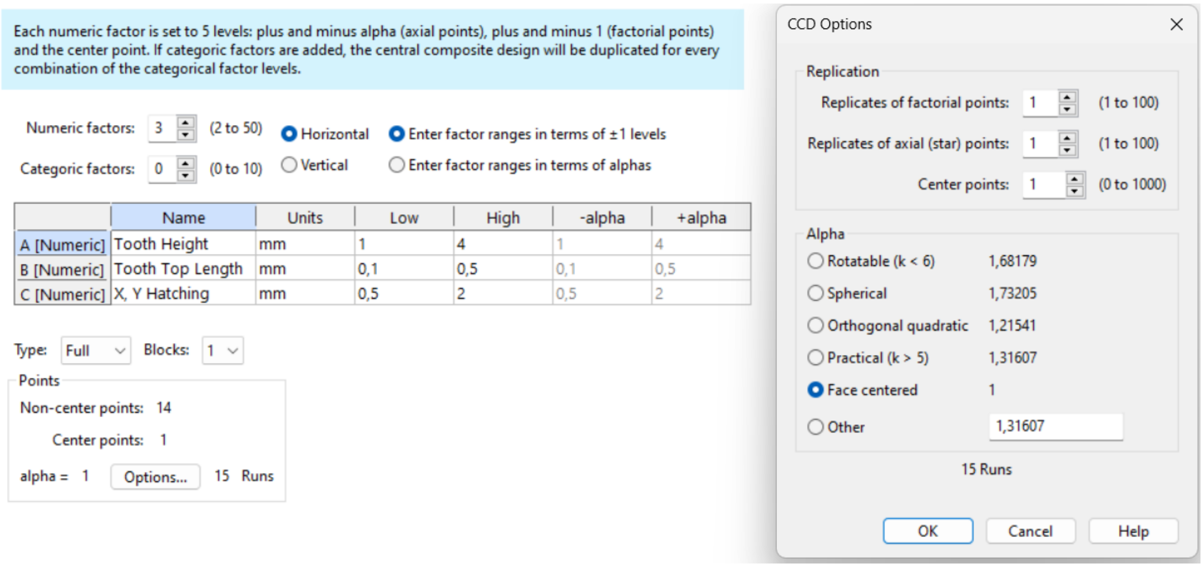

Each numeric factor is set to 5 levels: plus and minus alpha (axial points), plus and minus 1 (factorial points) and the center point. If categoric factors are added, the central composite design will be duplicated for every combination of the categorical factor levels.

Numeric factors: 3 (2 to 50) ● Horizontal ● Enter factor ranges in terms of ±1 levels

Categoric factors: 0 (0 to 10) ○ Vertical ○ Enter factor ranges in terms of alphas

	Name	Units	Low	High	-alpha	+alpha
A [Numeric]	Tooth Height	mm	1	4	1	4
B [Numeric]	Tooth Top Length	mm	0,1	0,5	0,1	0,5
C [Numeric]	X, Y Hatching	mm	0,5	2	0,5	2

Type: Full Blocks: 1

Points

Non-center points: 14

Center points: 1

alpha = 1 15 Runs

CCD Options

Replication

Replicates of factorial points: 1 (1 to 100)

Replicates of axial (star) points: 1 (1 to 100)

Center points: 1 (0 to 1000)

Alpha

○ Rotatable (k < 6) 1,68179

○ Spherical 1,73205

○ Orthogonal quadratic 1,21541

○ Practical (k > 5) 1,31607

● Face centered 1

○ Other 1,31607

15 Runs

Figure 56. DOE setup for block supports in Design-Expert 13.

The selection of parameter ranges, specifically tooth height (1-4 mm), tooth top length (0.1-0.5 mm), and hatching distance (0.5-2 mm), was based on a combination of insights from the literature, previous experimental outcomes in Chapter 3, and screening trials using the EOS M290 3D printing machine. These ranges reflect the practical feasible parameter range observed during initial SLM trials: parameters outside these bounds frequently led to collapsed, warped, or unprintable specimens, particularly for flat 0° overhangs. Additionally, the ranges were selected to include both conservative and extreme support configurations, enabling a comprehensive evaluation of thermo-mechanical behaviour under different support conditions. Moreover, as support removability could not be assessed through simulation alone and is instead evaluated in the experimental validation phase (Section 4.7), parameters primarily affecting mechanical detachment, such as laser speed and power, were held constant to isolate the thermal and structural performance of the support geometries. Therefore, the final set of parameters was defined through an iterative process of experimental refinement, ensuring that the chosen ranges are both practical and well-suited to support reliable and meaningful model-based optimization.

Response surface methodology (RSM) using central composite design (CCD) was employed to conduct the experiments and define the design alternatives. As in the experimental work presented in Chapter 3, this method was selected for its effectiveness in analysing, visualizing, and optimizing responses, while providing valuable insights into parameter interactions. However, RSM may present certain limitations, particularly under varying thermal and mechanical boundary conditions. It assumes a quadratic relationship between input variables and responses, which may not fully capture the highly nonlinear or complex behaviours inherent in support structure performance. Moreover, it relies on predefined parameter ranges and may miss global optima outside the explored design space. To address these limitations, future work could incorporate advanced optimization techniques such as topology optimization. This approach has the potential to automatically generate novel support geometries (beyond the commonly used types) that minimize material usage while maintaining mechanical stability and thermal efficiency, offering significant advantages over conventional support design heuristics [154], [155].

For the RSM-CCD setup, a face-centered approach with an alpha value of 1 was used, without replicates of factorial, axial, and center points. Consequently, 15 unique configurations (8 factorial, 6 axial, and 1 center) were selected for this investigation. For the DOE involving block-type supports, the CAD assembly used to set up and run the simulations is depicted in Figure 53. The L-shaped specimen, support domain 2, and the build plate area were kept constant, while in domain 1, the various support alternatives generated during the DOE were thermo-mechanically analysed individually. Figure 57 illustrates a sample of the designed block support structures along with some of their input parameters.

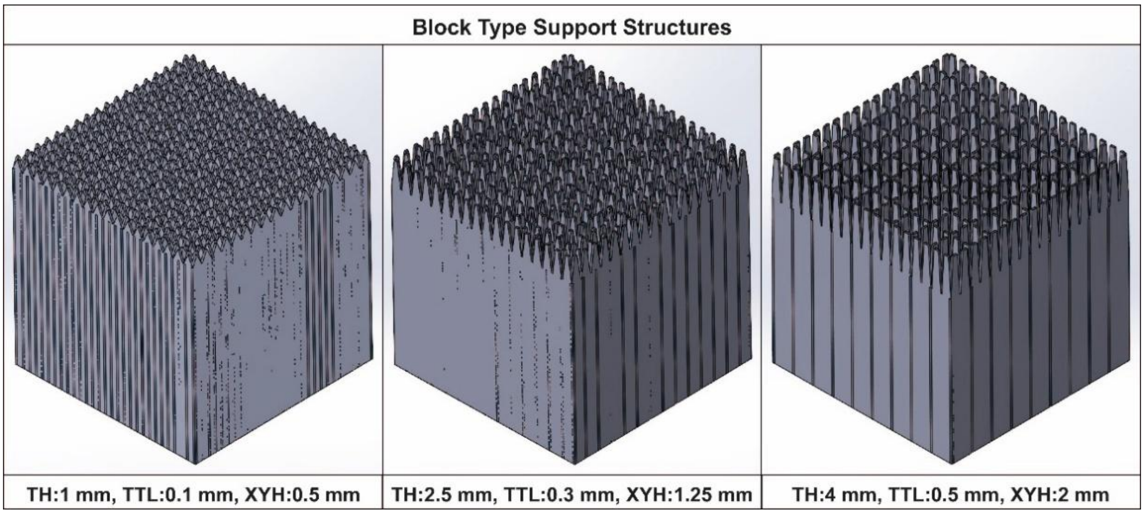

Figure 57. Sample of block support alternatives designed in SOLIDWORKS.

4.4.2 Performance Measures

Upon completing the thermo-mechanical simulations, four key responses were analysed: support volume, thermal stress, plate temperature, and overhang displacement, as each provides a distinct and essential perspective on support structure performance. It is important to note here that no single response can be considered universally dominant, as support effectiveness must be evaluated holistically. For instance, support volume directly affects material usage and post-processing effort. Thermal stress is linked to defect formation and residual stress accumulation. Plate temperature reflects heat dissipation efficiency, while overhang displacement indicates the degree of warping deformation and dimensional accuracy. Given their interdependence, all four responses were treated as critical and were jointly considered in the optimization process. A multi-response optimization strategy was employed to simultaneously balance these objectives, ensuring that no single performance criterion was prioritized at the expense of others. This approach reflects the complex trade-offs inherent in support structure design and emphasizes the need for a comprehensive evaluation to achieve robust and reliable printing outcomes.

Regarding the measurements, the various support volumes were measured in SOLIDWORKS, then exported in STEP, a file format used for exchanging 3D models and product data, and imported individually into COMSOL for simulation. Thermal stress was measured by recording the maximum stress values calculated in COMSOL, as the highest thermal stress typically occurred around the build plate where the supports were anchored (Figure 54a). This area was given special attention since it is the most critical point for developing warping and distortion defects. For improved visualization, an “algorithmic scale” was utilised (Figure 58a). The term “algorithmic scale” refers to the default stress visualization scale automatically generated by the simulation software (COMSOL Multiphysics), which is based on the computed range of values within each simulation. This relative or normalized scale was used to effectively visualize the thermal stress distribution on the build plate, support structures, and surrounding areas. It was particularly necessary due to the presence of extreme localised stress peaks (i.e., very high values occurring at sharp edges or at thin support structures) which would otherwise distort a linear or uniform scale and obscure the overall pattern of stress distribution. The algorithmic scaling approach ensured that stress concentration zones could still be visually interpreted, despite the presence of outliers.

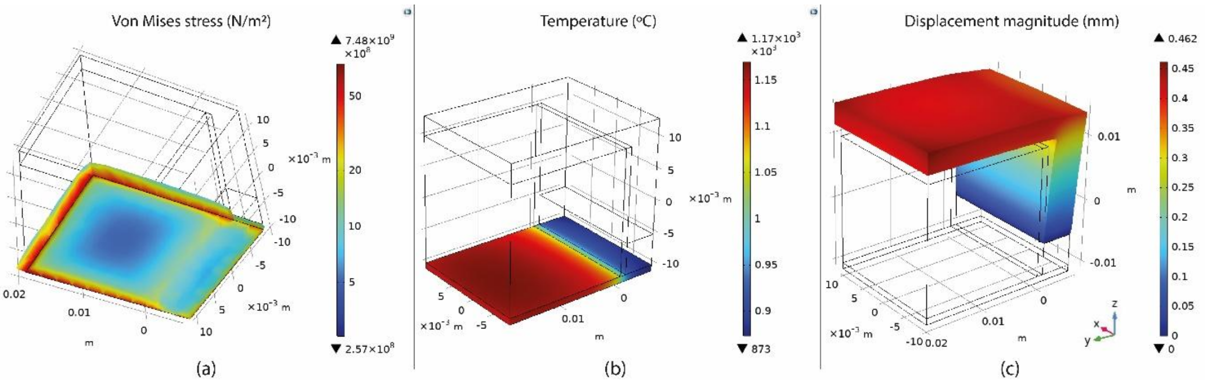

Figure 58. (a) Stresses on the build plate, (b) temperature on the build plate, (c) part deformation.

The temperature distribution was assessed by recording the maximum build plate temperature calculated in COMSOL, focusing on understanding heat transmission and the heat capacity of various support structures. Figure 58b illustrates higher temperatures observed on the top of the build plate where the support structures were anchored. It is important to note that thermal stress and temperature distribution are closely interconnected, and both significantly impact both the printed part and the supports. Displacement magnitude was measured as the maximum deformation value of the assembly based on the simulations. The greatest deformation was observed on the specimen’s overhang surface, primarily in the positive z-axis direction, particularly at the front edge (Figure 58c). After recording these measurements, the data were imported into Design-Expert 13 for analysis of variance to validate the selected models, analyse the data, visualise the results, and optimise the outcomes.

4.4.3 Results and Discussion

For a comprehensive investigation of block-type supports and their parameters, quadratic models were employed for all responses to analyse the simulations. According to the ANOVA results, all factors met the criteria for robust models, as discussed in detail in Section 3.3.1. The "F" and "P" values indicated that both the models and their terms were significant. Predicted R^2 and adjusted R^2 values, which are nearly equal to 1, demonstrated reasonable model agreement. Additionally, an Adeq precision value greater than 4, which measures the signal-to-noise ratio, was desirable. Consequently, all four quadratic models were validated for further analysis (detailed information regarding the various DOE setups and the ANOVA outcomes can be found in Appendix B).

The ANOVA results indicated that tooth height (A), tooth top length (B), and x, y hatching (C), along with their interactions, significantly impacted the support volume, thermal stress, plate temperature, and overhang displacement. Figure 59 illustrates the correlation between tooth height, tooth top length, and x, y hatching on the support volume. It was observed that tooth height and tooth top length had minimal effect on the support volume, whereas x, y hatching had the most substantial impact. As the hatching distance increased, the support volume decreased significantly. This reduction is due to a significant amount of material being removed from the supports' main body as the total number of inner grid walls decreases.

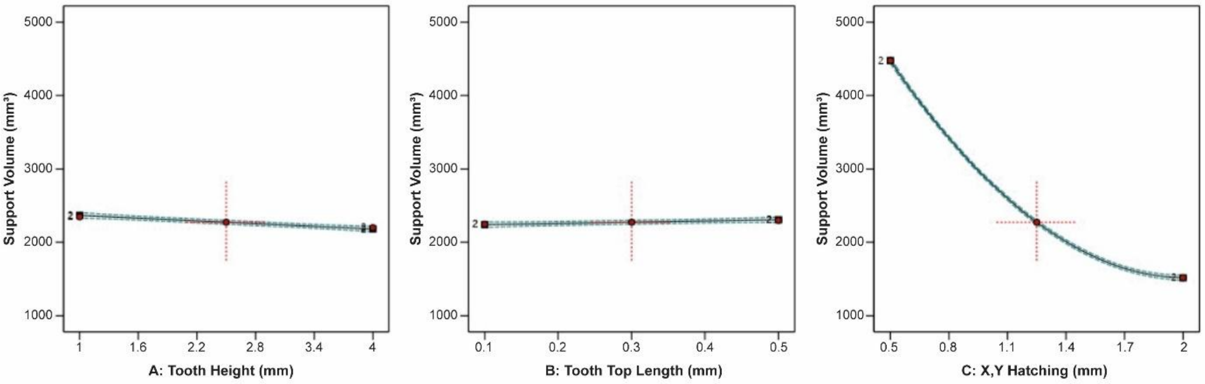

Figure 59. Main plots of support volume in Design-Expert 13 for block supports.

Figure 60 shows the effect of tooth height, tooth top length, and x, y hatching on the thermal stress applied to the build plate. The results indicated that tooth height had a minimal impact on thermal stress. However, thermal stress slightly increased with longer tooth top length. In contrast, increased x, y hatching significantly reduced thermal stress. This pattern is also reflected in the correlation between these factors and plate temperature, as depicted in Figure 61, due to the strong connection between these two responses. Specifically, as tooth height increased, plate temperature slightly decreased, while an increase in tooth top length caused a slight increase in plate temperature. Notably, x, y hatching had the most substantial effect, with increased hatching distance leading to a significant decrease in plate temperature. Figure 62 illustrates the impact of tooth height, tooth top length, and x, y hatching on the specimen's overhang displacement. The findings showed that tooth height and x, y hatching had the most pronounced effects on overhang displacement, while tooth top length had a negligible impact. As tooth height increased, overhang displacement also increased. Conversely, greater x, y hatching distance resulted in a substantial decrease in overhang displacement.

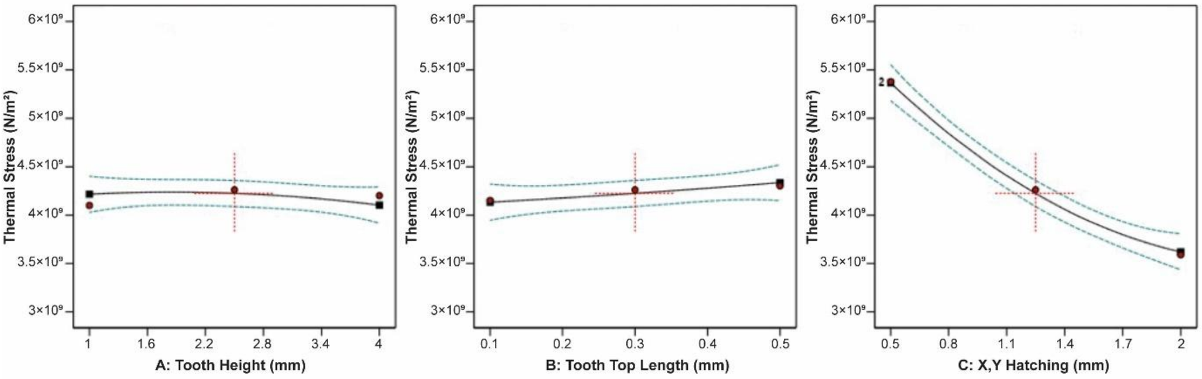

Figure 60. Main plots of thermal stress in Design-Expert 13 for block supports.

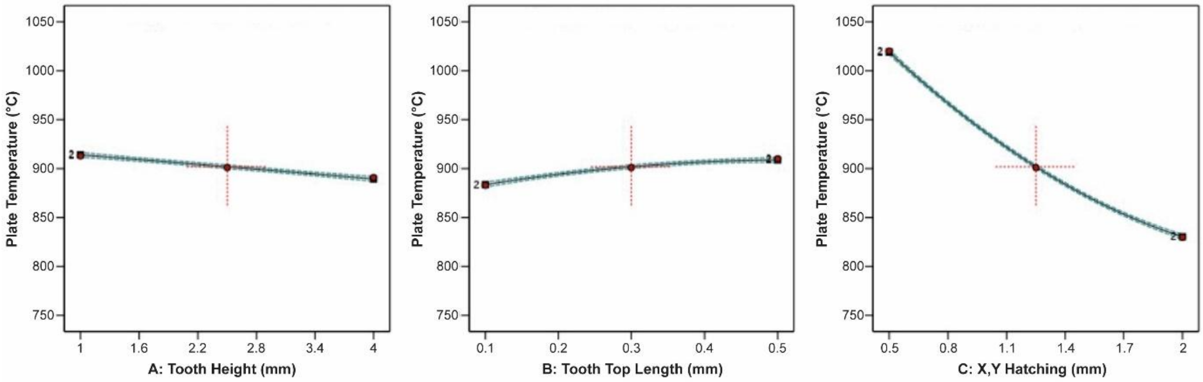

Figure 61. Main plots of plate temperature in Design-Expert 13 for block supports.

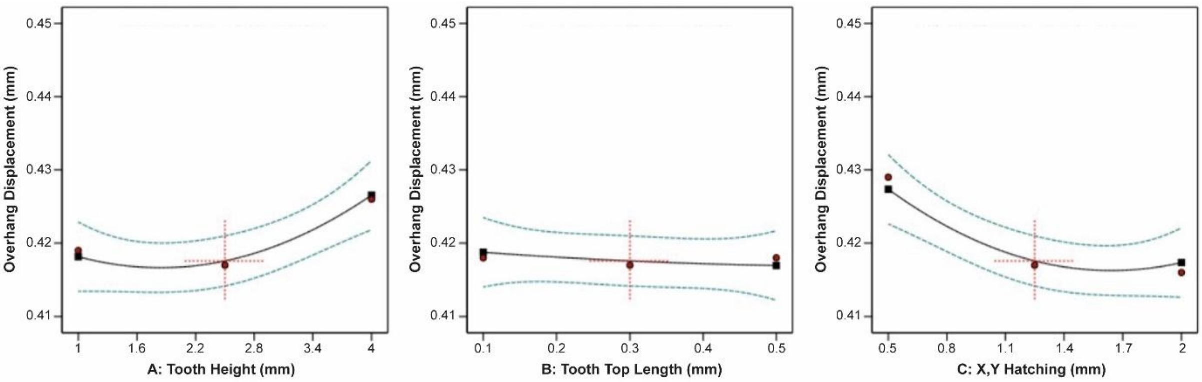

Figure 62. Main plots of overhang displacement in Design-Expert 13 for block supports.

4.4.4 Comparison with the Experimental Work

First, it is important to clarify that the primary aim of the comparison between numerical simulations and experimental results was not to match specific numerical values of displacement or thermal behaviour, but rather to identify and analyse the specific areas where defects are likely to occur. This approach allowed for a more targeted investigation of critical regions susceptible to thermal distortion or warping. Additionally, since the support geometries and the material used in the simulations differed from those used in the experimental setup, a direct one-to-one comparison of absolute values would not be meaningful. Instead, the comparison served to validate the predictive capability of the simulation in highlighting critical areas, guiding further refinement of support design and process parameters.

Thus, when comparing the numerical simulation findings with the results discussed in Section 4.3.3 and the experimental outcomes presented in Section 4.2, significant similarities emerged. The numerical simulations revealed that the highest thermal stress was applied to the build plate, as illustrated in Figure 54a. This correlated with the experimental observations in Figure 52, where the part and supports were more prone to warping. In several test prints, the base of the printed specimens exhibited early signs of distortion near the support connection zone, suggesting excessive thermal stress accumulation during the build. Additionally, the simulations showed the highest displacement occurring between the supports and the part's overhang surface, where the highest temperatures were applied (Figure 54c). This resulted in defective and warped overhangs, as seen in Figure 52. Moreover, the numerical optimization results obtained from Design-Expert 13, based on performance criteria and the desirability approach, indicated that configurations with low tooth height, average tooth top length, and average to high x, y hatching values led to optimized block support structures, as illustrated in Figure 63.

Figure 63. Optimal parameters for block-type supports.

These optimal parameters for block-type supports were selected with the goal of improving overall print quality and process efficiency in SLM. Specifically, the key targets (support volume, thermal stress, part displacement, and support heat transfer) were identified based on their direct influence on critical print outcomes. Reducing support volume minimizes material consumption and post-processing effort, especially during support removal. Lower thermal stress helps prevent common defects such as warping, cracking, or part detachment from the build plate. Minimizing part displacement ensures dimensional accuracy and surface integrity, which are essential in functional or load-bearing components. Lastly, maximizing heat transfer through the supports enhances thermal management during printing, improving layer adhesion and reducing residual stresses. These objectives were derived from a combination of literature review, preliminary experimental observations, and thermo-mechanical simulation results presented earlier in the study. Together, they form a multi-objective optimization strategy that aligns with both the practical requirements of industrial SLM and the scientific understanding of process-induced defects.

While the comparison between numerical and experimental results showed strong correlation in terms of displacement, thermal stress, and temperature distribution, it is important to acknowledge several limitations of the FEA model. First, the simulations were conducted under simplified thermal boundary conditions, excluding the effects of surrounding powder, gas convection, and the dynamic movement of the laser during scanning. These assumptions were necessary to isolate the performance of the support structures but inevitably introduce discrepancies from real-world conditions. Additionally, material properties such as thermal conductivity and elastic modulus were assumed constant, whereas in reality they vary with temperature. Titanium Grade 4 was used in the COMSOL model instead of the experimentally used Ti6Al4V Grade 5 due to software limitations in material availability, which may slightly affect the accuracy of thermal and mechanical responses. Furthermore, the fixed heat source model, while useful for comparing support geometries, does not capture the transient, layer-by-layer energy deposition inherent to the SLM process. These simplifications may result in deviations in absolute values, though the observed trends remain valid and informative for comparative analysis. Future work could incorporate more realistic process conditions, including scanning strategies and evolving material behaviour, to improve the predictive accuracy of such models.

4.5 Numerical Simulations for Line, Contour, and Cone Supports

4.5.1 Methodology and Simulations

With the numerical results for block supports validated against the experimental data, additional simulations, utilising the same boundary conditions and simulation setup, were conducted for line, contour, and cone support structures (DOE setups and ANOVA results are available in Appendix B). These types of supports are commonly used in PBF-LB systems, as noted in the literature, and the same methodology was applied for these simulations. Line and contour supports share a geometric similarity with block supports, as they both feature (i) a support main body that determines the support's shape and density and (ii) a tooth area characterized by the contact points between the supports and the overhanging surface of the part. In contrast, cone-type supports are composed of individual thin pillars with adjustable lower and upper diameters. The morphology of block, line, contour, and cone supports is illustrated in Figure 64.

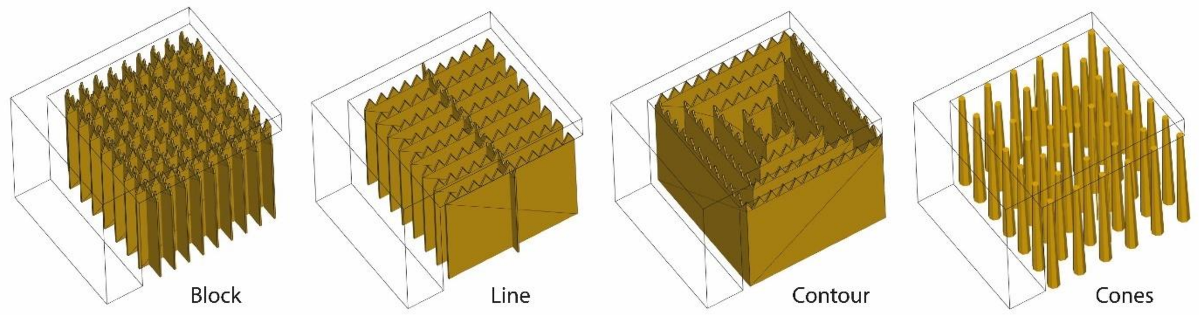

Figure 64. Morphology of block, line, contour, and cone support structures.

To conduct DOE for line, contour, and cone supports a similar approach to block-type supports was employed. Three primary geometric parameters were selected for investigation: For line-type supports, these parameters include tooth height, tooth top length, and cross line interval (depicted in Figure 65a, 65b). Contour-type supports also focus on tooth height, tooth top length, and contour offset (as shown in Figure 65a, 65c). Cone-type supports vary with contact platform diameter, contact part diameter, and cone spacing (illustrated in Figure 66). Across these support types, the areas under examination share similarities, defined by the overall density of the supports and the points of contact between the part and the supports. For block, line, and contour supports, the same input parameters were utilized, while a proportional approach was adopted for cone supports to determine the spacing between the cones and the contact points. Table *9* outlines these parameters for each support type, detailing their respective levels. Like block-type supports, each parameter was characterized by three levels: minimum, average, and maximum values. Three DOE setups, one for each support type, similar to Figure 56, were also performed in Design-Expert 13.

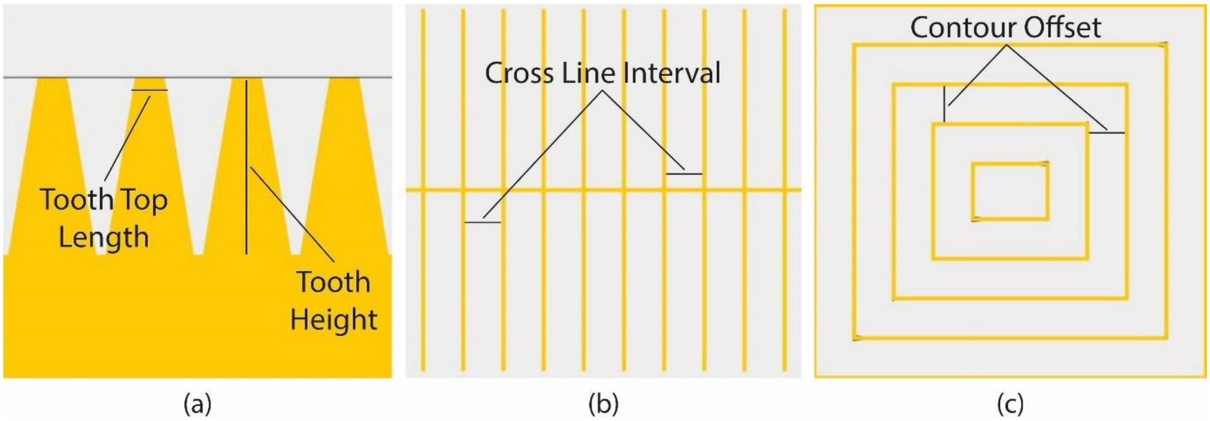

Figure 65. (a) Tooth area, (b) Cross line interval for line type, (c) Contour offset for contour type.

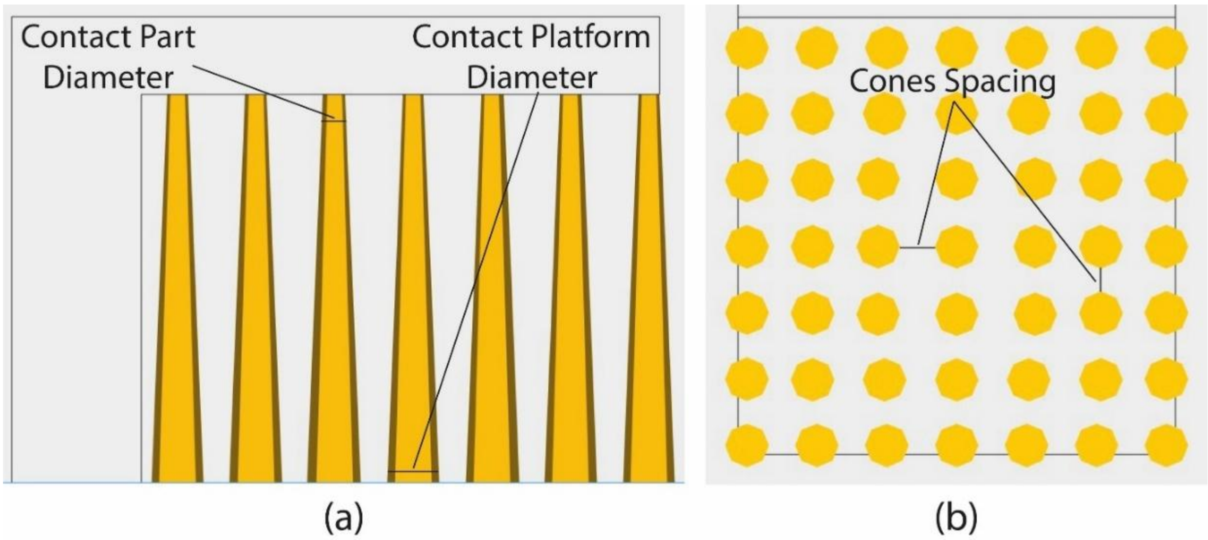

Figure 66. (a) Cone-type supports morphology, side view, (b) cone spacing, top view.

Table 9. Selected line, contour, and cone-type support parameters and levels.

Support Type	Parameter	Level 1	Level 2	Level 3
Line	Tooth Height	1 mm	2.5 mm	4 mm
	Tooth Top Length	0.1 mm	0.3 mm	0.5 mm
	Cross Line Interval	0.5 mm	1.25 mm	2 mm
Contour	Tooth Height	1 mm	2.5 mm	4 mm
	Tooth Top Length	0.1 mm	0.3 mm	0.5 mm
	Contour Offset	0.5 mm	1.25 mm	2 mm
Cones	Contact Platform Diameter (or Lower Diameter)	1 mm	1.5 mm	2 mm
	Contact Part Diameter (or Upper Diameter)	0.2 mm	0.3 mm	0.4 mm
	Cone Spacing	0.5 mm	1.25 mm	2 mm

Similar to the block-type supports, RSM using CCD was employed in Design-Expert 13 to conduct the experiments and define the alternatives. For the CCD setup, a face-centered approach with an alpha value of 1 was utilized, with no replicates of factorial, axial, and center points. As a result, 15 unique configurations for each support type (comprising 8 factorial, 6 axial, and 1 center point) were selected for investigation. In total, 45 simulations were performed (15 for each type of support).

The selected support types and their configurations can be generated using widely available slicer software, such as Materialise Magics. However, for this study, all support alternatives were custom-designed in SOLIDWORKS to ensure a parametric approach and reduce the risk of structural issues during simulations in COMSOL, which can be caused by damaged STL files. Furthermore, in addition to the specific parameters investigated, each support type has numerous other parameters that significantly influence their geometry and ease of removal. These parameters were standardized based on values derived from existing literature and relevant experimental research. For instance, line and contour supports, similar to block supports previously studied, were designed with a 0.2 mm wall thickness, 0.1 mm tooth base interval, and 1 mm tooth base length, while no perforations, fragmentation, or separation width was applied.

Based on the approach followed with the block-type supports, similar simulation configurations were also utilised to conduct thermo-mechanical analyses for line, contour, and cone support structures. The L-shaped specimen, support domain 2, and build plate area (refer to Figure 53) remained unchanged, while in domain 1, different support options were used during the design of experiments setup and individually subjected to thermo-mechanical analysis. Figure 67 illustrates examples of the designed line (Figure 67a), contour (Figure 67b), and cone (Figure 67c) support structures along with some of their input parameters including tooth height (TH), tooth top length (TTL), cross line interval (CLI), contour offset (CO), and cones spacing (CS).

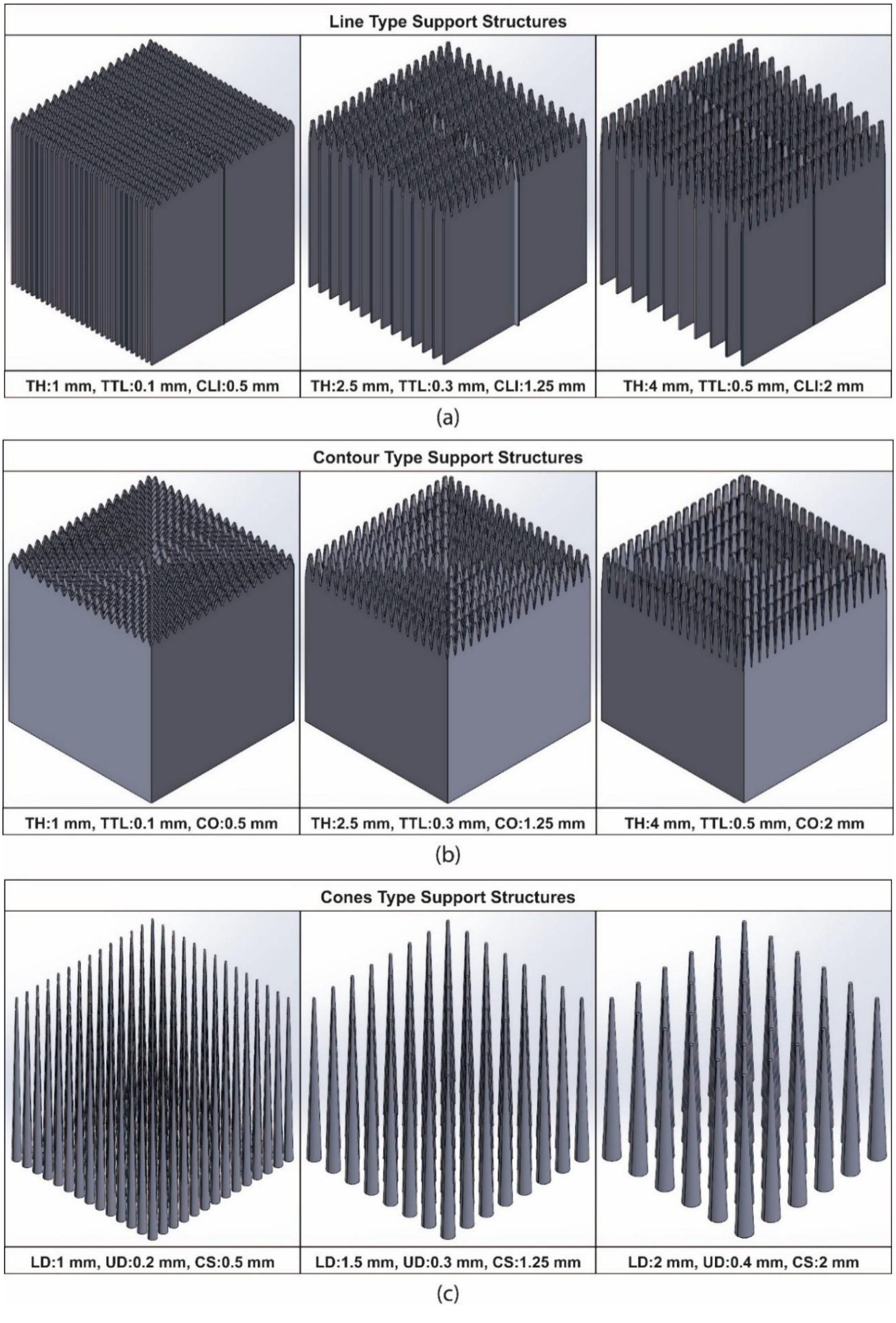

Figure 67. Sample of (a) line, (b) contour, and (c) cone support alternatives in SOLIDWORKS.

4.5.2 Results and Discussion for Line Supports

Initially, the ANOVA results of line-type support structures were analysed. Figure 68 illustrates the impact of tooth height, tooth top length, and cross line interval on the support volume. Similar to block-type supports, the tooth height and tooth top length had minimal influence on the support volume. In contrast, the cross line interval had a significant effect, as increasing the cross line interval substantially decreased the support volume. Figure 69 and Figure 70 show the correlation of tooth height, tooth top length, and cross line interval with thermal stress and temperature applied to the build plate, respectively. The tooth height and tooth top length barely affected thermal stress, but increasing the cross line interval significantly reduced thermal stress. Tooth height and tooth top length had a minor impact on plate temperature; specifically, an increase in tooth height marginally decreased plate temperature, while an increase in tooth top length slightly raised it. The cross line interval highly influenced plate temperature, causing a significant decrease as the interval increased.

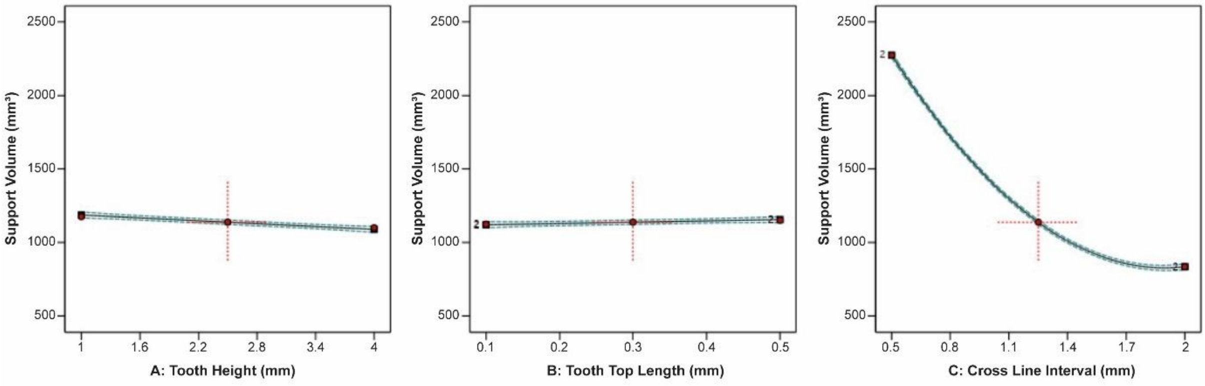

Figure 68. Main plots of support volume in Design-Expert 13 for line supports.

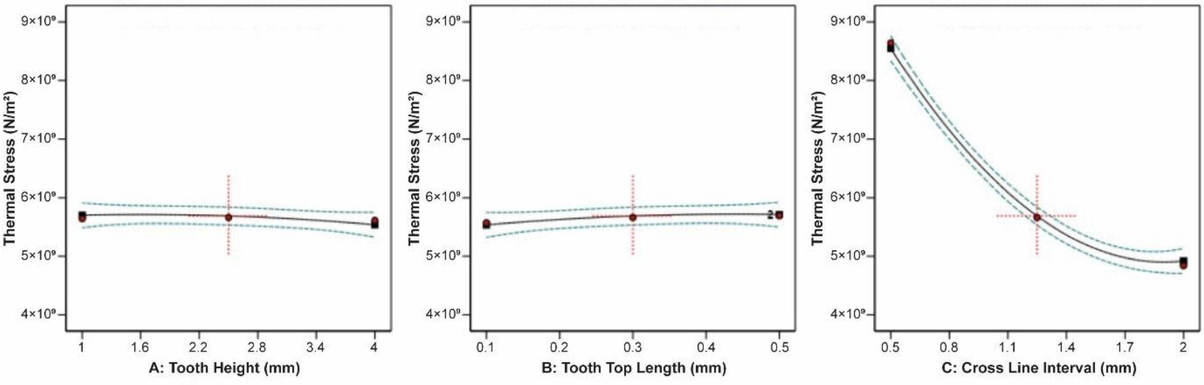

Figure 69. Main plots of thermal stress in Design-Expert 13 for line supports.

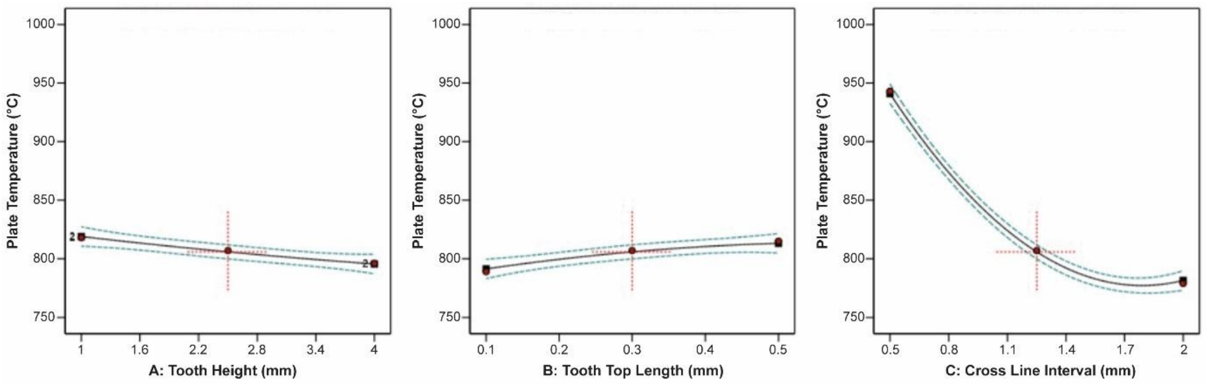

Figure 70. Main plots of plate temperature in Design-Expert 13 for line supports.

The influence of these parameters on thermal stress and plate temperature can be attributed to the thermal and mechanical behaviour of the support structures during the printing process. Tooth height and tooth top length are directly related to the contact area and mechanical rigidity of the supports. A taller tooth height increases the thermal path between the part and the build plate, slightly reducing heat conduction, which can lead to marginally lower plate temperatures but higher stress concentration at the tips of the supports. Conversely, a longer tooth top length increases the contact interface, promoting slightly better heat conduction, although it may also cause a minor increase in temperature due to larger localized heat accumulation. The cross line interval plays a more substantial role, as it determines the spacing and overall density of the support structure. A smaller interval results in denser supports, which facilitate more efficient heat transfer from the part to the build plate. This explains the strong inverse correlation observed between cross line interval and both thermal stress and plate temperature.

Similarly, Figure 71 illustrates the ANOVA results on overhang displacement in relation to tooth height, tooth top length, and cross line interval. An increase in tooth height corresponded with an increase in overhang displacement, whereas an increase in tooth top length resulted in a slight decrease. Notably, this support type showed unique behaviour since as the cross line interval increased from 0.5 mm to 1.1 mm, overhang displacement decreased, but from 1.4 mm to 2 mm, it increased. This phenomenon was likely due to the distinctive geometry of line-type support structures. Based on the above analysis and the numerical optimization results obtained from Design-Expert 13 following a desirability approach, Figure 72 presents the parameter set that optimally balances the four responses. These values, characterized by low tooth height, average tooth top length, and average cross line interval, represent a trade-off between thermal performance, dimensional accuracy, and structural stability, effectively lowering the risk of warping and residual stresses. In practical terms, implementing these parameters in SLM production helps ensure better heat dissipation, and reduced thermal distortion, especially in parts with moderate overhang angles.

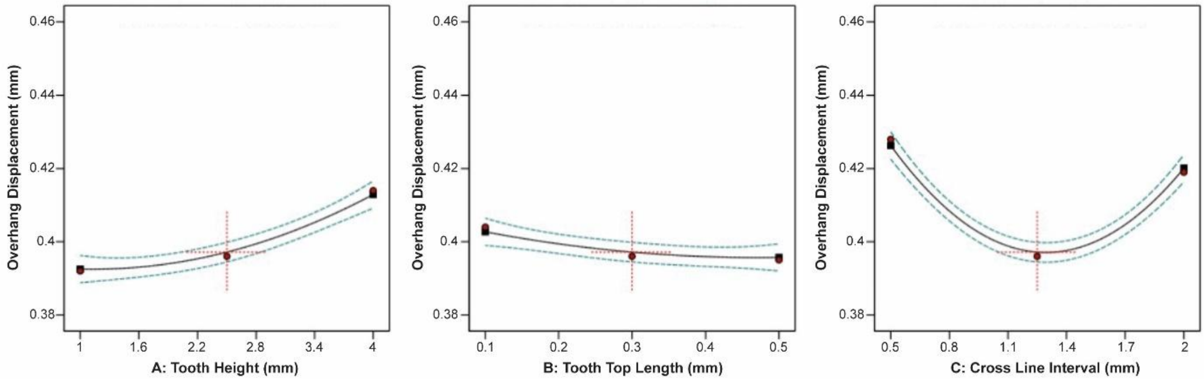

Figure 71. Main plots of overhang displacement in Design-Expert 13 for line supports.

Figure 72. Optimal parameters for line-type supports.

4.5.3 Results and Discussion for Contour Supports

Regarding the contour-type support structures, the ANOVA findings closely aligned with those of the block-type and line-type supports. As illustrated in Figure 73, tooth height and tooth top length did not significantly affect the support volume. In contrast, the contour offset had a substantial effect, with support volume decreasing significantly as the contour offset increased. Figure 74 and Figure 75 show the impact of tooth height, tooth top length, and contour offset on thermal stress and plate temperature, respectively. Tooth height and tooth top length did not significantly influence thermal stress or plate temperature. However, it was observed that increasing tooth height slightly decreased both thermal stress and plate temperature, while increasing tooth top length slightly increased them. Conversely, contour offset had a significant impact, since as the offset increased, both thermal stress and plate temperature greatly decreased. Figure 76 illustrates the effect of tooth height, tooth top length, and contour offset on overhang displacement. The plots revealed that all three input parameters substantially impacted overhang displacement. Specifically, increasing tooth height significantly increased overhang displacement, while increasing tooth top length and contour offset led to a decrease in overhang displacement. Similar to Figure 72, Figure 77 displays the values of tooth height, tooth top length, and contour offset that optimize the four responses, as determined by the ANOVA results and the numerical optimization performed in Design-Expert 13. These parameters are characterized by the lowest tooth height, and above-average tooth top length and contour offset.

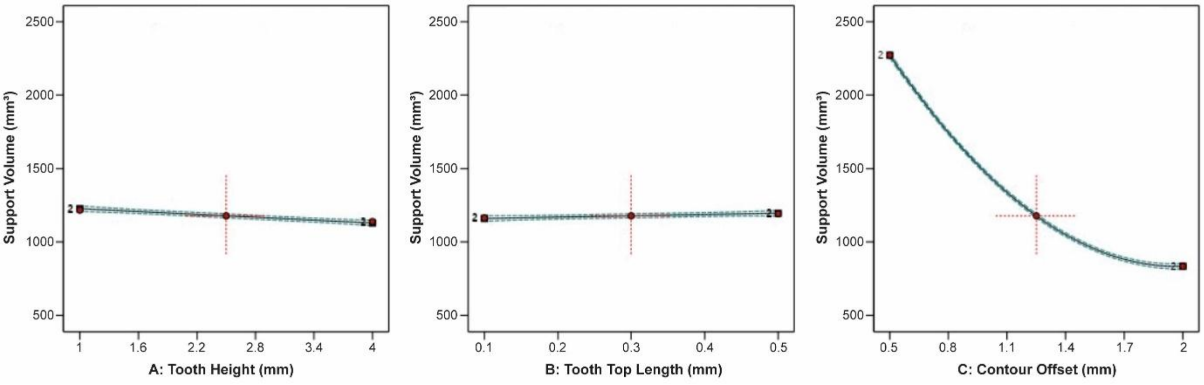

Figure 73. Main plots of support volume in Design-Expert 13 for contour supports.

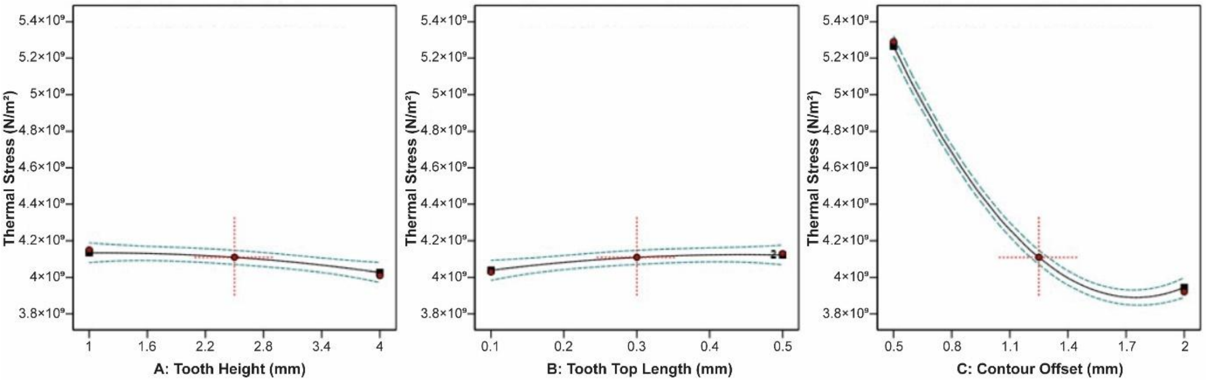

Figure 74. Main plots of thermal stress in Design-Expert 13 for contour supports.

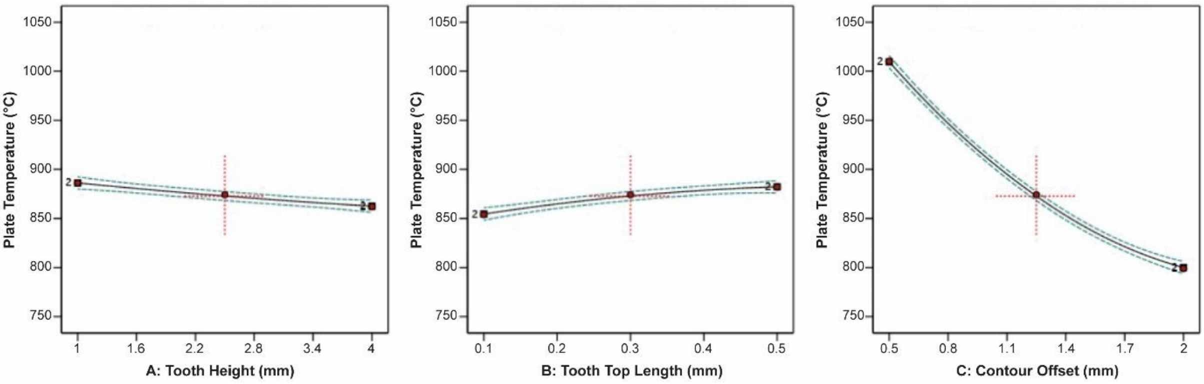

Figure 75. Main plots of plate temperature in Design-Expert 13 for contour supports.

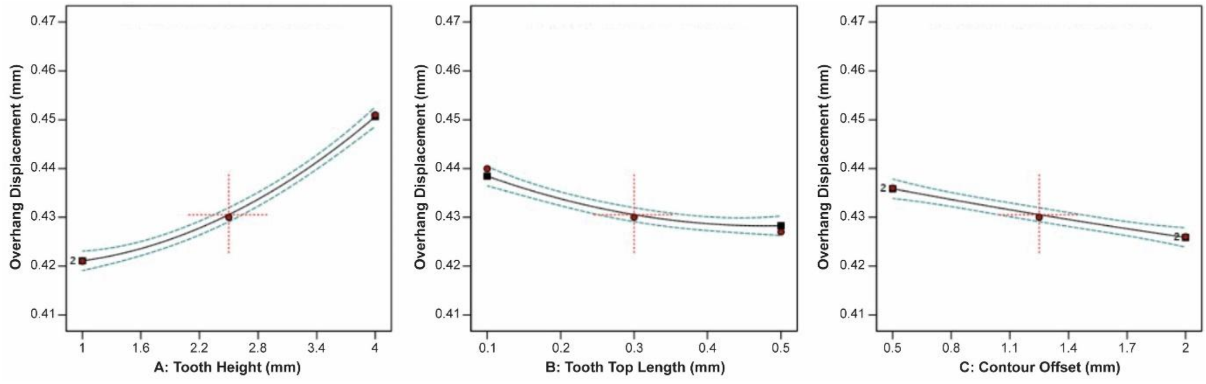

Figure 76. Main plots of overhang displacement in Design-Expert 13 for contour supports.

Figure 77. Optimal parameters for contour-type supports.

4.5.4 Results and Discussion for Cone Supports

The ANOVA results for cone-type support structures revealed significant differences compared to block, line, and contour supports. This distinction arises from their unique design, featuring individual pillars with adjustable lower and upper diameters. As a result, cone-type supports do not feature a defined tooth area with configurable parameters like other support types. Figure 78 depicts the impact of contact platform diameter, contact part diameter, and cone spacing on support volume. Increasing the contact platform and contact part diameters resulted in a corresponding increase in support volume. Conversely, increasing cone spacing led to a significant reduction in support volume. Figure 79 illustrates the correlation between contact platform diameter, contact part diameter, cone spacing, and thermal stress applied on the build plate. The plots indicated that none of these parameters had a significant impact on thermal stress. However, the data showed that the minimum thermal stress occurred at average values of contact platform diameter, contact part diameter, and cone spacing.

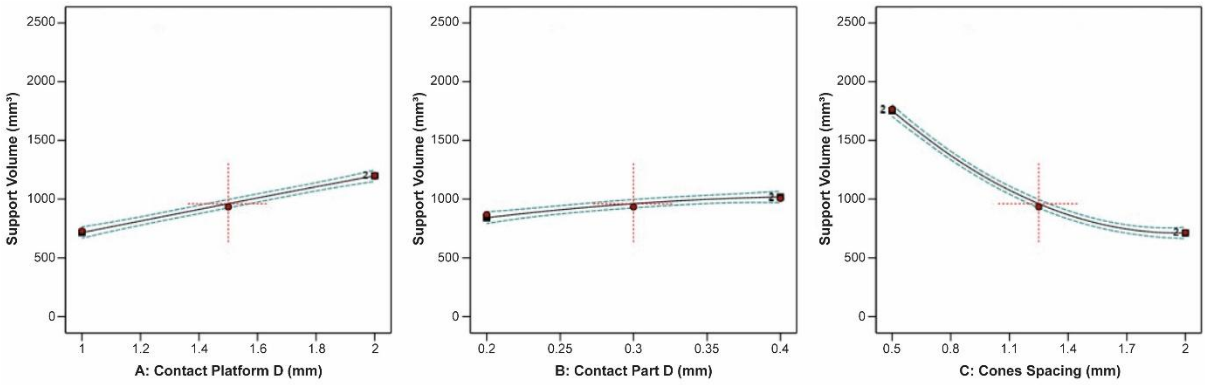

Figure 78. Main plots of support volume in Design-Expert 13 for cone supports.

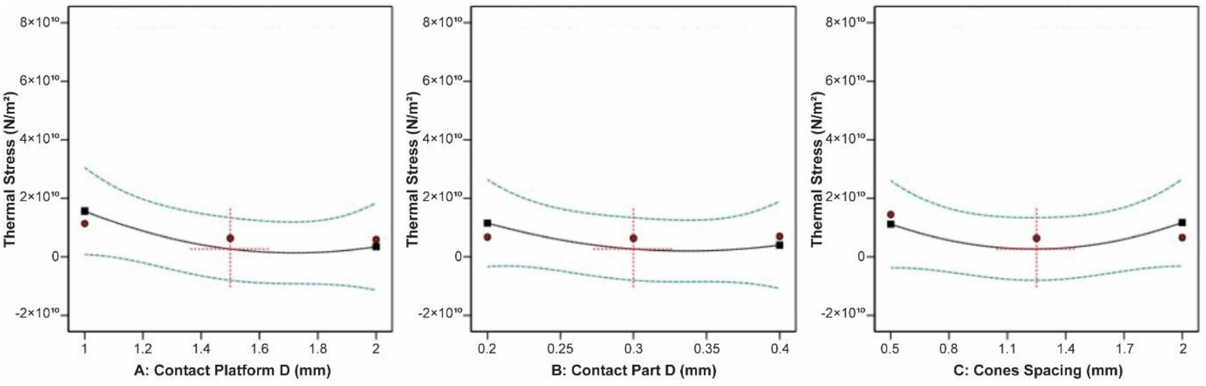

Figure 79. Main plots of thermal stress in Design-Expert 13 for cone supports.

On the contrary, plate temperature was significantly influenced by the contact part diameter and cone spacing, whereas the effect of the contact platform diameter on plate temperature was minimal. This relationship is clearly depicted in Figure 80. Increasing the contact part diameter corresponded to an increase in plate temperature, whereas increasing cone spacing led to a notable decrease in plate temperature. In terms of the overhang displacement of the specimen, it was notably affected by the contact platform diameter, contact part diameter, and cone spacing. As shown in Figure 81, increasing the contact platform diameter resulted in a decrease in overhang displacement, while increasing the contact part diameter led to an increase in displacement. Additionally, increasing cone spacing, which indicates fewer pillars, contributed to a decrease in overhang displacement. Similar to Figure 72, Figure 82 displays the values of contact platform diameter, contact part diameter, and cone spacing that optimize the responses, as determined by the ANOVA results and numerical optimization. These are characterized by a high contact platform diameter, the highest contact part diameter, and average cone spacing.

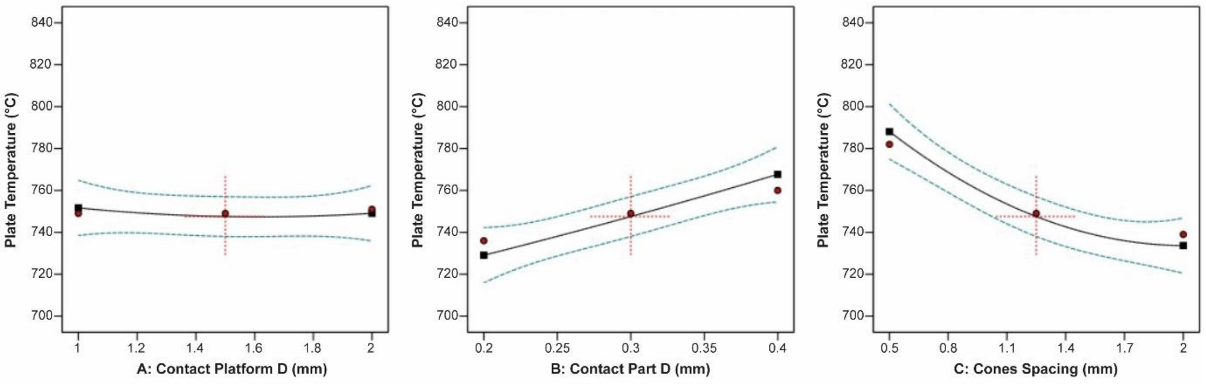

Figure 80. Main plots of plate temperature in Design-Expert 13 for cone supports.

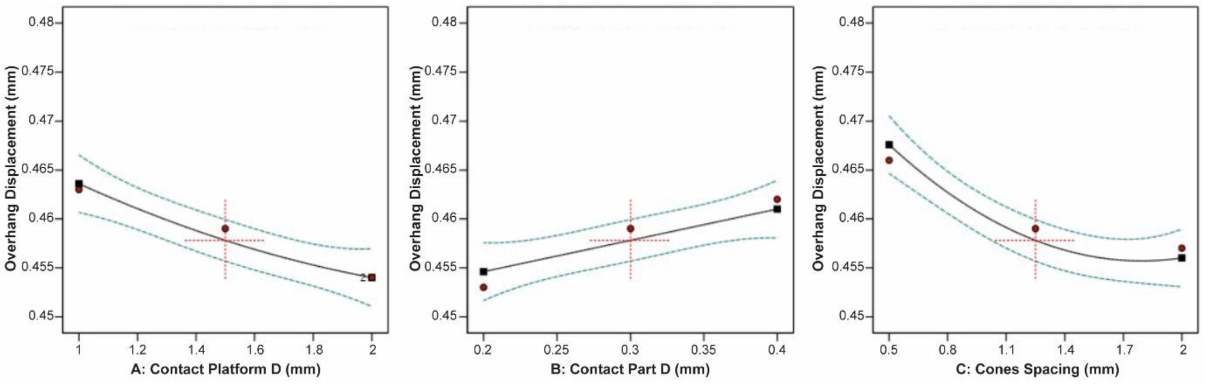

Figure 81. Main plots of overhang displacement in Design-Expert 13 for cone supports.

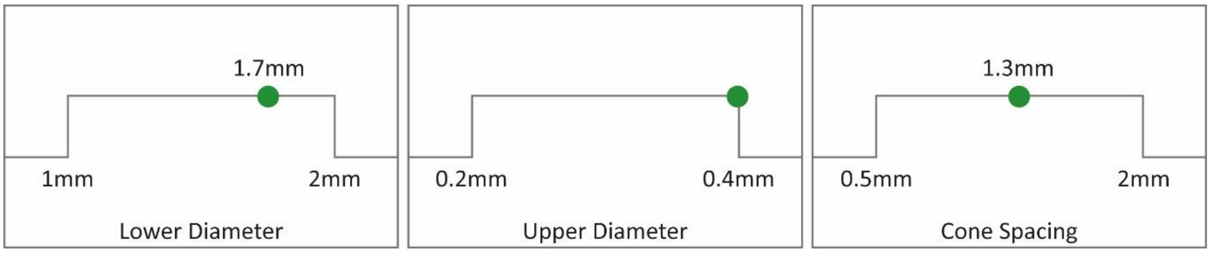

Figure 82. Optimal parameters for cone-type supports.

4.6 Summarized Results and Discussion

4.6.1 Numerical Optimisation for Block, Line, Contour, and Cone Supports

After analysing the ANOVA results and generating correlation plots between the input variables and output measures, numerical optimization was conducted for all four support types in Design-Expert 13. With some of the plots already presented in previous sections, the objective was to identify the optimal parameters for each support type, aiming to minimize support volume, thermal stress, and overhang displacement, while maximizing plate temperature. Prioritizing the reduction of support volume was crucial to lower material consumption, which in turn reduced printing time and overall costs. Minimizing thermal stress on the build plate was essential to prevent warping defects and ensure the supports remained securely attached. Additionally, minimizing overhang displacement was vital to maintain high print quality and avoid defects such as warping and curling. Conversely, maximizing the plate temperature was important because denser supports improve heat transfer and provide better control over residual stresses in the printed part. A desirability approach was employed for the numerical optimization. As described previously in Section 3.3.4, desirability measures how well the responses meet the specified criteria, ranging from 0 to 1. A score of 0 indicates that one or more responses are outside acceptable limits, while a score of 1 indicates that all goals are perfectly met. The four support types, block, line, contour, and cone, were analysed individually using the same goals and criteria constraints outlined in Table *10*.

Table 10. Goals and criteria constraints for block, line, contour, and cone supports.

Type	Name	Goal	Lower Limit	Upper Limit
Block	Tooth Height Tooth Top Length X, Y Hatching	in range in range in range	1 mm 0.1 mm 0.5 mm	4 mm 0.5 mm 2 mm
Line	Tooth Height Tooth Top Length Cross Line Interval	in range in range in range	1 mm 0.1 mm 0.5 mm	4 mm 0.5 mm 2 mm
Contour	Tooth Height Tooth Top Length Contour Offset	in range in range in range	1 mm 0.1 mm 0.5 mm	4 mm 0.5 mm 2 mm
Cones	Contact Platform Diameter Contact Part Diameter Cone Spacing	in range in range in range	1 mm 0.2 mm 0.5 mm	2 mm 0.4 mm 2 mm
All	Support Volume	minimise	417.4 mm^3	4643.3 mm^3
All	Thermal Stress	minimise	3.34×10^9 N/m^2	6.26×10^{10} N/m^2
All	Plate Temperature	maximise	724 °C	1030 °C
All	Overhang Displacement	minimise	0.392 mm	0.477 mm

The optimal solutions for each support type, determined by the highest desirability scores, are presented in Table *11*. For block supports, the optimal configuration included the lowest tooth height (1 mm), average tooth top length (0.295 mm), and average to high spacing (1.625 mm). Line supports featured the lowest tooth height (1 mm), average tooth top length (0.347 mm), and average spacing (1.242 mm). Contour supports also had the lowest tooth height (1 mm), average tooth top length (0.365 mm), and average spacing (1.402 mm). Conversely, cone supports were characterized by average to high lower diameter (1.7 mm), the highest upper diameter, and average spacing (1.27 mm). Figure 83 illustrates these optimal solutions for block, line, contour, and cone supports. Notably, cone supports achieved the minimum support volume (1091 mm²), block supports minimized thermal stress (3.83×10^9 N/m²) and maximized plate temperature (872.7 °C), while line supports had the minimum overhang displacement (0.393 mm). Although Table *11* and Figure 83 focus on thermal and mechanical performance, they do not explicitly include printing time or material usage—both critical factors in AM. However, support volume (as analysed below) serves as a useful indicator for both. Larger support volumes typically lead to increased material consumption and longer build times. For instance, while block-type supports offer better thermal performance, they are less efficient than cone or contour supports in terms of material usage.

Table 11. Optimal results of block, line, contour, and cone support structures.

Type	Tooth Height (mm)	Tooth Top Length (mm)	Spacing (mm)	Support Volume (mm^3)	Thermal Stress (N/m^2)	Plate Temperature (°C)	Overhang Displacement (mm)	Desirability
Block	1	0.295	1.625	1785	3.83×10^9	872.7	0.414	0.679
Line	1	0.347	1.242	1196	5.75×10^9	821.2	0.393	0.637
Contour	1	0.365	1.402	1094	4.02×10^9	867.7	0.420	0.695
Cones	1.7 (LD)	0.4 (UD)	1.270	1091	4.42×10^9	766.3	0.459	0.625

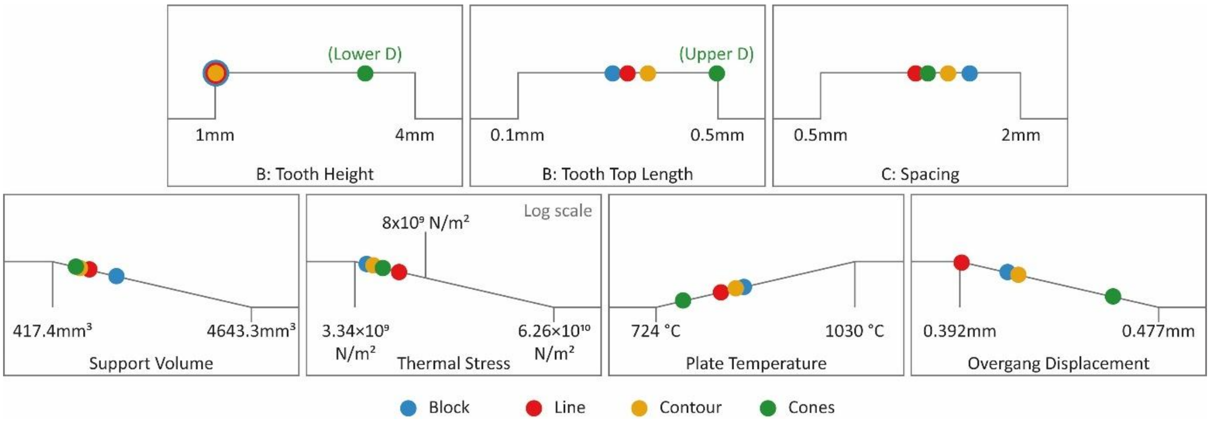

Figure 83. Summarised graphical representation of optimal solutions for block, line, contour, and cone support structures.

Based on the numerical results, parameters related to the contact area between the part and supports (tooth height and tooth top length), as well as those defining the geometry and density of the supports (x, y hatching or spacing), were crucial in producing non-defective parts while minimizing both printing time and overall costs. For example, block-type supports achieved optimal performance with the lowest tooth height, average tooth top length, and above-average hatching, which reduced material usage while maintaining adequate heat conduction. In contrast, line, contour, and cone supports performed best with average hatching values, offering a balanced trade-off between thermal dissipation and structural efficiency. In practice, these parameter combinations allow engineers to design support structures that are easier to remove, reduce build time and material waste, and minimize thermal distortion during printing, factors that are essential for reliable, cost-effective production in metal additive manufacturing environments. Further analyses of the four main responses (support volume, thermal stress, plate temperature, and overhang displacement), revealed key trends and performance differences among the support types, as discussed in the following sections.

It should also be noted that the optimal parameter settings identified for each support type in this study (block, line, contour, and cone) were based on a specific specimen geometry (e.g., a thin ledge with a 0° overhang) and a fixed material (e.g., Ti6Al4V Grade 4). As such, these settings are inherently sensitive to variations in geometry and material properties. Changes in overhang angle, part geometry and size, or thermal settings could significantly affect heat dissipation, stress distribution, and the overall effectiveness of the support structures. To improve the robustness and generalizability of the recommended settings, future work should include a parametric sensitivity analysis across a broader range of geometries and materials. Additionally, incorporating adaptive or geometry-aware optimization algorithms could enable more flexible parameter tuning based on specific design and material inputs, thereby enhancing the applicability of the findings across different industrial scenarios.

4.6.2 Support Volume

Figure 84 illustrates the correlation between support volume and various alternatives for the four support types. Based on the ANOVA, alternatives 1–8 represent the factorial points, 9–14 are the axial points, and alternative 15 is the center point. The distinction in support density is evident, with block-type supports being significantly denser than line, contour, and cone supports, which showed similar density values. Additionally, the block, line, and contour support plots demonstrated proportionality due to their closely aligned morphologies. In contrast, the plot for cone-type supports showed a slight deviation, attributed to their unique structure. Unlike the other types, cone supports consist of independent pillars with adjustable lengths and lower/upper diameters, rather than walls, specific grid patterns, or tooth areas.

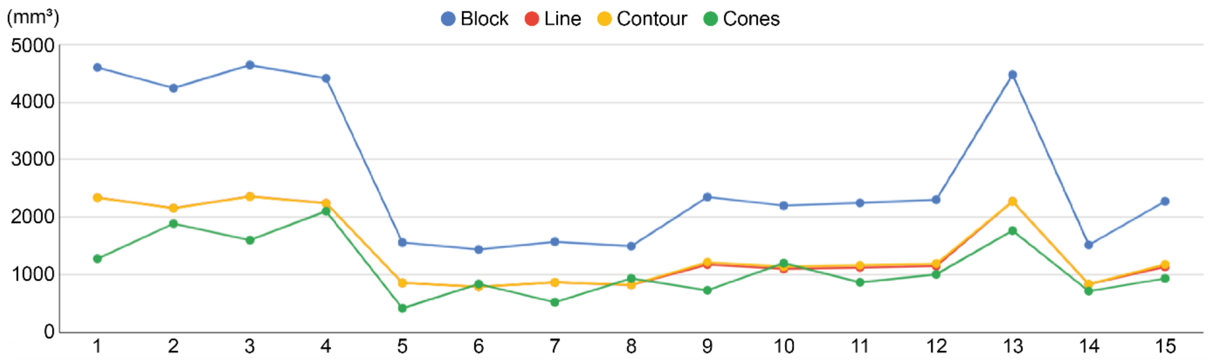

Figure 84. Support volume (y-axis, mm^3) and support alternatives (x-axis) plots.

4.6.3 Thermal Stress

Similar to support volume, Figure 85 displays the plots of the four support types, illustrating the correlation between thermal stresses on the build plate and the various support alternatives. Cone supports exhibited the highest thermal stress on the build plate, followed by line-type supports, which also showed relatively high thermal stress values. In contrast, block and contour support structures demonstrated the lowest levels of thermal stress. FEA revealed that, besides the stresses developed near the supports, significant stress was observed at the tops of the supports, particularly where they contacted the printed part. The highest stresses were found on supports with high tooth height and low tooth top length (Figure 86a), as well as on cone-type supports with the smallest upper and lower diameters (Figure 86b). These long and thin features were less able to withstand high laser temperatures, potentially causing collapse and adversely affecting the final part's quality. This conclusion is supported by the optimization results presented in Figure 83, which did not recommend such values for generating optimal support structures.

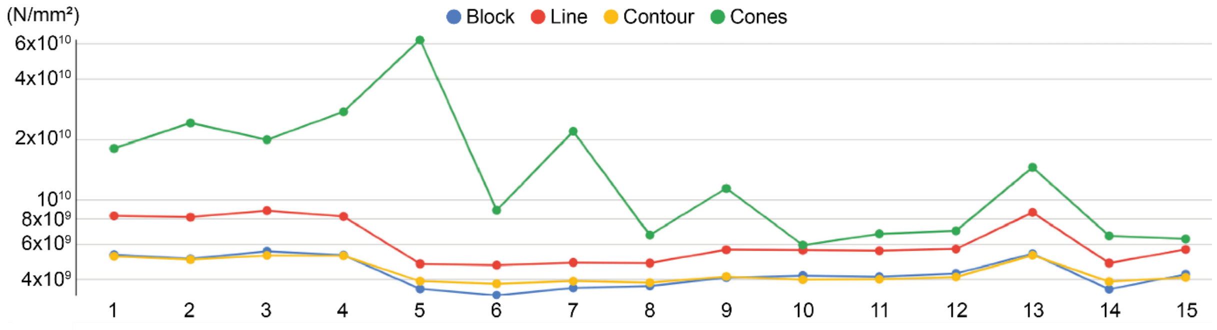

Figure 85. Thermal stress (y-axis, N/mm^2) and support alternatives (x-axis) log-scale plots.

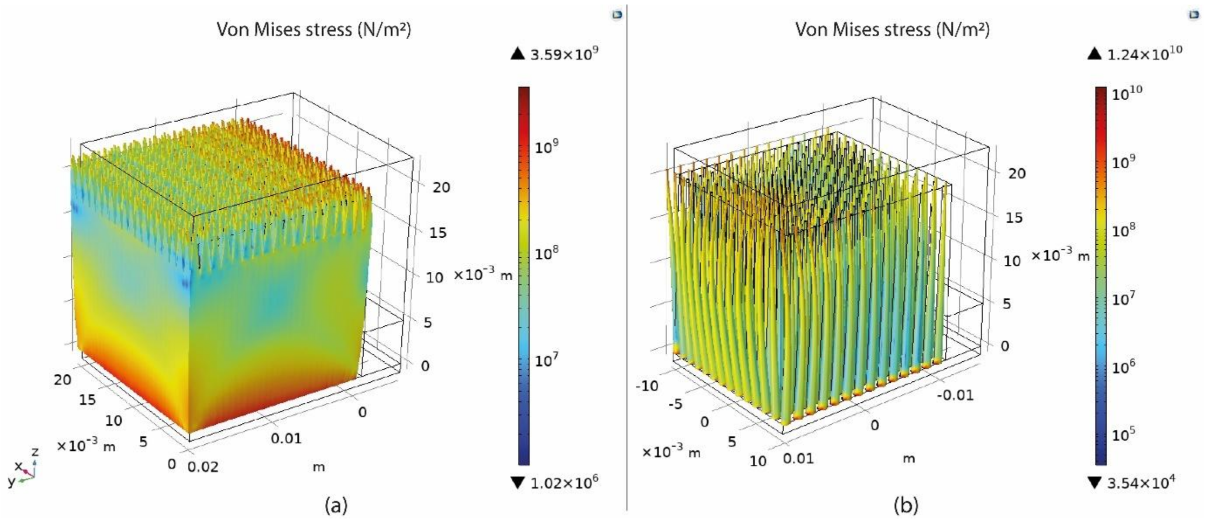

Figure 86. Thermal stress applied (a) on tooth area, (b) on thin cone supports.

4.6.4 Plate Temperature

Figure 87 presents four plots showing the measured temperatures of the build plate for each support alternative. The temperature range spanned from 724°C to 1030°C, with the highest values observed in block-type supports and the lowest in cone-type supports. The relationship between heat transfer and thermal stress is evident, as both factors significantly influence the part's performance during printing in PBF-LB at elevated temperatures. This study investigated the build plate temperature to evaluate the effectiveness of supports in terms of optimal heat conduction. According to simulations, higher build plate temperatures resulted in supports that facilitated better heat transmission. This effect was particularly noticeable in high-density support structures, as indicated by the optimization findings. However, it is crucial to note that such high-density supports also experience increased levels of thermal stress. Figure 88 provides a clear example of the temperature distribution among supports, where it is evident that high-density supports (Figure 88a) achieved better temperature distribution compared to low-density supports (Figure 88b).

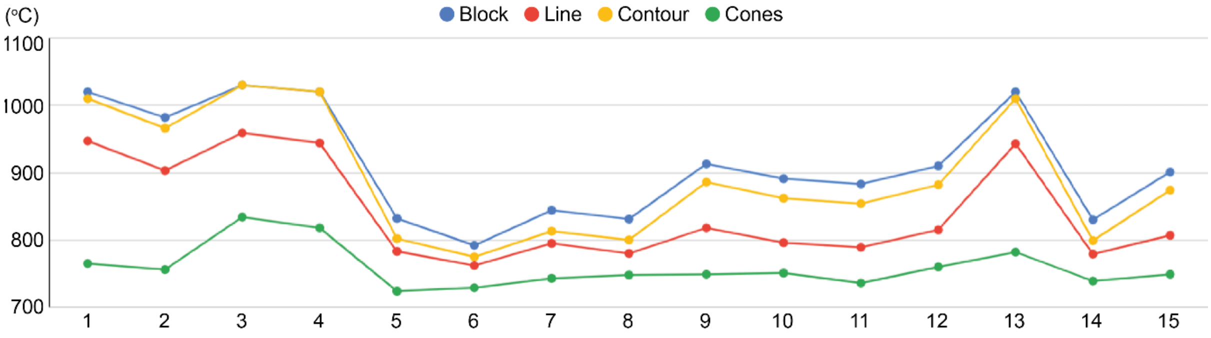

Figure 87. Plate temperature (y-axis, °C) and support alternatives (x-axis) plots

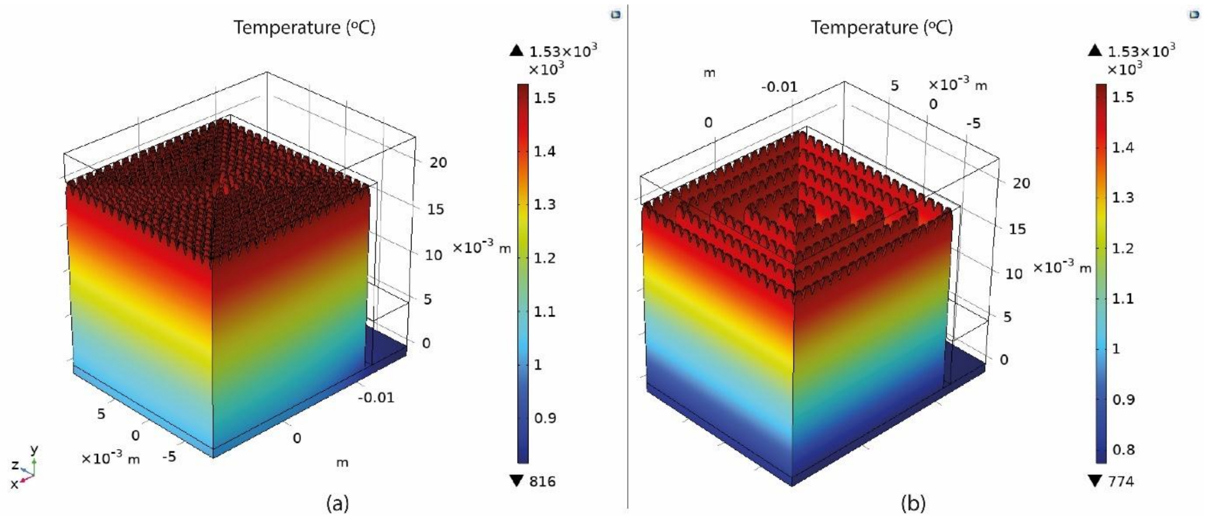

Figure 88. Temperature distribution (a) of high-dense supports, (b) of low-dense supports.

4.6.5 Overhang Displacement

Figure 89 displays the displacement plots of the part's overhang surface for each support alternative. This study measured the tendency of the part to distort under high temperatures developed in PBF-LB systems. The results indicated that overhangs supported by cone-type support structures were more susceptible to warping, whereas block, line, and contour support types had a comparable impact on the overhang displacement of the part. As shown in the graph, displacement ranged from 0.39 mm to 0.48 mm, with the smallest values observed in line-type support structures. During the thermo-mechanical simulations, another significant observation was made regarding the deformation of supports under high temperatures and thermal stresses in this area. Figure 90 demonstrates that higher values of tooth height (e.g., 4 mm) and lower values of lower/upper diameter (e.g., 1 mm/0.2 mm) resulted in supports that were more prone to distortion. It is important to note that significant distortion in the main body of the supports and at the contact area between the overhang surface and the supports can potentially lead to warping or, in severe cases, print failure. The most pronounced tooth deformation was observed in line supports (Figure 90a), while the thinnest cones exhibited the highest deformation (Figure 90b).

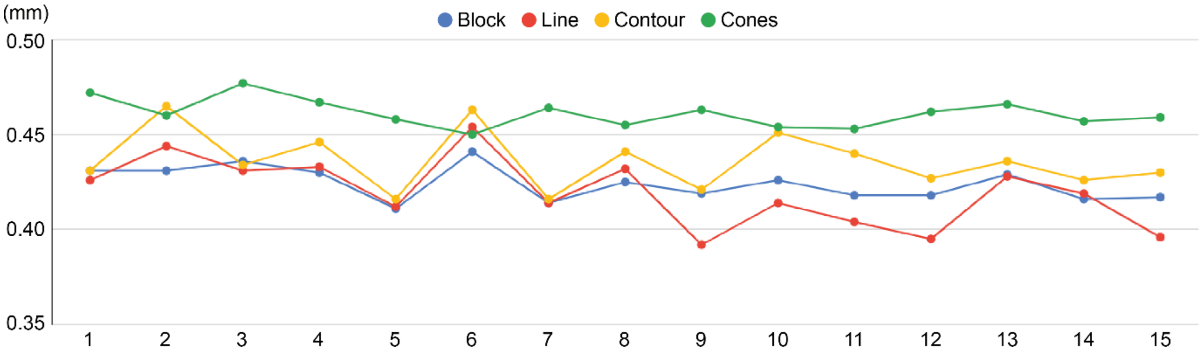

Figure 89. Overhang displacement (y-axis, mm) and support alternatives (x-axis) plots.

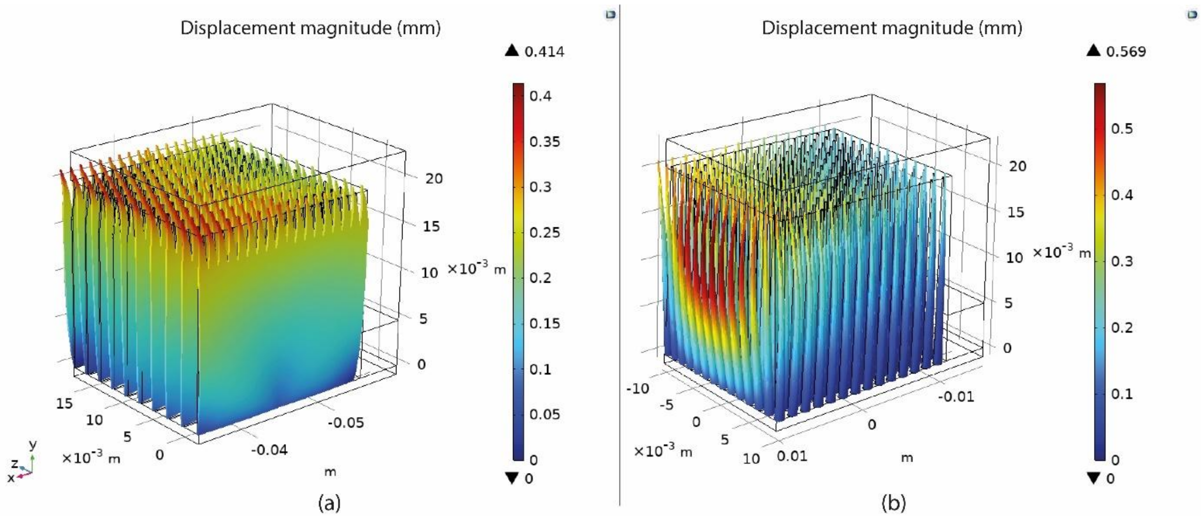

(a)

(b)

Figure 90. Distortion (a) of long teeth, (b) of thin cone structures.

4.7 Experiments with Ti6Al4V to Generalise Results

In addition to the geometric parameters of the various support types investigated in this chapter, several other factors significantly influence the distortion of an overhang surface and the support performance during the printing process. These factors, such as laser speed and laser power, are primarily associated with the heat source and affect both part distortion and the ease of support removal. As previously noted, to ensure consistent thermo-mechanical simulations in this research, the heat source was maintained at a constant level in accordance with techniques analysed in the literature. Furthermore, support removability and the occurrence of printing defects were evaluated through experimentation.

To validate the findings of the simulations and assess the performance of various support types in metal 3D printed parts, experimental work was conducted using SLM technology and Ti6Al4V alloy. Specifically, based on the optimal solutions identified during the ANOVA results (refer to Table *11* and Figure 83), four specimens were designed and fabricated using the optimal parameters for tooth height, tooth top length, and x, y hatching (or spacing) for each support type. To ensure the supports could be printed successfully and remain intact after detachment from the build plate, and to align with the simulation approach where the assembly included the heat source, support domain, and build plate, a "Π-shaped" specimen was designed. The support structure domain that connects the part to the build plate was not included in this study. Thus, the investigation area was based exclusively on the support domain and its connection with the specimen. Figure 91 illustrates this specimen, along with its dimensions (in milometers) and the print orientation. Furthermore, the optimal supports used for each support type are depicted in Figure 92 as generated in Materialise Magics Software. Due to the geometry of the specimen, the support structures were generated without direct attachment to the build plate but in contact with the part itself, where the tooth area was applied on both sides of the supports. Similarly, for cone-type supports, only the upper diameter was utilized to optimally connect the supports with the part, resulting in straight columns with a consistent diameter.

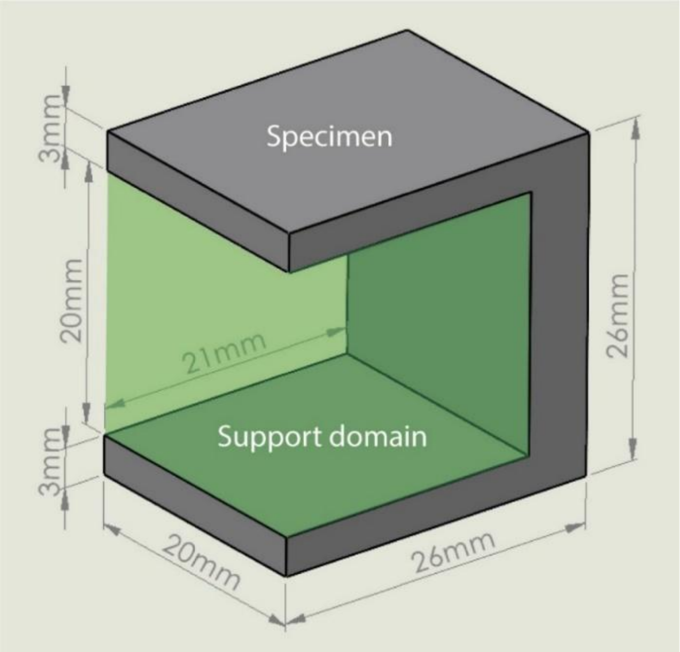

Figure 91. Specimen geometry and support domain.

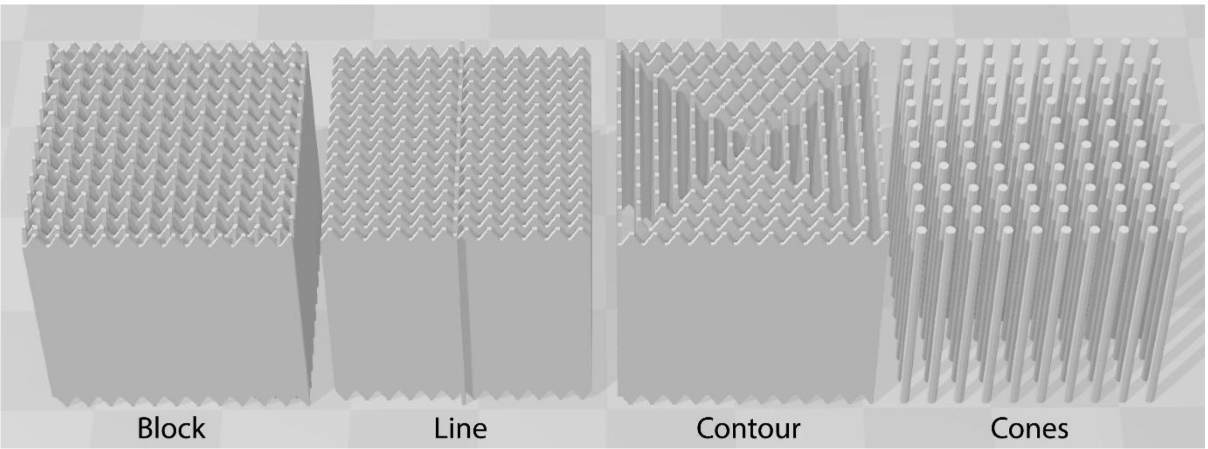

Figure 92. STL formats of the optimal supports used for block, line, contour, and cones.

Regarding the experiments, an EOS M290 printing machine was utilized, employing SLM technology with Ti64 Grade 23 titanium alloy as the material. EOS Titanium Ti64 Grade 23 is a variant of Ti6Al4V alloy with reduced levels of oxygen and iron compared to standard Ti64 alloy. This material is renowned for its outstanding mechanical properties, including low density, high strength, and excellent corrosion resistance. Similar to the titanium alloy used in Chapter 3, the powder had a generic particle size distribution of 20–80 µm and a chemical composition predominantly comprising Ti (balance), Al (5.50–6.5 wt%), V (3.50–4.50 wt%), Fe (0.25 wt%), and 0.3–0.4 wt% of other elements. Its mechanical and thermal properties are presented in Table *12* as referenced from MatWeb [146] and manufacturer datasheets.

Table 12. Material properties of EOS Titanium Ti64 Grade 23.

Property	**Value**
Density	4.42 g/cm³
Melting Point	1660-1670 °C
Young's Modulus (E)	110 GPa
Yield Strength	940 MPa
Ultimate Tensile Strength	1050 MPa
Elongation at Break	14-15%
Poisson's Ratio	0.34
Thermal Conductivity	6.7 W/(m·K) at 20°C
Specific Heat Capacity	0.56 J/g·K at 20°C

Figure 93 displays the printed outcome. The supports connecting the part to the build plate were removed immediately after printing, while those between the overhang surfaces remained intact, ensuring no significant printing failures occurred. The next step was to evaluate the performance measures. Specifically, three responses were assessed: support removability, measured by the effort required to remove the supports manually; surface roughness, determined by the roughness of both overhang surfaces; and part warping deformation, measured by comparing the distance between the overhang surfaces with that of the actual part. A digital calliper was used to measure this distance.

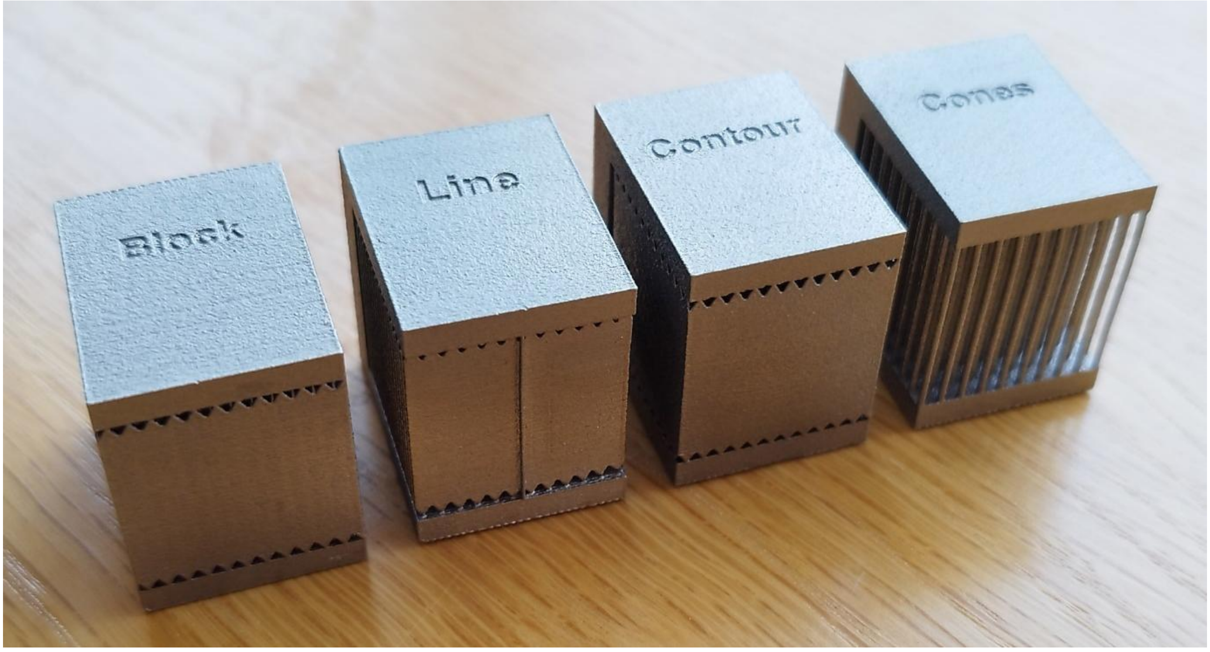

Figure 93. Printed outcome for block, line, contour, and cone support structures.

The removal process and tools used to detach the supports were consistent across all four specimens, employing simple, operator-accessible tools such as wire cutters, pliers, screwdrivers, and metal files. The manual removal of support structures using these tools was intentionally chosen to reflect real-world post-processing conditions in industrial AM environments. In practice, operators often remove supports by hand without the aid of sophisticated equipment, particularly for non-critical parts or during prototyping stages. Although qualitative, this method provides a realistic assessment of the removability effort and the potential risk of part damage. It also captures the variability and challenges encountered in typical workshop settings, where ease of detachment, surface residue, and operator safety are key considerations. Therefore, simulating this manual approach reinforces the relevance and applicability of the experimental validation to practical SLM scenarios.

Regarding support removability, cone supports were by far the easiest to remove. Minimal time (less than 1 minute) and effort were required to detach the thin columns, and the risk of damaging the part was negligible. Line supports were also relatively easy to remove (approximately 1–2 minutes), ranking second among the four types, though the risk of part damage was slightly higher. Both cone and line supports broke off into smaller pieces. Compared to cone and line supports, contour supports were more challenging to remove (approximately 3-4 minutes). Extra time and effort, along with the use of screwdrivers, were necessary to detach them. Ultimately, they were removed as a single support assembly, including the various contours. They ranked third in terms of removability, with an increased risk of damaging the part. Conversely, block-type supports were the most difficult to remove (approximately 4-5 minutes). Significant time and effort were needed, and the risk of part damage was high. They were ultimately removed as a single assembly. Figure 94 illustrates the technique used for hand removal, which involved applying torsional force with a screwdriver. Although no force gauge was employed to quantify the torsional effort, the manual removal process and the observed risk of part damage served as qualitative indicators aligned with practical AM post-processing standards. For improved scientific rigour and repeatability, future studies should incorporate quantitative measurements of torque or pull-off forces.

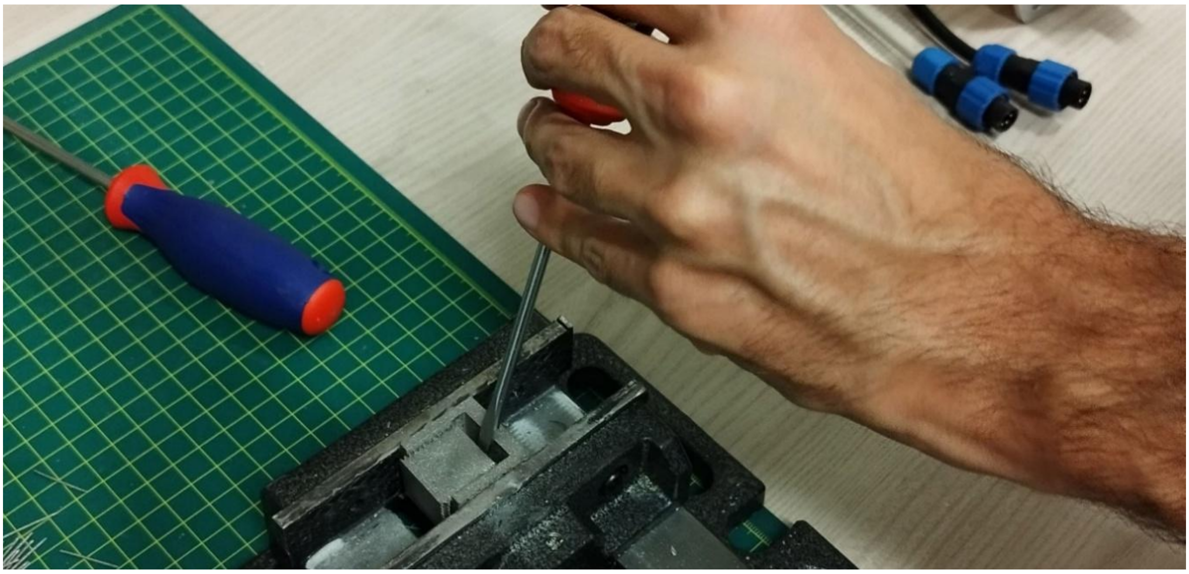

Figure 94. Hand removal process of support structures using basic tools.

After removing the support structures, the surface roughness was evaluated based on the contact areas between the specimens' overhang surfaces and the supports. The surface roughness of all specimens was found to be acceptable, however, further post-processing, such as sanding, was necessary for optimal results. As illustrated in Figure 95, block and line supports provided the best surface roughness compared to the other two types. Contour supports ranked third, while cone supports exhibited the roughest surfaces. This ranking is logical, considering that cone supports had the largest tooth top length or upper/lower diameter (0.4 mm), while block supports had the smallest (0.295 mm).

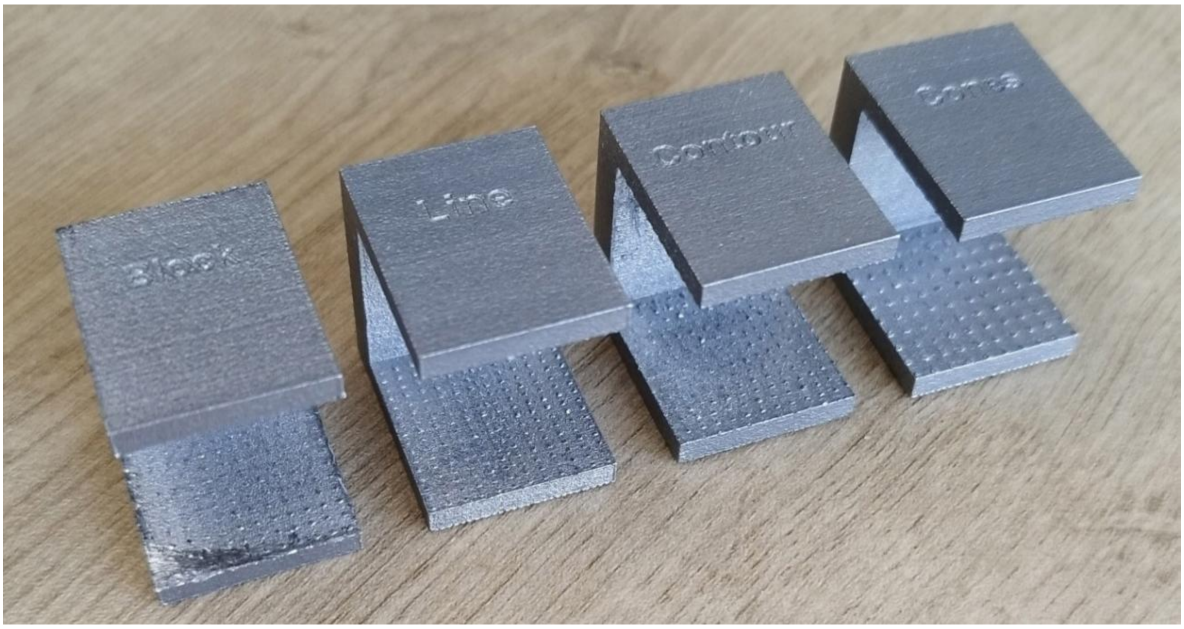

Figure 95. Surface roughness of block, line, contour, and cone support structures.

It should be noted that in this study, surface roughness was evaluated qualitatively through visual inspection of the printed specimens using optical images, allowing for a comparative assessment across the four support types. While this approach provided useful insights into relative differences—where block and line support structures appeared to yield smoother surfaces—it does not constitute a scientific measurement method. No surface profilometry or other quantitative instruments were used in this evaluation. Future research based on similar experiments should incorporate standardized surface roughness measurement techniques, such as contact or non-contact profilometers, to ensure accurate results.

Regarding warping deformation, the findings closely aligned with the thermo-mechanical simulation outcomes described in Section 4.6.1, where the overhang displacement of the specimens was recorded based on the optimal support parameters. Specifically, it was found that block-type supports exhibited a positive displacement of 0.36 mm at the external edge and 0.38 mm at the internal edge. Line-type supports had a positive displacement of 0.4 mm at the external edge and 0.04 mm at the internal edge. Contour-type supports showed a positive displacement of 0.32 mm at the external edge and 0 mm at the internal edge. Cone-type supports had a positive displacement of 0.4 mm at the external edge and a negative displacement of 0.05 mm at the internal edge. Overall, all cases exhibited positive deviations from the actual specimen, ranging from 0.15 mm to 0.4 mm, based on various measurements around the specimens. An indicative side view of the four specimens is depicted in Figure 96.

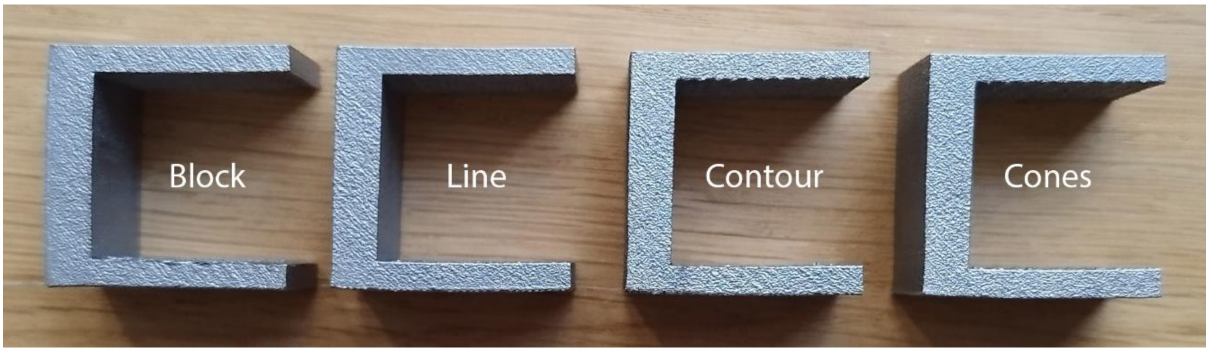

Figure 96. Side view of block, line, contour, and cone support structures.

In summary, the observed deviations from the actual specimen refer to the slight warping deformations measured on the printed parts, where dimensional offsets were greater than those predicted by simulations. This variation can be attributed to inherent characteristics of the SLM process and the respective printing machine, such as residual stresses induced by rapid thermal cycling, layer-by-layer heat accumulation, and potential anisotropy in material properties. Additionally, minor differences in part orientation, powder distribution, or recoating consistency may have contributed to these deviations. A more detailed experimental setup—including in-situ monitoring or thermographic analysis—could help quantify and isolate these process-induced effects in future studies.

4.8 Chapter Summary

The study presented in this chapter aimed to evaluate the performance of four common support structures used in metal AM and PBF-LB systems (block, line, contour, and cone) and design optimal support configurations that establish principles applicable across a wide range of cases. The research involved screening experiments using SLM technology, employing DOE and optimisation methodologies, and conducting thermo-mechanical simulations to analyse the thermal behaviour of 60 different support configurations applying a fixed thermal source. Additionally, 3D printings were conducted to evaluate and validate the simulation outcome. The goal was to identify optimal solutions for each support type, ensuring cost-efficiency, minimal material usage, high-quality printed parts, and easy support removal. The primary objectives were based on optimising the relief of residual stresses during printing, minimising specimen and support deformation, and reducing support volume. The key principles derived from the analysis and optimization are as follows:

- **Block Supports:** The optimal configuration featured the lowest tooth height (1 mm), average tooth top length (0.295 mm), and average to high x, y hatching (1.625 mm).
- **Line Supports:** The optimal setup had the lowest tooth height (1 mm), average tooth top length (0.347 mm), and average cross line interval (1.242 mm).
- **Contour Supports:** The optimal design included the lowest tooth height (1 mm), average tooth top length (0.365 mm), and average contour offset (1.402 mm).
- **Cone Supports:** The optimal parameters were characterised by average to high contact platform diameter (1.7 mm), the largest contact part diameter (0.4 mm), and average cone spacing (1.27 mm).
- **Support Volume:** Block-type supports had a significantly higher average support volume (approximately 45-50% more) compared to line, contour, and cone support structures with the same or similar input parameters.
- **Thermal Stresses:** High-density support structures exhibited greater thermal stresses on the build plate, with block and contour supports experiencing the lowest levels of thermal stress compared to line and cone supports with the same input parameters. Additionally, supports with larger tooth heights and thinner features, such as thin cone supports, were more susceptible to high thermal stresses.
- **Temperature Distribution:** High-density supports provided better temperature distribution compared to low-density support geometries, with block and contour types exhibiting the best heat transmission compared to line and cone supports with the same input parameters.
- **Warping and Distortion:** The part's overhang surface was less prone to warping when using block and line-type support structures, while contour and cone supports exhibited the greatest warping deformation on the part's overhang surface. Cone-type supports, particularly those with smaller diameters, as well as supports with higher tooth heights, were more prone to distortion.
- **Overall Support Performance:** Despite their larger volume, block-type supports demonstrated the best thermal behaviour according to the optimization criteria. They exhibited the lowest thermal stress compared to other types and optimal heat transfer, while the displacement of the part's overhang surface was considered adequate.

Towards the experimental outcome in which support removal effort, surface roughness, and part’s warping deformation were examined, each type of support exhibited unique advantages and limitations, necessitating careful selection based on the application and characteristics of the printed component:

- Block-type supports provided adequate surface roughness but were more challenging to remove and susceptible to warping deformation.
- Line-type supports offered a balanced compromise between ease of removal, surface roughness, and warping deformation.
- Contour-type supports were effective in preventing warping but posed challenges during removal.
- Cone-type supports were easier to remove but showed limitations in surface roughness.

Fragmented support structures, such as cones, lines, and contours, which can be disassembled into smaller pieces, were easier to remove, requiring less time and effort for removal. Additionally, research cited in the literature, along with the author's experimental findings, suggests that block-type support structures with similar wall fragmentations could facilitate easier and more controlled removal making them an ideal choice for printing in SLM and metal AM. This approach could potentially reduce removal time and improve thermal management during the printing process, making it a valuable consideration for future studies.

Overall, this research has highlighted the importance of parameters related to the contact area between the part and the support structures, particularly in terms of heat transfer, stress distribution, and ease of removal. To improve heat transfer and minimize thermal-induced distortions, the thermal simulation outcomes presented in Sections 4.4, 4.5, and 4.6 provide valuable insights into how variations in tooth height, tooth top length, and hatch spacing influence thermal conduction and stress accumulation. Conversely, strategies to facilitate support removal were experimentally assessed in Section 4.7 and earlier chapters, with findings indicating that reduced contact lengths and finer tooth structures enable easier detachment without compromising part stability or significantly increasing removal effort. For a balanced optimization of heat transfer, mechanical stability, and removability, the research framework must be considered holistically. The combination of experimental validation, multi-response optimization, and simulation-driven design presented throughout this chapter supports the development of well-informed strategies to tailor the contact interface for various application requirements.

Beyond the technical validation, the findings of this section carry several practical implications for professionals working with SLM. For instance, the comparative analysis of support types highlights that line and cone supports, despite their lower thermal performance compared to block supports, offer significantly easier post-processing and reduced material usage—factors critical in industrial workflows where efficiency and cost reduction are most important. A professional reviewing these results could prioritise these support types when printing parts with moderate overhangs or when ease of removal is essential, such as in aerospace or medical components. Conversely, block supports may still be preferred in applications requiring higher thermal stability or dimensional precision, particularly for large overhanging surfaces. Integrating these findings into the AM workflow enables better-informed decisions during build preparation, allowing users to balance print reliability, material consumption, and post-processing effort based on the part geometry and performance requirements. This supports a more strategic and application-driven use of support structures, ultimately reducing trial-and-error cycles and enhancing production rate.

Chapter 5: A Web-Based Platform for Automated Support Generation and Optimisation

5.1 Introduction

Generating and optimizing metal support structures for PBF-LB processes requires extensive expertise in AM and often involves a repetitive process heavily influenced by the user's experience with similar geometries. Additionally, most commercial software for this purpose lacks consideration for the thermal stresses generated by the thermal field in PBF, while the high cost of these software solutions makes them inaccessible to users who are engaged in more cost-effective solutions including universities, research institutions, and AM enthusiasts. Most published research on this topic focuses on optimizing support structures by examining geometric design and experimental results, typically neglecting the constraints of thermal stress and deformation. However, only a few studies have explored support optimization more comprehensively, addressing multiple factors simultaneously, including part orientation, geometric support parameters, and thermal stresses, as described in the literature. Additionally, generic algorithms and models have been extensively investigated for metal AM but are limited to generating only tree-like support structures.

This chapter introduces a design framework and an initial release of an interactive web-based platform for support generation and optimisation. This research tool is designed to assist companies and researchers in exploring and preparing SLM build jobs by integrating experimental data, with the aim of reducing both costs and the effort required to produce high-quality, defect-free parts with minimal in-house experimentation. The platform enables users to import 3D files, determine part orientation, and generate and visualize block-type support structures with diamond perforations using the open-source PySLM library [156]. Additionally, users can access optimisation suggestions for block, line, contour, and cone supports based on the outcomes presented in Chapter 4 and export the final build job in STL format directly for 3D printing or further processing. The platform targets both professionals and intermediate users involved in metal AM, offering intuitive functionality within a user-friendly interface. The first release (v0.6) is fully interactive and accessible online at no cost.

5.2 Proposed Design Framework

Before proceeding to the methodology and development of the online platform, an analytical design framework is discussed to better explain the philosophy and workflow of the steps required for effective support generation and optimisation in PBF-LB processes. As illustrated in the chart in Figure 97, a fundamental condition for exporting the build job is that the generated support structures meet the criteria for optimal support generation. These criteria include non-defective parts, minimised printing time and overall costs, reduced support material usage, elimination of thermal stress, and improved post-processing activities such as support removal. To optimize these outcomes, a sophisticated selection of input parameters is essential. Such input parameters, which are free variables that can be modified and controlled, include scan-related parameters, energy source-related parameters, material-related parameters, inner temperature-related parameters, as well as geometric support structure parameters and part geometry. To optimize these input parameters, data collection methods through experimentation, and numerical simulations utilising appropriate FEA software were employed. Consequently, if a build job meets the predefined optimisation criteria, it can be exported and proceed to the final print; otherwise, the input parameters should be revised. In the initial release of the support generation platform, the focus was primarily on modifying support structure parameters.

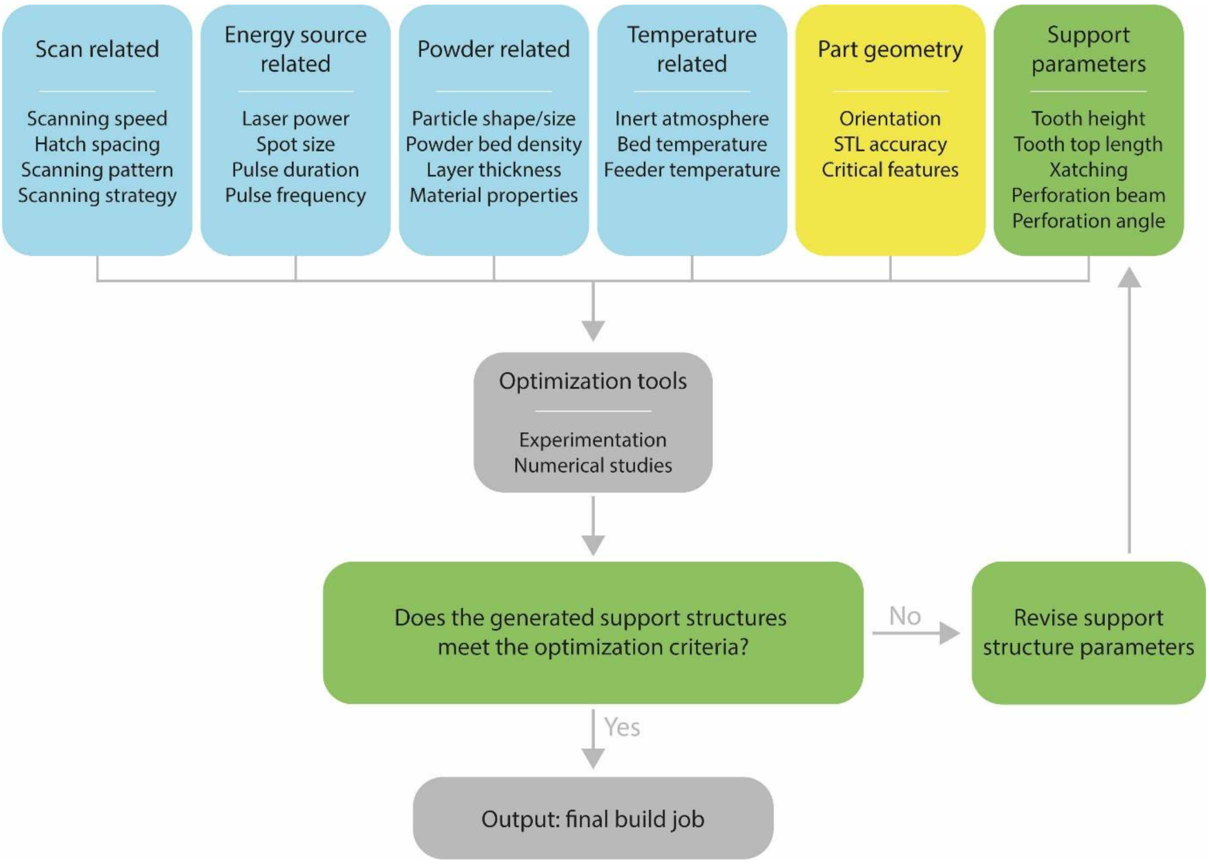

Figure 97. Chart illustrating the main approach for generating optimized support structures based on specific, predefined optimization criteria.

Figure 98 illustrates the proposed design framework, detailing the steps and features that characterize the support generation and optimisation platform. Most of these features have been fully developed in this study and are analytically presented in Section 5.3. However, some others, such as the support simulation module, require further development and are proposed for future work. Based on the design framework, actions are categorized into user-driven, platform-driven, and simulation-driven. User-driven actions primarily involve input parameters such as importing the STL part, selecting part orientation, and determining the support structure parameters. Platform-driven actions include reading STL files, analysing part geometry, defining support areas, and recommending part orientations, while the platform's main features include generating supports, proposing optimisation suggestions, visualizing simulation outcomes, and exporting the final build job. On the other hand, simulation-driven actions encompass all tasks required by the integrated simulation software, including setting up the scene, meshing the STL file, computing results, and exporting the data in the appropriate format. To implement the proposed design framework, it is essential to establish effective communication between the online platform and the simulation software server to manage the data required for analysis, optimization, and visualization.

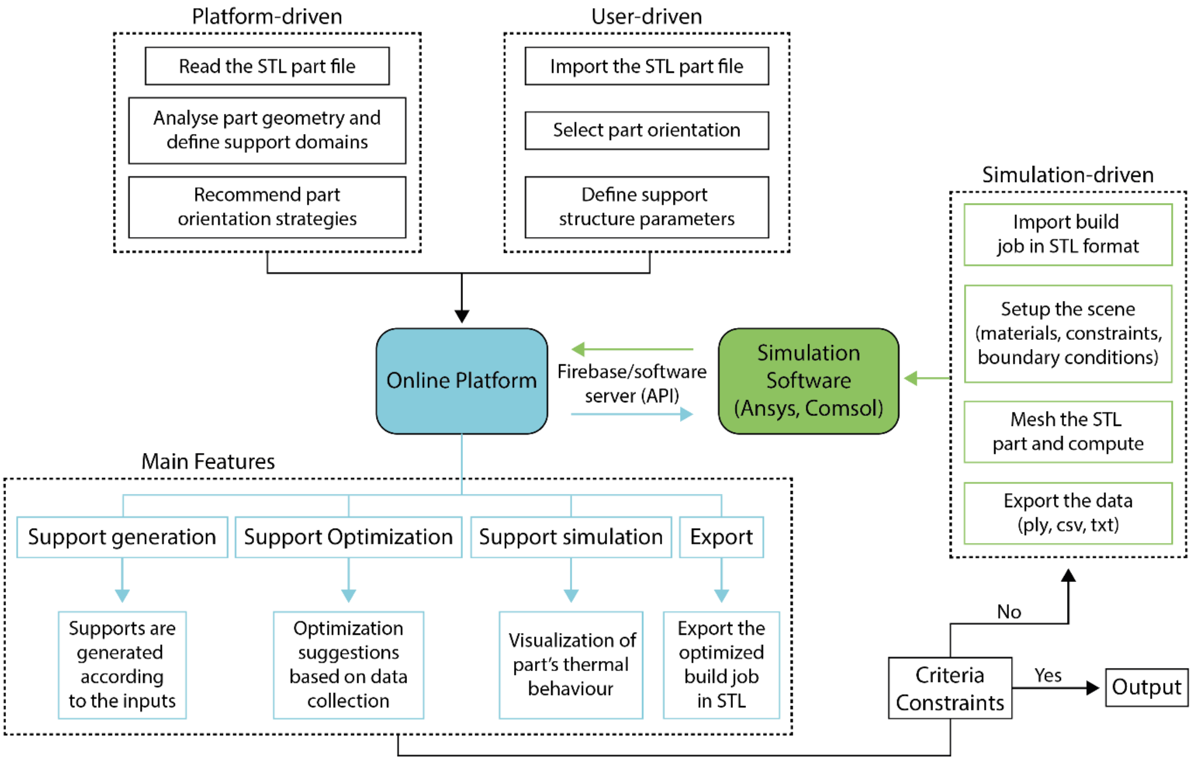

Figure 98. Proposed design framework detailing the platform's features.

5.3 Methodology and Features

5.3.1 Web Architecture

The web application utilizes the React.js [157] frontend framework, a JavaScript library for building user interfaces that excels in comparison to other frameworks and libraries for this purpose. A key advantage of React is its virtual Document Object Model (DOM), a virtual representation of the actual DOM tree. This virtual DOM renders quickly, which is essential for the application's high demand and the complexity of handling 3D objects on the web. React’s component-based architecture is a standout feature, promoting cleaner, more robust, and concise code throughout the application. Unlike conventional web applications, this platform requires web-based visualization of 3D models. Most web-based 3D applications typically rely on Three.js [158], an open-source JavaScript library that abstracts WebGL (Web Graphics Library) and provides a user-friendly Application Programming Interface (API) for creating and displaying animated 3D computer graphics. By integrating React and Three.js, the application demonstrates how these technologies can be combined to create a React application with 3D dynamics. React-three-fiber [159], a library that builds dynamic scene graphs declaratively with reusable components, simplifies the use of Three.js and aligns with React's component-oriented logic. These components dynamically respond to state changes and facilitate user interaction, enhancing the overall user experience.

The application's core functionality is consolidated within a web platform and a Python microservice—an independent, self-contained service written in Python [160] that performs a specific function within a larger distributed system. The web platform utilizes Firebase [161], a software development platform owned by Google. Concurrently, the Python microservice operates on a Google Virtual Machine (VM) server. During development, there was a necessity to integrate these two computing services—the backend Python microservice hosted on a Google Cloud VM and the frontend Firebase service. By unifying these components into a Google Cloud–Firebase project, users gain the flexibility to manage file uploads and downloads via Firebase Software Development Kits (SDKs) on the client side, alongside potential server-side processing using the Google Cloud Storage API [162]. Specifically, the web application communicates with the Python service through a Representational State Transfer Application Programming Interface (REST API) and shared cloud storage, as illustrated in Figure 99. Leveraging shared cloud storage eliminates the need for large binary file transfers via HyperText Transfer Protocol (HTTP) requests. Deploying both the Web Application and the Python Service within the same data-center region is expected to significantly enhance direct file Input/Output speeds compared to traditional HTTP-based file transfers. Integrating Firebase with the Google Cloud project not only streamlines file management but also simplifies the overall architecture, reducing costs and implementation time.

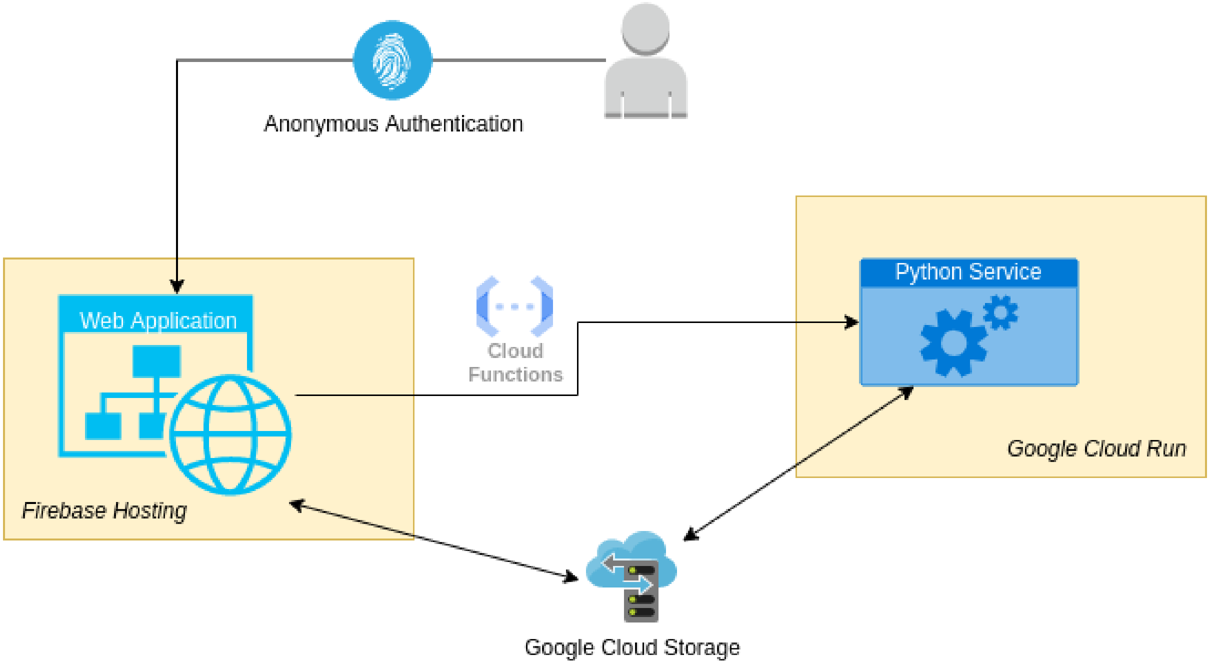

Figure 99. Web application and Python service connection scheme.

5.3.2 STL Import and Orientation

The platform can read various geometries in STL (stereolithography) format, which is widely employed in AM to represent the surface of CAD models using triangular meshes. Upon importing a part into the platform, overhang surfaces that require support structures are automatically highlighted in red. The part's orientations are automatically generated, offering users multiple options to choose from, allowing them to select the one that best meets the criteria for optimal printability. Additionally, the ‘surface angle’ feature allows users to set the minimum angle at which support structures can be generated. For scene manipulation, users can rotate the view with the right mouse button, zoom in and out with the mouse scroll wheel, and pan the view with the middle mouse button.

From a technical standpoint, various suggested orientations are generated for the imported part. Some orientations are created as ortho-canonical rotations based on the initial orientation, while others are determined by the part's geometric characteristics to minimize overhang surfaces. Orientation calculations and most geometric manipulations are performed using Trimesh [163], a Python library for 3D mesh manipulation.

5.3.3 Support Optimization Engine

The support optimization engine, accessible on the platform via the ‘book’ icon, is an interactive tool that offers optimization suggestions for commonly used support geometries in metal AM and PBF-LB systems, including block, line, contour, and cone support structures. These optimization results are based on the research presented in Chapter 4, which investigates the thermal behaviour of these support types to minimize support volume and residual stress while maintaining high print quality. Specifically, support density and tooth area were examined using various parameters, including x, y hatching, tooth height, and tooth top length, while design of experiments methodology was employed to create support alternatives. These alternatives and small ledge specimens were thermomechanically analysed to evaluate support performance and propose solutions that optimize support volume, thermal stress, support heat transmission, and part overhang displacement.

This optimization engine allows users to modify input support parameters for each support type separately through a user-friendly environment consisting of horizontal sliders, while simultaneously displaying the corresponding support optimization levels. Design-Expert 13 software was used to prepare the DOE and create alternatives for each support type. Based on the ANOVA results, mathematical models were employed within the same software to visualize the optimization outcomes using JavaScript [164], a scripting or programming language that allows the implementation of complex features on web pages such as animated 2D/3D graphics. An example of these models is illustrated by Equation 5.1, which demonstrates the volume of block-type support structures. The complete set of equations used to develop the support optimization engine is provided in Appendix C.

$$
\begin{aligned}
&Support\ Volume \\
&\quad = 6991.79410 - 137.65809 * Tooth\ Height + 137.90833 \\
&\quad * Tooth\ Top\ Length - 5247.51284 * X,Y\ Hatching + 71.08333 \\
&\quad * Tooth\ Height * Tooth\ Top\ Length + 43.15556 * Tooth\ Height \\
&\quad * X,Y\ Hatching - 117.00000 * Tooth\ Top\ Length * X,Y\ Hatching \\
&\quad - 0.004938 * Tooth\ Height^2 - 0.277778 * Tooth\ Top\ Length^2 \\
&\quad + 1281.04691 * X,Y\ Hatching^2
\end{aligned}
$$

Equation 5.1. Actual equation of block type support structures in Design-Expert 13

The accuracy and reliability of the ANOVA equations implemented within the web-based platform were validated through the performance plots and results discussed in detail in Chapter 4, which demonstrated strong agreement between the experimental data and model predictions. These plots, generated using Design-Expert 13 software, confirmed the robustness and predictive strength of the regression models within the defined parameter space. Design-Expert 13 itself is a well-established and credible tool for statistical modelling and multi-response optimization, widely used in engineering research. Additionally, to prevent overfitting or extrapolation errors, the platform was designed to operate strictly within the predefined parameter ranges established during the experimental design. No predictions or optimization suggestions are generated beyond these validated ranges, ensuring that the outputs remain reliable and experimentally supported.

The proposed support optimisation engine can be further improved and provide more advanced optimisation suggestions by integrating additional data from relevant experimental and simulation-based research. This would significantly enhance the engine's capabilities, enabling more refined and data-driven recommendations across various support types such as line, contour, and cone. Ultimately, it could become a fundamental research tool for optimising SLM processes and achieving defect-free printed parts. Such integration is proposed as a key direction for future development.

5.3.4 Support Generation Module

Through the support generation module, block-type support structures with diamond perforations are generated beneath the overhang surfaces highlighted in red. These supports are commonly employed in PBF-LB and SLM 3D printers due to their ability to enhance the printability of complex parts, reduce significant defects like warping, minimize build time, and reduce material consumption by trapping less powder. They also facilitate high standards for post-processing activities such as support removal and sanding. The morphology of these support structures is characterized by vertical thin walls arranged in a grid pattern, with diamond perforations on each wall and a tooth area that represents the contact point between the part and the supports, as illustrated in Figure 100. It is also important to note that these geometries and their specific parameters (e.g., perforation beam, angle, shape) were not investigated in terms of mechanical or thermal performance. The focus of this chapter is on demonstrating the functionality and accuracy of the web-based platform for support generation, rather than evaluating support efficiency. Performance assessments of support geometries were conducted in previous chapters, particularly Chapter 4. Future work could extend this approach to systematically evaluate the effect of perforation parameters on thermal behaviour and mechanical stability.

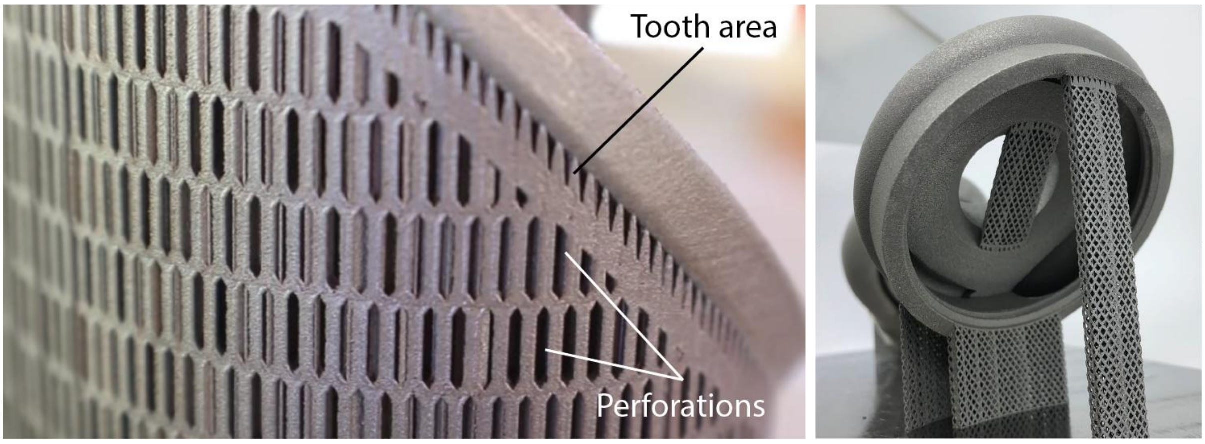

Figure 100. Morphology of block-type support structures with diamond perforations in SLM [38].

Using the support generation engine, users can modify and fine-tune various support parameters through a user-friendly interface, resulting in the final geometry of the supports. These parameters include x, y hatching, perforation beam, perforation angle, tooth height, tooth top length, support thickness, and more. X, y hatching refers to the spacing between vertical walls, defining the density of the support structures. Beam and angle define the shape and frequency of the diamond-shaped pattern, while tooth height and tooth top length specify the geometry of the tooth area.

In this iteration, support hatching distance, tooth area, and diamond perforation patterns have been investigated and developed among the various parameters of block-type support structures typically found in many commercial AM slicing software. From a technical perspective, support generation is accomplished using the PySLM library [156], an open-source Python library that provides utilities such as slicing, hatching, and support generation for SLM and other AM processes including DMLS, SLS, SLA, and DLP. Although PySLM is still in the development phase, its support generation functionality meets the requirements for further research and experimental validation.

However, during integration, several limitations were identified. Firstly, the library exhibited issues related to robust geometry processing, particularly when handling STL files with non-manifold edges, intersecting triangles, or mesh inconsistencies. These errors frequently disrupted the generation of reliable support structures. Secondly, while the PySLM library included basic block support functionalities, the generation of the tooth area, a critical feature in this research representing the localized contact region between the supports and the part, was still under development and not yet available in the stable release. To overcome these challenges, two key modifications were implemented. The first involved the incorporation of error-handling and mesh-repair strategies to resolve common geometric issues in imported meshes. The second and more substantial modification involved extending the under-development tooth area functionality within the PySLM framework to enable full control through user-defined parameters (e.g., tooth height, tooth top length, and x, y hatching). This allowed for precise control of the support-part interface and aligned with the experimental configurations evaluated throughout the thesis. These adaptations extended the core functionality of the PySLM library to support advanced support strategies, making it suitable for the aims of this research.

It should also be noted that support domain selection is not implemented in the current phase of the research, as the platform was specifically developed to evaluate block-type support structures on simple ledge specimens with one or, at most, two support domains. While more complex geometries can be imported, the ability to select specific regions for generating supports with different parameter settings has not yet been developed. Expanding the platform to enable domain-specific support generation is proposed as future work, aiming to accommodate more complex parts and enhance design flexibility.

Therefore, this platform was designed to keep a balance between user flexibility and data-driven optimization. While users can manually adjust key support parameters (e.g., hatching, perforation beam, perforation angle, tooth height, tooth top length, support thickness), these inputs are complemented by an integrated optimization engine that offers default suggestions based on experimental and simulation data presented in earlier chapters. To guide users toward effective support designs, the platform provides visual elements, parameter boundaries, and predefined presets tailored to specific support types. This approach ensures that even non-expert users can make informed decisions without compromising the quality or reliability of the generated supports. Furthermore, as discussed above, thermomechanical simulations of block-type supports with diamond perforations (those generated within the platform) have not yet been conducted. Consequently, their performance may differ from the support types examined in the simulations presented in previous chapters (those incorporated into the support optimization engine). Nevertheless, their inclusion is intended to demonstrate the platform's functionality and showcase its capabilities. Future work could build on this framework by investigating perforated support structures in more depth and integrating the resulting data into the optimization engine to further enhance its capabilities.

5.3.5 Solid Supports and Export

The platform utilizes the PySLM library to generate block-type support structures, initially characterized by non-solid geometries. Consequently, converting these into solid geometries or generating them directly as solid poses a significant challenge. Solid supports offer distinct advantages: they provide clearer visualization in relation to the imported part, are compatible with many commercial software and online platforms for further preparation of the build job and are essential for conducting and visualizing finite element analysis using appropriate simulation software. Non-solid geometries are incompatible with simulation and other CAD software due to the inability to generate meshes, making solid supports essential for such applications.

This platform allows users to convert initially generated non-solid supports into solid support structures and provides flexibility to adjust the thickness of these supports. The assembled model, including both the imported part and the generated supports, can be exported in STL format to facilitate further analysis or slicing preparation before the final printing process. From a technical standpoint, to generate solid support structures from the original 2D supports, the Pymadcad Python library [165] was employed. This library performs all necessary calculations to extrude the 2D support shapes into 3D shapes with the desired thickness. During this process, problematic triangles within the 2D supports were identified and filtered out based on characteristics such as triangle area and normal vectors.

To ensure the exported STL files were compatible with a wide range of 3D printers and slicing software, the output from the platform was tested using several widely adopted additive manufacturing slicers, including Raise3D ideaMaker [166], Materialise Magics, and popular online 3D printing platforms capable of processing both metal and plastic parts. In all cases, the STL files were successfully imported and processed without any defects, inaccuracies, or repair warnings, confirming geometric integrity and mesh closure. This indicates strong compatibility with standard slicing environments and printing workflows.

However, some geometric inaccuracies such as non-manifold edges or intersecting triangles were observed in certain exported STL files. These issues are highly dependent on the geometry of the imported part, as well as the size and inclination of its overhang surfaces. Complex or irregular geometries tend to generate more intricate support structures, which can result in occasional mesh irregularities. Addressing these issues through mesh repair tools or improved export settings is proposed as future work.

Additionally, support thickness was intentionally excluded from the platform’s real-time visualization to avoid excessive processing times and to maintain smooth performance. Instead, thickness is applied and made visible only at the STL export stage. This approach aligns with common practices in most slicing software, where non-solid supports are used to streamline visualization and reduce computational demands.

5.3.6 3D Printing and Further Processing

Drawing from the solid supports and export functionalities discussed in Section 5.3.5, users have a variety of options to utilise the exported STL file, encompassing both the part and the generated support structures. First, experienced users and companies with industrial 3D printing machines based on SLM technology can proceed directly with printing the exported STL file or upload it to compatible slicing software for further editing. In the slicing software, users can adjust process-related parameters such as laser speed and laser power to ensure the desired printing outcomes. Moreover, the exported STL file can be used for online 3D printing services, accommodating both average and experienced users. Many companies offer these services, allowing users to upload their desired components and receive a quote. However, most of these platforms lack accurate cost estimation features. They typically calculate the supports as fully dense structures, which increases the overall volume and material required, leading to higher cost estimates for the user. An example demonstrating the validation of online printability, and its associated advantages will be provided later in this chapter.

Another option for utilizing the exported STL file is to import it into simulation software for conducting finite element analysis, such as static and thermal simulations. This approach provides valuable insights into the mechanical and thermal behaviour of the part and ensures optimal printability and pat accuracy. However, this approach will not be further investigated in this research since the exported STL file needs to be properly meshed to ensure compatibility with various simulation software. This step is proposed as future work.

5.3.7 Support Simulation Module

One of the platform's key features is the support simulation module. This module allows users to conduct thermomechanical simulations on both the imported part and the generated support structures through the online platform. It provides detailed insights into thermal stress, temperature distribution, and displacement utilizing an interactive, user-friendly web interface. Designed to assess the thermal behaviour of a print job under PBF printing conditions, this feature aims to help users predict potential issues that could lead to defective or collapsed parts, thereby ensuring optimal printability. As described in Figure 98, the platform's Firebase communicates with the respective simulation software server (e.g. ANSYS or COMSOL), managing the data required for conducting numerical studies and visualizing the results on the platform's web frontend.

Although this module is not yet fully developed, a methodology for implementing this feature has been proposed. Specifically, a finalized build job, exported from Materialise Magics in STL format and comprising both the part and its supports, was used as shown in Figure 101. The build job was then imported into the simulation software, where the scene was set up and numerical studies were performed. During the setup, grade 4 titanium was selected as the material, and a temperature of 1550 °C was applied to the overhang surface. The simulations were conducted using COMSOL Multiphysics.

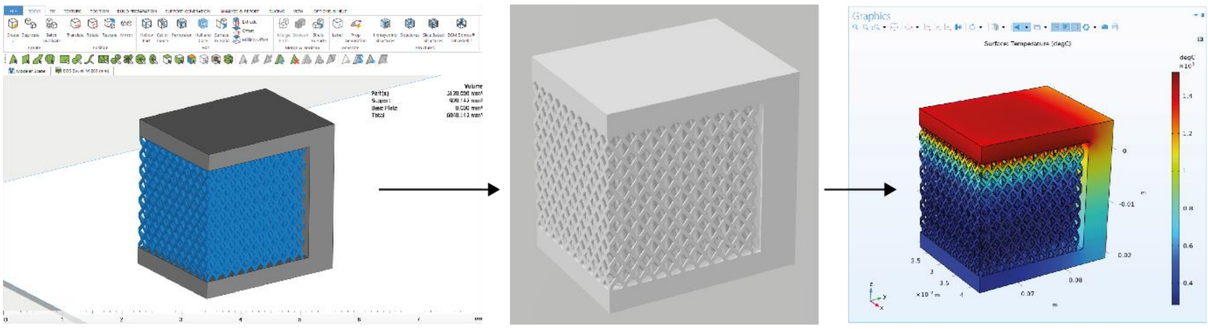

Final build job

STL export

Numerical study

Figure 101. The methodology followed to export data from a numerical study.

Consequently, to visualize the simulation outcomes in the web frontend of the platform, including part mesh, thermal stress, temperature distribution, and displacement, the required data were exported from the simulation software in two formats: PLY binary file (.ply) and text file (.txt). The PLY file contains the mesh, including nodes and elements generated for the thermal simulation, while the text file provides the coordinates and temperatures for each node in the simulation. The Trimesh Python library was also employed to create and export the coloured mesh. Figure 102 illustrates the simulation interface of the online platform and the temperature distribution of the finalized build job described above, utilizing the data exported from the numerical simulations. In addition to temperature distribution, users can select and receive feedback on other options such as thermal stress and displacement.

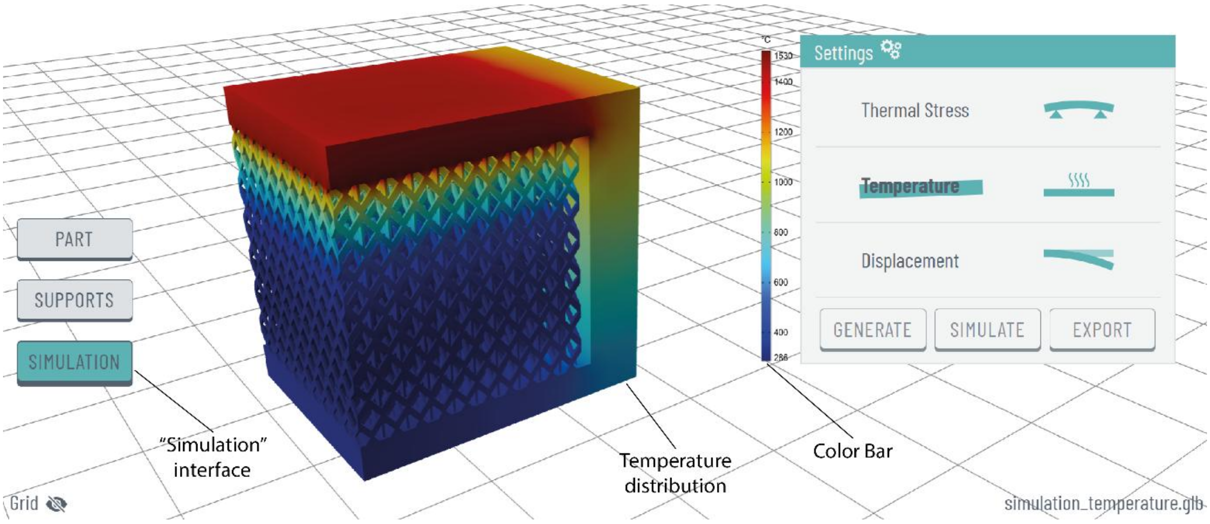

Figure 102. Simulation interface illustrating the temperature distribution on the finished build job.

Establishing real-time communication between the front-end support simulation interface and external simulation software servers would require additional software development, licensing, and computing infrastructure that exceed the scope of the current research. Future iterations will focus on implementing effective communication between the web-based support generation and optimization platform and simulation software servers such as ANSYS and COMSOL. From a technical standpoint, this will involve establishing a middleware layer that serves as an intermediary between Google Firebase and the simulation software. The process includes configuring Firebase for data storage and retrieval and setting up the server environment where COMSOL or ANSYS operates. The middleware must facilitate the transfer of data between Firebase and the simulation software, including tasks like importing simulation parameters, initiating simulations, and exporting results. The server environment must be equipped to handle these data exchanges, ensuring efficient management of simulation requests and results. This setup aims to enable seamless integration and data flow between Firebase's cloud-based services and the simulation software's computational resources [161], [167], [168]. Therefore, completing the support simulation module is proposed as a key recommendation for future work, where server-side computational resources and simulation capabilities can be fully integrated into the web-based platform to further streamline defect prediction and support optimization in SLM.

5.4 Implementation - A step-by-step Demonstration

5.4.1 User Journey Overview

To gain a deeper understanding of the functionality and features of the proposed web-based support generation and optimisation platform, this section outlines a detailed user journey using a small component based on a custom mounting bracket for DC (Direct Current) motors. The complexity, size, and design requirements of this part result in increased manufacturing costs through traditional processes such as machining, making additive manufacturing the preferred production method. The component along with its main dimensions (in milometers) are illustrated in Figure 103.

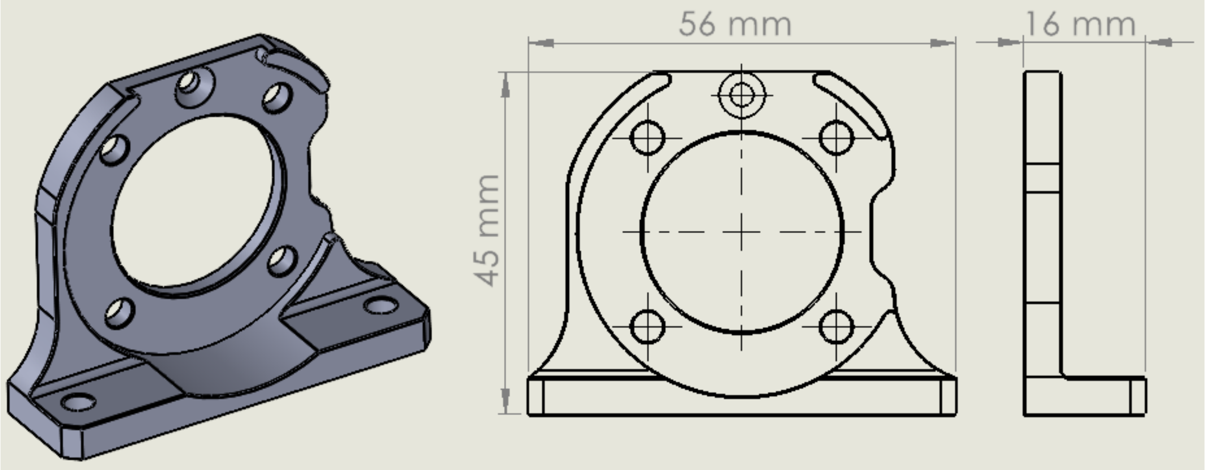

Figure 103. Mounting bracket used for demonstration purposes.

The initial step involves importing the 3D model in STL format into the online platform. Users can achieve this by dragging and dropping the file directly into the platform or selecting it from their local file system. After importing the part, users can select their preferred orientation from multiple options available in the 'orientation' drop-down menu. The part was positioned with a 45° inclination to ensure optimal printability and minimise support volume, improve support removal, reduce thermal stress, and prevent warping deformation, adhering to SLM printing guidelines detailed in the literature. After specifying the support generation angle, which determines the minimum angle for generating supports, the platform identifies critical overhang areas by marking them in red, indicating where support structures are required. This process is visually demonstrated in Figure 104, depicting the imported part alongside highlighted areas and the primary 'settings' panel within the 'part' interface. Regarding the uneven distribution of red highlighting observed in some overhang areas, this was due to the triangulation of the STL file. To address this issue, selecting a finer STL resolution would increase the number of triangles and improve distribution, although this would result in a larger STL file size. In this example, a balanced approach was followed to find a compromise between the resolution of the STL and its overall size.

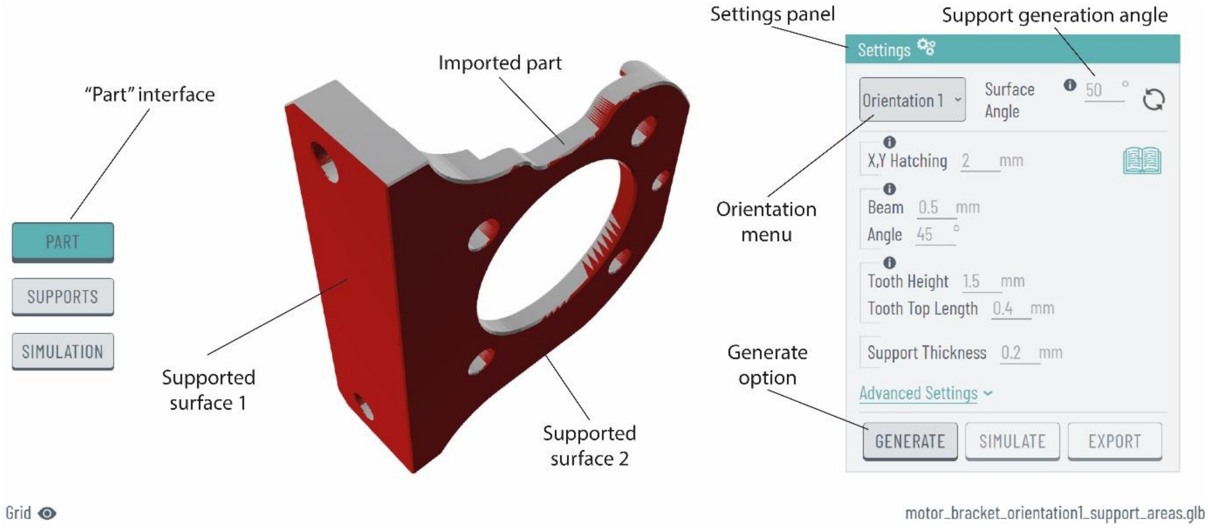

Orientation 1
Surface Angle 50 °
X,Y Hatching 2 mm
Beam 0.5 mm
Angle 45 °
Tooth Height 1.5 mm
Tooth Top Length 0.4 mm
Support Thickness 0.2 mm

Figure 104. ‘Part’ interface and commands after importing the part into the platform

When selecting the ‘generate’ option and proceeding to the ‘supports’ interface, the platform utilises the PySLM Python library to create block-type support structures with diamond perforations, as shown in Figure 105 for the bracket model. In the ‘settings’ panel, default values have been assigned to parameters such as x, y hatching, perforation beam and angle, tooth height, tooth top length, and support thickness. However, users have the flexibility to customise these values according to their preferences. For those with advanced expertise in metal additive manufacturing and support generation, the ‘advanced settings’ option provides additional configurable parameters, including support border distance, projection resolution, inner/outer support edge gap, and triangulation spacing. For a clearer visualization of the various support configurations, Figure 106 depicts three examples of block support structures generated using a ledge specimen, each employing different support parameters. It should also be noted that the same parameters are applied to all domains where supports are required. Future iterations will include domain selection, allowing users to generate different support structures for each support domain.

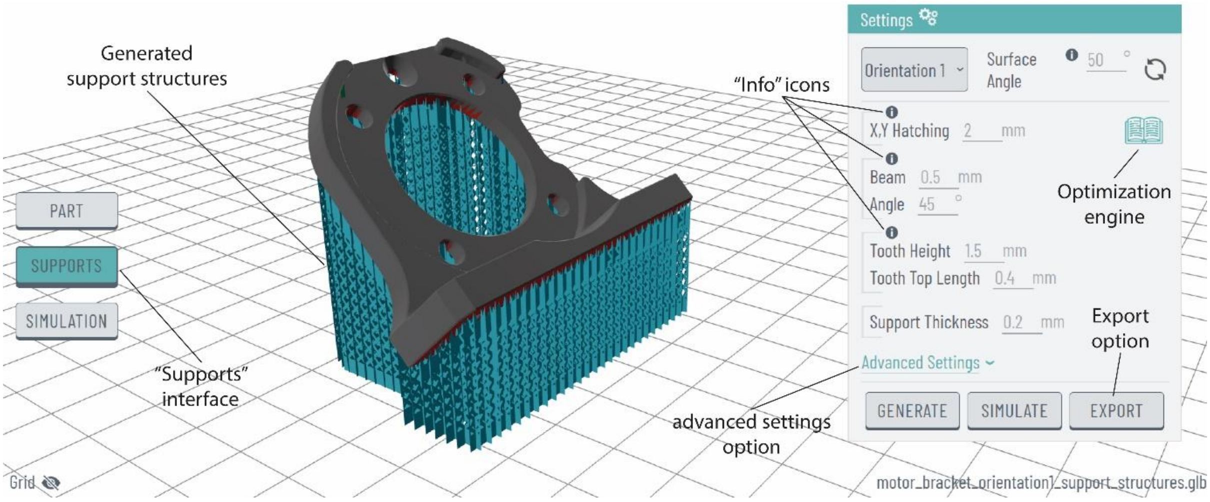

Orientation 1
Surface Angle 50 °
X,Y Hatching 2 mm
Beam 0.5 mm
Angle 45 °
Tooth Height 1.5 mm
Tooth Top Length 0.4 mm
Support Thickness 0.2 mm
Advanced Settings
motor_bracket_orientation1_support_structures.glb

Figure 105. 'Supports' interface, generated support structures, and commands.

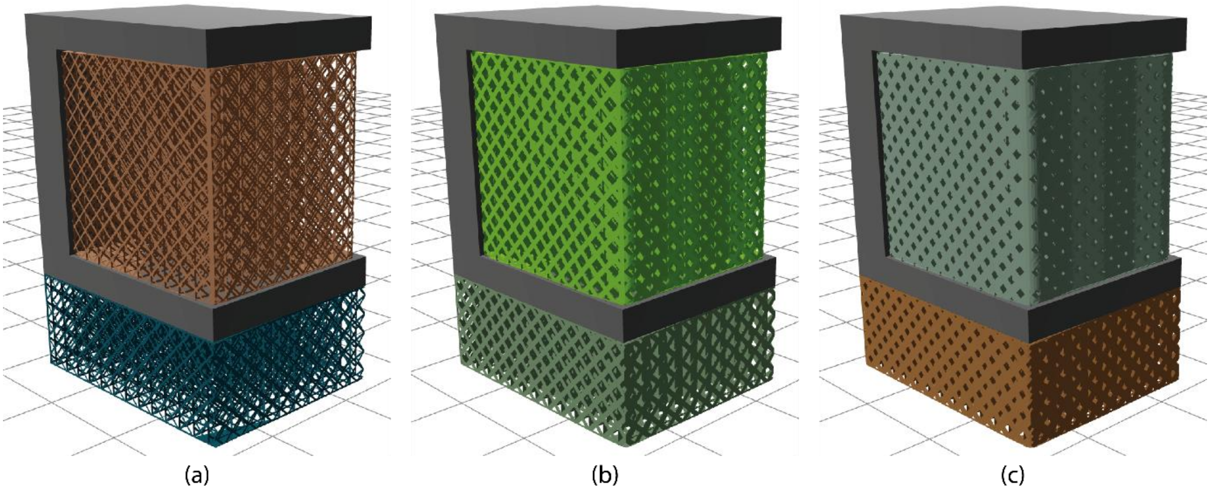

Figure 106. Three support samples of different beam values: (a) x, y hatching = 2, beam = 0.2; (b) x, y hatching = 2, beam = 0.4; (c) x, y hatching = 2, beam = 0.8.

Additionally, the 'information' icons located above each parameter (refer to Figure 105) serve as a useful guide, providing users with detailed information in graphical panels, including explanatory content and figures, related to each support parameter. For example, Figure 107a offers a graphical representation of the support generation angle, Figure 107b illustrates x, y hatching characteristics, Figure 107c depicts the perforation beam and angle, while Figure 107d details the tooth area, including tooth height and tooth top length of the supports.

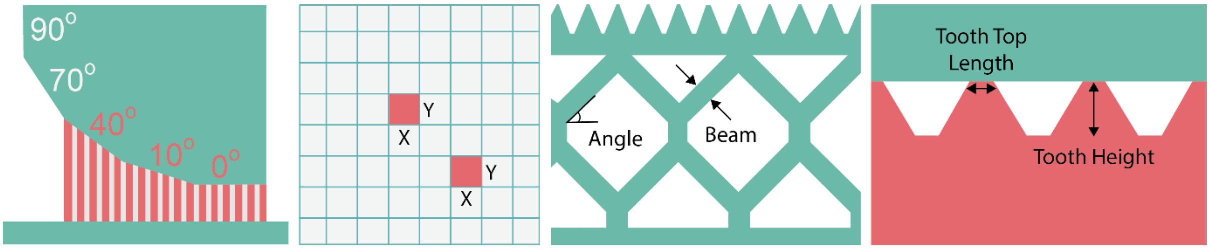

(a) (b) (c) (d)

Figure 107. (a) Generation angle; (b) x, y hatching; (c) beam, angle; (d) tooth height, tooth top length.

Regarding the support optimization engine, this tool is accessible in the top-right corner of the ‘settings’ panel, indicated by an open-book icon as depicted in Figure 105. Featuring an interactive interface, it allows users to receive optimization suggestions for block, line, contour, and cone support structures, as shown in Figure 108.

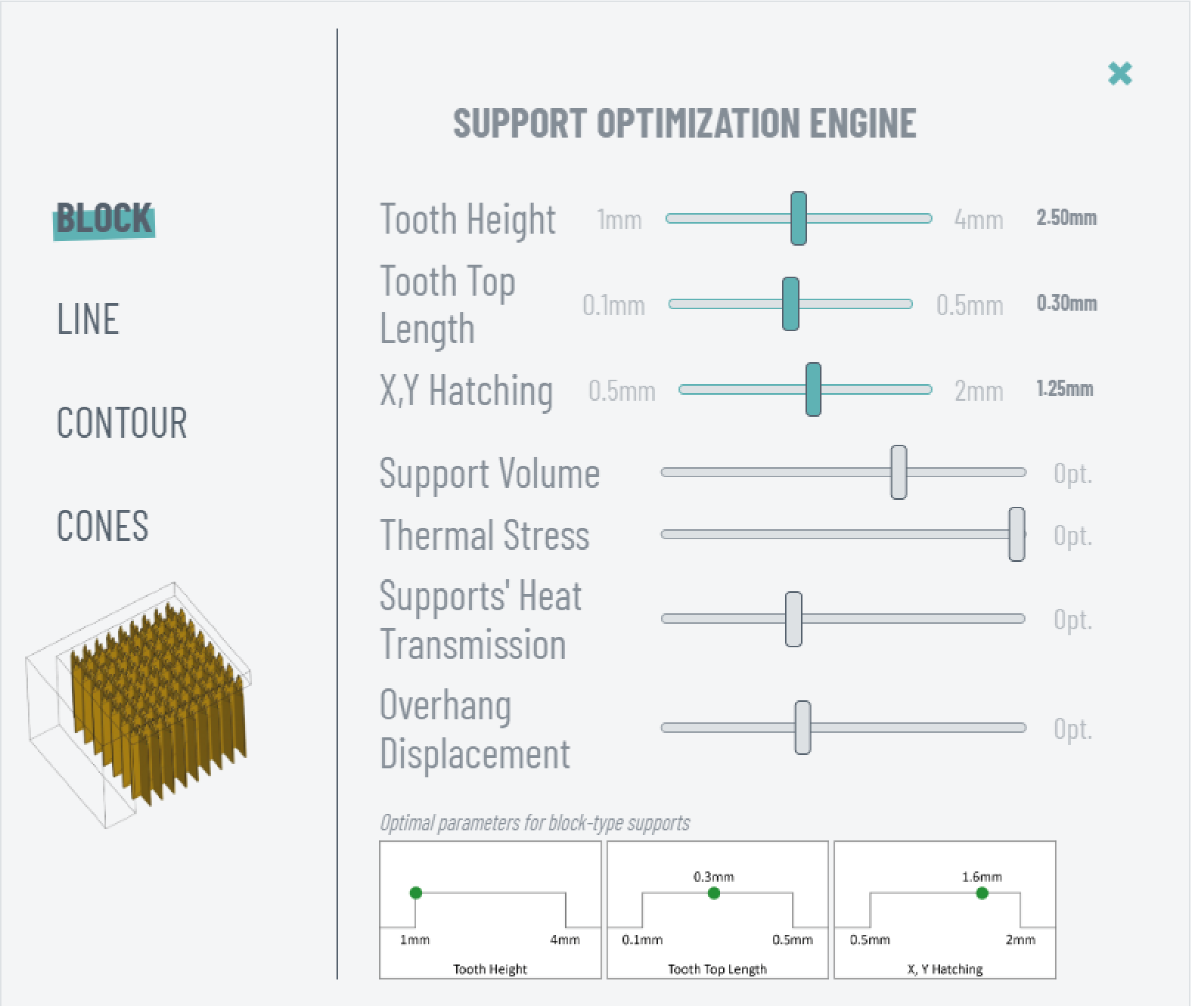

SUPPORT OPTIMIZATION ENGINE

BLOCK
LINE
CONTOUR
CONES

Tooth Height 1mm 4mm 2.50mm
Tooth Top Length 0.1mm 0.5mm 0.30mm
X,Y Hatching 0.5mm 2mm 1.25mm
Support Volume Opt.
Thermal Stress Opt.
Supports' Heat Transmission Opt.
Overhang Displacement Opt.

Optimal parameters for block-type supports

Figure 108. ‘Support optimisation engine’ interface for block-type support structures.

Through three dynamic horizontal sliders, users can select and adjust input parameters such as x, y hatching, tooth height, and tooth top length, receiving feedback on parameters that optimize support volume, thermal stress, supports' heat transmission, and part overhang displacement, displayed on four grey horizontal sliders. These optimization results were derived from research detailed in Chapter 4, which utilized numerical simulations to investigate the thermal characteristics of these four support types using L-shaped titanium specimens. Future experiments, numerical studies, and data collection are expected to enhance the functionality of the support optimization engine by incorporating additional input parameters and optimization outputs, including support removability and surface roughness.

After optimizing and generating support structures through the platform, the final step involves exporting the completed build job. While the platform initially visualizes supports using non-solid geometries, users have the flexibility to adjust support thickness through the 'settings panel, as previously discussed. This feature allows exporting supports in STL format as solid structures or non-solid if zero thickness is selected. Figure 109 illustrates both the exported model and the generated support structures in STL format from various perspectives, utilizing a default support thickness of 0.2 mm. Generating solid supports within the platform is critical for proceeding to 3D printing or further processing, as detailed in Section 5.3.6. Users can directly print the exported STL file or import it to compatible slicing software for refinement. The exported model is also suitable for online 3D printing services, accommodating both average and experienced users. Moreover, the solid assembly, comprising both the part and supports, can be imported into advanced simulation software to conduct finite element analysis, including static and thermal simulations. This enables a detailed exploration of its printability and mechanical behaviour.

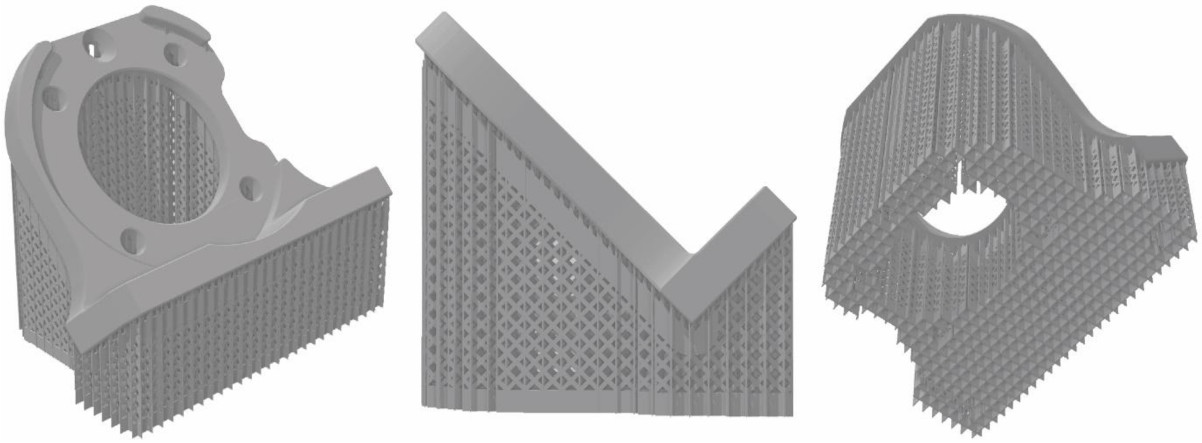

Figure 109. STL of solid support structures resulting from exporting the build job through the platform.

5.4.2 Online Access and Functionality Accuracy

The initial release of the web-based support generation and optimization platform is accessible online at no cost [169]. Users can import 3D components of varying sizes and complexities and generate block-type support structures with diamond perforations for PBF/LB systems. To ensure the accuracy of the platform's functionality concerning input parameters, their numerical ranges, and the resulting outcomes, the following guidelines are recommended:

- **Imported Model:** Only STL format parts can be imported.
- **Build Plate Volume:** There is no specific volume limit, but smaller parts are easier to manage as they require less time for import and support generation.
- **Orientation:** Users can choose from 11 orientation options based on their preferences.
- **Surface Angle:** The default surface angle is set at 50°. Users can adjust this value as needed, and then update and generate the support structures.
- **Hatching:** The default value is 2 mm, with a recommended range of 1 mm to 3 mm. Values below 1 mm may cause geometric issues, while values above 3 mm can result in collapsed overhangs and are not recommended.
- **Beam:** The default beam width is 0.5 mm, with a suggested range between 0.1 mm and 1 mm. Values exceeding 1 mm may lead to geometric problems.
- **Angle:** The default and recommended angle is 45°. Other values are experimental and may cause incorrect support generation.
- **Tooth Height:** The default value is 0 mm, meaning supports will be generated without a tooth area. A recommended range for tooth height is between 1 mm and 4 mm.
- **Tooth Top Length:** The default value is 0 mm, meaning no tooth area will be generated. A recommended range for this value is between 0.1 mm and 0.5 mm.
- **Support Thickness:** The default value is 0.2 mm, with a suggested range from 0 mm (non-solid) to 0.5 mm. After setting a new value, supports should be generated first and then exported. The thickness is not displayed on the platform interface but will be visible upon export in STL format.
- **Advanced Settings:** These values can be customized based on the user's expertise.
- **Export:** Both the part and support structures are exported in STL format, incorporating the selected support thickness.
- **Simulation:** This feature is currently unavailable and proposed for future work.
- **Loading Times:** Importing and modifying the surface angle may take up to 45 seconds for parts with coarse mesh, while support generation typically requires up to 30 seconds.

Some parts with finer mesh may take up to 60 seconds and 45 seconds, respectively. Much longer durations may indicate issues due to the finer mesh and larger part sizes.

- **Troubleshooting:** If loading exceeds 1 minute or support generation is incorrect based on selected parameters, return to the 'part' interface to adjust inputs and regenerate, or reload the page to re-import the model. Starting a new browser session might also resolve the issue.

5.5 Discussion

5.5.1 The Platform as a Valuable Tool in Research

The web-based support generation and optimisation platform, based on the design framework outlined in section 5.2, was developed as part of this PhD research to provide a flexible solution for analysing, managing, and implementing the collected experimental data. By incorporating libraries, algorithms, and equations that can be tailored to specific research objectives and desired outcomes, the platform provides a highly customizable approach. Drawing inspiration from commercial software discussed in the literature, it serves as a valuable tool for researchers investigating key aspects of SLM preparation, such as part orientation and support geometry, with the goal of optimizing process efficiency. Ultimately, the platform enables both researchers and companies involved in metal additive manufacturing to achieve optimal printing results while minimising overall costs and time.

Part orientation, for instance, is a critical factor in SLM printing, as the optimal orientation can enhance part quality, minimize the material needed for support structures, and reduce both printing time and overall costs. Additionally, post-processing tasks such as support removal and finishing can be streamlined with the correct orientation. The proposed platform facilitates future investigation and optimization of these aspects, including automated part orientation, to further improve the efficiency and effectiveness of the printing process.

Support structure design and generation are also crucial in SLM printing, as the correct support geometry ensures high-quality prints while minimizing post-processing requirements and overall printing costs. Currently, the proposed platform exclusively generates block-type supports with diamond perforations using the PySLM library. However, researchers have the flexibility to design and create additional support types using Python, including custom geometries that may not be available in conventional commercial software, and visualize them through the proposed web-based platform.

In summary, this platform, which integrates experimental and numerically simulated data, provides researchers with a valuable tool for further exploring SLM build preparation procedures. By enabling in-depth investigation and optimization of critical factors such as part orientation and support structures, the platform contributes to the development of more efficient, cost-effective, and defect-free SLM printing. Through continued research and platform enhancements, the potential for improving the quality and efficiency of metal additive manufacturing will grow, making this research tool an essential asset for advancing the field. The following sections will present how the collected data were used in this research through the platform, providing a practical example of the implementation of all the above assumptions.

5.5.2 Collected Data from Printing Experiments and Simulations

Previously, Chapters 3 and 4 described a series of 3D printing experiments and thermomechanical simulations conducted to collect data and evaluate the performance of various support geometries in SLM. The evaluation focused on key metrics, including support volume, support removability, warping defects, and thermal behaviour. All of this data was analysed to propose efficient solutions capable of optimizing the printing process in terms of saving both money and time, thereby establishing SLM as a valuable and accurate production method in the additive manufacturing industry. Subsequently, this data was utilized within the proposed web-based platform to enhance outcome visualization and implement the platform's customizable functionalities for support generation and optimisation. The most significant conclusions are presented below and summarized in Table *13*:

- **Screening Experiments:** This set of 3D printing experiments was initially conducted to define the limits of input parameters and the "printable area" of support structures, focusing on the most significant variables, including tooth height, tooth top length, and hatching distance. Various support and process parameters were tested using small "L-shaped" specimens printed with SLM technology. Based on the outcomes, which included both successful and failed parts, the final ranges were determined as follows: tooth height between 1 mm and 4 mm, tooth top length between 0.1 mm and 0.5 mm, and hatching distance between 0.5 mm and 2 mm. Values outside of these ranges were excluded, as they resulted in defective or collapsed parts. Other parameters, such as laser speed, laser power, and additional geometric parameters, were also examined but kept constant at their optimal values.
- **Main Experiments:** In this series of SLM 3D printing experiments, various combinations of support parameters were investigated by printing small specimens with

differing overhang inclinations. The objective was to evaluate the performance of the various support structures in terms of support volume, support removal effort, and part warping deformation. The results revealed that hatching distance had a significant impact on support volume, while tooth top length played a key role in the effort required for support removal. For overhangs at 0°, the optimal configuration for minimising cost and avoiding defects was found to be a tooth height of approximately 2.7 mm, a tooth top length of about 0.3 mm, and a hatching distance of around 0.8 mm.

- **Thermomechanical Simulations:** This numerical analysis aimed to evaluate the performance of various support structures in SLM, including block, line, contour, and cone types. Key factors such as support volume, thermal stress, heat transfer, and displacement were analysed to identify the optimal parameters for producing efficient, defect-free parts. The optimal results showed that block supports were most effective with a tooth height of 1 mm, a tooth top length of approximately 0.3 mm, and a hatching distance of 1.6 mm. Line supports performed best with similar tooth height and top length values, but a hatching distance of 1.2 mm. For contour supports, the ideal configuration involved a tooth height of 1 mm, a tooth top length of about 0.4 mm, and a hatching distance of 1.4 mm. Cone supports were optimized with a contact platform diameter of 1.7 mm, a contact part diameter of 0.4 mm, and a cone spacing of 1.3 mm.
- **Validation Experiments:** Based on the simulation outcomes, the optimal support configurations for each type were validated through SLM 3D printing experiments, focusing on support removal, surface roughness, and part warping. The results showed that block supports had good surface quality but were somewhat difficult to remove and prone to warping. Line supports provided a balanced compromise between ease of removal, surface quality, and warp resistance. Contour supports were effective in minimizing warping but presented significant challenges during removal, while cone supports were the easiest to remove but exhibited limitations in surface roughness.
- **ANOVA Equations:** To analyse the collected experimental data and identify the optimal parameters that best satisfy the responses, an analysis of variance (ANOVA) was conducted. This analysis generated various plots, as presented earlier in this research. The resulting equations were integrated into the web-based platform to visualize the outcomes and propose optimal support generation solutions based on user preferences. Similar equations can also be imported into the platform from relevant experimental work to further enhance its functionality.

- **Python Libraries:** To develop the web-based platform and integrate features such as part import and orientation, support generation and visualization, and exporting solid geometries, several Python libraries were utilized and modified. These libraries include Trimesh for 3D mesh manipulation, PySLM for generating block-type support structures, and Pymadcad for converting 2D shapes into 3D. All of these libraries are open-access and can be adapted based on the collected data and the research objectives.

Table 13. Key conclusions derived from experiments and simulations.

Screening Experiments	**Suggested “printable area” for 0° overhangs**			
		Tooth Height	Tooth Top Length	Hatching
		1 - 4 mm	0.1 - 0.5 mm	0.5 - 2 mm
Main Experiments	**Optimal parameters for block supports**			
		Tooth Height	Tooth Top Length	Hatching
		2.7 mm	0.3 mm	0.8 mm
Thermomechanical Simulations	**Optimal parameters for block, line, contour and cone supports**			
	Type	Tooth Height	Tooth Top Length	Hatching
	Block	1 mm	0.3 mm	1.6 mm
	Line	1 mm	0.3 mm	1.2 mm
	Contour	1 mm	0.4 mm	1.4 mm
	Cone	1.7 mm (LD)	0.4 mm (UD)	1.3 mm
Validation Experiments	**Rating measurements of support performance**			
	Type	Support Removal	Surface Roughness	Part Warping
	Block	Good	Very Good	Good
	Line	Very Good	Very Good	Very Good
	Contour	Good	Good	Excellent
	Cone	Excellent	Poor	Very Good
ANOVA Equations	**Equations used - derived from ANOVA results during DOE**			
	Type	Support Removal	Surface Roughness	Part Warping
	Block	✓	✓	✓
	Line	✓	✓	✓
	Contour	✓	✓	✓
	Cone	✓	✓	✓

	Libraries utilised to develop the web-based platform		
Python Libraries	Trimesh	PySLM	Pymadcad
	For 3D mesh manipulation	For support generation	To extrude 2D shapes into 3D

Most of the experimental data mentioned above, along with the ANOVA-derived equations and Python libraries, were utilized to develop the proposed web-based platform. This platform serves as a valuable research tool for managing and visualizing this type of data while also generating optimized custom support structures for SLM processes. Aimed at improving the efficiency of metal additive manufacturing, this platform facilitates future research initiatives, enabling researchers to adapt and leverage similar data based on their specific objectives and preferences.

5.5.3 The Role of the Support Optimization Engine

In addition to the support structure generation and other features developed to meet the platform's requirements, the support optimisation engine, as described earlier in section 5.3.3, is of particular importance. This tool enables users to visualise ANOVA results by utilizing relevant data and equations, aiming to provide optimization suggestions for input and output parameters based on the user's preferences and prioritisation criteria.

In this version of the platform, data from the thermomechanical simulation outcomes of block, line, contour, and cone supports, as presented in Chapter 4, are utilized and visualized. Users receive optimization suggestions for these support types by examining their thermal behaviour, intending to minimize support volume and residual stress while maintaining high print quality. Support density and tooth area are assessed using input parameters, including x, y hatching, tooth height, and tooth top length. This optimization engine enables users to adjust input support parameters for each support type individually, while simultaneously displaying the corresponding levels of support optimization for output parameters, such as support volume, thermal stress, heat transmission, and part displacement. Examples of its significance in preparing slicing jobs for SLM are provided next.

As shown in Figure 110, the support optimization engine interface provides users with tailored optimization suggestions for block, line, contour, and cone support structures, derived from the thermomechanical simulation results discussed earlier. Users can adjust input parameters, such as hatching distance, tooth height, and tooth top length, using three interactive horizontal sliders. This functionality allows users to receive targeted optimization recommendations for support volume, thermal stress, heat transfer, and part displacement. With this tool, users can prepare a build job for SLM by analysing and adjusting the thermal behaviour of the part according to their specific requirements and preferences.

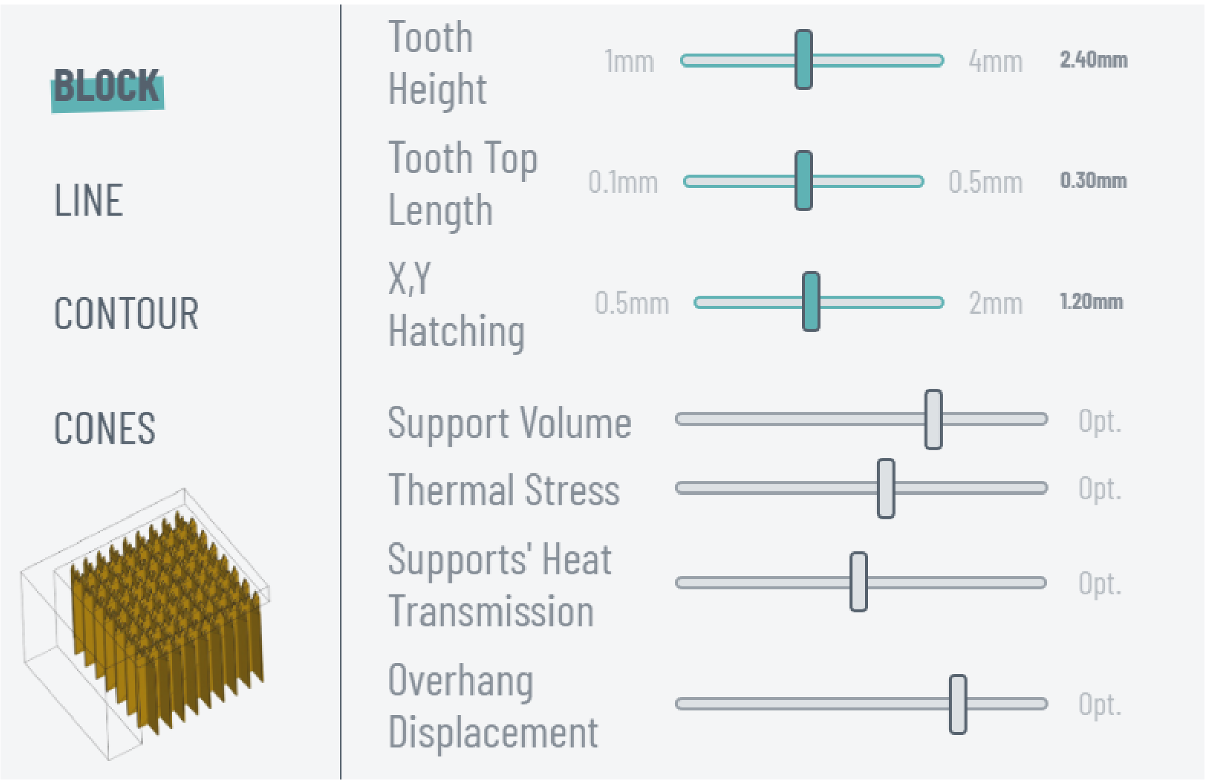

Tooth Height 1mm 4mm 2.40mm

Tooth Top Length 0.1mm 0.5mm 0.30mm

X,Y Hatching 0.5mm 2mm 1.20mm

Support Volume Opt.

Thermal Stress Opt.

Supports' Heat Transmission Opt.

Overhang Displacement Opt.

Figure 110. Support optimisation engine interface.

Numerical optimization, guided by ANOVA results and corresponding equations, determined that the optimal configuration for block-type support structures consists of a tooth height of 1 mm, a tooth top length of 0.3 mm, and a hatching distance of 1.6 mm. Similarly, optimal configurations were identified for line, contour, and cone support types (see Table *13*). Applying these parameters within the support optimization engine achieves the highest possible response values based on predefined goals and constraints, which include minimizing support volume, thermal stress, and displacement while maximizing supports’ heat transmission. To achieve this, a desirability approach was employed to measure how well the responses simultaneously meet the specified criteria. Figure 111 illustrates the interfaces of the support optimization engine, showcasing the optimal solutions for each support type.

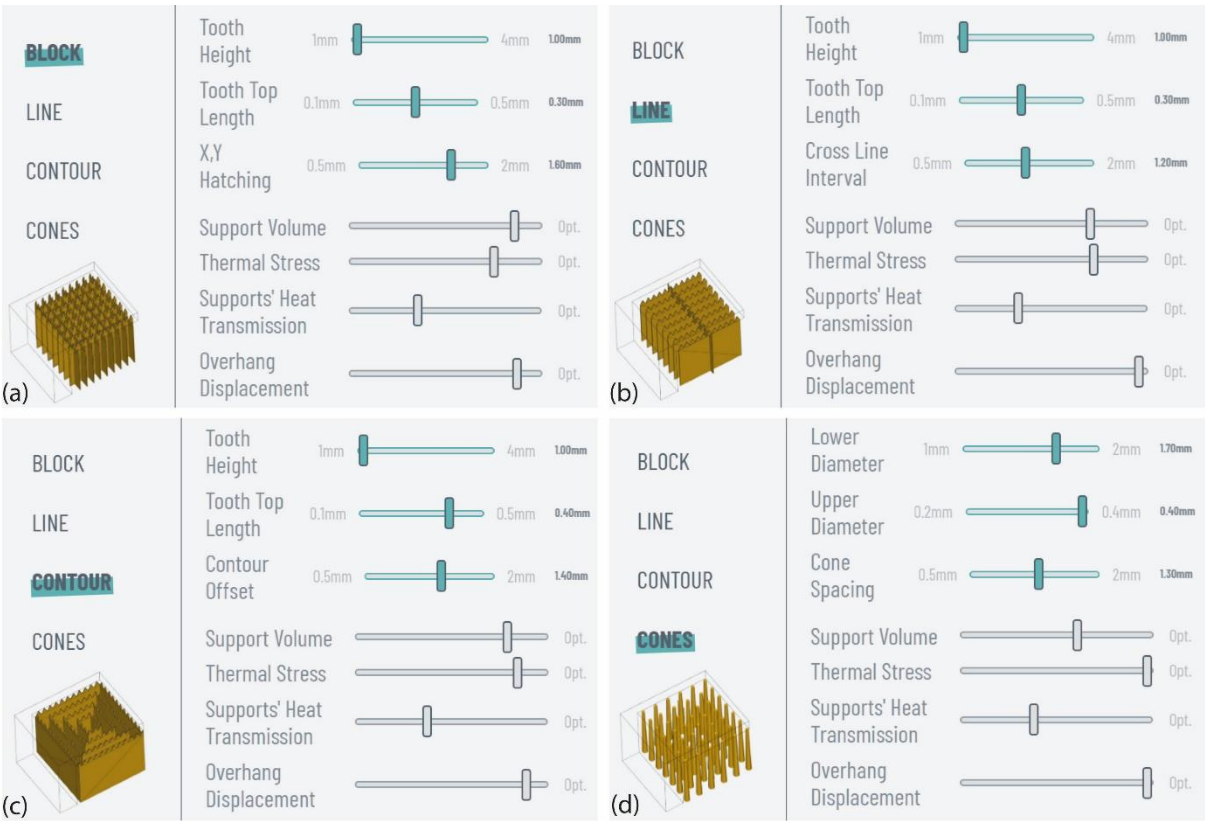
(a)
Tooth Height 1mm 4mm 1.00mm
Tooth Top Length 0.1mm 0.5mm 0.30mm
X,Y Hatching 0.5mm 2mm 1.60mm

(b)
Tooth Height 1mm 4mm 1.00mm
Tooth Top Length 0.1mm 0.5mm 0.30mm
Cross Line Interval 0.5mm 2mm 1.20mm

(c)
Tooth Height 1mm 4mm 1.00mm
Tooth Top Length 0.1mm 0.5mm 0.40mm
Contour Offset 0.5mm 2mm 1.40mm

(d)
Lower Diameter 1mm 2mm 1.70mm
Upper Diameter 0.2mm 0.4mm 0.40mm
Cone Spacing 0.5mm 2mm 1.30mm

Figure 111. Optimal input parameters for (a) block, (b) line, (c) contour, and (d) cone supports.

In the previous example, optimization suggestions were provided for input parameters that meet all response criteria simultaneously. However, users have the flexibility to select a variety of input parameters to optimize the responses according to their specific requirements and preferences. For instance, Figure 112 illustrates a case for block-type supports where the hatching distance has been reduced from 1.6 mm to 1 mm. This adjustment results in a less optimised support volume, which may require a build job with more material and increased printing time. However, the other three responses achieve a more balanced optimization. Notably, heat transmission improves significantly, while thermal stress and part displacement show slight decreases in optimization. Specifically, a 0.6 mm reduction in x, y hatching resulted in a significant 67% decrease in support volume optimization, with the actual support volume rising from 1800 mm^3 to 3000 mm^3. Thermal stress optimization declined by about 19%, as the actual thermal stress increased from 3.87×10^9 N/m^2 to 4.6×10^9 N/m^2, while heat transmission optimisation improved by approximately 9%, reflecting an increase in plate temperature from 870 °C to 950 °C. Finally, overhang displacement optimization decreased by roughly 2.4%, as the actual overhang displacement increased from 0.414 mm to 0.424 mm.

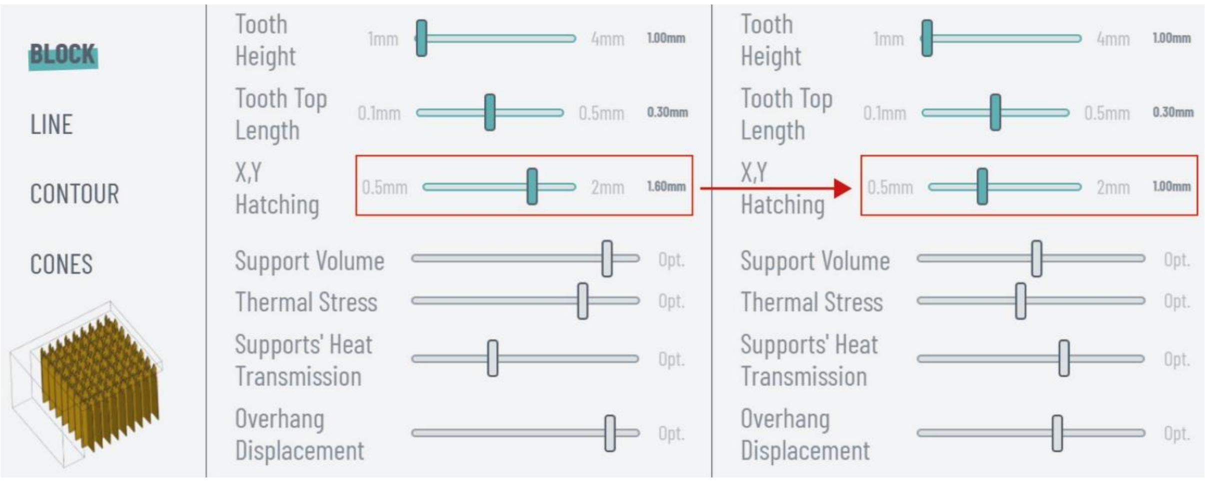

Tooth Height 1mm 4mm 1.00mm
Tooth Top Length 0.1mm 0.5mm 0.30mm
X,Y Hatching 0.5mm 2mm 1.60mm
Support Volume Opt.
Thermal Stress Opt.
Supports' Heat Transmission Opt.
Overhang Displacement Opt.

Tooth Height 1mm 4mm 1.00mm
Tooth Top Length 0.1mm 0.5mm 0.30mm
X,Y Hatching 0.5mm 2mm 1.00mm
Support Volume Opt.
Thermal Stress Opt.
Supports' Heat Transmission Opt.
Overhang Displacement Opt.

Figure 112. Different optimization outcomes based on 1.6 mm and 1 mm of x, y hatching, respectively.

5.6 Exported Build Job Validation Utilizing SLM Technology

To validate the exported feature and ensure the functional accuracy of the platform, a new build job was generated, consisting of both the part and its support structures. This build was based on a simplified mounting bracket, as shown in Figure 113, along with its key dimensions (in millimetres). Figure 114 illustrates the finalised build job on the platform, including the generated supports and the part's printing orientation at 45°. Based on the optimization suggestions received from the support optimization engine, the following parameters were applied: a hatching distance of 1.6 mm, a tooth height of 1 mm, a tooth top length of 0.3 mm, a perforation beam of 0.5 mm, a perforation angle of 45°, and a support thickness of 0.2 mm.

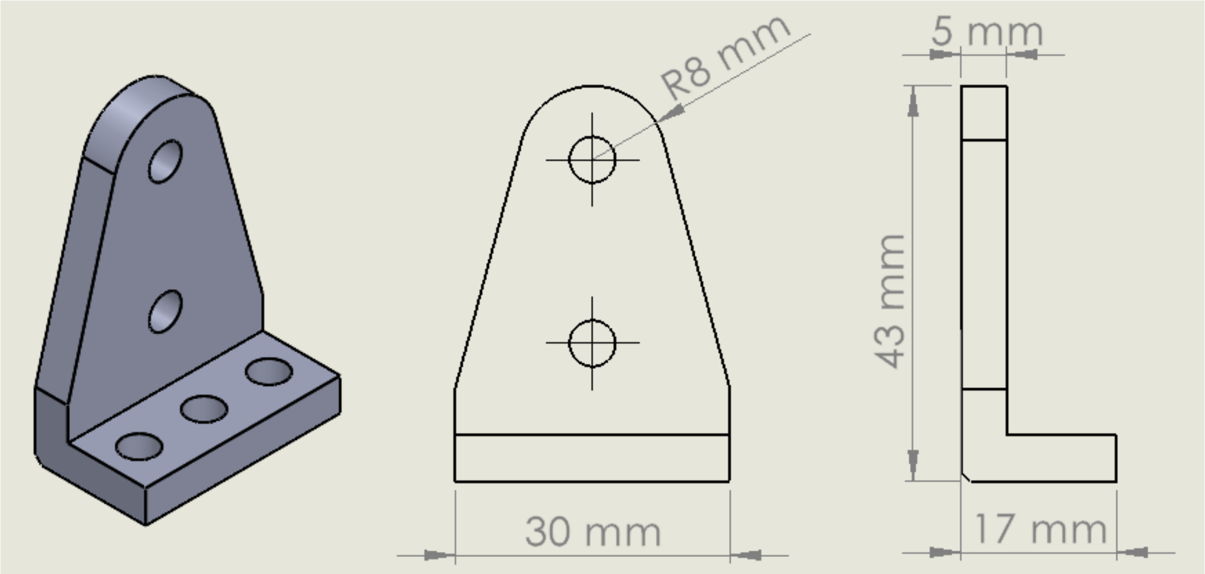

Figure 113. Mounting bracket model with key dimensions.

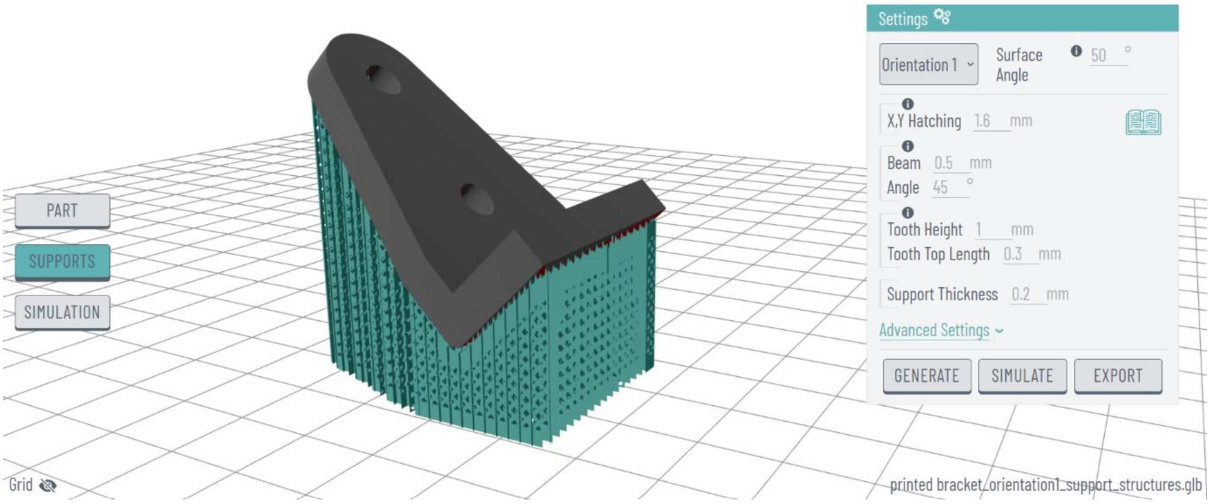

Orientation 1
Surface Angle 50 °
X,Y Hatching 1.6 mm
Beam 0.5 mm
Angle 45 °
Tooth Height 1 mm
Tooth Top Length 0.3 mm
Support Thickness 0.2 mm

Figure 114. Finalized build job with print orientation and applied support parameters.

After exporting the final job in STL format, the file was sent for 3D printing. The print was carried out using an EOS M290 machine, which utilizes SLM technology. The material used was Ti64 Grade 23 titanium alloy, with its characteristics and chemical composition detailed earlier in Chapter 4. Regarding the printed outcome, despite some minor geometric issues observed around the teeth perimeter in the STL file, the job was successfully printed. Figure 115a illustrates the exported STL job while Figure 115b the printed outcome.

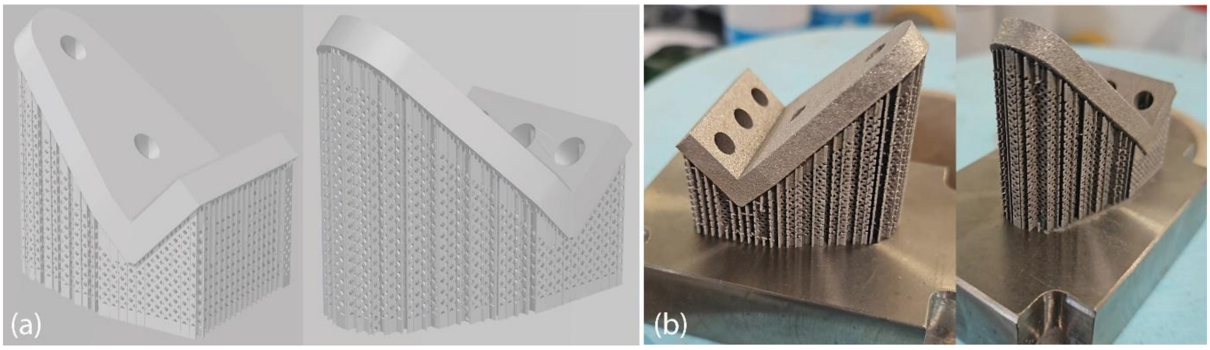

Figure 115. exported build job in STL format; (b) printed outcome in SLM.

Post-processing involved removing support structures, evaluating surface quality, and assessing the part’s dimensional accuracy compared to the original CAD model. The supports were removed manually using basic tools, such as cutters and pliers, where necessary. The entire process of support removal took approximately 2 to 4 minutes. The surface quality was generally good: the upper surfaces were smooth, while the areas in contact with the supports were slightly rough, as shown in Figure 116. However, light sanding could effectively improve the roughness of these areas. Dimensional accuracy was assessed using a digital calliper. The measurements indicated that all surfaces not in contact with the supports aligned with the original CAD model. However, the surfaces that contacted the supports showed an excess material of 0.1 to 0.25 mm, suggesting the need for sanding to remove the solidified material remnants. It is worth noting that no signs of warping or deformation were observed.

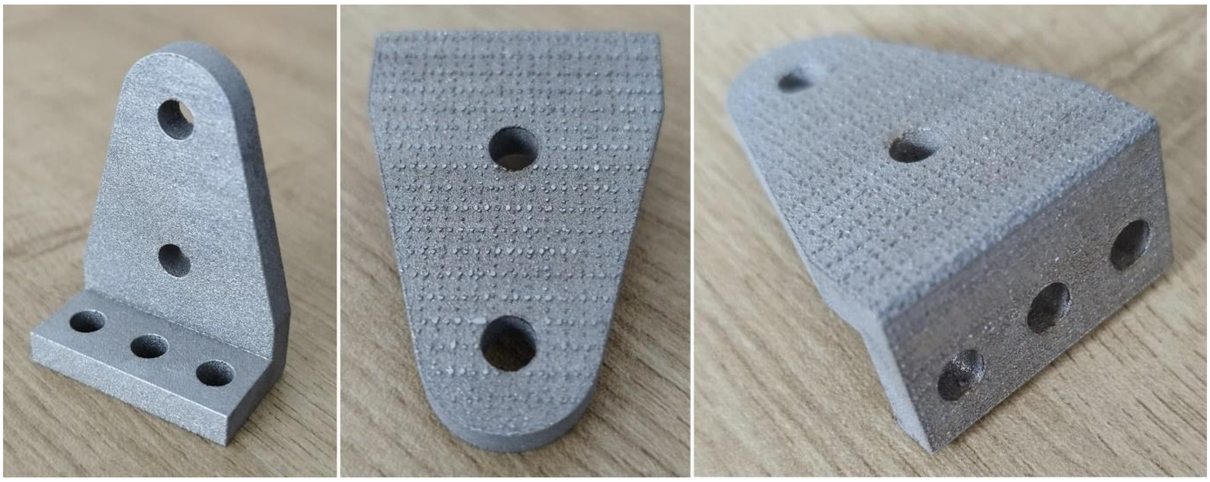

Figure 116. Surface quality of the 3D-printed part.

Although the validation of the platform's printability was successfully achieved, as the exported build job can be imported into any slicer or online instant quoting platform and printed directly, the validation of the exported STL file through numerical simulations has encountered some issues. These issues arise from geometric inaccuracies in the exported STL, such as non-manifold edges, intersecting triangles, and form union errors, which prevent it from being fully read by compatible simulation software such as COMSOL. To address this, the geometric accuracy of the STL file needs further refinement, possibly through mesh repair or more advanced export settings, including modifications to the PySLM library using Python. This improvement will enhance the accuracy of future simulations and is considered for future work.

5.7 Chapter Summary

This chapter presented an innovative design framework for improving efficiency in additive manufacturing, alongside the initial release of a web-based platform for automating the generation and optimization of support structures in metal AM and PBF-LB systems. The platform efficiently generates custom support structures and leveraged experimental data, offering a user-friendly interface that allowed users to import 3D files, orient components, generate support structures with custom geometric parameters, access optimization recommendations, and export finalized build jobs in STL format for further processing.

Unlike existing slicing and simulation software, this research tool provides several key advantages. It was developed to help companies and researchers further explore and prepare build jobs in SLM, minimizing overall costs and the effort required to produce efficient, defect-free parts. It is accessible online at no cost, compatible with any web browser, and designed for both experts and less experienced users in metal additive manufacturing. Additionally, it supports a broad range of 3D printing machines, from industrial and desktop models to machines designed exclusively for research purposes.

The platform was also validated through 3D printing using SLM technology to assess support removability and part accuracy. By utilizing this platform, the AM industry could expect several benefits, including enhanced adoption of PBF-LB/M as a production method, reduced printing and post-processing times, assured defect-free prints, minimized support material usage, and decreased CO_2 laser emissions along with overall printing costs.

Summarizing, although no quantitative cost analysis was conducted in this phase of the research, the platform was designed with a clear focus on providing a cost-effective and research-oriented tool for support structure generation and optimization in SLM processes. The primary aim was to develop and validate a framework that can reduce the cost implications associated with defective builds, excessive material usage, and inefficient support designs, common issues in traditional trial-and-error approaches. Unlike commercial software, which often involves high licensing fees and limited flexibility for adaptation or data integration, this platform provides an open and customizable environment that can be effectively incorporated into research workflows. By minimizing print failures and optimizing material usage through informed design decisions, the platform serves as a practical and efficient solution for achieving cost reductions in research, experimental, and prototyping contexts.

Chapter 6: Conclusion and Future Work

6.1 Conclusion

This research aimed to investigate the performance of various support geometries in metal 3D printing using PBF-LB through experimental frameworks and numerical studies. The goal was to evaluate and propose design principles for optimized support structures that enhance SLM efficiency by minimizing defects and reducing production time and cost. Efficiency and cost-related improvements were quantified through experimental metrics, primarily focusing on support removal effort and part validation outcomes. Support removal effort was assessed by measuring the time and manual effort required to detach support structures from printed specimens, reflecting both post-processing efficiency and labour intensity. This was complemented by dimensional accuracy checks and surface quality evaluations conducted during experimental validation. Together, these indicators provided tangible evidence that the proposed support strategies not only improve the manufacturability of parts but also significantly reduce post-processing time, material waste, and the overall cost of SLM production.

Additionally, a design framework was developed and implemented to create a web-based platform for automated support generation and optimization, leveraging experimental data. Through this research tool, users can import 3D files, set part orientation, receive optimization suggestions based on thermal analysis, generate block support structures with diamond perforations according to preferred support parameters, and export the final build job in STL format for direct printing or further pre-printing processing.

6.1.1 Multi-Response Optimisation of Block-type Supports

Initially, block-type support structures made of titanium alloy (Ti6Al4V) were investigated and evaluated in terms of support and process parameters to propose optimal solutions that minimize support volume, support removal effort, and part warping deformation. Key factors such as tooth height, tooth top length, hatch distance, laser speed, laser power, and various overhang inclinations were examined. The methodologies employed included multi-response optimisation, SLM 3D printing, design of experiments, performance measurements, data analysis, numerical optimization, and the generalization of findings.

The results indicated that hatching distance had the most significant impact on support volume, with the lowest volume achieved at higher hatching levels (4 mm). In contrast, tooth height and tooth top length had minimal effect on support volume. Tooth top length was found to have the greatest influence on support removal effort, with the least effort required at smaller tooth top lengths (0.05 mm), while other parameters had little impact on removal effort. Overhang angle played the most critical role in warping deformation, with the least deformation occurring at larger angles (45°), whereas other parameters showed only minor effects on deformation. Based on the findings, this work serves as a valuable guide for comparing various support and process parameters, with the aim of generating block support structures that minimize material usage and removal effort while ensuring defect-free parts. This approach enhances the efficiency of metal AM, positioning SLM as an effective production method suitable for widespread industrial use.

It is also important to note that the prioritization between minimizing support volume and ensuring easy support removal depends largely on the specific application requirements. In scenarios where material consumption, build time, or thermal management are critical, such as large-volume parts, aerospace components, or batch production runs, minimizing support volume becomes the primary objective. In such cases, parameters like hatching distance are tuned to maximize spacing and reduce the amount of support material used, even if this results in slightly more effort during post-processing. Conversely, for parts requiring high surface quality or intricate geometries, such as medical implants or customized tooling inserts, ease of support removal becomes more important, and therefore, parameters like tooth top length are prioritized to reduce contact areas, post-processing effort, and the risk of part damage. This trade-off highlights the importance of an adaptive optimization strategy tailored to application-specific constraints.

6.1.2 Finite Element Analysis of Alternative Support Types

Subsequently, various support types commonly used in SLM, including block, line, contour, and cone support structures, were investigated. Initial 3D printing experiments revealed defects in critical areas, such as warping deformation and displacement, caused by thermal stresses during the process. To address these issues, the thermal behaviour of these support types was further analysed and evaluated using thermo-mechanical simulation studies. The objective was to propose optimized support geometries that minimize thermal stress, improve heat transfer, enhance part accuracy, and reduce support removal effort. The methodology included screening experiments, design of experiments, finite element modelling, data analysis and numerical optimization, as well as validation of support removal through SLM 3D printing trials.

The main simulation results revealed that block-type supports had a significantly larger average support volume, approximately 45-50% more than line, contour, and cone supports with the same parameters. High-density supports experienced greater thermal stresses, especially those with larger tooth heights and thin features like cone supports. However, high-density supports also offered better temperature distribution compared to low-density ones. Cone-type supports were more prone to warping and distortion, particularly when they had higher tooth heights and smaller diameters. Despite their larger volume, block supports demonstrated the best thermal behaviour, with the lowest thermal stress, highest heat transmission, and optimal thermal performance compared to other support types.

On the other hand, the experimental outcome indicated that cone supports were easier to remove but showed limitations in surface roughness. Block supports provided adequate surface roughness but were more challenging to remove and susceptible to warping deformation. Contour supports were effective in preventing warping but posed challenges during removal. Line supports offered a balanced compromise between ease of removal, surface roughness, and warping deformation. According to the findings, this work also serves as a valuable guide for using block, line, contour, and cone support structures in SLM, aiming to achieve successful prints with zero defects, reduce printing time and material usage, and lower post-processing and labour costs.

While the thermo-mechanical simulations provided valuable insights into the thermal behaviour and stress distribution across different support geometries, certain limitations must be acknowledged. The simulations employed a simplified heat source model and assumed uniform material properties and boundary conditions, which may not fully capture the dynamic nature of the SLM process. Factors such as evolving material properties during melting and solidification, powder-to-solid phase transitions, laser absorption variability, and thermal contact resistance at the part-support interface were either simplified. Additionally, the mesh resolution and computational constraints limited the accuracy in some complex geometries. These assumptions, while necessary for computational feasibility, may affect the precision of the predicted thermal gradients and deformation levels. To improve the reliability of future simulations, more advanced modelling techniques could be employed, such as incorporating temperature-dependent material properties, dynamic phase change modelling, and localized laser scanning strategies. Furthermore, real-time in-situ thermal monitoring could be integrated to validate and refine simulation inputs, improving alignment with experimental conditions.

6.1.3 Web-Based Platform for Support Generation and Optimisation

Finally, an innovative design framework for support generation and optimization was proposed. This framework aims to enhance confidence in SLM as a production method while maintaining its mass production potential. Subsequently, a web-based platform for automated support generation and optimization was developed. This research tool is designed to efficiently generate custom support structures and manage experimental data, assisting both companies and researchers in further exploring and preparing build jobs for SLM. To support this platform, a Firebase hosting server was created from scratch, and JavaScript, Python, and other libraries were used to design the interface and develop its functionality. This platform leverages a wide range of data, allowing users to import their chosen components and prepare them for 3D printing with SLM by generating optimized block support structures. It also offers recommendations to enhance printability and improve overall printing success.

Most of the features outlined in the design framework have been implemented, however, some aspects still require further development and refinement and are proposed as future work. The validation phase demonstrated that the platform successfully generates supports for imported parts and enables successful printing with SLM. The printed outcome exhibited excellent dimensional accuracy and ease of support removal. However, minor post-processing, such as sanding, was needed to address the surfaces where the supports attached. By utilizing this platform, which is free to use and does not require expert knowledge, the AM industry can benefit from an accessible, user-friendly online build preparation tool that facilitates successful prints with zero defects, reduces printing time and costs, and enhances the adoption of PBF-LB as a production method. In addition, this tool offers significant potential for further development and could contribute to advancing research in SLM and metal additive manufacturing.

Throughout the platform's development, feedback was actively received from both academic researchers and industry professionals involved in metal additive manufacturing and SLM printing. This valuable input, gathered during demonstration sessions and research collaborations, played a crucial role in shaping the platform’s interface, functionality, and overall usability. These recommendations were systematically incorporated into subsequent development iterations, resulting in a more intuitive and effective tool. The positive reception across both sectors confirmed the platform’s practical value, particularly in reducing print preparation time, streamlining experimental workflows, and supporting non-expert users in generating and optimizing support structures.

6.2 Future Work

Future work could involve further research and experimentation on a range of support and process parameters in metal AM and PBF-LB systems. By applying the methodologies primarily outlined in Chapters 3 and 4, the goal would be to propose optimized support geometries that minimize material usage, removal effort, and printing costs while maintaining high-quality print results. A primary focus would be ensuring the scalability of this analysis, including investigating different overhang surface sizes, exploring new materials, and addressing the challenges posed by more complex part geometries. It is expected that factors such as overhang surface size, material type, and part complexity will significantly influence the optimal support design. Specifically, the optimal solution will depend on the input parameters, including geometrical features, thermal properties, and mechanical behaviour of the selected material. For example, larger overhangs may require denser or differently distributed supports, while materials with lower thermal conductivity may demand enhanced heat dissipation strategies. To test these hypotheses, the methodology presented throughout this thesis—combining multi-response optimization, experimental validation, and thermo-mechanical simulation—will be applied to a range of case studies with varying geometries and materials. This approach will allow for systematic evaluation of how each factor affects support performance and will help refine the support generation framework accordingly.

The numerical modelling approach could be further refined by incorporating additional factors related to the printing process and specific machine conditions, such as internal chamber temperature, surrounding powder behaviour, and other relevant process variables. Including these parameters will allow for a more realistic simulation environment, resulting in more accurate predictions of thermal and mechanical responses. This enhancement will not only support the development of a more reliable support optimization model but will also contribute to improving the accuracy and effectiveness of the platform's optimization engine, enabling users to make better-informed decisions tailored to their specific printing setup.

However, while the methodologies outlined in Chapters 3 and 4 show promising results in optimizing support geometries to reduce material usage, removal effort, and printing costs, applying these methods to more complex geometries presents several challenges. A primary limitation is the limited availability and high operational cost of SLM machines, which makes extensive experimentation difficult, particularly for academic or early-stage research environments. Additionally, complex geometries often require highly customized print setups to avoid common defects such as warping, detachment, or incomplete fusion, increasing the risk of failed prints. Addressing these challenges will involve expanding the platform's simulation capabilities and optimize print parameters before physical builds, minimizing trial-and-error. Collaboration with industry partners for machine access and the development of advanced heuristics within the optimization engine to predict failure-prone configurations will also be considered to reduce dependence on costly experiments and ensure reliable implementation of the proposed methodologies on complex designs.

The first version (v0.6) of the support generation and optimization platform has been released and is available online at no cost. To enhance its capabilities and expand its user base, several specific features are proposed for future development. First, the integration of more experimental data tailored to specific research needs will be prioritized to refine and improve the accuracy of the support optimization engine. This will allow the platform to provide more reliable and context-specific recommendations. Second, the orientation feature should be refined by prioritizing the optimal solution at the top of the list, with a focus on minimizing support material, reducing printing time, and lowering overall costs. Additionally, dedicated libraries, similar to PySLM, will be developed to enable the generation of various support geometries, with a focus on topology optimization and the creation of custom, application-specific support structures. These additions will increase the flexibility and adaptability of the platform across different use cases. Finally, a key objective is to finalize the platform's communication with external simulation software (e.g., ANSYS or COMSOL), enabling users to perform real-time thermomechanical simulations directly within the platform environment. This integration will streamline the design-to-simulation workflow and significantly enhance the platform's value as a research and engineering tool.

Improvements to the exported STL file should also be considered. While the exported build job is currently printable, certain geometrical errors, particularly in the tooth area, can prevent simulation software from forming a solid object, thus hindering the simulation process. To address these minor geometric inaccuracies, future work should involve the use of mesh repair tools such as Meshmixer, Netfabb, or Magics to resolve issues like non-manifold edges and overlapping triangles. Additionally, improvements to the custom support generation library, particularly in the meshing algorithms or triangulation density, can enhance geometric precision in complex regions. These steps will not only improve the accuracy of the exported models but also enhance printability by ensuring better layer connection and part representation. Addressing these issues will be critical to ensuring smoother workflows and improving overall platform performance.

In conclusion, the proposed directions for future work present significant opportunities to enhance the efficiency, reliability, and practicality of support structures in metal additive manufacturing, particularly in PBF-LB processes. By refining support optimization methodologies, improving scalability, and incorporating real-time process conditions into numerical models, this research aims to deliver more accurate and application-driven solutions. The continued development of the web-based support generation and optimization platform will play a key role in achieving these goals, focusing on the integration of extensive experimental data, refinement of the orientation feature, efficient communication with simulation software, resolution of geometric issues in exported STL files, and the introduction of new design principles tailored to a broader range of printing scenarios. While the proposed design principles have shown strong potential, their current limitations, such as dependence on specific geometries and materials, will be addressed through expanded datasets, simulation integration, and more adaptable optimization rules. Collectively, these advancements are expected to reduce production costs, improve print quality, and expand the applicability of metal additive manufacturing technologies across industrial, research, and academic environments, enabling more innovative and reliable manufacturing outcomes.

Appendix A

DOE setup

		Factor 1	Factor 2	Factor 3	Factor 4	Factor 5	Response 1	Response 2	Response 3
Std	**Space Type**	**A: Tooth Height**	**B: Top Length**	**C: X, Y Hatching**	**D: Laser Speed**	**E: Angle**	**Support Volume**	**Support Removal**	**Warping**
		mm	mm	mm	mm/s	degC	mm^3	Effort	mm
1	Factorial	1	0,05	0,5	1000	0	4,9	1	1,83
2	Factorial	1	0,05	0,5	1000	0	4,9	1	1,83
3	Factorial	4	0,05	0,5	1000	0	4,6	n/a	2
4	Factorial	4	0,05	0,5	1000	0	4,6	n/a	2
5	Factorial	1	0,3	0,5	1000	0	5	3	1,27
6	Factorial	1	0,3	0,5	1000	0	5	3	1,27
7	Factorial	4	0,3	0,5	1000	0	4,8	3	1,13
8	Factorial	4	0,3	0,5	1000	0	4,8	3	1,13
9	Factorial	1	0,05	2,5	1000	0	1,4	n/a	2
10	Factorial	1	0,05	2,5	1000	0	1,4	n/a	2
11	Factorial	4	0,05	2,5	1000	0	1,3	n/a	2
12	Factorial	4	0,05	2,5	1000	0	1,3	n/a	2
13	Factorial	1	0,3	2,5	1000	0	1,4	n/a	2
14	Factorial	1	0,3	2,5	1000	0	1,4	n/a	2
15	Factorial	4	0,3	2,5	1000	0	1,4	n/a	2
16	Factorial	4	0,3	2,5	1000	0	1,4	n/a	2
17	Factorial	1	0,05	0,5	1800	0	4,9	1	1,2
18	Factorial	1	0,05	0,5	1800	0	4,9	1	1,2
19	Factorial	4	0,05	0,5	1800	0	4,5	n/a	2
20	Factorial	4	0,05	0,5	1800	0	4,5	n/a	2
21	Factorial	1	0,3	0,5	1800	0	5	3	1,37
22	Factorial	1	0,3	0,5	1800	0	5	3	1,37
23	Factorial	4	0,3	0,5	1800	0	4,8	3	1,27
24	Factorial	4	0,3	0,5	1800	0	4,8	3	1,27
25	Factorial	1	0,05	2,5	1800	0	1,4	n/a	2
26	Factorial	1	0,05	2,5	1800	0	1,4	n/a	2
27	Factorial	4	0,05	2,5	1800	0	1,3	n/a	2
28	Factorial	4	0,05	2,5	1800	0	1,3	n/a	2
29	Factorial	1	0,3	2,5	1800	0	1,4	n/a	2
30	Factorial	1	0,3	2,5	1800	0	1,4	n/a	2
31	Factorial	4	0,3	2,5	1800	0	1,3	n/a	2
32	Factorial	4	0,3	2,5	1800	0	1,3	n/a	2

33	Factorial	1	0,05	0,5	1000	45	3,5	1	1,43
34	Factorial	1	0,05	0,5	1000	45	3,5	1	1,43
35	Factorial	4	0,05	0,5	1000	45	3,2	1	0,4
36	Factorial	4	0,05	0,5	1000	45	3,2	1	0,4
37	Factorial	1	0,3	0,5	1000	45	3,6	3	0,47
38	Factorial	1	0,3	0,5	1000	45	3,6	3	0,47
39	Factorial	4	0,3	0,5	1000	45	3,5	3	1,23
40	Factorial	4	0,3	0,5	1000	45	3,5	3	1,23
41	Factorial	1	0,05	2,5	1000	45	1,1	1	0,37
42	Factorial	1	0,05	2,5	1000	45	1,1	1	0,37
43	Factorial	4	0,05	2,5	1000	45	1	1	0,3
44	Factorial	4	0,05	2,5	1000	45	1	1	0,3
45	Factorial	1	0,3	2,5	1000	45	1,1	2	0,7
46	Factorial	1	0,3	2,5	1000	45	1,1	2	0,7
47	Factorial	4	0,3	2,5	1000	45	1	2	1,2
48	Factorial	4	0,3	2,5	1000	45	1	2	1,2
49	Factorial	1	0,05	0,5	1800	45	3,5	1	1,23
50	Factorial	1	0,05	0,5	1800	45	3,5	1	1,23
51	Factorial	4	0,05	0,5	1800	45	3,2	1	1,03
52	Factorial	4	0,05	0,5	1800	45	3,2	1	1,03
53	Factorial	1	0,3	0,5	1800	45	3,6	3	1,43
54	Factorial	1	0,3	0,5	1800	45	3,6	3	1,43
55	Factorial	4	0,3	0,5	1800	45	3,5	3	0,33
56	Factorial	4	0,3	0,5	1800	45	3,5	3	0,33
57	Factorial	1	0,05	2,5	1800	45	1,1	1	0,47
58	Factorial	1	0,05	2,5	1800	45	1,1	1	0,47
59	Factorial	4	0,05	2,5	1800	45	1	1	0,37
60	Factorial	4	0,05	2,5	1800	45	1	1	0,37
61	Factorial	1	0,3	2,5	1800	45	1,1	2	1
62	Factorial	1	0,3	2,5	1800	45	1,1	2	1
63	Factorial	4	0,3	2,5	1800	45	1	1	0,37
64	Factorial	4	0,3	2,5	1800	45	1	1	0,37
65	Axial	1	0,175	1,5	1400	22,5	1,9	2	0,67
66	Axial	1	0,175	1,5	1400	22,5	1,9	2	0,67
67	Axial	4	0,175	1,5	1400	22,5	1,8	1	0,6
68	Axial	4	0,175	1,5	1400	22,5	1,8	1	0,6
69	Axial	2,5	0,05	1,5	1400	22,5	1,8	1	0,13
70	Axial	2,5	0,05	1,5	1400	22,5	1,8	1	0,13
71	Axial	2,5	0,3	1,5	1400	22,5	1,9	2	0,9

72	Axial	2,5	0,3	1,5	1400	22,5	1,9	2	0,9
73	Axial	2,5	0,175	0,5	1400	22,5	4,6	1	0,97
74	Axial	2,5	0,175	0,5	1400	22,5	4,6	1	0,97
75	Axial	2,5	0,175	2,5	1400	22,5	1,3	1	0,27
76	Axial	2,5	0,175	2,5	1400	22,5	1,3	1	0,27
77	Axial	2,5	0,175	1,5	1000	22,5	1,8	1	0,57
78	Axial	2,5	0,175	1,5	1000	22,5	1,8	1	0,57
79	Axial	2,5	0,175	1,5	1800	22,5	1,9	1	0,47
80	Axial	2,5	0,175	1,5	1800	22,5	1,9	1	0,47
81	Axial	2,5	0,175	1,5	1400	0	1,9	n/a	2
82	Axial	2,5	0,175	1,5	1400	0	1,9	n/a	2
83	Axial	2,5	0,175	1,5	1400	45	1,5	1	0,63
84	Axial	2,5	0,175	1,5	1400	45	1,5	1	0,63
85	Center	2,5	0,175	1,5	1400	22,5	1,9	1	0,3
86	Center	2,5	0,175	1,5	1400	22,5	1,9	1	0,3
87	Center	2,5	0,175	1,5	1400	22,5	1,9	1	0,3
88	Center	2,5	0,175	1,5	1400	22,5	1,9	1	0,3
89	Center	2,5	0,175	1,5	1400	22,5	1,9	1	0,3
90	Center	2,5	0,175	1,5	1400	22,5	1,9	1	0,3

Fit statistics of Support Volume.

Std. Dev.	0.0741	**R^2**	0.9979
Mean	2.48	**Adjusted R^2**	0.9972
C.V. %	2.99	**Predicted R^2**	0.9962
-	-	**Adeq Precision**	112.346

Fit statistics of Support Removal.

Std. Dev.	0.1838	**R^2**	0.9669
Mean	1.62	**Adjusted R^2**	0.9529
C.V. %	11.36	**Predicted R^2**	0.9323
-	-	**Adeq Precision**	22.3995

Fit statistics of Warping Deformation.

Std. Dev.	0.2876	**R^2**	0.8503
Mean	1.08	**Adjusted R^2**	0.8069
C.V. %	26.68	**Predicted R^2**	0.7403
-	-	**Adeq Precision**	14.2794

Appendix B

1. Block Type - DOE

		Factor 1	Factor 2	Factor 3	Response 1	Response 2	Response 3	Response 4
Std	**Space Type**	**A: Tooth Height**	**B: Tooth Top Length**	**C: X, Y Hatching**	**Support Volume**	**Plate Temperature**	**Thermal Stress**	**Overhang Displacement**
		(mm)	(mm)	(mm)	(mm^3)	(degC)	(N/m$^{2)}$	(mm)
1	Factorial	1	0,1	0,5	4600,8	1020	5,32E+09	0,431
2	Factorial	4	0,1	0,5	4243,3	982	5,08E+09	0,431
3	Factorial	1	0,5	0,5	4643,3	1030	5,54E+09	0,436
4	Factorial	4	0,5	0,5	4413,2	1020	5,3E+09	0,43
5	Factorial	1	0,1	2	1559,6	832	3,6E+09	0,411
6	Factorial	4	0,1	2	1438,4	792	3,34E+09	0,441
7	Factorial	1	0,5	2	1574	844	3,64E+09	0,414
8	Factorial	4	0,5	2	1496	831	3,72E+09	0,425
9	Axial	1	0,3	1,25	2350,2	913	4,1E+09	0,419
10	Axial	4	0,3	1,25	2200,8	891	4,2E+09	0,426
11	Axial	2,5	0,1	1,25	2248,5	883	4,15E+09	0,418
12	Axial	2,5	0,5	1,25	2302,5	910	4,3E+09	0,418
13	Axial	2,5	0,3	0,5	4475,2	1020	5,38E+09	0,429
14	Axial	2,5	0,3	2	1517	830	3,59E+09	0,416
15	Center	2,5	0,3	1,25	2275,5	901	4,26E+09	0,417

Support Volume – ANOVA for Quadratic model

Source	Sum of Squares	df	Mean Square	F-value	p-value	
Model	2,373E+07	9	2,637E+06	6946,07	< 0.0001	significant
A-Tooth Height	87647,04	1	87647,04	230,88	< 0.0001	
B-Tooth Top Length	11451,46	1	11451,46	30,17	0,0027	
C-X, Y Hatching	2,188E+07	1	2,188E+07	57628,51	< 0.0001	
AB	3638,05	1	3638,05	9,58	0,0270	
AC	18856,82	1	18856,82	49,67	0,0009	
BC	2464,02	1	2464,02	6,49	0,0514	
A^2	0,0003	1	0,0003	8,363E-07	0,9993	
B^2	0,0003	1	0,0003	8,363E-07	0,9993	
C^2	1,335E+06	1	1,335E+06	3517,25	< 0.0001	
Residual	1898,09	5	379,62			
Cor Total	2,373E+07	14				

Factor coding is **Coded**.
Sum of squares is **Type III – Partial**
The **Model F-value** of 6946,07 implies the model is significant. There is only a 0,01% chance that an F-value this large could occur due to noise.
P-values less than 0,0500 indicate model terms are significant. In this case A, B, C, AB, AC, C^2 are significant model terms. Values greater than 0.1000 indicate the model terms are not significant. If there are many insignificant model terms (not counting those required to support hierarchy), model reduction may improve your model.

Plate Temperature – ANOVA for Quadratic model

Source	Sum of Squares	df	Mean Square	F-value	p-value	
Model	93900,11	9	10433,35	5911,24	< 0.0001	significant
A-Tooth Height	1512,90	1	1512,90	857,17	< 0.0001	
B-Tooth Top Length	1587,60	1	1587,60	899,49	< 0.0001	
C-X, Y Hatching	88924,90	1	88924,90	50382,38	< 0.0001	
AB	378,13	1	378,13	214,24	< 0.0001	
AC	3,13	1	3,13	1,77	0,2408	
BC	1,13	1	1,13	0,6374	0,4609	
A^2	0,0714	1	0,0714	0,0405	0,8485	
B^2	82,57	1	82,57	46,78	0,0010	
C^2	1340,64	1	1340,64	759,57	< 0.0001	
Residual	8,82	5	1,76			
Cor Total	93908,93	14				

Factor coding is **Coded**.
Sum of squares is **Type III – Partial**
The **Model F-value** of 5911,24 implies the model is significant. There is only a 0,01% chance that an F-value this large could occur due to noise.
P-values less than 0,0500 indicate model terms are significant. In this case A, B, C, AB, B^2, C^2 are significant model terms. Values greater than 0.1000 indicate the model terms are not significant. If there are many insignificant model terms (not counting those required to support hierarchy), model reduction may improve your model.

Thermal Stress – ANOVA for Quadratic model

Source	Sum of Squares	df	Mean Square	F-value	p-value	
Model	7,998E+18	9	8,887E+17	93,92	< 0.0001	significant
A-Tooth Height	3,136E+16	1	3,136E+16	3,31	0,1283	
B-Tooth Top Length	1,020E+17	1	1,020E+17	10,78	0,0219	
C-X, Y Hatching	7,621E+18	1	7,621E+18	805,50	< 0.0001	
AB	1,445E+16	1	1,445E+16	1,53	0,2714	
AC	1,125E+16	1	1,125E+16	1,19	0,3253	
BC	5,000E+13	1	5,000E+13	0,0053	0,9449	
A^2	1,068E+16	1	1,068E+16	1,13	0,3366	
B^2	2,865E+14	1	2,865E+14	0,0303	0,8687	
C^2	1,882E+17	1	1,882E+17	19,89	0,0066	
Residual	4,731E+16	5	9,462E+15			
Cor Total	8,045E+18	14				

Factor coding is **Coded**.
Sum of squares is **Type III – Partial**
The **Model F-value** of 93,92 implies the model is significant. There is only a 0,01% chance that an F-value this large could occur due to noise.
P-values less than 0,0500 indicate model terms are significant. In this case B, C, C^2 are significant model terms. Values greater than 0.1000 indicate the model terms are not significant. If there are many insignificant model terms (not counting those required to support hierarchy), model reduction may improve your model.

Overhang Displacement – ANOVA for Quadratic model

Source	Sum of Squares	df	Mean Square	F-value	p-value	
Model	0,0010	9	0,0001	19,06	0,0023	significant
A-Tooth Height	0,0002	1	0,0002	28,95	0,0030	
B-Tooth Top Length	8,100E-06	1	8,100E-06	1,33	0,3011	
C-X, Y Hatching	0,0003	1	0,0003	41,02	0,0014	
AB	0,0001	1	0,0001	12,82	0,0159	
AC	0,0003	1	0,0003	45,31	0,0011	
BC	0,0000	1	0,0000	5,93	0,0590	
A^2	0,0001	1	0,0001	9,63	0,0267	
B^2	1,984E-07	1	1,984E-07	0,0326	0,8639	
C^2	0,0001	1	0,0001	9,63	0,0267	
Residual	0,0000	5	6,094E-06			
Cor Total	0,0011	14				

Factor coding is **Coded**.
Sum of squares is **Type III – Partial**
The **Model F-value** of 19,06 implies the model is significant. There is only a 0,23% chance that an F-value this large could occur due to noise.
P-values less than 0,0500 indicate model terms are significant. In this case A, C, AB, AC, A^2, C^2 are significant model terms. Values greater than 0.1000 indicate the model terms are not significant. If there are many insignificant model terms (not counting those required to support hierarchy), model reduction may improve your model.

2. Line Type - DOE

		Factor 1	Factor 2	Factor 3	Response 1	Response 2	Response 3	Response 4
Std	**Space Type**	**A: Tooth Height** (mm)	**B: Tooth Top Length** (mm)	**C: Cross Line Interval** (mm)	**Support Volume** (mm^3)	**Plate Temperature** (degC)	**Thermal Stress** (N/m^2)	**Overhang Displacement** (mm)
1	Factorial	1	0,1	0,5	2339,4	947	8,31E+09	0,426
2	Factorial	4	0,1	0,5	2157,6	903	8,19E+09	0,444
3	Factorial	1	0,5	0,5	2361	959	8,82E+09	0,431
4	Factorial	4	0,5	0,5	2244	944	8,26E+09	0,433
5	Factorial	1	0,1	2	857,8	783	4,8E+09	0,412
6	Factorial	4	0,1	2	791,1	762	4,73E+09	0,454
7	Factorial	1	0,5	2	865,7	795	4,87E+09	0,414
8	Factorial	4	0,5	2	822,8	780	4,84E+09	0,432
9	Axial	1	0,3	1,25	1175,1	818	5,64E+09	0,392
10	Axial	4	0,3	1,25	1100,4	796	5,61E+09	0,414
11	Axial	2,5	0,1	1,25	1124,3	789	5,57E+09	0,404
12	Axial	2,5	0,5	1,25	1151,3	815	5,69E+09	0,395
13	Axial	2,5	0,3	0,5	2275,5	943	8,64E+09	0,428
14	Axial	2,5	0,3	2	834,4	779	4,84E+09	0,419
15	Center	2,5	0,3	1,25	1137,8	807	5,66E+09	0,396

Support Volume – ANOVA for Quadratic model

Source	Sum of Squares	df	Mean Square	F-value	p-value	
Model	5,805E+06	9	6,450E+05	5867,22	< 0.0001	significant
A-Tooth Height	23338,56	1	23338,56	212,31	< 0.0001	
B-Tooth Top Length	3048,52	1	3048,52	27,73	0,0033	
C-Cross Line Interval	5,192E+06	1	5,192E+06	47233,34	< 0.0001	
AB	981,25	1	981,25	8,93	0,0305	
AC	4474,58	1	4474,58	40,71	0,0014	
BC	584,82	1	584,82	5,32	0,0692	
A^2	0,0039	1	0,0039	0,0000	0,9955	
B^2	0,0003	1	0,0003	2,888E-06	0,9987	
C^2	4,475E+05	1	4,475E+05	4070,79	< 0.0001	
Residual	549,63	5	109,93			
Cor Total	5,805E+06	14				

Factor coding is **Coded**.
Sum of squares is **Type III – Partial**
The **Model F-value** of 5867,22 implies the model is significant. There is only a 0,01% chance that an F-value this large could occur due to noise.
P-values less than 0,0500 indicate model terms are significant. In this case A, B, C, AB, AC, C^2 are significant model terms. Values greater than 0.1000 indicate the model terms are not significant. If there are many insignificant model terms (not counting those required to support hierarchy), model reduction may improve your model.

Plate Temperature – ANOVA for Quadratic model

Source	Sum of Squares	df	Mean Square	F-value	p-value	
Model	76298,00	9	8477,56	454,14	< 0.0001	significant
A-Tooth Height	1368,90	1	1368,90	73,33	0,0004	
B-Tooth Top Length	1188,10	1	1188,10	63,65	0,0005	
C-Cross Line Interval	63520,90	1	63520,90	3402,80	< 0.0001	
AB	153,13	1	153,13	8,20	0,0352	
AC	66,13	1	66,13	3,54	0,1186	
BC	66,13	1	66,13	3,54	0,1186	
A^2	4,96	1	4,96	0,2657	0,6282	
B^2	33,53	1	33,53	1,80	0,2378	
C^2	7888,96	1	7888,96	422,61	< 0.0001	
Residual	93,34	5	18,67			
Cor Total	76391,33	14				

Factor coding is **Coded**.
Sum of squares is **Type III – Partial**
The **Model F-value** of 454,14 implies the model is significant. There is only a 0,01% chance that an F-value this large could occur due to noise.
P-values less than 0,0500 indicate model terms are significant. In this case A, B, C, AB, C^2 are significant model terms. Values greater than 0.1000 indicate the model terms are not significant. If there are many insignificant model terms (not counting those required to support hierarchy), model reduction may improve your model.

Thermal Stress – ANOVA for Quadratic model

Source	Sum of Squares	df	Mean Square	F-value	p-value	
Model	3,647E+19	9	4,052E+18	331,73	< 0.0001	significant
A-Tooth Height	6,561E+16	1	6,561E+16	5,37	0,0683	
B-Tooth Top Length	7,744E+16	1	7,744E+16	6,34	0,0533	
C-Cross Line Interval	3,291E+19	1	3,291E+19	2693,92	< 0.0001	
AB	2,000E+16	1	2,000E+16	1,64	0,2568	
AC	4,205E+16	1	4,205E+16	3,44	0,1227	
BC	2,000E+16	1	2,000E+16	1,64	0,2568	
A^2	1,162E+16	1	1,162E+16	0,9513	0,3742	
B^2	9,956E+15	1	9,956E+15	0,8150	0,4080	
C^2	2,823E+18	1	2,823E+18	231,11	< 0.0001	
Residual	6,107E+16	5	1,221E+16			
Cor Total	3,653E+19	14				

Factor coding is **Coded**.
Sum of squares is **Type III – Partial**
The **Model F-value** of 331,73 implies the model is significant. There is only a 0,01% chance that an F-value this large could occur due to noise.
P-values less than 0,0500 indicate model terms are significant. In this case C, C^2 are significant model terms. Values greater than 0.1000 indicate the model terms are not significant. If there are many insignificant model terms (not counting those required to support hierarchy), model reduction may improve your model.

Overhang Displacement – ANOVA for Quadratic model

Source	Sum of Squares	df	Mean Square	F-value	p-value	
Model	0,0046	9	0,0005	136,04	< 0.0001	significant
A-Tooth Height	0,0010	1	0,0010	275,56	< 0.0001	
B-Tooth Top Length	0,0001	1	0,0001	32,45	0,0023	
C-Cross Line Interval	0,0001	1	0,0001	25,45	0,0039	
AB	0,0002	1	0,0002	52,97	0,0008	
AC	0,0002	1	0,0002	52,97	0,0008	
BC	0,0000	1	0,0000	6,49	0,0514	
A^2	0,0001	1	0,0001	21,02	0,0059	
B^2	0,0000	1	0,0000	2,88	0,1506	
C^2	0,0017	1	0,0017	462,37	< 0.0001	
Residual	0,0000	5	3,776E-06			
Cor Total	0,0046	14				

Factor coding is **Coded**.
Sum of squares is **Type III – Partial**
The **Model F-value** of 136,04 implies the model is significant. There is only a 0,01% chance that an F-value this large could occur due to noise.
P-values less than 0,0500 indicate model terms are significant. In this case A, B, C, AB, AC, A^2, C^2 are significant model terms. Values greater than 0.1000 indicate the model terms are not significant. If there are many insignificant model terms (not counting those required to support hierarchy), model reduction may improve your model.

3. Contour Type - DOE

		Factor 1	Factor 2	Factor 3	Response 1	Response 2	Response 3	Response 4
Std	Space Type	A: Tooth Height (mm)	B: Tooth Top Length (mm)	C: Contour Offset (mm)	Support Volume (mm³)	Plate Temperature (degC)	Thermal Stress (N/mm²)	Overhang Displacement (mm)
1	Factorial	1	0,1	0,5	2336,4	1010	5,23E+09	0,431
2	Factorial	4	0,1	0,5	2155	966	5,04E+09	0,465
3	Factorial	1	0,5	0,5	2358	1030	5,28E+09	0,434
4	Factorial	4	0,5	0,5	2241,4	1020	5,26E+09	0,446
5	Factorial	1	0,1	2	858	802	3,94E+09	0,416
6	Factorial	4	0,1	2	792	775	3,82E+09	0,463
7	Factorial	1	0,5	2	866	813	3,94E+09	0,416
8	Factorial	4	0,5	2	824	800	3,87E+09	0,441
9	Axial	1	0,3	1,25	1217,4	886	4,15E+09	0,421
10	Axial	4	0,3	1,25	1140,1	862	4,01E+09	0,451
11	Axial	2,5	0,1	1,25	1164,8	854	4,03E+09	0,44
12	Axial	2,5	0,5	1,25	1192,8	882	4,13E+09	0,427
13	Axial	2,5	0,3	0,5	2272,7	1010	5,29E+09	0,436
14	Axial	2,5	0,3	2	835	799	3,92E+09	0,426
15	Center	2,5	0,3	1,25	1178,8	874	4,11E+09	0,43

Support Volume – ANOVA for Quadratic model

Source	Sum of Squares	df	Mean Square	F-value	p-value	
Model	5,669E+06	9	6,299E+05	6633,98	< 0.0001	significant
A-Tooth Height	23357,89	1	23357,89	246,01	< 0.0001	
B-Tooth Top Length	3097,60	1	3097,60	32,62	0,0023	
C-Contour Offset	5,167E+06	1	5,167E+06	54424,44	< 0.0001	
AB	985,68	1	985,68	10,38	0,0234	
AC	4512,50	1	4512,50	47,53	0,0010	
BC	578,00	1	578,00	6,09	0,0567	
A²	0,0020	1	0,0020	0,0000	0,9965	
B²	0,0013	1	0,0013	0,0000	0,9972	
C²	3,617E+05	1	3,617E+05	3809,97	< 0.0001	
Residual	474,74	5	94,95			
Cor Total	5,669E+06	14				

Factor coding is **Coded**.
Sum of squares is **Type III – Partial**
The **Model F-value** of 6633,98 implies the model is significant. There is only a 0,01% chance that an F-value this large could occur due to noise.
P-values less than 0,0500 indicate model terms are significant. In this case A, B, C, AB, AC, C² are significant model terms. Values greater than 0.1000 indicate the model terms are not significant. If there are many insignificant model terms (not counting those required to support hierarchy), model reduction may improve your model.

Plate Temperature – ANOVA for Quadratic model

Source	Sum of Squares	df	Mean Square	F-value	p-value	
Model	1,166E+05	9	12960,49	1200,54	< 0.0001	significant
A-Tooth Height	1392,40	1	1392,40	128,98	< 0.0001	
B-Tooth Top Length	1904,40	1	1904,40	176,41	< 0.0001	
C-Contour Offset	1,096E+05	1	1,096E+05	10154,26	< 0.0001	
AB	288,00	1	288,00	26,68	0,0036	
AC	24,50	1	24,50	2,27	0,1923	
BC	180,50	1	180,50	16,72	0,0095	
A^2	6,22	1	6,22	0,5764	0,4820	
B^2	50,79	1	50,79	4,71	0,0822	
C^2	2642,29	1	2642,29	244,76	< 0.0001	
Residual	53,98	5	10,80			
Cor Total	1,167E+05	14				

Factor coding is **Coded**.
Sum of squares is **Type III – Partial**
The **Model F-value** of 1200,54 implies the model is significant. There is only a 0,01% chance that an F-value this large could occur due to noise.
P-values less than 0,0500 indicate model terms are significant. In this case A, B, C, AB, BC, C^2 are significant model terms. Values greater than 0.1000 indicate the model terms are not significant. If there are many insignificant model terms (not counting those required to support hierarchy), model reduction may improve your model.

Thermal Stress – ANOVA for Quadratic model

Source	Sum of Squares	df	Mean Square	F-value	p-value	
Model	5,180E+18	9	5,755E+17	712,12	< 0.0001	significant
A-Tooth Height	2,916E+16	1	2,916E+16	36,08	0,0018	
B-Tooth Top Length	1,764E+16	1	1,764E+16	21,83	0,0055	
C-Contour Offset	4,369E+18	1	4,369E+18	5405,95	< 0.0001	
AB	6,050E+15	1	6,050E+15	7,49	0,0410	
AC	5,000E+13	1	5,000E+13	0,0619	0,8135	
BC	6,050E+15	1	6,050E+15	7,49	0,0410	
A^2	2,146E+15	1	2,146E+15	2,66	0,1641	
B^2	2,146E+15	1	2,146E+15	2,66	0,1641	
C^2	6,329E+17	1	6,329E+17	783,07	< 0.0001	
Residual	4,041E+15	5	8,082E+14			
Cor Total	5,184E+18	14				

Factor coding is **Coded**.
Sum of squares is **Type III – Partial**
The **Model F-value** of 712,12 implies the model is significant. There is only a 0,01% chance that an F-value this large could occur due to noise.
P-values less than 0,0500 indicate model terms are significant. In this case A, B, C, AB, BC, C^2 are significant model terms. Values greater than 0.1000 indicate the model terms are not significant. If there are many insignificant model terms (not counting those required to support hierarchy), model reduction may improve your model.

Overhang Displacement – ANOVA for Quadratic model

Source	Sum of Squares	df	Mean Square	F-value	p-value	
Model	0,0032	9	0,0004	329,32	< 0.0001	significant
A-Tooth Height	0,0022	1	0,0022	2028,15	< 0.0001	
B-Tooth Top Length	0,0003	1	0,0003	240,83	< 0.0001	
C-Contour Offset	0,0003	1	0,0003	231,48	< 0.0001	
AB	0,0002	1	0,0002	224,07	< 0.0001	
AC	0,0001	1	0,0001	78,24	0,0003	
BC	4,500E-06	1	4,500E-06	4,17	0,0967	
A^2	0,0001	1	0,0001	67,72	0,0004	
B^2	0,0000	1	0,0000	19,11	0,0072	
C^2	2,857E-07	1	2,857E-07	0,2646	0,6289	
Residual	5,400E-06	5	1,080E-06			
Cor Total	0,0032	14				

Factor coding is **Coded**.
Sum of squares is **Type III – Partial**
The **Model F-value** of 329,32 implies the model is significant. There is only a 0,01% chance that an F-value this large could occur due to noise.
P-values less than 0,0500 indicate model terms are significant. In this case A, B, C, AB, AC, A^2, B^2 are significant model terms. Values greater than 0.1000 indicate the model terms are not significant. If there are many insignificant model terms (not counting those required to support hierarchy), model reduction may improve your model.

4. Cones Type - DOE

		Factor 1	Factor 2	Factor 3	Response 1	Response 2	Response 3	Response 4
Std	**Space Type**	**A: Contact Platform**	**B: Contact Part**	**C: Spacing**	**Support Volume**	**Plate Temperature**	**Thermal Stress**	**Overhang Displacement**
		D mm	D mm	mm	mm^3	degC	N/mm^2	mm
1	Factorial	1	0,2	0,5	1278,4	765	1,8E+10	0,472
2	Factorial	2	0,2	0,5	1887,8	756	2,41E+10	0,46
3	Factorial	1	0,4	0,5	1600,2	834	1,99E+10	0,477
4	Factorial	2	0,4	0,5	2104,1	818	2,74E+10	0,467
5	Factorial	1	0,2	2	417,4	724	6,26E+10	0,458
6	Factorial	2	0,2	2	839	729	8,86E+09	0,45
7	Factorial	1	0,4	2	522,5	743	2,19E+10	0,464
8	Factorial	2	0,4	2	935,2	748	6,67E+09	0,455
9	Axial	1	0,3	1,25	729,3	749	1,14E+10	0,463
10	Axial	2	0,3	1,25	1200,3	751	5,95E+09	0,454
11	Axial	1,5	0,2	1,25	868,6	736	6,77E+09	0,453
12	Axial	1,5	0,4	1,25	1006,1	760	7,01E+09	0,462
13	Axial	1,5	0,3	0,5	1766,1	782	1,45E+10	0,466
14	Axial	1,5	0,3	2	715,2	739	6,61E+09	0,457
15	Center	1,5	0,3	1,25	934,1	749	6,39E+09	0,459

Support Volume – ANOVA for Quadratic model

Source	Sum of Squares	df	Mean Square	F-value	p-value	
Model	3,625E+06	9	4,028E+05	617,59	< 0.0001	significant
A-Contact Platform	5,850E+05	1	5,850E+05	896,86	< 0.0001	
B-Contact Part	76895,36	1	76895,36	117,90	0,0001	
C-Spacing	2,712E+06	1	2,712E+06	4157,42	< 0.0001	
AB	1635,92	1	1635,92	2,51	0,1741	
AC	9730,13	1	9730,13	14,92	0,0119	
BC	14179,28	1	14179,28	21,74	0,0055	
A^2	28,19	1	28,19	0,0432	0,8435	
B^2	2433,20	1	2433,20	3,73	0,1113	
C^2	1,910E+05	1	1,910E+05	292,84	< 0.0001	
Residual	3261,15	5	652,23			
Cor Total	3,629E+06	14				

Factor coding is **Coded**.
Sum of squares is **Type III – Partial**
The **Model F-value** of 617,59 implies the model is significant. There is only a 0,01% chance that an F-value this large could occur due to noise.
P-values less than 0,0500 indicate model terms are significant. In this case A, B, C, AC, BC, C^2 are significant model terms. Values greater than 0.1000 indicate the model terms are not significant. If there are many insignificant model terms (not counting those required to support hierarchy), model reduction may improve your model.

Plate Temperature – ANOVA for Quadratic model

Source	Sum of Squares	df	Mean Square	F-value	p-value	
Model	13138,91	9	1459,88	30,82	0,0007	significant
A-Contact Platform	16,90	1	16,90	0,3568	0,5763	
B-Contact Part	3724,90	1	3724,90	78,64	0,0003	
C-Spacing	7398,40	1	7398,40	156,20	< 0.0001	
AB	6,13	1	6,13	0,1293	0,7338	
AC	153,13	1	153,13	3,23	0,1321	
BC	1081,12	1	1081,12	22,83	0,0050	
A^2	20,64	1	20,64	0,4358	0,5383	
B^2	1,79	1	1,79	0,0377	0,8537	
C^2	457,14	1	457,14	9,65	0,0267	
Residual	236,82	5	47,36			
Cor Total	13375,73	14				

Factor coding is **Coded**.
Sum of squares is **Type III – Partial**
The **Model F-value** of 30,82 implies the model is significant. There is only a 0,07% chance that an F-value this large could occur due to noise.
P-values less than 0,0500 indicate model terms are significant. In this case B, C, BC, C^2 are significant model terms. Values greater than 0.1000 indicate the model terms are not significant. If there are many insignificant model terms (not counting those required to support hierarchy), model reduction may improve your model.

Thermal Stress – ANOVA for Quadratic model

Source	Sum of Squares	df	Mean Square	F-value	p-value	
Model	2,725E+21	9	3,027E+20	5,03	0,0451	significant
A-Contact Platform	3,699E+20	1	3,699E+20	6,14	0,0560	
B-Contact Part	1,403E+20	1	1,403E+20	2,33	0,1875	
C-Spacing	7,508E+17	1	7,508E+17	0,0125	0,9154	
AB	1,991E+20	1	1,991E+20	3,31	0,1287	
AC	8,522E+20	1	8,522E+20	14,15	0,0131	
BC	2,891E+20	1	2,891E+20	4,80	0,0800	
A^2	1,217E+20	1	1,217E+20	2,02	0,2144	
B^2	6,675E+19	1	6,675E+19	1,11	0,3407	
C^2	1,973E+20	1	1,973E+20	3,28	0,1301	
Residual	3,012E+20	5	6,023E+19			
Cor Total	3,026E+21	14				

Factor coding is **Coded**.
Sum of squares is **Type III – Partial**
The **Model F-value** of 5,03 implies the model is significant. There is only a 4,51% chance that an F-value this large could occur due to noise.
P-values less than 0,0500 indicate model terms are significant. In this case AC is a significant model term. Values greater than 0.1000 indicate the model terms are not significant. If there are many insignificant model terms (not counting those required to support hierarchy), model reduction may improve your model.

Overhang Displacement – ANOVA for Quadratic model

Source	Sum of Squares	df	Mean Square	F-value	p-value	
Model	0,0007	9	0,0001	34,76	0,0006	significant
A-Contact Platform	0,0002	1	0,0002	97,42	0,0002	
B-Contact Part	0,0001	1	0,0001	43,30	0,0012	
C-Spacing	0,0003	1	0,0003	142,24	< 0.0001	
AB	1,250E-07	1	1,250E-07	0,0529	0,8273	
AC	3,125E-06	1	3,125E-06	1,32	0,3023	
BC	1,250E-07	1	1,250E-07	0,0529	0,8273	
A^2	2,571E-06	1	2,571E-06	1,09	0,3448	
B^2	0,0000	1	0,0000	0,0000	1.0000	
C^2	0,0000	1	0,0000	17,40	0,0087	
Residual	0,0000	5	2,365E-06			
Cor Total	0,0008	14				

Factor coding is **Coded**.
Sum of squares is **Type III – Partial**
The **Model F-value** of 34,76 implies the model is significant. There is only a 0,06% chance that an F-value this large could occur due to noise.
P-values less than 0,0500 indicate model terms are significant. In this case A, B, C, C^2 are significant model terms. Values greater than 0.1000 indicate the model terms are not significant. If there are many insignificant model terms (not counting those required to support hierarchy), model reduction may improve your model.

Appendix C

Actual equations of Block-type support structures

$$\begin{aligned}
&\mathit{Thermal\ Stress}\\
&\quad = 6{,}42084e + 09 + 2{,}17099e + 07 * \mathit{Tooth\ Height} + 1{,}33333e + 07\\
&\quad * \mathit{Tooth\ Top\ Length} - 2{,}44480e + 09 * \mathit{X, Y\ Hatching} + 1{,}41667e + 08\\
&\quad * \mathit{Tooth\ Height} * \mathit{Tooth\ Top\ Length} + 3{,}33333e + 07 * \mathit{Tooth\ Height}\\
&\quad * \mathit{X, Y\ Hatching} - 1{,}66667e + 07 * \mathit{Tooth\ Top\ Length} * \mathit{X, Y\ Hatching}\\
&\quad - 2{,}86420e + 07 * \mathit{Tooth\ Height}^2 + 2{,}63889e + 08 * \mathit{Tooth\ Top\ Length}^2\\
&\quad + 4{,}80988e + 08 * \mathit{X, Y\ Hatching}^2
\end{aligned}$$

$$\begin{aligned}
&\mathit{Plate\ Temperature}\\
&\quad = 1127{,}30185 - 14{,}01019 * \mathit{Tooth\ Height} + 87{,}58333\\
&\quad * \mathit{Tooth\ Top\ Length} - 226{,}57593 * \mathit{X, Y\ Hatching} + 22{,}91667\\
&\quad * \mathit{Tooth\ Height} * \mathit{Tooth\ Top\ Length} - 0{,}555556 * \mathit{Tooth\ Height}\\
&\quad * \mathit{X, Y\ Hatching} + 2{,}50000 * \mathit{Tooth\ Top\ Length} * \mathit{X, Y\ Hatching}\\
&\quad - 0{,}074074 * \mathit{Tooth\ Height}^2 - 141{,}66667 * \mathit{Tooth\ Top\ Length}^2\\
&\quad + 40{,}59259 * \mathit{X, Y\ Hatching}^2
\end{aligned}$$

$$\begin{aligned}
&\mathit{Overhang\ Displacement}\\
&\quad = 0{,}450624 - 0{,}011220 * \mathit{Tooth\ Height} + 0{,}035083 * \mathit{Tooth\ Top\ Length}\\
&\quad - 0{,}036707 * \mathit{X, Y\ Hatching} - 0{,}010417 * \mathit{Tooth\ Height}\\
&\quad * \mathit{Tooth\ Top\ Length} + 0{,}005222 * \mathit{Tooth\ Height} * \mathit{X, Y\ Hatching}\\
&\quad - 0{,}014167 * \mathit{Tooth\ Top\ Length} * \mathit{X, Y\ Hatching} + 0{,}002123\\
&\quad * \mathit{Tooth\ Height}^2 + 0{,}006944 * \mathit{Tooth\ Top\ Length}^2 + 0{,}008494\\
&\quad * \mathit{X, Y\ Hatching}^2
\end{aligned}$$

Actual equations of Line-type support structures

$$\begin{aligned}
&\mathit{Support\ Volume}\\
&\quad = 3623{,}77256 - 69{,}47302 * \mathit{Tooth\ Height} + 66{,}09167\\
&\quad * \mathit{Tooth\ Top\ Length} - 2850{,}26494 * \mathit{Cross\ Line\ Interval} + 36{,}91667\\
&\quad * \mathit{Tooth\ Height} * \mathit{Tooth\ Top\ Length} + 21{,}02222 * \mathit{Tooth\ Height}\\
&\quad * \mathit{Cross\ Line\ Interval} - 57{,}00000 * \mathit{Tooth\ Top\ Length}\\
&\quad * \mathit{Cross\ Line\ Interval} - 0{,}017284 * \mathit{Tooth\ Height}^2 + 0{,}277778\\
&\quad * \mathit{Tooth\ Top\ Length}^2 + 741{,}61975 * \mathit{Cross\ Line\ Interval}^2
\end{aligned}$$

$$\begin{aligned}
&\mathit{Thermal\ Stress}\\
&\quad = 1{,}12473e + 10 + 6{,}48272e + 07 * \mathit{Tooth\ Height} + 2{,}20667e + 09\\
&\quad * \mathit{Tooth\ Top\ Length} - 7{,}13657e + 09 * \mathit{Cross\ Line\ Interval} - 1{,}66667e\\
&\quad + 08 * \mathit{Tooth\ Height} * \mathit{Tooth\ Top\ Length} + 6{,}44444e + 07\\
&\quad * \mathit{Tooth\ Height} * \mathit{Cross\ Line\ Interval} - 3{,}33333e + 08\\
&\quad * \mathit{Tooth\ Top\ Length} * \mathit{Cross\ Line\ Interval} - 2{,}98765e + 07\\
&\quad * \mathit{Tooth\ Height}^2 - 1{,}55556e + 09 * \mathit{Tooth\ Top\ Length}^2 + 1{,}86272e + 09\\
&\quad * \mathit{Cross\ Line\ Interval}^2
\end{aligned}$$

$$
\begin{aligned}
&\mathit{Plate\ Temperature}\\
&\quad = 1103{,}19938 - 18{,}45586 * \mathit{Tooth\ Height}\ 96{,}16667 * \mathit{Tooth\ Top\ Length}\\
&\quad - 353{,}07840 * \mathit{Cross\ Line\ Interval} + 14{,}58333 * \mathit{Tooth\ Height}\\
&\quad * \mathit{Tooth\ Top\ Length} + 2{,}55556 * \mathit{Tooth\ Height} * \mathit{Cross\ Line\ Interval}\\
&\quad - 19{,}16667 * \mathit{Tooth\ Top\ Length} * \mathit{Cross\ Line\ Interval} + 0{,}617284\\
&\quad * \mathit{Tooth\ Height}^2 - 90{,}27778 * \mathit{Tooth\ Top\ Length}^2 + 98{,}46914\\
&\quad * \mathit{Cross\ Line\ Interval}^2
\end{aligned}
$$

$$
\begin{aligned}
&\mathit{Overhang\ Displacement}\\
&\quad = 0{,}480020 - 0{,}006101 * \mathit{Tooth\ Height} + 0{,}007917\\
&\quad * \mathit{Tooth\ Top\ Length} - 0{,}127547 * \mathit{Cross\ Line\ Interval} - 0{,}016667\\
&\quad * \mathit{Tooth\ Height} * \mathit{Tooth\ Top\ Length} + 0{,}004444 * \mathit{Tooth\ Height}\\
&\quad * \mathit{Cross\ Line\ Interval} - 0{,}011667 * \mathit{Tooth\ Top\ Length}\\
&\quad * \mathit{Cross\ Line\ Interval} + 0{,}002469 * \mathit{Tooth\ Height}^2 + 0{,}051389\\
&\quad * \mathit{Tooth\ Top\ Length}^2 + 0{,}046321 * \mathit{Cross\ Line\ Interval}^2
\end{aligned}
$$

Actual equations of Contour-type support structures

$$
\begin{aligned}
&\mathit{Support\ Volume}\\
&\quad = 3545{,}32790 - 69{,}64716 * \mathit{Tooth\ Height} + 66{,}00000\\
&\quad * \mathit{Tooth\ Top\ Length} - 2661{,}23210 * \mathit{Contour\ Offset} + 37{,}00000\\
&\quad * \mathit{Tooth\ Height} * \mathit{Tooth\ Top\ Length} + 21{,}11111 * \mathit{Tooth\ Height}\\
&\quad * \mathit{Contour\ Offset} - 56{,}66667 * \mathit{Tooth\ Top\ Length} * \mathit{Contour\ Offset}\\
&\quad - 0{,}012346 * \mathit{Tooth\ Height}^2 + 0{,}555556 * \mathit{Tooth\ Top\ Length}^2\\
&\quad + 666{,}79506 * \mathit{Contour\ Offset}^2
\end{aligned}
$$

$$
\begin{aligned}
&\mathit{Thermal\ Stress}\\
&\quad = 6{,}47756e + 09 - 2{,}08025e + 06 * \mathit{Tooth\ Height} + 6{,}43333e + 08\\
&\quad * \mathit{Tooth\ Top\ Length} - 3{,}03683e + 09 * \mathit{Contour\ Offset} + 9{,}16667e\\
&\quad + 07 * \mathit{Tooth\ Height} * \mathit{Tooth\ Top\ Length} + 2{,}22222e + 06\\
&\quad * \mathit{Tooth\ Height} * \mathit{Contour\ Offset} - 1{,}83333e + 08 * \mathit{Tooth\ Top\ Length}\\
&\quad * \mathit{Contour\ Offset} - 1{,}28395e + 07 * \mathit{Tooth\ Height}^2 - 7{,}22222e + 08\\
&\quad * \mathit{Tooth\ Top\ Length}^2 + 8{,}81975e + 08 * \mathit{Contour\ Offset}^2
\end{aligned}
$$

$$
\begin{aligned}
&\mathit{Plate\ Temperature}\\
&\quad = 1137{,}57253 - 19{,}26790 * \mathit{Tooth\ Height} + 125{,}25000\\
&\quad * \mathit{Tooth\ Top\ Length} - 276{,}45802 * \mathit{Contour\ Offset} + 20{,}00000\\
&\quad * \mathit{Tooth\ Height} * \mathit{Tooth\ Top\ Length} + 1{,}55556 * \mathit{Tooth\ Height}\\
&\quad * \mathit{Contour\ Offset} - 31{,}66667 * \mathit{Tooth\ Top\ Length} * \mathit{Contour\ Offset}\\
&\quad + 0{,}691358 * \mathit{Tooth\ Height}^2 - 111{,}11111 * \mathit{Tooth\ Top\ Length}^2\\
&\quad + 56{,}98765 * \mathit{Contour\ Offset}^2
\end{aligned}
$$

$$Overhang\ Displacement = 0{,}437369 - 0{,}000096 * Tooth\ Height - 0{,}015917 * Tooth\ Top\ Length - 0{,}013870 * Contour\ Offset - 0{,}018333 * Tooth\ Height * Tooth\ Top\ Length + 0{,}002889 * Tooth\ Height * Contour\ Offset - 0{,}005000 * Tooth\ Top\ Length * Contour\ Offset + 0{,}002370 * Tooth\ Height^2 + 0{,}070833 * Tooth\ Top\ Length^2 + 0{,}000593 * Contour\ Offset^2$$

Actual equations of Cone-type support structures

$$Support\ Volume = 777{,}36969 + 725{,}50333 * Contact\ Platform + 3853{,}23333 * Contact\ Part - 1597{,}69062 * Spacing - 286{,}00000 * Contact\ Platform * Contact\ Part - 93{,}00000 * Contact\ Platform * Spacing - 561{,}33333 * Contact\ Part * Spacing - 13{,}24444 * Contact\ Platform^2 - 3076{,}11111 * Contact\ Part^2 + 484{,}51358 * Spacing^2$$

$$Thermal\ Stress = 1{,}27083e + 11 - 9{,}02523e + 10 * Contact\ Platform - 3{,}92625e + 11 * Contact\ Part + 2{,}67620e + 10 * Spacing + 9{,}97750e + 10 * Contact\ Platform * Contact\ Part - 2{,}75233e + 10 * Contact\ Platform * Spacing - 8{,}01500e + 10 * Contact\ Part * Spacing + 2{,}75200e + 10 * Contact\ Platform^2 + 5{,}09500e + 11 * Contact\ Part^2 + 1{,}55733e + 10 * Spacing^2$$

$$Plate\ Temperature = 764{,}77870 - 45{,}93333 * Contact\ Platform + 363{,}00000 * Contact\ Part - 66{,}52593 * Spacing - 17{,}50000 * Contact\ Platform * Contact\ Part + 11{,}66667 * Contact\ Platform * Spacing - 155{,}00000 * Contact\ Part * Spacing + 11{,}33333 * Contact\ Platform^2 + 83{,}33333 * Contact\ Part^2 + 23{,}70370 * Spacing^2$$

$$Overhang\ Displacement = 0{,}496003 - 0{,}024433 * Contact\ Platform + 0{,}030333 * Contact\ Part - 0{,}027511 * Spacing + 0{,}002500 * Contact\ Platform * Contact\ Part + 0{,}001667 * Contact\ Platform * Spacing - 0{,}001667 * Contact\ Part * Spacing + 0{,}004000 * Contact\ Platform^2 + 8{,}25825e - 16 * Contact\ Part^2 + 0{,}007111 * Spacing^2$$

Online Platform Availability

The latest version of the web-based platform is available at no cost via the link below:

https://slmsupportgeneration.web.app/

References and Bibliography

[1] I. Kauppila, “What Is Additive Manufacturing? – Simply Explained,” All3DP, 2021. [Online].

[2] “Precedence Research, Additive Manufacturing Market Size to Surpass USD 95.62 Billion by 2032,” GlobeNewswire, 2023. [Online].

[3] “ISO/ASTM 52900:2021, Additive manufacturing - General principles - Fundamentals and vocabulary, 2nd ed., ISO,” 2021. [Online].

[4] J. Coyne, “I want to break free: The journey towards reducing or eliminating support structures in Additive Manufacturing,” *Metal AM,* vol. 6, 2021.

[5] A. Sinha, “A Review on the Processing of Aero-Turbine Blade Using 3D Print Techniques,” *J. Manuf. Mater. Process.,* vol. 6, no. 1, 2022.

[6] J. Telega, “Suitableness of SLM Manufactured Turbine Blade for Aerodynamical Tests,” *Materials,* vol. 16, no. 7, 2023.

[7] A. A. Al-Tamimi, “Structural optimisation for medical implants through additive manufacturing,” *Progress in Additive Manufacturing,* vol. 5, p. 95–110, 2020.

[8] grafikcadsadditive, “What are the 6 main cost factors of 3D metal printing?,” CADS Additive, May 2021. [Online]. Available: https://www.cads-additive.com/en/what-are-the-6-main-cost-factors-of-3d-metal-printing/. [Accessed April 2025].

[9] FacFox, “How Much Does a Metal 3D Printer Cost?,” Docs, FacFox, August 2022. [Online]. Available: https://facfox.com/docs/kb/how-much-does-a-metal-3d-printer-cost. [Accessed April 2025].

[10] COMSOL, *COMSOL Multiphysics® v6.1,* Stockholm, Sweden: COMSOL AB, 2023.

[11] I. Gibson, Additive Manufacturing Technologies, 3rd ed., Springer, 2021.

[12] *ASTM International, Standard terminology relating to additive manufacturing technologies, ASTM F2792-12,* 2012.

[13] Materialise, *Magics Software, Version 22.03,* 2022.

[14] Ultimaker, *Cura Software, Version 4.11.0,* 2020.

[15] “3D Hubs, Additive Manufacturing Infographic, VoxelMatters,” 2016. [Online].

[16] “Reeves Insight, Shaping our National Competency in Additive Manufacturing,” 2012. [Online].

[17] C. Chen, “Residual stress of typical parts in laser powder bed fusion,” *Journal of Manufacturing Processes,* vol. 59, pp. 621-628, 2020.

[18] S. Chowdhury, “Laser powder bed fusion: a state-of-the-art review of the technology, materials, properties & defects, and numerical modelling,” *Journal of Materials Research and Technology,* vol. 20, pp. 2109-2172, 2022.

[19] Materflow, “SLM – Selective Laser Melting,” [Online]. [Accessed 2022].

[20] P. R. Maina, “A Study on the Effect of Varying Selective Laser Melting Process Parameters by Build Process Simulation,” *Thesis ,* 2020.

[21] Microtrac, “Metal Powders - particle characterization for additive manufacturing processes,” [Online]. [Accessed 2023].

[22] L. Jiao, “Femtosecond Laser Produced Hydrophobic Hierarchical Structures on Additive Manufacturing Parts,” *Nanomaterials,* vol. 8, p. 601, 2018.

[23] C. Y. Yap, “Review of selective laser melting: Materials and applications,” *Appl. Phys. Rev.,* vol. 2, no. 4, 2015.

[24] P. Krakhmalev, “Microstructure and properties of intermetallic composite coatings fabricated by selective laser melting of Ti–SiC powder mixtures,” *Intermetallics,* vol. 46, pp. 147-155, 2014.

[25] K. Le, “On the study of keyhole-mode melting in selective laser melting process,” *International Journal of Thermal Sciences,* vol. 145, 2019.

[26] P. Ninpetch, “Computational Investigation of Thermal Behavior and Molten Metal Flow with Moving Laser Heat Source for Selective Laser Melting Process,” *Case Studies in Thermal Engineering,* vol. 24, 2021.

[27] S. Dhiman, “A framework for effective and clean conversion of machining waste into metal powder feedstock for additive manufacturing,” *Cleaner Engineering and Technology,* vol. 4, 2021.

[28] N. T. Aboulkhair, “The role of powder properties on the processability of Aluminium alloys in selective laser melting,” *Lasers in Manufacturing Conference 2015,* 2015.

[29] K. Zeng, “Optimization of support structures for selective laser melting,” *Electronic Theses and Dissertations,* 2015.

[30] B. Zhang, “Defect Formation Mechanisms in Selective Laser Melting: A Review,” *Chinese Journal of Mechanical Engineering,* vol. 30, p. 515–527, 2017.

[31] W. J. Sames, “The metallurgy and processing science of metal additive manufacturing,” *International Materials Reviews,* vol. 61, no. 5, 2016.

[32] Z. Zhao, “Simulation of Stress Field during the Selective Laser Melting Process of the Nickel-Based Superalloy, GH4169,” *Materials ,* vol. 11, no. 9, 2018.

[33] R. Mertens, “Influence of Powder Bed Preheating on Microstructure and Mechanical Properties of H13 Tool Steel SLM Parts,” *Physics Procedia,* vol. 83, pp. 882-890, 2016.

[34] C. Li, “Residual Stress in Metal Additive Manufacturing,” *Procedia CIRP,* vol. 71, pp. 348-353, 2018.

[35] Y.-S. Chen, “Cake formation and growth in cake filtration,” *Powder Technology,* vol. 192, no. 2, pp. 217-224, 2009.

[36] J. Jiang, “Support Structures for Additive Manufacturing: A Review,” *J. Manuf. Mater. Process,* vol. 2, no. 4, 2018.

[37] K. Stevenson, “SLM Solutions Making Things Easier,” Fabbaloo, 2018 . [Online]. [Accessed 2022].

[38] AMFG, “3D Printing Support Structures: A Complete Guide,” AMFG Autonomous Manufacturing, 2018. [Online]. [Accessed 2022].

[39] Ö. Poyraz, “Investigation of Support Structures for Direct Metal Laser Sintering (DMLS) of IN625 Parts,” *University of Texas at Austin,* 2015.

[40] C. K. Cheng Bo, “Thermal Stresses Associated with Part Overhang Geometry in Electron Beam Additive Manufacturing: Process Parameter Effects,” *University of Texas at Austin,* 2014.

[41] V. Griffiths, “Cost-driven build orientation and bin packing of parts in Selective Laser Melting (SLM),” *European Journal of Operational Research,* vol. 273, no. 1, pp. 334-352, 2019.

[42] A. Z. A. Kadir, “Additive manufacturing cost estimation models—a classification review,” *The International Journal of Advanced Manufacturing Technology,* vol. 107, p. 4033–4053, 2020.

[43] C. Lindermann, “Analyzing Product Lifecycle Costs for a Better Understanding of Cost Drivers in Additive Manufacturing,” *University of Texas at Austin,* 2012.

[44] L. Rickenbacher, “An integrated cost-model for selective laser melting (SLM),” *Rapid Prototyping Journal,* 2013.

[45] T. Krol, “Optimization of Supports in Metal-Based Additive Manufacturing by Means of Finite Element Models,” *University of Texas at Austin,* 2012.

[46] D. Thomas, “The development of design rules for selective laser melting,” *Ph.D. Thesis,* 2009.

[47] F. Calignano, “Design optimization of supports for overhanging structures in aluminum and titanium alloys by selective laser melting,” *Materials & Design,* vol. 64, pp. 203-213, 2014.

[48] M. Langelaar, “Topology optimization of 3D self-supporting structures for additive manufacturing,” *Additive Manufacturing,* vol. 12, pp. 60-70, 2016.

[49] C. Kamath, “Density of additively-manufactured, 316L SS parts using laser powder-bed fusion at powers up to 400 W,” *The International Journal of Advanced Manufacturing Technology,* vol. 74, p. 65–78, 2014.

[50] H. R. Javidrad, “Review of state-of-the-art research on the design and manufacturing of support structures for powder-bed fusion additive manufacturing,” *Progress in Additive Manufacturing,* vol. 8, p. 1517–1542, 2023.

[51] A. Hussein, “Advanced lattice support structures for metal additive manufacturing,” *Journal of Materials Processing Technology,* vol. 213, no. 7, pp. 1019-1026, 2013.

[52] D. Frank, “Expert system-based selection of the preferred direction of build for rapid prototyping processes,” *Journal of Intelligent Manufacturing,* vol. 6, p. 339–345, 1995.

[53] J. Majhi, “Multi-criteria geometric optimization problems in Layered Manufacturing,” in *Fourteenth annual symposium on Computational geometry*, 1998.

[54] P. K. Jain, “Effect of delay time on part strength in selective laser sintering,” *The International Journal of Advanced Manufacturing Technology,* vol. 43, p. 117–126, 2008.

[55] D. Wang, “Research on the fabricating quality optimization of the overhanging surface in SLM process,” *The International Journal of Advanced Manufacturing Technology,* vol. 65, p. 1471–1484, 2013.

[56] S. E. Brika, “Multi-Objective Build Orientation Optimization for Powder Bed Fusion by Laser,” *J. Manuf. Sci. Eng.,* 2017.

[57] R. Samant, “Octree data structure for support accessibility and removal analysis in additive manufacturing,” *Additive Manufacturing,* vol. 22, pp. 618-633, 2018.

[58] Y. Qin, “Automatic determination of part build orientation for laser powder bed fusion,” *Virtual and Physical Prototyping,* vol. 16, no. 1, pp. 29-49 , 2020.

[59] A. Hussein, “Evaluations of cellular lattice structures manufactured using selective laser melting,” *International Journal of Machine Tools and Manufacture,* vol. 62, pp. 32-38, 2012.

[60] M. Cloots, “Assessing New Support Minimizing Strategies for the Additive Manufacturing Technology SLM,” *University of Texas at Austin,* 2013.

[61] G. Strano, “A new approach to the design and optimisation of support structures in additive manufacturing,” *The International Journal of Advanced Manufacturing Technology,* vol. 66, p. 1247–1254, 2013.

[62] Z. Li, “A lightweight and support-free design method for selective laser melting,” *The International Journal of Advanced Manufacturing Technology,* vol. 90, p. 2943–2953, 2016.

[63] M. Langelaar, "Combined optimization of part topology, support structure layout and build orientation for additive manufacturing," *Structural and Multidisciplinary Optimization,* vol. 57, p. 1985–2004, 2018.

[64] Z. Omid, "Design of Easily Removable Lattice-Based Support Structures for L-Pbf," *Preprints ,* 2021.

[65] G. Allaire, "Minimum stress optimal design with the level set method," *Engineering Analysis with Boundary Elements,* vol. 32, no. 11, pp. 909-918, 2008.

[66] D. Brackett, "Topology Optimization for Additive Manufacturing," *University of Texas at Austin,* 2011.

[67] F. v. Keulen, "Topology optimization and additive manufacturing, Natural counterparts for precision systems," in *ASPE 2014 Spring Topical Meeting*, Berkeley, United States, 2014.

[68] V. G. Sundararajan, "Topology optimization for additive manufacturing of customized meso-structures using homogenization and parametric smoothing functions," *UT Electronic Theses and Dissertations,* 2010.

[69] Y. Li, "Beam Structure Optimization for Additive Manufacturing based on Principal Stress Lines," *2010 International Solid Freeform Fabrication Symposium,* 2010.

[70] J.-P. Järvinen, "Characterization of Effect of Support Structures in Laser Additive Manufacturing of Stainless Steel," *Physics Procedia,* vol. 56, pp. 72-81, 2014.

[71] P. N. J. Lindecke, "Optimization of support structures for the laser additive manufacturing of TiAl6V4 parts," *Procedia CIRP,* vol. 74, pp. 53-58, 2018.

[72] Z. Zhang, "Design of internal branch support structures for selective laser melting," *Rapid Prototyping Journal,* 2018 .

[73] K. Zhang, "Study on the Geometric Design of Supports for Overhanging Structures Fabricated by Selective Laser Melting," *Materials,* vol. 12, no. 1, 2019.

[74] W. Ameen, "Design the support structures for easy removal of un-melted powder in metal additive manufacturing," *International Journal of Advanced Science and Technology,* vol. 29, pp. 1847-1854, 2020.

[75] W. Ameen, "Multi-objective optimization of support structures for metal additive manufacturing," *The International Journal of Advanced Manufacturing Technology,* vol. 116, p. 2613–2632, 2021.

[76] W. Ameen, "Optimization of perforated support structures for electron beam additive manufacturing," *The International Journal of Advanced Manufacturing Technology,* vol. 120, p. 7305–7323, 2022.

[77] M. Schmitt, "Parameter identification approach for support structures in laser powder bed fusion and analysis of influencing factors," *Procedia CIRP,* vol. 94, pp. 260-265, 2020.

[78] S. Weber, “Parameters on Support Structure Design for Metal Additive Manufacturing,” *Proceedings of the Design Society: DESIGN Conference,* vol. 1, pp. 1145 - 1154, 2020.

[79] M. Mele, “Experimental investigation into the effect of supports and overhangs on accuracy and roughness in laser powder bed fusion,” *Optics & Laser Technology,* vol. 140, 2021.

[80] T. Markovits, “Characterizing the strength of support-model connection in the case of laser powder bed fusion technology by torsion test,” *Optics & Laser Technology,* vol. 154, 2022.

[81] J. Jhabvala, “An innovative method to build support structures with a pulsed laser in the selective laser melting process,” *The International Journal of Advanced Manufacturing Technology,* vol. 59, p. 137–142, 2011.

[82] C. S. Lefky, “Dissolvable Supports in Powder Bed Fusion-Printed Stainless Steel,” *3D Printing and Additive Manufacturing,* 2017.

[83] C. S. Lefky, “Microstructure and corrosion properties of sensitized laser powder bed fusion printed Inconel 718 to dissolve support structures in a self-terminating manner,” *Additive Manufacturing,* vol. 27, pp. 526-532, 2019.

[84] V. Tripathi, “Milling of Inconel 718 block supports fabricated using laser powder bed fusion,” *Journal of Manufacturing Processes,* vol. 34, pp. 740-749, 2018.

[85] Q. Cao, “Removability of 316L stainless steel cone and block support structures fabricated by Selective Laser Melting (SLM),” *Materials & Design,* vol. 191, 2020.

[86] C. Wei, “Easy-To-Remove Composite Support Material and Procedure in Additive Manufacturing of Metallic Components Using Multiple Material Laser-Based Powder Bed Fusion,” *J. Manuf. Sci. Eng.,* 2019.

[87] I. Roberts, “A three-dimensional finite element analysis of the temperature field during laser melting of metal powders in additive layer manufacturing,” *International Journal of Machine Tools and Manufacture,* vol. 49, pp. 916-923, 2009.

[88] Z. Luo, “A survey of finite element analysis of temperature and thermal stress fields in powder bed fusion Additive Manufacturing,” *Additive Manufacturing,* vol. 21, pp. 318-332, 2018.

[89] Y. Li, “Thermal behavior during selective laser melting of commercially pure titanium powder: Numerical simulation and experimental study,” *Additive Manufacturing,* Vols. 1-4, pp. 99-109, 2014.

[90] EOS, “Additive Manufacturing Technology,” EOS GmbH. [Online]. [Accessed 2023].

[91] H. Shipley, “Optimisation of process parameters to address fundamental challenges during selective laser melting of Ti-6Al-4V: A review,” *International Journal of Machine Tools and Manufacture,* vol. 128, pp. 1-20, 2018.

[92] K. G. Prashanth, "Is the energy density a reliable parameter for materials synthesis by selective laser melting?," *Materials Research Letters,* vol. 5, no. 6, 2017.

[93] S. K. Everton, "Review of in-situ process monitoring and in-situ metrology for metal additive manufacturing," *Materials & Design,* vol. 95, pp. 431-445, 2016.

[94] ScienceDirect, "Fourier Law," Physics of Life Reviews, 2005. [Online]. [Accessed 2023].

[95] X. C. Wang, "Direct Selective Laser Sintering of Hard Metal Powders: Experimental Study and Simulation," *The International Journal of Advanced Manufacturing Technology,* vol. 19, p. 351–357, 2002.

[96] Abaqus, Dassault Systèmes. [Online]. [Accessed 2023].

[97] A. D. Plessi, "10 - Non-destructive testing of parts produced by laser powder bed fusion," *Fundamentals of Laser Powder Bed Fusion of Metals,* pp. 277-300, 2021.

[98] D. Goetz, "A novel approach for the quantitative characterization of shrink lines in the Powder Bed Fusion of metals using a laser beam," *Procedia CIRP,* vol. 111, pp. 832-837, 2022.

[99] U. Lohbauer, "The effect of resin composite pre-heating on monomer conversion and polymerization shrinkage," *Dental Materials,* vol. 25, no. 4, pp. 514-519, 2009.

[100] A. Nickel, "Thermal stresses and deposition patterns in layered manufacturing," *Materials Science and Engineering: A,* vol. 317, no. 1-2, pp. 59-64, 2001.

[101] K. Dai, "Thermal and mechanical finite element modeling of laser forming from metal and ceramic powders," *Acta Materialia,* vol. 52, no. 1, pp. 69-80, 2004.

[102] M. F. Zaeh, "Investigations on residual stresses and deformations in selective laser melting," *Production Engineering,* vol. 4, p. 35–45, 2009.

[103] X. Song, "Residual stresses and microstructure in Powder Bed Direct Laser Deposition (PB DLD) samples," *International Journal of Material Forming,* vol. 8, p. 245–254, 2014.

[104] C. Li, "A multiscale modeling approach for fast prediction of part distortion in selective laser melting," *Journal of Materials Processing Technology,* vol. 229, pp. 703-712, 2016.

[105] Y. Javid, "Thermo-mechanical analysis in pulsed laser cladding of WC powder on Inconel 718," *The International Journal of Advanced Manufacturing Technology,* vol. 92, p. 69–79, 2017.

[106] K.-T. Yang, "Investigation of laser powder bed fusion manufacturing and post-processing for surface quality of as-built 17-4PH stainless steel," *Surface and Coatings Technology,* vol. 422, 2021.

[107] C. Burkhardt, "Thermo-mechanical simulations of powder bed fusion processes: accuracy and efficiency," *Advanced Modeling and Simulation in Engineering Sciences,* 2022.

[108] H. Ruan, “A thermo-mechanical phase-field fracture model: Application to hot cracking simulations in additive manufacturing,” *Journal of the Mechanics and Physics of Solids,* vol. 172, 2023.

[109] K. Zeng, “Evaluations of effective thermal conductivity of support structures in selective laser melting,” *Additive Manufacturing,* vol. 6, pp. 67-73, 2015.

[110] M. Gan, “Practical support structures for selective laser melting,” *Journal of Materials Processing Technology,* vol. 238, pp. 474-484, 2016.

[111] E. Malekipour, “Heat Conduction and Geometry Topology Optimization of Support Structure in Laser-Based Additive Manufacturing,” *Mechanics of Additive and Advanced Manufacturing,* vol. 9, p. 17–27, 2017.

[112] MATLAB, *MathWorks,* version 2021.

[113] L. Cheng, “On utilizing topology optimization to design support structure to prevent residual stress induced build failure in laser powder bed metal additive manufacturing,” *Additive Manufacturing,* vol. 27, pp. 290-304, 2019.

[114] L. Cheng, “Part-scale build orientation optimization for minimizing residual stress and support volume for metal additive manufacturing: Theory and experimental validation,” *Computer-Aided Design,* vol. 113, pp. 1-23, 2019.

[115] U. Umer, “Modeling the Effect of Different Support Structures in Electron Beam Melting of Titanium Alloy Using Finite Element Models,” *Metals,* vol. 9, no. 7, 2019.

[116] K. Bartsch, “Benchmark parts for the evaluation of optimized support structures in Laser Powder Bed Fusion of metals,” *Procedia CIRP,* vol. 94, pp. 254-259, 2020.

[117] B. B. Ravichander, “Cost-Aware Design and Fabrication of New Support Structures in Laser Powder Bed Fusion: Microstructure and Metallurgical Properties,” *Applied Sciences,* vol. 11, no. 21, 2021.

[118] J. Xiaohui, “Effect of supporting structure design on residual stresses in selective laser melting of AlSi10Mg,” *The International Journal of Advanced Manufacturing Technology,* vol. 118, p. 1597–1608, 2021.

[119] T. Miki, “Topology optimization of the support structure for heat dissipation in additive manufacturing,” *Finite Elements in Analysis and Design,* vol. 203, 2022.

[120] U. Paggi, “Implementation of contactless supports for industrially relevant additively manufactured parts in metal,” *Additive Manufacturing Letters,* vol. 3, 2022.

[121] B. Cheng, “Geometric consideration of support structures in part overhang fabrications by electron beam additive manufacturing,” *Computer-Aided Design,* vol. 69, pp. 102-111, 2015.

[122] B. Cheng, “A numerical investigation of support structure designs for overhangs in powder bed electron beam additive manufacturing,” *Journal of Manufacturing Processes,* vol. 49, pp. 187-195, 2020.

[123] K. Cooper, “Contact-Free Support Structures for Part Overhangs in Powder-Bed Metal Additive Manufacturing,” *Inventions,* vol. 3, no. 1, 2018.

[124] U. Paggi, “New Support Structures for Reduced Overheating on Downfacing Regions of Direct Metal Printed Parts,” *International Solid Freeform Fabrication Symposium,* 2019.

[125] A. Çelik, “Contact-Free Support Structures for the Direct Metal Laser Melting Process,” *Materials ,* vol. 15, no. 11, 2022.

[126] O. Gülcan, “The effect of contactless support parameters on the mechanical properties of laser powder bed fusion produced overhang parts,” *The International Journal of Advanced Manufacturing Technology,* vol. 122, p. 3235–3253, 2022.

[127] J. Vanek, “Clever Support: Efficient Support Structure Generation for Digital Fabrication,” *Computer Graphics Forum,* vol. 33, no. 5, pp. 117-125, 2014.

[128] Autodesk, “Meshmixer,” [Online]. [Accessed 2022].

[129] B. Zhang, “CAD-based design and pre-processing tools for additive manufacturing,” *Journal of Manufacturing Systems,* vol. 52, pp. 227-241, 2019.

[130] B. Vaissier, “Genetic-algorithm based framework for lattice support structure optimization in additive manufacturing,” *Computer-Aided Design,* vol. 110, pp. 11-23, 2019.

[131] Y. Zhang, “Bio-inspired generative design for support structure generation and optimization in Additive Manufacturing (AM),” *CIRP Annals,* vol. 69, no. 1, pp. 117-120, 2020.

[132] T.-H. Kwok, “Escaping Tree-Support (ET-Sup): minimizing contact points for tree-like support structures in additive manufacturing,” *Rapid Prototyping Journal,* vol. 27, no. 8, 2021 .

[133] S. Weber, “Parametric design optimisation of tree-like support structure for the laser-based powder bed fusion of metals,” *Journal of Manufacturing Processes,* vol. 84, pp. 660-668, 2022.

[134] Materialise, “Support Generation for Metal,” e-Stage for Metal+. [Online]. [Accessed 2023].

[135] Materialise, “Materialise Magics, Ansys Simulation Software,” [Online]. [Accessed 2023].

[136] Oqton, “Metal additive manufacturing simulation software,” Amphyon. [Online]. [Accessed 2023].

[137] Oqton, “All-In-One Industrial Additive Manufacturing Software,” 3DXpert. [Online]. [Accessed 2023].

[138] Hexagon, “CADS Additive,” AM-Studio. [Online]. [Accessed 2023].

[139] CoreTechnologies, 4D_Additive Manufacturing. [Online]. [Accessed 2023].

[140] VoxelDance, VoxelDance Additive 4.1. [Online]. [Accessed 2024].

[141] Autodesk, “Additive manufacturing, design, and simulation,” Fusion 360 with Netfabb. [Online]. [Accessed 2023].

[142] G. Derringer, “Simultaneous Optimization of Several Response Variables,” *Journal of Quality Technology,* vol. 12, no. 4, 1980.

[143] R. H. Myers, Response Surface Methodology: Process and Product Optimization Using Designed Experiments, 4th ed.

[144] SolidWorks, *version 2021, 3D CAD Design Software,* Dassault Systèmes.

[145] *Design-Expert, version 13, Stat-Ease, Inc..*

[146] MatWeb, “Material Property Data,” [Online]. [Accessed 2022].

[147] E. GmbH, “Material Data Sheet EOS Titanium Ti64 Grade 5,” [Online]. [Accessed 2022].

[148] EOS, *EOS Build and EOS Build+ Software.*

[149] “ViewSTL,” [Online]. Available: https://www.viewstl.com/.

[150] A. Joshi, “Likert scale: Explored and explained,” *British Journal of Applied Science & Technology,* p. 396–403, 2015.

[151] G. Taguchi, Robust Engineering: Learn How to Boost Quality While Reducing Costs & Time to Market, 1999.

[152] D. Montgomery, Design and analysis of experiments, 9th ed., 2017.

[153] G. Box, Statistics for experimenters, 2nd ed., 2005.

[154] F. Mezzadri, “Topology optimization of self-supporting support structures for additive manufacturing,” *Additive Manufacturing,* vol. 21, pp. 666-682, 2018.

[155] M. Seabra, “Selective laser melting (SLM) and topology optimization for lighter aerospace componentes,” *Procedia Structural Integrity,* vol. 1, pp. 289-296, 2016.

[156] L. Parry, “PySLM v0.4.0,” [Online]. Available: https://github.com/drlukeparry/pyslm. [Accessed 2023].

[157] I. Meta Platforms, “React documentation,” [Online]. Available: https://react.dev/. [Accessed 2023].

[158] Mr.doob, “three.js documentation, GitHub repository,” [Online]. Available: https://github.com/mrdoob/three.js. [Accessed 2023].

[159] Pmndrs, “react-three-fiber, GitHub repository,” [Online]. Available: https://github.com/pmndrs/react-three-fiber. [Accessed 2023].

[160] Python.Software.Foundation, “Python programming language,” [Online]. Available: https://www.python.org/.

[161] Google, “Firebase documentation, version 13.6.0,” [Online]. Available: https://firebase.google.com/. [Accessed 2023].

[162] Google, “Google Cloud Storage API,” [Online]. Available: https://cloud.google.com/storage/docs/apis. [Accessed 2023].

[163] M.Dawson-Haggerty, “Trimesh: Python library for loading and using triangular meshes, GitHub repository,” [Online]. Available: https://github.com/mikedh/trimesh. [Accessed 2023].

[164] B. Eich, “JavaScript, Programming Language,” [Online]. Available: https://www.javascript.com/. [Accessed 2023].

[165] J. Byerley, “"pymadcad," GitHub, v0.16,” [Online]. Available: https://github.com/jimy-byerley/pymadcad. [Accessed 2023].

[166] Raise3D, *ideaMaker Software, Version 4.3.3,* 2020.

[167] COMSOL, “Reference Manual, COMSOL Documentation,” [Online]. Available: https://doc.comsol.com/6.2/docserver/#!/com.comsol.help.comsol/helpdesk/helpdesk.html. [Accessed 2024].

[168] Ansys, “Developer Documentation,” [Online]. Available: https://developer.ansys.com/docs. [Accessed 2024].

[169] A. Dimopoulos, “SLM Support Generation Platform,” TWI Hellas, [Online]. Available: https://slmsupportgeneration.web.app/. [Accessed 2024].

[170] R. Myers, Response surface methodology: process and product optimization using designed experiments, 4th ed., 2016.